

Simulations and Data analysis for the 35 ton Liquid Argon detector as a prototype for the DUNE experiment



The
University
Of
Sheffield.

Thomas Karl Warburton

Department of Physics and Astronomy
University of Sheffield

This dissertation is submitted for the degree of
Doctor of Philosophy

March 2017

I would like to dedicate this thesis to my loving parents ...

Declaration

I hereby declare that except where specific reference is made to the work of others, the contents of this dissertation are original and have not been submitted in whole or in part for consideration for any other degree or qualification in this, or any other university. This dissertation is my own work, and where work has been done in collaboration with others the best attempts have been made to indicate this. Any work which was performed by another individual has been expressed as such, with these figures and tables being labelled with a source.

The information contained in Chapters 1 and 2 are highly level summaries of the theory necessary to support this thesis, and the various facets of the DUNE experiment. These summaries have been taken from a number of articles, and are referenced as such. When discussing the LArSoft software which DUNE uses, it is necessary to point out that this is a multi-experiment project, and so many people have contributed to its development in their own small ways, including myself.

Chapter 3 details the camera system which was installed in the 35 ton detector. The selection and basic design of the camera system was principally done by Dr. Nicola McConkey, and Matthew Thiesse, with only very minor input from the author. All work performed at Fermilab was done in conjunction with Michael Wallbank, and would have been impossible without the assistance of Dr. Linda Bagby.

Chapter 4 details the simulations performed on the 35 ton detector. All work presented here is my own, though it builds on large pieces of work developed by others, such as the reconstruction of both TPC and photon detector data, as well as the premise of the particle identification method which is proposed. I must thank Dr. Tingjun Yang and Dr. Tom Junk for their helpful insights in developing the methods shown here.

Chapter 5 details all aspects of the 35 ton data which was recorded. The method of data refactorisation is my own work, as is the inclusion of a Wiener filter to the data, other work is referenced to the working group presentations where they were proposed. The final section

on electron diffusion is my own work, though I must thank Dr. Michelle Stancari and Dr. Dominic Brailsford for their helpful discussions.

Chapter 6 details the far detector simulations which were performed. Section 6.1 details simulations performed for the LBNE surface detector, where the authors work concentrated on the implementation of the accurate detector geometry and surface profile. Simulations involving the simple geometry, and simple surface profile were performed by Dr. Martin Richardson. All work was shown in his thesis, with according references, and so all tables have been taken from there, as these had used an improved analysis to the one which we had used in partnership. The generator used for the underground location is accordingly referenced, and the generation of the sample of muons which is used was done by Dr. Matthew Robinson. The analysis presented is unique to the author, though thanks must be given to all members of the cosmogenics working group for their helpful insights.

Thomas Karl Warburton

March 2017

Acknowledgements

First of all, I would like to express my deepest thanks to my supervisor, Dr. Vitaly Kudryavtsev. I could not have produced this work without your ever watchful guidance and support. It has been a truly wonderful experience working with you for the last four and a half years.

A huge thanks must also go to Dr. Michelle Stancari, Dr. Tingjun Yang, and Dr. Tom Junk, who supervised me during my attachment at Fermilab. I could not have asked for more friendly, knowledgeable and passionate people to be in collaboration with, and if I can become the half the physicists that any of you are, I would be immensely proud. I would also like to thank every single member of the dedicated team of people who worked on the 35 ton, you all contributed to my development as a physicist. A special mention must of course go to Michael Wallbank, who I have spent the majority of my PhD living with and sitting next to, and whose laugh will forever be etched in my psyche. Concerning Fermilab, it is impossible to list all of the amazing (and truly interesting) people that I met there, though every single one of them made my stay at Fermilab two of the best years of my life. I look forward to the next four years being as memorable as the last two!

It would be impossible to not thank everyone in the Particle Physics group of Sheffield, whose sometimes constant distractions only made to make living Sheffield more enjoyable. Special thanks must go to those people that I shared an office with, Martin Richardson, Andrew Scarff, Matthew Thiesse, David Woodward, Anthony Ezeribe, Patrick Stowell, Dr. Nicola McConkey, Dr. Celeste and Liam.

Finally, it goes without saying that none of this would have been possible without the fantastic support that I receive from my entire family. I wouldn't swap their feigning of interest and sarcastic comments about Sheldon for anything. It is immeasurably valuable to have a best friend for a sister, a bed of support for a mother, a rock for a grandmother, and a Pete for a "Pete". None of this would have been possible without each and every one of you.

Abstract

This is where you write your abstract ...

Table of contents

List of figures	x
List of tables	xvii
Nomenclature	xix
1 Introduction and Theory	1
1.1 Neutrino physics	3
1.1.1 The history of neutrino oscillation	3
1.1.2 The theory of neutrino oscillations	5
1.1.3 CP-Violation and matter effects	5
1.1.4 Current experimental limits, and future experiments	5
1.2 Grand Unifying Theories and nucleon decay	5
1.2.1 The cosmogenic background to nucleon decay	5
2 The Deep Underground Neutrino Experiment	6
2.1 The DUNE schedule	7
2.2 LBNF - the DUNE detector location and neutrino beam	8
2.3 The potential DUNE Detector designs	13
2.3.1 The single phase detector design	13
2.3.2 The dual phase detector design	15
2.3.3 Reference near detector design	17
2.4 The physics capabilities of DUNE	20
2.4.1 Neutrino physics	20
2.4.2 Nucleon decay	27
2.4.3 The detection of supernova neutrino bursts and other physics opportunities	30
2.5 Path to building DUNE - The 35 ton prototype	31
2.6 The DUNE software	38

3 The 35 ton camera system	47
3.1 The selection and characterisation of cameras	48
3.2 The design of the camera system	49
3.3 Performance in the 35 ton	53
4 Simulations of the 35 ton prototype	57
4.1 Determination of interaction times	57
4.2 Calibrating calorimetric constants	62
4.3 Discerning reconstruction efficiencies	63
4.4 Performing particle identification	72
5 The 35 ton data sample	93
5.1 Organisation of the data structure	93
5.2 Reformatting the data to the offline structure	97
5.3 Observations on data quality and noise mitigation	98
5.4 Performance of reconstruction algorithms	104
5.5 Measuring interaction times using electron diffusion	112
5.5.1 Determining interaction times in 35 ton data	115
5.5.2 Determining interaction times in a low-noise detector using Monte Carlo, and differences with data	124
5.5.3 Discerning the impact of changing detector properties using Monte Carlo samples	132
5.5.4 The limitations of and future improvements to the method of interaction time determination using diffusion	143
6 Simulations of the DUNE Far Detector	145
6.1 Simulations of the LBNE surface detector	145
6.1.1 Classifying signal and background events	148
6.1.2 Description of cuts used	149
6.1.3 Generating particles for background studies	151
6.1.4 Results from background simulations	153
6.1.5 Summary of simulations for the LBNE surface detector	157
6.2 The use of MUSUN in LArSoft	158
6.3 Nucleon decay channels in DUNE	161
6.3.1 Cosmogenic background to the $n \rightarrow K^+ + e^-$ decay channel	164
6.3.2 Signal events in the $n \rightarrow K^+ + e^-$ decay channel	170

6.3.3	Energy constraints on the cosmogenic background to the $n \rightarrow K^+ + e^-$ decay channel	179
6.3.4	Future improvements to nucleon decay studies and conclusions . . .	190
7	Conclusion	192
	References	193
	Appendix A Supporting figures to Monte Carlo studies concerning determining interaction times using the effects of diffusion	202
	Appendix B Something else mildly interesting	212

List of figures

1.1	How the interaction of a cosmic muon can mimic a nucleon decay signature	5
2.1	A representation of the DUNE experimental setup	7
2.2	A high level summary of the DUNE schedule	8
2.3	A representation of the future LBNF cavern system at SURF	11
2.4	A representation of the future LBNF near site at Fermilab	12
2.5	A cross section of the DUNE single phase detector design	14
2.6	An illustration of the wire wrapping in the DUNE single phase design . . .	16
2.7	An illustration of the process of charge extraction in the DUNE dual phase detector design	18
2.8	A schematic representation of what the reference DUNE ND could look like	19
2.9	The ν_e appearance probability at 1300 km as a function of neutrino energy, for a range of values of δ_{CP}	21
2.10	The significance with which DUNE will be able to determine the neutrino mass hierarchy, for all values of δ_{CP}	22
2.11	The significance with which DUNE will be able to determine the value of δ_{CP} , for all values of δ_{CP}	23
2.12	The resolution with which DUNE will be able to determine the value of δ_{CP} , for increasing exposures	24
2.13	The significance to which the octant of θ_{23} can be determined, for values of θ_{23}	25
2.14	The resolution with which DUNE will be able to determine the value of $\sin^2 \theta_{23}$ for increasing exposures	26
2.15	The resolution with which DUNE will be able to determine the value of $\sin^2 \theta_{13}$ for increasing exposures	26
2.16	The resolution with which DUNE will be able to determine the value of Δm_{31}^2 for increasing exposures	27
2.17	A comparison of current, and future, nucleon decay lifetime limits, compared with the ranges predicted by Grand Unifying Theories.	29

2.18 A kaon event which was observed in the ICARUS T600 detector, in the CNGS data	30
2.19 The predicted time-dependant signal, for an electron-capture supernova, at a distance of 10 kpc from Earth	32
2.20 An overview of the DUNE prototyping schedule, including complementary experiments	33
2.21 A schematic representation of the TPC installed in 35 ton prototype, for the Phase II run	36
2.22 A representation of the counter locations in the 35 ton	37
2.23 The LArSoft co-ordinate system as it is represented in the 35 ton.	40
2.24 A selection of reconstructed hits, from simulated energy depositions	42
2.25 Performing disambiguation with different wire pitches.	44
3.1 The components which made up a camera module used in the 35 ton camera system	50
3.2 Two camera modules which are mounted in the 35 ton prototype detector . .	51
3.3 The system diagram for the 35 ton camera system	52
3.4 The calibration images for the 8 cameras used in the 35 ton camera system .	54
3.5 The signal degradation over time for two cameras in the 35 ton camera system	55
4.1 Matching tracks and flashes in the 35 ton using positions in the yz plane . .	59
4.2 The central x position of a reconstructed track versus the number of detected photoelectrons	60
4.3 The predicted x positions of flashes using the relationship between photo-electron and drift distance	60
4.4 The number of events as a function of the difference between Monte Carlo and photon detector times	61
4.5 The calibration of the calorimetric constants in the 35 ton	64
4.6 The reconstruction efficiencies for simulated events as a function of the track length in the detector from Monte Carlo truth.	67
4.7 The reconstruction efficiencies for simulated events as a function of the deposited energy from Monte Carlo truth.	67
4.8 The reconstruction efficiencies for simulated events as a function of the θ track angle from Monte Carlo truth track.	68
4.9 The reconstruction efficiencies for simulated events as a function of the ϕ track angle from Monte Carlo truth track.	68

4.10	The reconstruction efficiencies for simulated events as a function of the θ and ϕ track angles from Monte Carlo truth track.	69
4.11	The mean energy loss per unit track length of different particle masses in different materials	73
4.12	Stopping power for different particle masses as a function of residual range in liquid argon	75
4.13	The distribution of PIDA values, calculated using Monte Carlo truth, for different particle masses	76
4.14	The reconstruction efficiencies for protons in a sample generated using CRY.	77
4.15	The reconstruction efficiencies for the simulated isolated muon and proton samples in the 35 ton detector.	79
4.16	The calculated PIDA values for the simulated isolated muon and proton samples in the 35 ton detector.	80
4.17	The $\frac{dE}{dx}$ versus residual range plot for the simulated isolated muon and proton samples in the 35 ton detector.	81
4.18	The calculated PIDA values for the simulated proton enriched sample in the 35 ton detector	86
4.19	The calculated PIDA values, as a function of the reconstructed track length, for the simulated proton enriched sample in the 35 ton detector	88
4.20	The calculated PIDA values, as a function of the reconstructed track length, for the simulated proton enriched sample in the 35 ton detector	89
4.21	The calculated PIDA values for the simulated proton enriched sample in the 35 ton detector, after a cut on the minimum reconstructed track length is applied	90
4.22	The calculated PIDA values for the simulated proton enriched sample in the 35 ton detector, after tracks from particles which do not stop in the detector are removed	91
5.1	The 35 ton data sample	94
5.2	The 35 ton data structure	96
5.3	Dropped TPC data in the 35 ton	99
5.4	Recovering stuck ADC codes in the 35 ton	100
5.5	Removing coherent noise in the 35 ton	101
5.6	Applying Wiener filters to the 35 ton data	102
5.7	The effect of noise removal algorithms in the 35 ton	103
5.8	dQ/dx in the 35 ton as a function of drift time	106
5.9	The numbering scheme for the East - West counters in the 35 ton	107

5.10	The dot product of the track and vector joining the centres of the coincidence counters in the yz plane	108
5.11	The alignment of reconstructed tracks with the vectors joining the centres of the coincidence counters	108
5.12	Reconstruction efficiencies of through going tracks in the 35 ton data	111
5.13	Schematic showing the process of diffusion	113
5.14	A simulated event display showing multiple tracks and flashes in the 35 ton	114
5.15	The effect of adding a noise baseline to a hit	116
5.16	The most probable values of the <i>RMS</i> and <i>RMS/Charge</i> distributions for tracks with a counter difference of 4 in the 35 ton data	117
5.17	The drift distance dependence of diffusion in the 35 ton dataset for coincidences with a counter difference of 4	118
5.18	The angular dependence of diffusion in the 35 ton dataset for hits within 10 cm of the APAs	119
5.19	The distribution of normalised hit charge in the 35 ton dataset	120
5.20	The difference between the predicted and reconstructed hit times in the 35 ton dataset	121
5.21	The accuracy of the hit <i>RMS</i> method in the 35 ton dataset	122
5.22	The accuracy of the hit <i>RMS/Charge</i> method in the 35 ton dataset	123
5.23	The most probable values of the <i>RMS</i> and <i>RMS/Charge</i> distributions for tracks with a counter difference of 4 in the 35 ton data and a low noise 35 ton detector	126
5.24	The drift distance dependence of diffusion in the 35 ton dataset and Monte Carlo for coincidences with a counter difference of 4	127
5.25	The angular dependence of diffusion in the 35 ton dataset and Monte Carlo for hits within 10 cm of the APAs	127
5.26	The distribution of normalised hit charge in the 35 ton dataset and a Monte Carlo sample	128
5.27	Comparing the accuracy of the hit <i>RMS</i> method in the 35 ton dataset and a Monte Carlo simulation	129
5.28	Comparing the accuracy of the hit <i>RMS</i> method in the 35 ton dataset and a Monte Carlo simulation	131
5.29	Comparing the accuracy of the hit <i>RMS</i> method, as the electronic noise changes	134
5.30	Comparing the accuracy of the hit <i>RMS</i> method, as the electronic noise level changes	135

5.31 Comparing the accuracy of the hit <i>RMS</i> method, as the electron lifetime changes	136
5.32 Comparing the accuracy of the hit <i>RMS</i> method, as the electron lifetime changes	137
5.33 Comparing the accuracy of the hit <i>RMS</i> method, as the electric field changes	138
5.34 Comparing the accuracy of the hit <i>RMS</i> method, as the electric field changes	139
5.35 Comparing the accuracy of the hit <i>RMS</i> method, as the constant of longitudinal diffusion changes	140
5.36 Comparing the accuracy of the hit <i>RMS</i> method, as the constant of longitudinal diffusion changes	141
6.1 The <i>complex</i> detector geometry used in the LBNE surface detector simulations	147
6.2 A diagram of the PoCA, and the angle w.r.t the beam, calculations in the LBNE surface detector simulations	150
6.3 The correlation between the surface profile, and the distribution of azimuthal angles at the DUNE far detector site	160
6.4 The distributions of some of the important quantities for a sample of 10^6 muons generated by MUSUN, in LArSoft	162
6.5 The initial positions of muons generated by MUSUN, around a DUNE 10 kt module	163
6.6 A simulated $n \rightarrow K^+ + e^-$ decay which occurred in a gap between TPCs . .	167
6.7 The energy distribution of background events surviving the application of sequential cuts in the $n \rightarrow K^+ + e^-$ channel	169
6.8 The normalised energy distribution of background events surviving the application of sequential cuts in the $n \rightarrow K^+ + e^-$ channel	169
6.9 A simulated $n \rightarrow K^+ + e^-$ decay which occurred near the edge of the detector volume	171
6.10 The energy distribution of signal events surviving the application of sequential cuts in the $n \rightarrow K^+ + e^-$ channel	172
6.11 The normalised energy distribution of signal events surviving the application of sequential cuts in the $n \rightarrow K^+ + e^-$ channel	172
6.12 A simulated $n \rightarrow K^+ + e^-$ decay where the kaon did not deposit any energy in the active volume	174
6.13 The number of events, as a function of the energy deposited within 2 cm, 5 cm, and 10 cm of the detector edges.	176
6.14 The separation of the kaon and the electron produced in the $n \rightarrow K^+ + e^-$ decay channel	177

6.15	The normalised energy distribution of signal events, and cosmic background events, surviving the application of sequential cuts, after the fiducial cut is modified	178
6.16	The energy directly deposited by kaons, as a function of the energy directly deposited by electrons, in the simulated nucleon decay, and cosmic background samples	182
6.17	The energy directly deposited by kaons, plus the energy directly deposited by electrons, as a function of the energy deposited near the kaon and electron vertex, in the simulated nucleon decay, and cosmic background samples . .	183
6.18	The energy directly deposited by kaons, plus the energy deposited by the kaon decay products, as a function of the energy depositions which do not fit any of the other criteria, in the simulated nucleon decay, and cosmic background samples	184
6.19	The energy directly deposited by kaons, plus the energy deposited by the kaon decay products, plus the energy directly deposited by electrons, plus the energy deposited near the kaon and electron vertex, as a function of the energy depositions which do not fit any of the other criteria, in the simulated nucleon decay, and cosmic background samples	185
6.20	The number of events, as a function of the energy deposited by the kaon decay products.	187
A.1	The most probable values of the hit <i>RMS</i> and hit <i>RMS/Charge</i> distributions for tracks with a counter difference of 4, as the electronics noise changes . .	203
A.2	The drift distance dependence of diffusion in the 35 ton dataset and Monte Carlo for coincidences with a counter difference of 4, as the electronics noise changes	203
A.3	The angular dependence of diffusion in the 35 ton dataset and Monte Carlo for hits within 10 cm of the APAs, as the electronics noise changes	204
A.4	The normalised hit charge distribution as the electronics noise changes . .	204
A.5	The most probable values of the hit <i>RMS</i> and hit <i>RMS/Charge</i> distributions for tracks with a counter difference of 4, as the electron lifetime changes . .	205
A.6	The drift distance dependence of diffusion in the 35 ton dataset and Monte Carlo for coincidences with a counter difference of 4, as the electron lifetime changes	205
A.7	The angular dependence of diffusion in the 35 ton dataset and Monte Carlo for hits within 10 cm of the APAs, as the electron lifetime changes	206
A.8	The normalised hit charge distribution as the electron lifetime changes . .	206

A.9 The most probable values of the hit <i>RMS</i> and hit <i>RMS/Charge</i> distributions for tracks with a counter difference of 4, as the electric field changes	207
A.10 The drift distance dependence of diffusion in the 35 ton dataset and Monte Carlo for coincidences with a counter difference of 4, as the electric field changes	208
A.11 The angular dependence of diffusion in the 35 ton dataset and Monte Carlo for hits within 10 cm of the APAs, as the electric field changes	208
A.12 The normalised hit charge distribution as the electric field changes	209
A.13 The most probable values of the hit <i>RMS</i> and hit <i>RMS/Charge</i> distributions for tracks with a counter difference of 4, as the constant of longitudinal diffusion changes	209
A.14 The drift distance dependence of diffusion in the 35 ton dataset and Monte Carlo for coincidences with a counter difference of 4, as the constant of longitudinal diffusion changes	210
A.15 The angular dependence of diffusion in the 35 ton dataset and Monte Carlo for hits within 10 cm of the APAs, as the constant of longitudinal changes .	210
A.16 The normalised hit charge distribution as the constant of longitudinal diffusion changes	211

List of tables

2.1	The parameters of the wire planes in the DUNE FD single phase design	15
2.2	The exposure in units in units of kt MW years, as a function of time, assuming a staged DUNE construction	21
2.3	Nucleon decay limits in DUNE and Super-Kamiokande, in some favoured decay channels	29
4.1	Stopping power parameterisation for various particle types in liquid argon	74
4.2	The properties of initial particles simulated in the muon and proton samples. The angles θ_{xz} , and θ_{yz} , are defined as the angle that a vector makes in the xz , and yz planes, respectively.	78
4.3	A summary of the PIDA values calculated for the simulated isolated proton sample, as sequential cuts are applied	83
4.4	A summary of the PIDA values calculated for the simulated isolated muon sample, as sequential cuts are applied	83
4.5	A summary of the PIDA values calculated for the primary particles in the simulated isolated proton sample, as sequential cuts are applied	84
5.1	The angles which tracks, with given counter differences have, relative to the APA frames	110
6.1	The minimum energies of simulated particles, when determining the cosmogenic background for the LBNE surface detector	152
6.2	The normalised annual background rate for the <i>simple</i> detector geometry, using the flat surface profile	153
6.3	The normalised annual background rate, for events where a primary muon enters the active volume of the detector, for the <i>complex</i> geometry and accurate surface profile	154

6.4	The normalised annual background rate, for events where a primary muon misses the active volume of the detector, for the <i>complex</i> geometry and accurate surface profile	155
6.5	The normalised annual background rate, for proton induced events, for the <i>complex</i> geometry	156
6.6	The normalised annual background rate, for neutron induced events, for the <i>complex</i> geometry	157
6.7	The normalised annual background rate for the <i>simple</i> detector geometry and flat surface profile, and for the <i>complex</i> geometry and accurate surface profile	158
6.8	Muon flux parameters as calculated with MUSIC/MUSUN.	159
6.9	The number of events which could mimic a $n \rightarrow K^+ + e^-$ decay, when cuts are applied in isolation	170
6.10	The most common decay modes of charged kaons, and their probabilities .	187

Nomenclature

Roman Symbols

tick Unit of time equal to 500 ns

Acronyms / Abbreviations

art analysis reconstruction framework

ADC Analogue to Digital Converter

APA Anode Plane Assembly

CCD Charge-Couple Device

CDR Conceptual Design Review

CMOS Complementary Metal-Oxide Semiconductor

CPA Cathode Plane Assembly

CP Charge-Parity

CRC Cosmic Ray Counter

CRP Charge Readout Planes

CRY Cosmic-ray Shower Library

DUNE Deep Underground Neutrino Experiment

DVR Digital Video Recorder

ECal Electromagnetic Calorimeter

FD Far Detector

Fermilab Fermi National Lab

FGT Fine-Grained Tracker

FNAL Fermi National Lab

GENIE Generates Events for Neutrino Interaction Experiments

GUT Grand Unified Theory

HV High Voltage

LAr Liquid Argon

LArSoft Liquid Argon Software

LArTPC Liquid Argon Time Projection Chamber

LAS LEM/Anode Sandwiches

LBNE Long Baseline Neutrino Experiment

LBNF Long Baseline Neutrino Facility

LBNO Long Baseline Neutrino Observatory

LEM Large Electron Multipliers

MIP Minimally Ionising Particle

MPV Most Probable Value

MUSIC MUon Simulation Code

MUSUN MUon Simulations UNderground

ND Near Detector

PCB Printed Circuit Board

PD Photon Detector

PID Particle IDentification

PIP-II Proton Improvement Plan II

PMT Photo Multiplier Tubes

PoCA Point of Closest Approach

ROI Region Of Interest

RPC Resistive Plate Chambers

SiPM Silicon Photo Multiplier

SK Super Kamiokande

SM Standard Model

SSP SiPM Signal Processor

SURF Sanford Underground Research Facility

TPC Time Projection Chamber

Chapter 1

Introduction and Theory

The “Standard Model of Particle Physics” (SM) is a set of theories which has been widely tested and has been found to accurately predict the interactions of fundamental particles. These tests have come in many forms throughout the 20th and 21st centuries, and include the observation of all of the particles which it predicts, as well as measurements of the properties of these particles. The recent discovery of the Higgs boson [1, 2] “completed” the SM, as this was the last particle which it predicted to be observed. However, despite its many successes the SM does not represent the “final” theory of fundamental particle physics, should one exist. This is because there are many questions made by recent experimental observations which the SM is unable to address, some of these will be briefly discussed below.

Firstly, though the SM accurately predicts the interactions made by the electromagnetic, weak nuclear, and strong nuclear forces, it makes no mention of gravity. This is a major flaw of the SM as gravity is one of the driving forces in the formation of astronomical objects such as planets, stars, and galaxies. With the recent detection of gravitational waves [3] this issue has again been brought into focus. Secondly, when studying rotational velocities of galaxies, the measured velocities exceed the speeds predicted unless there is a significant amount of matter present in the galaxies which we are unable to detect. The SM makes no prediction as to what this “dark-matter” is comprised of. Thirdly, from measurements of distant supernovae it appears that the expansion of the universe is accelerating, not decelerating as would be expected, this implies the presence of some form of unknown energy source. Again, the SM makes no prediction as to what this unknown energy source, or “dark-energy” is. A further point of consternation with the SM is that it is not “elegant,” as it has as many as 19 free parameters, which each appear unrelated to each other. There are also unresolved questions regarding the particles which are predicted by the SM, such as, why charge is quantised, why there are exactly 3 families of quarks and leptons, and why they have the observed

hierarchy of masses. The SM also does not predict the matter-antimatter asymmetry which is observed in the universe today. Finally, the neutrinos predicted by the SM are massless, however, numerous measurements of neutrino oscillation show that this is highly unlikely. This is because, it is largely accepted that in order for oscillations to occur, at least two of the neutrino flavours must have non-zero mass. A rigorous discussion of neutrino oscillations is presented in Section 1.1.

Extensive efforts have been made to resolve many of these issues with the SM, in the form of a so-called Grand Unifying Theory (GUT). Many of these theories propose that the electroweak and strong nuclear forces belong to an overarching symmetry group, though this is predicted to occur at extremely high energies, far beyond the reaches of current experiments. As a result, many of the experimental signatures which these GUTs predict are difficult to measure. However, many GUTs predict that the proton, a stable particle in the SM, should decay with a lifetime of the order of 10^{34} years. Some of the more common mechanisms by which GUTs are predicted are briefly discussed in Section 1.2, with reference to the proton lifetimes which they predict.

The Deep Underground Neutrino Experiment (DUNE) is a next generation experiment situated at the Sanford Underground Research Facility (SURF), which aims to measure many of the properties of neutrinos, as well as to search for nucleon decays. The experimental setup, physics capabilities, and prototyping schedule for DUNE are outlined in Chapter 2. A camera system which was installed in the DUNE 35 ton prototype detector is described in Chapter 3. Chapter 4 describes simulations which were made in preparation for data taking of the 35 ton prototype, and conclude with a description of how Particle Identification (PID) could be performed in the 35 ton data. An overview of the data gathered by the 35 ton prototype is shown in Chapter 5, and a novel method of interaction time determination using the effects of diffusion is presented. Following this, Chapter 6 concerns simulations of the cosmogenic backgrounds seen in large Liquid Argon Time Projection Chambers (LArTPCs) detectors at SURF. These simulations are first presented with respect to a surface detector measuring neutrino oscillations, and then to a detector at depth searching for nucleon decay events. Finally, Chapter 7 contains some final remarks and observations.

1.1 Neutrino physics

As alluded to earlier, the study of neutrinos offers a chance to probe the limitations of the SM. This is because the neutrinos predicted by the SM are massless and do not oscillate. However, numerous measurements have shown that neutrino oscillation occurs, and that at least two of the neutrino flavours are massive. Notably, the 2015 Nobel prize in physics was given to T. Kajita and A. McDonald for “the discovery of neutrino oscillations, which shows that neutrinos have mass,” for their work on Super-Kamiokande (SK) [4] and SNO [5] respectively. This means that through studying neutrino oscillations, it is possible to begin to get a handle on physics beyond the SM. The history of the discovery of neutrino oscillations, which culminated in this nobel prize, is briefly outlined in Section 1.1.1. Following this, the formalism by which neutrino oscillation occurs is presented in Section 1.1.2, with some of the effects of these oscillations being expanded on in Section 1.1.2. Finally, the current state of neutrino physics, including the current best fit values for the various mixing parameters, is summarised in Section 1.1.4.

1.1.1 The history of neutrino oscillation

Neutrinos were first proposed to explain the continuous energy spectrum of the electrons produced in β decay, as due to kinematic constraints, it could not be explained by a two body decay. To this end, Pauli proposed the idea of a neutral particle, with mass less than that of the electron, which would not be observed in the reaction [6]. Pauli called this particle a “neutron.” Upon the discovery that the “neutron” was in fact of a similar mass to the proton, and that the nucleus was a bound state of protons and neutrons, Fermi proposed a more complete theory of β decay in 1934. In this theory, Fermi proposed that the light, neutral particle, that was initially proposed by Pauli did exist, and was emitted from the nucleus in the reaction. Fermi called this particle a “neutrino,” meaning “little neutrino one” in Italian. He also proposed that its mass could be measured by looking at the end point of the β spectrum [7]. The first experiments designed to measure the neutrino mass in this way set an upper mass limit of 500 eV [8, 9], which was improved to 250 eV in the 1950’s[10]. After becoming evident that the neutrino mass was much less than that of the electron, the idea that neutrinos were massless gained traction.

The existence of neutrinos was confirmed in 1956 [11], and in 1962 conclusive proof emerged that the electron and muon neutrinos were distinct particles [12]. The experiment which found this, did so by observing that it was far more likely for muons to be produced in

the decay of pions, as opposed to electrons. This meant that the pion coupled more strongly to the muon, and so there had to exist two distinct particles, each with a different coupling to the pion. However, soon after this in 1968, an experiment by Ray Davis at the Homestake Mine gave rise to the “Solar neutrino problem” [13]. The Homestake experiment used a chlorine detector to look for the electron neutrinos produced by the sun, and initially measured a flux which was roughly $\frac{1}{3}$ of the predicted flux from solar models. The experiment ran for over 20 years, with the measured ν_e flux being unchanged, at roughly $\frac{1}{3}$ of the predicted solar flux [14].

The long standing observation that the solar ν_e flux was significantly lower than predicted, meant that either, there was some mechanism by which the electron neutrinos were evading detection, or that the solar model was incorrect. It was plausible that the solar model was incorrect, however the scale of the difference in the observed, and predicted, ν_e flux proved difficult to resolve. As a result, the idea of neutrino oscillation grew momentum, drawing on a prediction made by Pontecorvo as far back as 1957 [15]. The SK experiment measured high energy solar neutrinos, and in 1989 measured an energy dependant deficit in the solar ν_e flux [16]. When studying the atmospheric neutrino flux, SK found an angular dependent deficit in the expected muon neutrino flux, though the electron neutrino flux was consistent with predictions. It was found that this deficit was consistent with oscillations of $\nu_\mu \leftrightarrow \nu_\tau$ [4]. The existence of the third flavour of leptons was found in the 1970s [17], though the ν_τ neutrino was itself not directly measured until 2000 [18].

Conclusive proof for neutrino oscillations came in 2001, when the SNO experiment measured both the Neutral Current (NC) and Charged Current (CC) interactions of solar neutrinos. The SNO experiment measured a charge current interaction rate which was consistent with the experiments which had gone before it [19], i.e. a deficit in the predicted solar flux. However, it found that the neutral current interaction rate, which is sensitive to all flavours of neutrinos, matched the predicted solar flux [5]. This demonstrated that a significant part of the ν_e flux from the sun had oscillated into ν_μ and ν_τ as they travelled to Earth. This flux of oscillated ν_μ and ν_τ could not interact via CC interactions due to the high mass of the associated leptons relative to the neutrino energy, however, they are able to interact via NC interactions.

These highlighted results, as well as many other accompanying results, form the basis of our current understanding of neutrino oscillations. This is explained below.

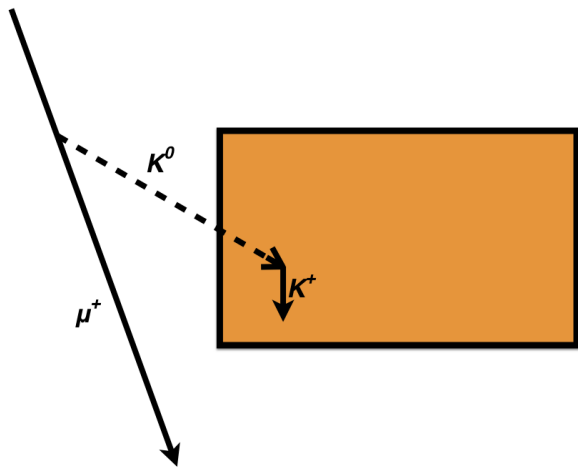


Fig. 1.1 How the interaction of a cosmic muon can mimic a nucleon decay signature, by producing a K_L^0 which interacts far from the detector wall, producing an isolated kaon.

1.1.2 The theory of neutrino oscillations

1.1.3 CP-Violation and matter effects

1.1.4 Current experimental limits, and future experiments

1.2 Grand Unifying Theories and nucleon decay

1.2.1 The cosmogenic background to nucleon decay

Chapter 2

The Deep Underground Neutrino Experiment

The Deep Underground Neutrino Experiment (DUNE) is a next-generation neutrino experiment, which came about through the recommendations of the P5 report in 2014 [20]. It was largely formed by the merger of two competing next-generation neutrino experiments, the Long Baseline Neutrino Experiment (LBNE) [21–26] a US-based experiment, and the Long Baseline Neutrino Observatory (LBNO) [27] a European-based experiment.

The DUNE Far Detector (FD) will consist of four modules, each of which is a 10 kt Liquid Argon (LAr) Time Projection Chamber (TPC) (LArTPC). The four FD modules will be 4850 ft below ground, at the Sanford Underground Research Facility (SURF). This detector location is 1300 km away Fermi National Lab (FNAL, Fermilab), from which DUNE will receive a neutrino beam with a beam power of 1.2 MW, this will increase to 2.4 MW during the lifetime of the experiment. There will also be a high resolution, and high precision, Near Detector (ND) located at Fermilab. A schematic of the DUNE experimental setup is shown in Figure 2.1. Given this experimental setup, DUNE will have a wide range of physics opportunities, these are discussed in detail in Section 2.4. There is extensive documentation concerning all aspects of DUNE, this can be found in a suite of four Conceptual Design Review (CDR) documents [28–31], and numerous annexes [32]. What follows is a high level summary of the information contained in these CDR volumes, and annexes.

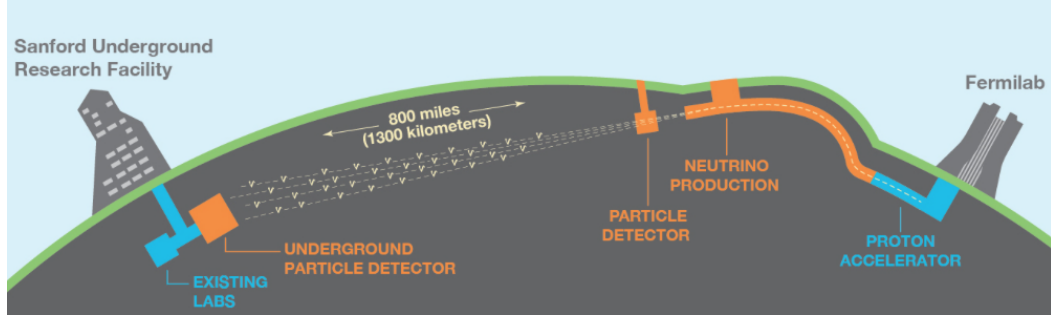


Fig. 2.1 A representation of the DUNE experimental setup. Fermilab, the host lab is shown right. The neutrino beam will be produced at Fermilab, and a high resolution near detector will also be located there. SURF is shown left, this is 1300 km away from Fermilab, and is where the far detector will be located. Objects in orange need to be built during the lifetime of the experiment, whilst objects in blue already exist. The figure is not to scale, and is taken from [28].

2.1 The DUNE schedule

As DUNE is a very large project it requires extensive planning, so that man-power can be used effectively. This planning has to outline the expected timescales of when the beamline, and the numerous detectors, will become operational. A high level summary of the DUNE schedule is shown in Figure 2.2, the efforts at both SURF (top) and Fermilab (bottom) are shown, as well as the numerous reviews DUNE has to be complete.

Figure 2.2 shows that when the beam becomes fully operational in 2026, two of the four 10 kt modules will have been fully commissioned, and will be ready to take beam data. Shortly after the beam becomes operational, the ND will also become operational, allowing the full physics scope of DUNE to begin to be realised. Following this, it is envisioned that the third and fourth detectors will become operational before the end of 2028. One thing which is not shown on the figure, is the planned upgrade of the beam to 2.14 MW, this is currently assumed to happen in 2032. This staged approach is necessary both from logistical, and physics positions, as it would be very difficult to build all four detectors simultaneously, and staging allows for improvements to be iteratively made in the construction of the TPCs in each of the four modules. A staged approach is also beneficial from a physics position, as it means that the first 10 kt module will begin taking physics data in 2024, two years before the beamline is completed. This physics data will be using atmospheric and solar neutrinos, as well as looking for signals from supernova and proton decays.

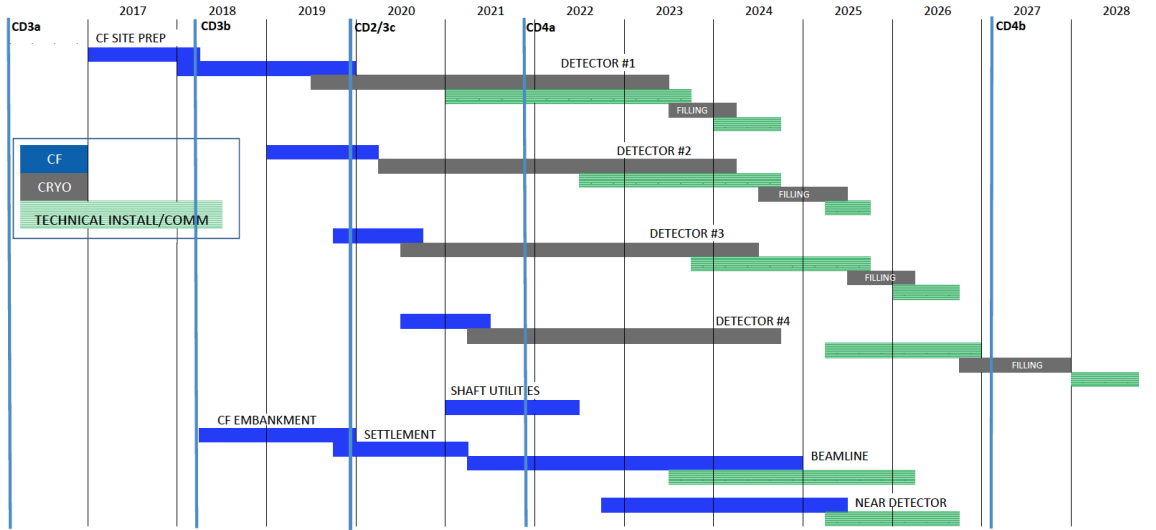


Fig. 2.2 A high level summary of the DUNE schedule. The phased construction of the four FD modules can be seen, with two of the four modules being commissioned before the beam becomes operational in 2026. The time required for construction of the facilities required for the detectors, and the beamline, are shown as blue boxes. The time required for the installation of cryogenic equipment, and filling, are shown as grey boxes. The time required for installation and commissioning, are shown as green boxes. The figure is taken from [28].

2.2 LBNF - the DUNE detector location and neutrino beam

Formally the preparation of the far detector site of DUNE, and the construction of the beam line which DUNE will use, do not fall under the remit of DUNE. This is because what may be thought of as the DUNE 'project' is formally split into two separate projects. One of these projects, the experiment called DUNE, is responsible for [28]:

- The scientific research goals which the experiment aims to accomplish, as well as the program needed to achieve this.
- Formulating the technical requirements needed from the beamline in order to satisfy the physics goals outlined above.
- The design, building, and maintenance, of the far and near detector systems, in order to achieve the physics program outlined above.

The other project, the Long Baseline Neutrino Facility (LBNF), is responsible for [28]:

- The design, and construction of a 1.2 MW neutrino beam, utilising the Proton Improvement Plan II (PIP-II) upgrade at Fermilab [33].
- The civil construction for the near detector site.

- The excavation of the far detector site, and the preparation of the caverns for the detector modules, including the cryostats and cryogenic systems, needed by the DUNE FDs.

As such, the design and construction of the neutrino beam, as well as the preparation of both the near and far detector sites, is not within the remit of responsibility for DUNE, but is instead under the remit of LBNF. This model, whereby there are two separate projects, one responsible for the facilities used in the experiment, and another, responsible for the design, construction, and maintenance of the experiments, is the model used at CERN, for the LHC and its associated experiments. Fermilab, as the host lab for LBNF, is thus intimately involved in LBNF, as CERN was in the completion of the LHC.

A discussion of the wider DUNE experiment is clearly not possible without first discussing the facilities which LBNF is responsible for building. What follows is thus a brief discussion of the LBNF project.

As will be discussed in Section 2.4, DUNE is first and foremost, a neutrino oscillation experiment, and so it is important to select a far detector location which allows for the largest possible physics opportunities. When a detailed study was performed by the LBNE collaboration to determine the location of the far detector for that experiment, it was determined that the Homestake Mine at SURF was the most optimal site [34]. The reason for this was that this baseline allowed LBNE to deliver the full physics potential which it had hoped to be able to accomplish, see Section 2.4. It was further noted that this detector location could be the “start of a long-term world-leading program...with subsequent phases.” Following the formation of DUNE a similar review was performed, and the conclusion reached was that the FD site chosen by LBNE, was also the location at which DUNE could best achieve its physics goals. This determination was made under the remit that the subsequent phases outlined by the LBNE reconfiguration report were performed. These were that a highly capable near detector is built, that the FD consists of at least 35 kton at the 4850 ft level, and that a multi-MW beamline is used.

SURF is located in Lead, South Dakota, and is the refurbished Homestake gold mine. Upon mining operations finishing, the mine became briefly disused before being reopened as the Deep Underground Science and Engineering Laboratory (DUSEL). When funding for DUSEL ceased, the US Department of Energy (DOE), through Lawrence Berkeley National Lab agreed to support ongoing research efforts, thus SURF was created [35]. DUNE will be located near the Ross shaft, one of two shafts which go to the 4850 level. Near the other

shaft, the Yates Shaft, is what is now called the Davis Campus, named after Ray Davis who performed the experiment bearing his name at the Homestake mine in the late 1960's [13, 14].

In order to prepare SURF for an experiment of the size of DUNE, a major renovation effort is required. This is because both shafts down to the 4850 level need to be reinforced to be able to cope with the amount of rock which has to be excavated, and the amount of building materials which need to be brought down to the 4850 level to build the DUNE detectors, and cryogenic equipment [30]. Before excavation could occur extensive studies were required, this was to ensure that the rock around the proposed cavern system is of high enough quality to accommodate the cavern system required for DUNE. These studies confirmed that the chosen site was suitable [30].

The dimensions of the cavern system which need to be excavated in order to accommodate the DUNE detectors is shown in Figure 2.3. From Figure 2.3 it can be seen that the DUNE FDs will be located in two large caverns, either side of a central reservation, with each cavern housing two detector pits. Each detector will be contained within a self-standing, steel framed structure, within this structure will be a membrane cryostat which will house a total of 17.1 kt of LAr [30]. Further information regarding the DUNE FDs can be found in Section 2.3.

The other remit of LBNF is the design, and construction, of the beam line, as well as providing the facilities to house the DUNE ND. A schematic showing the near site facilities which will be built by LBNF is shown in Figure 2.4. From Figure 2.4, it can be seen that upon extraction from the Main Injector, the proton beam will be sent through a man-made embankment, the height of which will be approximately 18 m. This proton beam will then be bent 7.2° westward, and 5.8° downwards, so as to point towards the FD location at SURF. After being pointed towards SURF, the protons will hit a graphite target, producing mesons which will then be focused by a set of magnetic horns, before being passed to a 'decay pipe' where they decay to muons and neutrinos. The magnetic horns are able to 'sign select' the mesons produced by the interactions with the target, so as to only focus mesons which will decay into either neutrinos, or antineutrinos. This allows the beam produced by LBNF to operate in either neutrino or antineutrino mode, by focusing either positive, or negatively charged mesons, respectively. The energies of the neutrinos produced by the meson decays are between 0.5 and 5 GeV, this allows for a wide band neutrino beam to be used. The advantage of using a wide band neutrino beam is that the DUNE FD can then observe the maxima from the both the first, and second, oscillation maxima, at approximately 2.4 GeV,

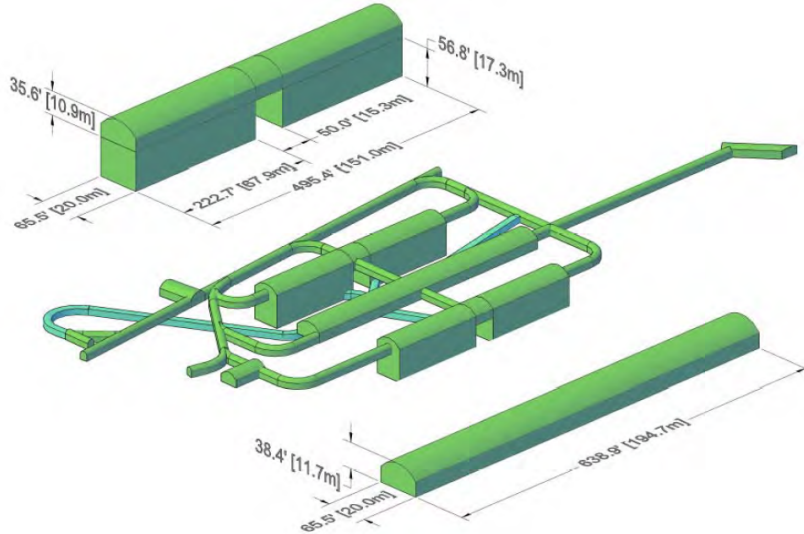


Fig. 2.3 A representation of the future LBNF cavern system at SURF. The top of the figure shows one of the main caverns, composed of two detector pits. The centre of the figure shows the entire cavern system, whilst the bottom of the figure shows area which will house the cryogenic equipment. All caverns shown need to be excavated. The Ross Shaft is located a small distance from the bottom left corner of the figure. The Yates Shaft is located roughly 1 km from the cavern system, in the direction of the top left hand corner of the figure. The dimensions shown are estimations, and the final dimensions may be slightly smaller. The figure is taken from [30].

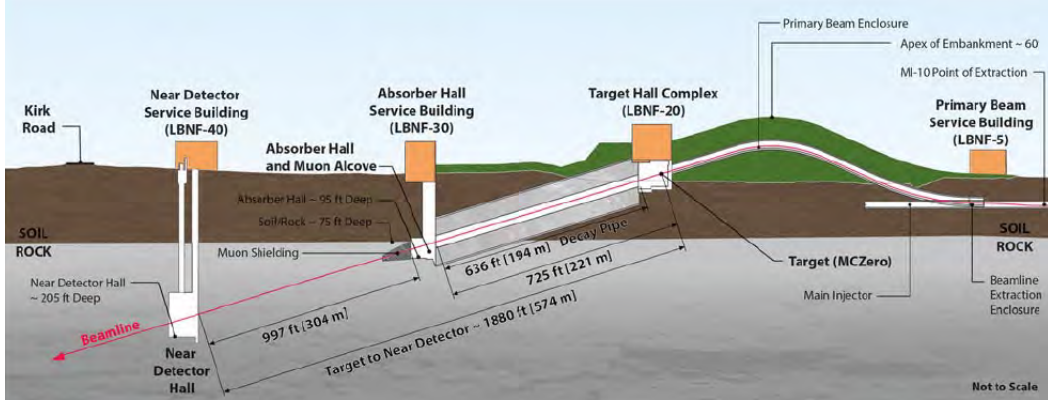


Fig. 2.4 A representation of the future LBNF near site at Fermilab. From right to left, the beam extraction point, man-made hill, target hall complex, meson decay pipe, absorber hall, and the near detector hall can be seen. Measurements are shown for the decay pipe (a reference design, top, and an alternative design, bottom), and the distance between the absorber hall and near detector are shown, though the figure is not to scale. All facilities need to be built, including the extraction point from the Main Injector, and the man-made hill. The figure is taken from [30].

and 0.8 GeV, respectively. The reference design for the 'decay pipe' is 194 m long and filled with Helium. Studies are on-going to determine the most optimal separation of the beam-horns, and the most optimal length of the decay pipe [29, 30]. At the end of the 'decay pipe' is an 'absorber' which will absorb any protons which did not interact with the target, and any mesons which have not decayed.

The beamline illustrated above will utilise the Main Injector beamline after the PIP-II upgrade [33], whereby protons will be delivered with energies between 60 and 120 GeV, corresponding to a beam power of 1.0 to 1.2 MW. The ability to vary the beam power will give DUNE the ability to optimise the flux spectrum, and to better understand the systematic effects of the beam [28].

Also associated with the near site is the construction of the DUNE ND. The distance between the ND and the absorber hall will be a minimum of 210 m, due to the muon-range-out distance, and is 304 m in the reference design [30]. The DUNE ND will be comprised of at least one detector, the exact details of the ND are covered in Section 2.3.3.

2.3 The potential DUNE Detector designs

Though all four FD modules will be LArTPCs, it has not been decided whether they will use a single (liquid) phase design, or a dual phase (liquid/gas) design. This is not true for the first 10 kt module, which will use a single phase design. The single phase design is outlined in Section 2.3.1. Though this thesis concentrates on the single phase design, the dual phase design is also outlined in Section 2.3.2 for completeness. Similarly, though little mention will be made concerning the DUNE near detector, the reference design for the DUNE ND is outlined in Section 2.3.3. These sections only present a relatively brief overview of the potential designs, for more detailed descriptions see [31].

2.3.1 The single phase detector design

In the single phase design, the charge generation, electron drift, and charge collection, all occur in the LAr. As the charge collection occurs in the LAr, this means that all of the TPC structure, including the electronics, have to be submerged. The fiducial volume of 10 kt, measuring 12 m high, 14.5 m wide (in the drift direction), and 58 m long (in the beam direction), is too big to be contained in a single TPC, and so many individual TPCs are required. The reason for this, is that it is not practical to collect electrons after they drift this far, or to construct an Anode Plane Assembly (APA) frame, and Cathode Plane Assembly (CPA) frame, which could accommodate this. There is also the added complication that the APA and CPA frames would have to be transported underground, and the mine shafts would not be able to accommodate frames this large.

Therefore, the active volume is separated into many TPCs, each produced by applying voltages to planes of APAs and CPAs. These planes of APAs and CPAs are enclosed by a field cage, constructed of FR4 Printed Circuit Board(PCB). In total there are 3 planes of APAs and 2 planes of CPAs, ordered such that there is a CPA plane in between any two APA planes, and there are APA planes on the outer faces of the detector. The separation of the APA and CPA planes is 3.6 m, with the ionised electrons drifting towards the APA planes, in an electric field of 500 V cm^{-1} . This means that the maximum drift length of the electrons is 3.6 m. The APA and CPA planes are orientated vertically, parallel to the beamline. Each plane of APAs contains 25 sets of APA rows, where each APA row contains two APA frames, stacked on top of each other. Each APA frame is 6 m high, and 2.3 m wide, meaning that two stacked APA frames give the total active volume height of 12 m. The 25 sets of 2.3 m wide APA frames, produce the total active volume in the beam direction of 58 m, after a small separation between

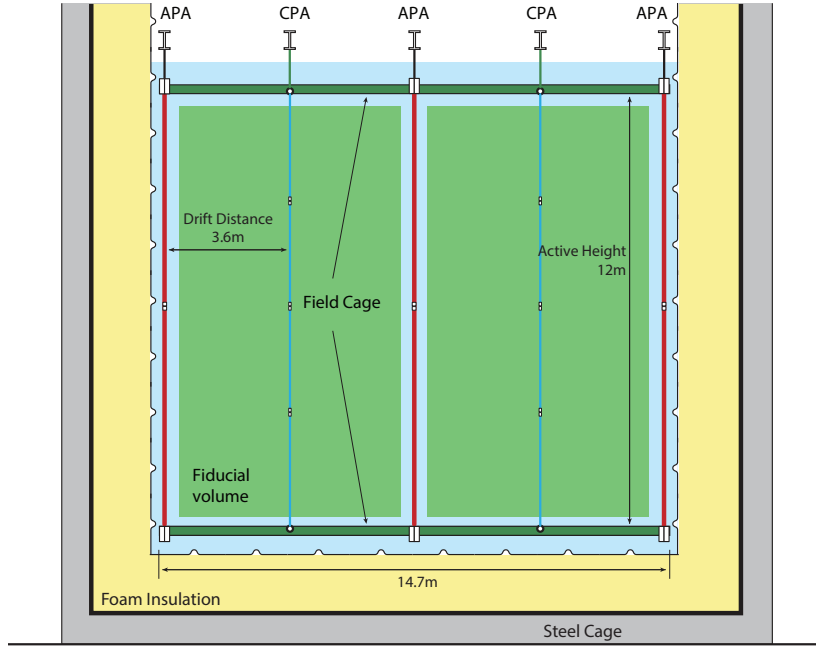


Fig. 2.5 A cross section of the DUNE signal phase detector design. The plane shown is looking along the beamline, such that the detector extends a total of 58 m into the page. Planes of APAs (purple) and CPAs (blue) are shown on top of the fiducial volume (green), inside the foam insulation (yellow), which is further contained in the concrete (black line) and steel cage (grey) structures. A supporting structure, holding the APAs and CPAs is also shown (dark green). The boundaries between APA (CPA) frames are shown as black squares, such that each APA (CPA) plane contains 2 APA (4 CPA) frames.

APA rows is accounted for. The CPA planes are structured in an identical fashion, though each CPA frame is only 3 m high, therefore each CPA row contains 4 CPA frames. This results in there being a total of 150 APA frames, and 200 CPA frames in a given 10 kt module. Figure 2.5, shows a graphical representation of this APA and CPA frame structure, where in reality there would be an additional 24 planes, going into the page, identical to the one shown.

Each APA frame is instrumented on both sides with 4 wires planes, the properties of which are outlined in Table 2.1. The induction plane wires are wrapped around the long edges of the APA frames. This means that on each APA frame there are two sets of grid and collection planes, one on each side of the APA, and two induction plane wires, both of which are sensitive to both sides of the APA. The two induction planes are wrapped around the long edge of the APA frame, so that readout electronics are only required at one of the short ends of the APA frames. The electronics for the APAs at the top (base) of the detector,

Table 2.1 The parameters of the wire planes in the DUNE FD single phase design.

Function	Orientation ($^{\circ}$)	Pitch (mm)	Num. Wires	Bias Voltage (V)
Grid (G)	0	4.79	960	-655
1 st induction (U)	35.7	4.67	800	-365
2 nd induction (V)	-35.7	4.67	800	0
Collection (Z)	0	4.79	960	860

are placed on the edge of the APA frame which is closest to the top (base) of the detector. The electronics are outside of the active volume, but still submerged in the LAr. Though the induction plane wires are sensitive to particles in two different TPCs, the wire pitch is chosen such that there is no degeneracy between pairs of induction and collection wire pairs. The wire planes are biased such that the electrons will drift past the first three wire planes, and will be collected on the collection plane. An illustration of the wire wrapping is shown in Figure 2.25, where it is presented in the context of resolving degeneracy's between induction and collection plane wires. It is presented in this way because the 35 ton prototype, which is discussed in Section 2.5, had degeneracy's between the induction and collection plane wires, due to the wire pitches being different from the FD reference design.

It is also envisioned that there will be a system of Photon Detectors (PDs), to measure interaction times of both beam, and non-beam, events. An individual PD will be comprised of a light guide, and 12 Silicon Photo Multipliers (SiPMs). Each APA frame will contain 10 equally spaced PDs. The PDs will use a wavelength shifter on the surface of the light guide, to convert the 128 nm scintillation photons from the LAr, to photons with a wavelength of 430 nm. This wavelength shifted light will be collected by the SiPMs. The front end electronics for the SiPMs will reside outside of the cryostat, where a SiPM Signal Processor (SSP) digitises the signals from the SiPMs.

2.3.2 The dual phase detector design

In the dual phase detector design the electrons are not collected in the LAr, but are extracted at the interface between liquid and gaseous argon, before being amplified, and collected, in the gaseous argon. This design follows the GLACIER concept[36], whereby the electrons are drifted vertically, before being collected by a finely segmented anode [37–39]. The amplification of electrons at the liquid/gas boundary is done using Large Electron Multipliers (LEMs). As a result of amplifying the drifted electrons the *signal/noise* ratio can be increased by at

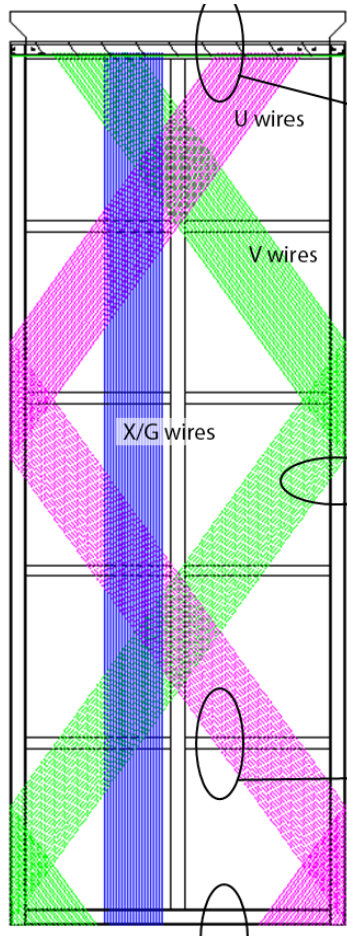


Fig. 2.6 An illustration of the wire wrapping in the DUNE single phase design. A small number of the wires in each plane are shown. The wire planes shown, in the order that the electrons drift past them, are shown as follows; the 1st induction plane (U) is magenta, the 2nd induction plane (V) is green, and the collection plane (Z) is blue. The grid plane, which is in front of the 1st induction plane is parallel to the collection plane. The figure is taken from [31].

least an order of magnitude. It also allows the threshold for measuring energy depositions to be lowered.

The dual phase design also has a larger fiducial volume, as there are no inactive regions in the LAr. This is because there are no gaps between the modules which read out the charge, called Charge Readout Planes (CRPs). The CRPs measure $3 \times 3 \text{ m}^2$, and are composed of 36 LEM/Anode Sandwiches (LAS) modules which each measure $0.5 \times 5 \text{ m}^2$. The LAS modules, are themselves composed of an anode and a LEM, both measuring $0.5 \times 5 \text{ m}^2$. The process by which charge is read out, is as follows; the drifted electrons are first extracted by a grid plane, submerged in the LAr by comb-teeth blades, which is made of wires with a separation of 3.125 mm. After extraction, done by applying an electric field of the order of 2 kV cm^{-1} , the electrons pass through the LEMs. The LEMs have a honeycombed structure of $500 \mu\text{m}$ holes, with a separation of $800 \mu\text{m}$, giving a total of around 200 holes per cm^2 . An electric field of the order 30 kV cm^{-1} is applied between the electrodes of the LEMs, causing large avalanches, this is how large *signal/noise* ratios can be measured. These electrons then experience a field of roughly 5 kV cm^{-1} , before finally being collected at the anodes. The anodes are composed of a pattern of gold plated copper tracks, on a single multi-layered PCB, the layout of which is composed such that both x and y views collect the same amount of charge, independent of track angle. The CRPs are produced by attaching LAS modules together, which are then further attached to the grid planes. Figure 2.7 is an illustration showing the charge collection process in the dual phase design.

As was the case with the single phase design, the dual phase detector design contains a system to collect the scintillation light. However, in the dual phase design, this will be done using 8-inch Photo Multiplier Tubes (PMTs), coated with TPB, which are located about 1 m below the cathode. The use of PMTs like this have been used extensively in giant water Cherenkov detectors, and so it is envisioned that many of the techniques used there will be utilised [40, 41].

2.3.3 Reference near detector design

The reference DUNE ND is a Fine-Grained Tracker (FGT), which consists of a Straw-Tube Tracking (STT) module, and an Electromagnetic Calorimeter (ECal), inside a 0.4 T dipole magnet. This is a design which builds on existing ND systems in experiments such as MINOS, NO_νA, and T2K, as well as the NOMAD detector at CERN. The DUNE ND will also have a set of muon identifiers in the dipole magnet. A detector of this structure will

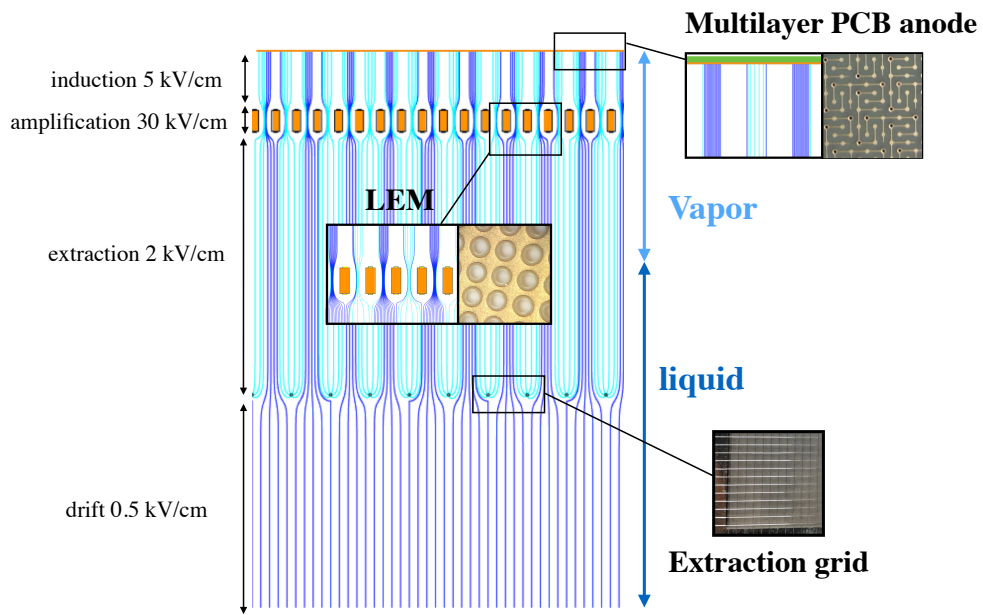


Fig. 2.7 An illustration of the process of charge extraction in the DUNE dual phase detector design. The liquid/gas boundary can be seen to be between the grid plane and the LEMs. The various electric fields which electrons experience at the different stages of extraction can be seen, as well as small pictorial representations of the various instruments used in the extraction process. The figure is taken from [31].

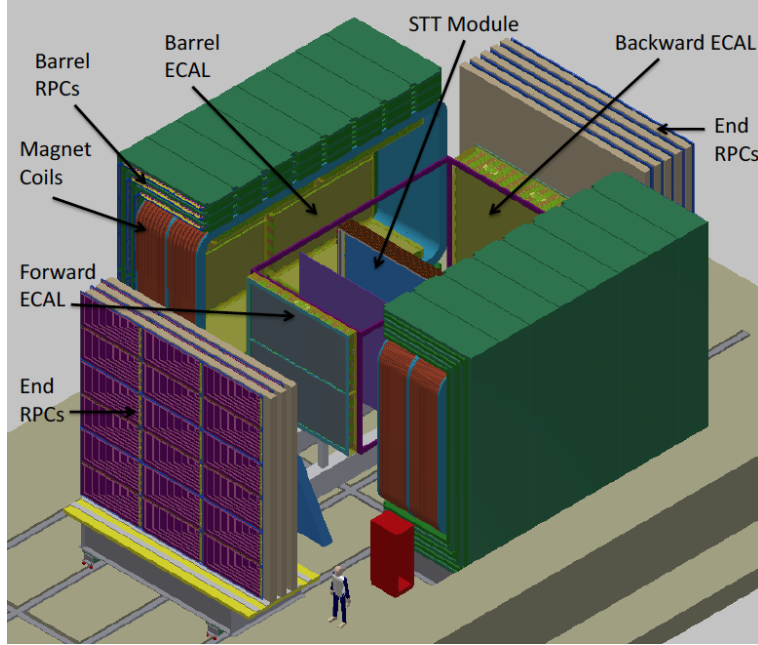


Fig. 2.8 A schematic representing of what the reference DUNE ND could look like. The main features of the detector, namely, the Straw-Tube Tracking (STT) modules, the Electromagnetic Calorimeter (ECAL), the Resistive Plate Chambers (RPCs) which make up the muon-identifiers, and the magnetic coils, can all be seen. The figure is taken from [31].

allow the DUNE ND to make precision measurements of the neutrino flux, cross section, and the signal and background rates. A schematic of the potential ND system in DUNE is shown in Figure 2.8.

There is also the possibility of building multiple NDs, to complement the FGT. One such potential ND would be a small (~ 100 ton) LArTPC. This would have the advantage of using the same technology as the DUNE FD, and so systematic effects could be better accounted for between the ND and FD. However, due to the slow drift time of LArTPCs, and the high luminosity of the beam, pile-up could become a problem. This is because there would be such a large number of neutrino interactions when the beam is operating at full power. The effect of pile-up would, however, be reduced when the beam is at running at low intensities such as, during the initial ramp-up, during periodic shut downs, or during upgrades to the beam.

2.4 The physics capabilities of DUNE

As mentioned above, DUNE hopes to be able to deliver a wide ranging physics program. These topics include, but are not limited to, precision measurements of neutrino oscillation physics, discussed in Section 2.4.1, searching for nucleon decay in several important decay modes, discussed in Section 2.4.2, and the detection and measurement of the ν_e flux from a core-collapse supernovae in our galaxy, should one occur, this is discussed in Section 2.4.3.

2.4.1 Neutrino physics

The primary goals of DUNE concern neutrino physics, many of these ideas were introduced in Section 1.1. The primary goals of DUNE are outlined now, and illustrated more fully below [29]:

- Determine the neutrino mass hierarchy.
- Measure the charge-parity (CP) violating phase - δ_{CP} .
- Make precision measurements of the neutrino mixing parameters, such as θ_{13} , θ_{23} , and Δm_{31}^2 .

There are also secondary physics goals concerning neutrino physics, these include:

- Measuring the rate of ν_τ appearance.
- Measuring neutrino oscillations using atmospheric neutrinos.
- Measuring a wide range of neutrino cross-sections, using the ND.
- Measuring nuclear effects, particularly neutrino final-state interaction, using the ND.

Section 2.1, presented the idea of a staged approach to DUNE. As such, the annual exposure which DUNE is exposed to, will increase as a function of time. The exposure as a function of time is shown in Table 2.2, these exposures are important when considering the figures presented below.

As presented in Section 1.1, both the matter effect, and δ_{CP} introduce an asymmetry between neutrino and anti-neutrino oscillations. As the matter effect is caused by the difference in the presence/absence of electrons/positrons in the Earth, it increases with distance. The result of this is that for baselines longer than approximately 1000 km the two effects can be

Table 2.2 The exposure in units in units of kt MW years, as a function of time, assuming a staged DUNE contraction. The table is taken from [42].

Exposure (kt MW years)	Exposure (years)
171	5
300	7
556	10
984	15

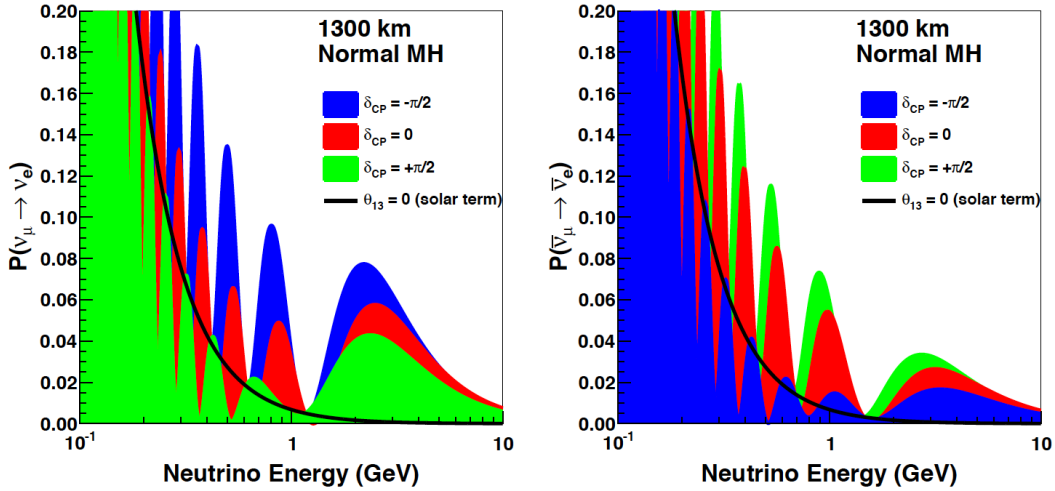


Fig. 2.9 The ν_e appearance probability at 1300 km as a function of neutrino energy, for a range of values of δ_{CP} . Left shows the probabilities for neutrinos, whilst right shows the probabilities for anti-neutrinos. Both figures assume normal mass hierarchy (ν_e is the lightest state). The probabilities for different values of δ_{CP} are shown, $\delta_{CP} = -\pi/2$ (blue), $\delta_{CP} = 0$ (red), $\delta_{CP} = \pi/2$ (green). The figure is taken from [29].

resolved [43]. It is for this reason that with a baseline of 1300 km, DUNE will be able to unambiguously determine the neutrino mass hierarchy, and determine δ_{CP} [44].

The reason for requiring a broadband neutrino beam can be seen in Figure 2.9, where it can be seen that whilst the energy of the first neutrino oscillation maxima is relatively unaffected by the value of δ_{CP} , the energies of the higher oscillation maxima are strongly affected by the value of δ_{CP} . The result of this, is that it is vital that DUNE is able to accurately measure the rate of ν_e appearance at the lowest energies of the neutrino beam it receives from LBNF. It can also be seen that there are large differences in the expected oscillation probabilities for neutrinos and anti-neutrinos. Therefore, in order to measure the effect of δ_{CP} , the beam from LBNF will also have to be able to operate in both neutrino and anti-neutrino mode.

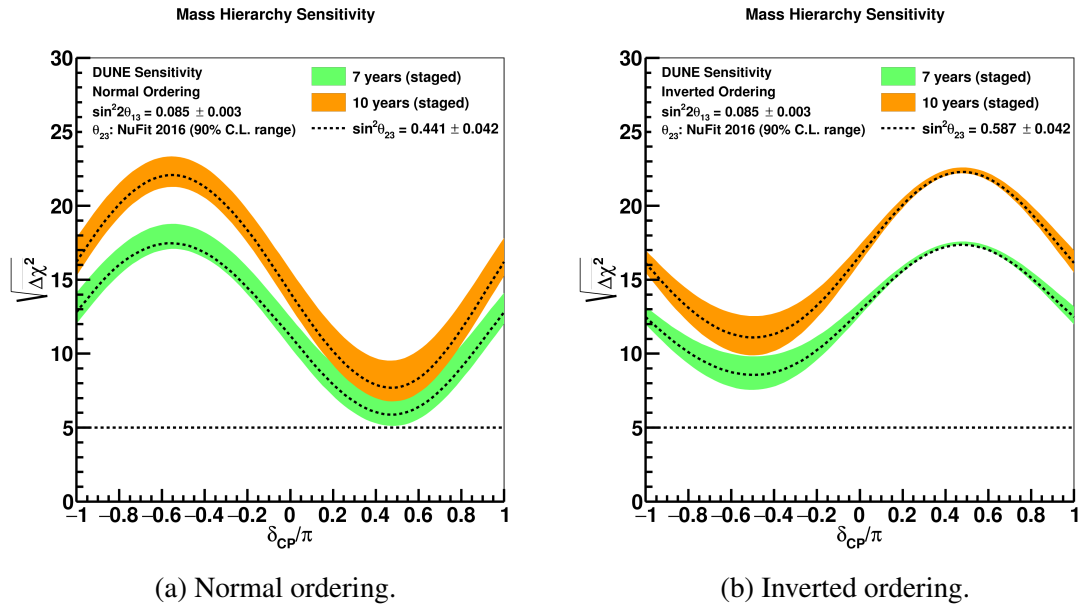


Fig. 2.10 The significance with which DUNE will be able to determine the neutrino mass hierarchy, for all values of δ_{CP} . Left shows the sensitivity assuming normal ordering, whilst right shows the sensitivities assuming inverted ordering. The shaded region shows the range of sensitivities for the 90% confidence level range for θ_{23} values, the dashed line shows the sensitivity for the NuFit central value of θ_{23} . The figure is taken from [47].

When presenting the DUNE sensitivities to the determinations of the mass hierarchy, and the value of δ_{CP} , figures are shown with exposures corresponding to 7 and 10 years worth of data taking [42]. These exposures are calculated given the phased approach to DUNE which was outlined in Section 2.1. As such, 7 years of data corresponds to a beam exposure 300 kt MW yrs, whilst 10 years of data corresponds to a beam exposure of 556 kt MW yrs. The best fit values from NuFit 2016 [45] are used when making the figures, and equal running in neutrino and antineutrino mode is assumed. These figures are different to those presented in the DUNE CDR [29], where only exposures of 300 kt MW yrs were shown. The figures taken from the CDR [29] show the effect that the two beam designs have on the sensitivities, whilst in the newer plots [46–50] the optimised beam design is assumed.

Figure 2.10 shows the significance with which DUNE will be able to determine the neutrino mass hierarchy, for all values of δ_{CP} . It can be seen that the mass hierarchy can be determined with a significance of $\sqrt{\Delta\chi^2} = 5$, for all values of δ_{CP} , after 7 years of data taking. It can also be seen that the mass hierarchy can be more conclusively determined if the hierarchy is inverted.

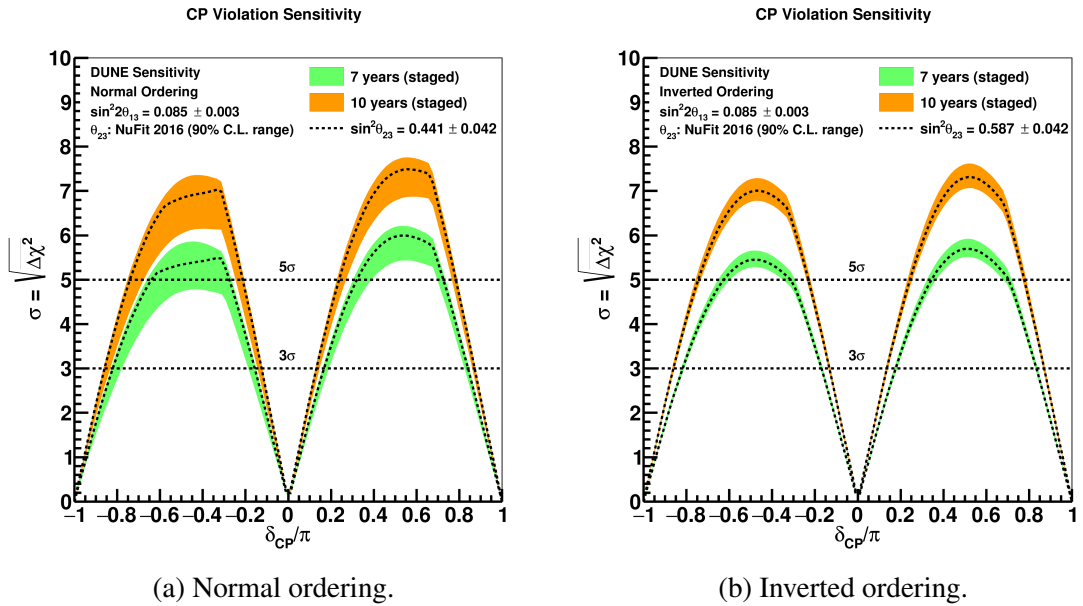


Fig. 2.11 The significance with which DUNE will be able to determine the value of δ_{CP} , for all values of δ_{CP} . Left shows the sensitivity assuming the normal ordering, whilst right shows the sensitivities assuming inverted ordering. The shaded region shows the range of sensitivities for the 90% confidence level range for θ_{23} values, the dashed line shows the sensitivity for the NuFit central value of θ_{23} . The figure is taken from [46].

Figure 2.11 shows the significance with which DUNE will be able to determine the value of δ_{CP} , for all values of δ_{CP} . It can be seen that even with 10 years worth of data there are regions where the value of δ_{CP} cannot be determined accurately, this is because if δ_{CP} equals $-\pi$, 0, or π there would be no CP-violation. Therefore, for values of δ_{CP} around these values, the significance to which δ_{CP} can be determined must approach 0. As such, even at very large exposures of over 800 kt MW yr, corresponding to around 13 years of data taking according to Table 2.2, only 75% of the δ_{CP} values can be determined to a significance of 3σ , when using the optimised beam design [49]. However, even with a relatively modest exposure of 150 (550) kt MW yr, DUNE can determine the value of δ_{CP} for over 50% of the values for δ_{CP} to a significance of 3σ (5σ) using the optimised beam design [49]. This shows that should the value of δ_{CP} be close to a CP-conserving value, it would be very difficult to determine the value of δ_{CP} . However, if it is far away from these values, DUNE could make a measurement, with a significance of over 5σ , in a matter of years.

Given the structure of Figure 2.11, it can be instructive to instead observe the resolution to which the value of δ_{CP} can be determined with increasing exposures, this is shown in Figure 2.12. Figure 2.12 shows curves for the cases when the value of δ_{CP} is both maximally

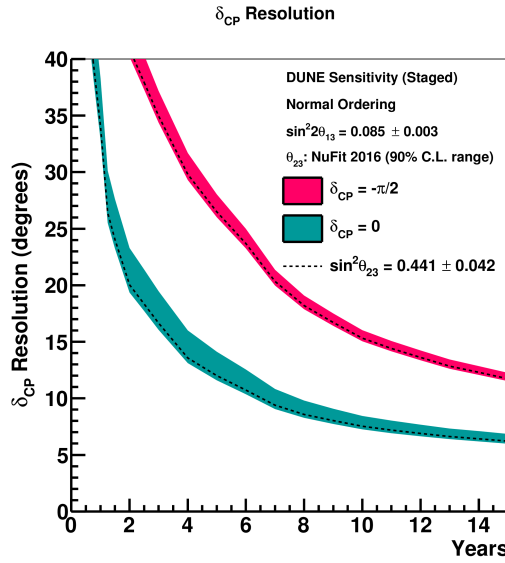


Fig. 2.12 The resolution with which DUNE will be able to determine the value of δ_{CP} , for increasing exposures (in years). Two bands are shown, one for a value of δ_{CP} which could cause maximal CP-violation ($\delta_{CP} = 90^\circ$), and another where there would be no CP-violation ($\delta_{CP} = 0^\circ$). A normal hierarchy is assumed, and the shaded region shows the range of sensitivities for the 90% confidence level range for θ_{23} values. The dashed line shows the sensitivity for the NuFit central value of θ_{23} . The figure is taken from [48].

CP-violating ($\delta_{CP} = 90^\circ$), and when it is CP-conserving ($\delta_{CP} = 0^\circ$). Somewhat paradoxically, the resolution is better when $\delta_{CP} = 0^\circ$, the reason for this, is that the region of values of δ_{CP} for which CP-violation would not be observed, becomes increasingly small, as exposure increases. This means that the resolution to which δ_{CP} can be determined increases. However, the more interesting result, would be the one which supported δ_{CP} having a value which causes maximal CP-violation.

DUNE also aims to perform precision measurements of the neutrino mixing parameters, in order to improve sensitivity to any physics beyond the standard three-flavour oscillation model. As discussed in Section 1.1, the current best limit for the value of θ_{23} does not determine which octant it is in, specifically whether it is more than, or less than, 45° . Determining the octant of θ_{23} is important, as should it be found that θ_{23} is equal to 45° , it would hint at an unknown symmetry. DUNE will determine the value of θ_{23} by combining measurements of $\nu_\mu \rightarrow \nu_\mu$, and $\nu_\mu \rightarrow \nu_e$, which are sensitive to $\sin^2 2\theta_{23}$, and $\sin^2 \theta_{23}$, respectively. Figure 2.13 shows the significance to which the octant of θ_{23} can be determined for different values of θ_{23} . Correspondingly, Figure 2.14 shows the resolution to which the value of

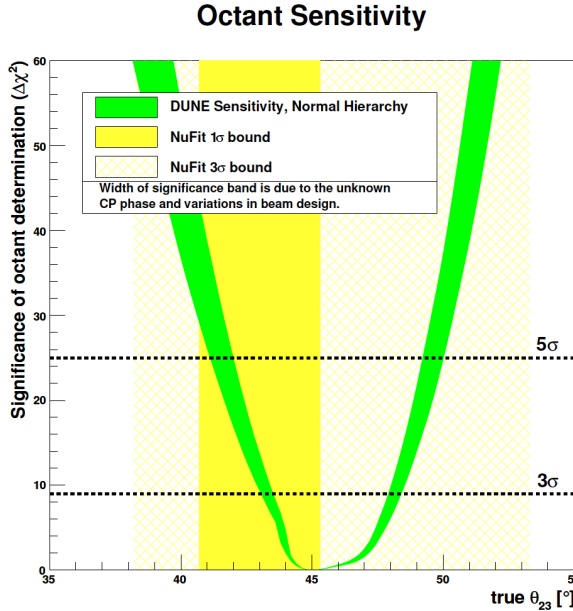


Fig. 2.13 The significance to which the octant of θ_{23} can be determined, for values of θ_{23} . An exposure offering a 3σ determination of the value of δ_{CP} for 75% of the values of δ_{CP} is assumed. The green band shows the effect of different values of δ_{CP} and beam configurations. The yellow region show the 1σ and 3σ at the time of writing. The figure is taken from [29].

$\sin^2 \theta_{23}$ can be determined with increasing exposures.

The precision with which the values for $\sin^2 \theta_{13}$ and Δm_{31}^2 can be measured by DUNE are shown in Figure 2.15 and Figure 2.16 respectively.

The resolution to which DUNE can measure the value of $\sin^2 \theta_{13}$ is unlikely to surpass that of reactor experiments, outlined in Section 1.1.4. However, DUNE will measure $\sin^2 \theta_{13}$ using ν_e and $\bar{\nu}_e$ appearance, as opposed to $\bar{\nu}_e$ disappearance, as is done in reactor experiments. This complementary measurement of $\sin^2 \theta_{13}$ will provide an independent constraint on the three-flavour mixing matrix. DUNE will also be able to greatly improve the resolution to which the Δm_{31}^2 mass splitting can be determined.

It is also possible to measure many of the properties of neutrino mixing using atmospheric neutrinos. This is because, as mentioned in Section 1.1.4, atmospheric neutrinos contain all flavors of neutrinos and antineutrinos, and cover a wide range of L/E values. Also, atmospheric neutrinos are always available. This is particularly useful because, as discussed in Section 2.3, the DUNE schedule has at least one 10 kt module becoming operational before the beam is operational. As is the case in experiments such as Super-Kamiokande, DUNE

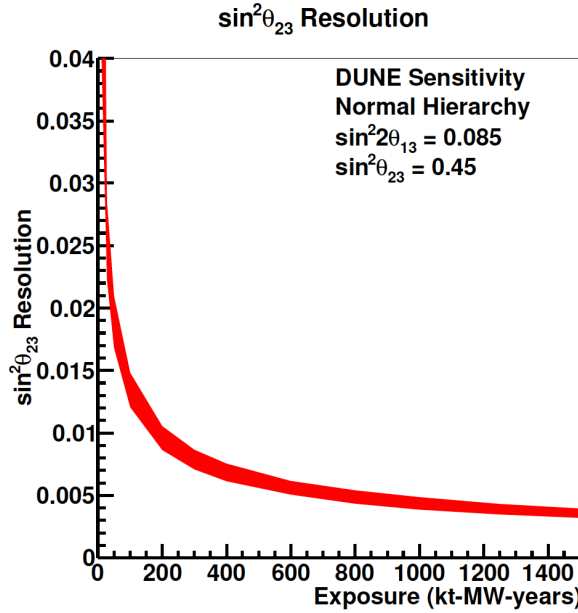


Fig. 2.14 The resolution with which DUNE will be able to determine the value of $\sin^2 \theta_{23}$ for increasing exposures. A normal hierarchy is assumed, and the bands show the sensitivities to the potential beam designs. The figure is taken from [29].

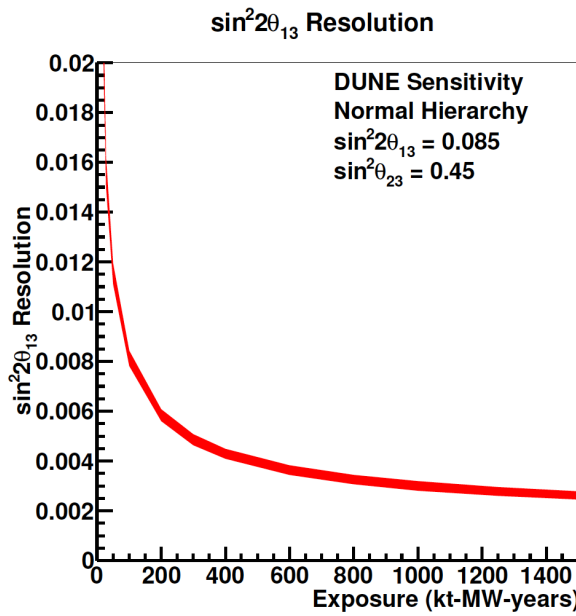


Fig. 2.15 The resolution with which DUNE will be able to determine the value of $\sin^2 \theta_{13}$ for increasing exposures. A normal hierarchy is assumed, and the bands show the sensitivities to the potential beam designs. The figure is taken from [29].

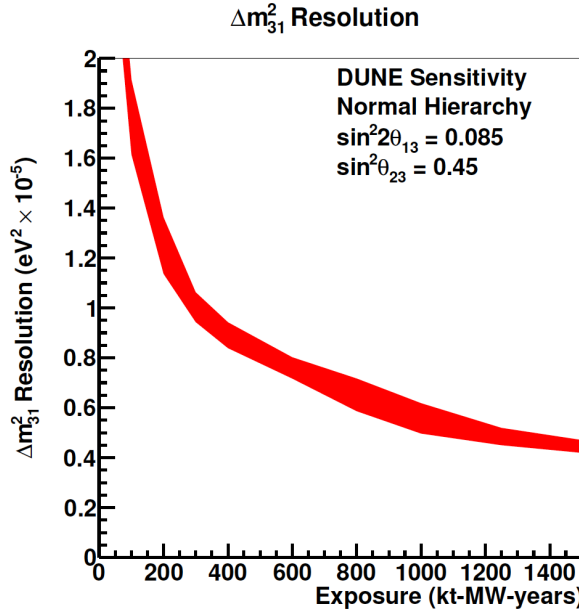


Fig. 2.16 The resolution with which DUNE will be able to determine the value of Δm_{31}^2 for increasing exposures. A normal hierarchy is assumed, and the bands show the sensitivities to the potential beam designs. The figure is taken from [29].

can observe the differences in upwards and downwards going neutrinos. The enhanced detector resolution of DUNE, allows the possibility that features expected in neutrino and antineutrino events can be resolved. This enhanced detector resolution also allows DUNE to have a comparable sensitivity to the mass hierarchy as the proposed Hyper-Kamiokande experiment, despite having a much smaller fiducial mass [29].

2.4.2 Nucleon decay

As presented in Section 1.2, many so called Grand Unified Theories (GUTs) predict some form of nucleon decay. Though nucleon decay has never been observed, there are still regions of phase space where nucleon decay could occur. As DUNE will be located deep underground, it will have a low background rate. This, combined with the high detector resolution of a LArTPC, means that DUNE offers an ideal candidate to continue the search for nucleon decay.

The search for nucleon decay in DUNE is primarily focused on two proton decay modes, $p \rightarrow e^+ \pi^0$ and $p \rightarrow K^+ \bar{v}_e$. In the first of these decay modes, the total mass of the proton should be converted into the electromagnetic showers produced by the two particles, and their net momentum should be zero. This is a signal which can be clearly identified in water

Cherenkov detectors, such as Super-Kamiokande, and so is the main decay mode which these detectors look for. This decay mode should also produce a clear signal in a LArTPC such as DUNE. However, the second decay mode is particularly interesting in DUNE, as kaons should be able to be accurately identified in a LArTPC. This is not the case in a water Cherenkov detector, as the kaons produced are not energetic enough to produce Cherenkov light. Though particular emphasis will be given to the $p \rightarrow K^+ \bar{\nu}_e$ decay mode in this section, the same strengths in particle identification are true for all decay modes which feature a kaon in the final state. It is also important to note that DUNE will search for all type of nucleon decays, including bound neutron decays and neutron to antineutron oscillations, the former will be given particular focus in Section 6.3.

It is hoped that DUNE will be able to reach sensitivities to nucleon decay lifetimes of between $10^{33} - 10^{35}$ years. A comparison of current, and potential lifetime limits, from a range of experiments is shown in Figure 2.17. It can be seen that DUNE will provide very stringent limits to nucleon decay lifetimes, which will compete with the proposed Hyper-Kamiokande in all decay modes other than the $p \rightarrow e^+ \pi^0$ decay mode. As outlined earlier, Cherenkov detectors are able to perform relatively background free studies in this channel, and so due to the much larger mass of Hyper-Kamiokande, it is able to achieve a limit which is superior to DUNE. In the other channels however, the excellent spatial resolution of LArTPCs allow DUNE to compete with, and in many cases improve on, any limit which could be set by Hyper-Kamiokande.

When calculating the expected sensitivity of DUNE to a range of nucleon decay modes, previous studies can be used [53, 54]. Some of the channels where one would expect a LArTPC, such as DUNE, to have an advantage in signal efficiency when compared to a water Cherenkov detector, such as Super/Hyper-Kamiokande, are shown in Table 2.3. The accurate tracking of the kaon, and its subsequent decay products, is the reason for the increased efficiency that is expected in LArTPCs. The ability for LArTPCs to perform tracking to this accuracy was seen by the ICARUS collaboration, using the T600 detector [55]. Figure 2.18, shows an example event where a kaon enters the detector and is seen to decay to a muon, which subsequently decays to an electron.

Preliminary studies, at the time of writing the DUNE CDR documents, showed that after considering the backgrounds due to cosmic rays at depth, the backgrounds due to atmospheric neutrinos, and the impact of reconstruction failures, the number of background events for the $p \rightarrow K^+ \bar{\nu}_e$ decay mode should be less than 1 per Mt yr [54, 58, 59]. With a background

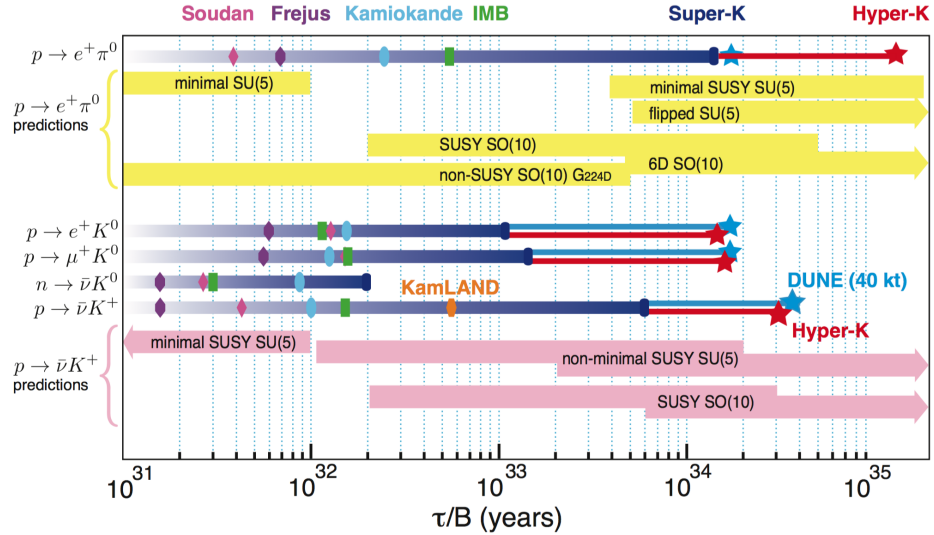


Fig. 2.17 A comparison of current, and future, nucleon decay lifetime limits, compared with the ranges predicted by Grand Unifying Theories. Coloured bars are shown for published limits by a number of experiments [51, 52]. Stars are shown for projected limits by future experiments, these limits are calculated using Poisson statistics, and include predicted background rates. The lifetimes predicted by different models are shown for the $p \rightarrow e^+\pi^0$, and $p \rightarrow K^+\bar{\nu}_e$, decay modes. The figure is taken from [29].

Table 2.3 Nucleon decay limits in DUNE and Super-Kamiokande, in some favoured decay channels. The current lifetime limits currently measured (Curr. limit), the estimated DUNE reconstruction efficiencies (DUNE ϵ), and the estimated DUNE lifetime limit in 2034 (DUNE limit) are shown. For comparison, the published Super-Kamiokande reconstruction efficiencies (SK ϵ), and the estimated Super-Kamiokande lifetime limit in 2034 (SK limit) are also shown. All lifetimes shown, are partial lifetimes, in units of 10^{33} years. The table is taken from [56], which uses [57].

Decay mode	Curr. limit	DUNE ϵ (%)	DUNE limit	SK ϵ (%)	SK limit
$p \rightarrow e^+\pi^0$	16.7	45.3	21.4	54	50.8
$p \rightarrow \pi^+\bar{\nu}_e$	0.016	41.9	19.8	54	N/A
$p \rightarrow K^+\bar{\nu}_e$	0.051	41.8	29.7	11	2.1
$p \rightarrow \mu^+\pi^0$	6.6	44.8	21.1	54	50.8
$p \rightarrow K^0\mu^+$	1.6	46.7	22.0	100	22.2
$n \rightarrow \pi^0\bar{\nu}_e$	0.112	45.1	26.0	30	7.1
$n \rightarrow K^+e^-$	0.032	96	55.4	100	1.8

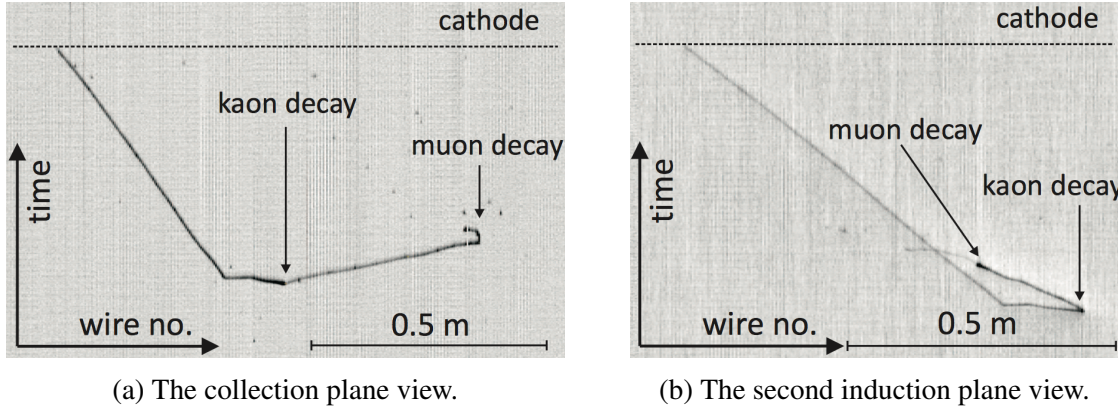


Fig. 2.18 A kaon event which was observed in the ICARUS T600 detector, in the CNGS data. Left shows the single on the collection plane, whilst right shows the signal second induction plane. The kaon enters the detector, and decays via $K \rightarrow \mu\nu$, the muon then decays via $\mu \rightarrow e\nu$. The figure is taken from [55].

rate this low, the observation of a single, well reconstructed event, could provide evidence of nucleon decay [29].

2.4.3 The detection of supernova neutrino bursts and other physics opportunities

Many of the largest detectors in the World would hope to observe neutrinos from a core-collapse supernova, should one occur during their lifetimes. However, DUNE will have particularly good sensitivity to the electron flavour supernova neutrinos. This means that it should be possible to get a large, clean, supernova ν_e signal from DUNE, which is not possible using water Cherenkov detectors [60, 61]. The observation of neutrino interactions from a supernova would consist of short electron tracks, which were potentially accompanied by a few gamma rays. Should a core-collapse supernova occur during the lifetime of DUNE, it is hoped that many of the open questions which still remain after the observation of SN1987A [62, 63], could be answered by observing a large number of events.

The production of neutrinos from a core-collapse supernova goes as follows. Once the core of a large star reaches about $1.4 M_{\odot}$, the core begins collapsing because the iron core begins disintegrating as electrons and protons combine. This collapse briefly stops once densities of nuclear values are reached, before the degenerate Fermi sea of electrons and electron neutrinos breaks out of the core. As this happens, the rest of the star is blasted away by a shock wave, producing the spectacular images we see of supernova remnants.

This shockwave is produced as the 10^{58} neutrinos, carrying 99% of the gravitational binding energy of the core, escape the remnants of the stellar core. It takes a few seconds for all of the neutrinos to escape the stellar environment, and once they have done this, the electron neutrinos have oscillated into neutrinos and antineutrinos, of all flavours, with energies of around 10 MeV. The flavor content of the neutrinos emitted changes significantly over time, this is shown in Figure 2.19.

The model used in Figure 2.19 is just one of many, but most models predict that in the full DUNE 40 kt detector, around 3000 events should be observed for a supernova at a distance of 10 kpc. This reduces to the observation of a few events for a supernova in the Andromeda galaxy, which is around 780 kpc away. The observation of a supernova within the Milky Way would allow a large suite of topics to be analysed. These include, but are by no means limited to: measurements of the neutrino mass splittings, measurements of the neutrino mixing parameters, measurements of neutrino “self-refraction” (possible due to the high density of neutrinos around the supernova), tests of Lorentz and CPT invariance, and of course testing all aspects of the predictions made by models of supernova [29].

There are also other physics aspects which DUNE could make progress in. One such aspect is the indirect searches for WIMPs. This is possible because, should a flux of high energy neutrinos be observed, which originate from regions of high mass, such as the Sun, it could support the idea of dark matter annihilation. Searches for these interactions have been performed by IceCube [65] and [66], but have not observed any signals. It is hoped that with the increased angular resolution of LArTPCs the number of background events could be substantially reduced though [29]. Other aspects where DUNE could make contributions are in searches for the diffuse supernova neutrino background [67], searches for neutrinos from accretion disks [68], and searches for black-hole/neutron star mergers [69].

The result of this, is that there is a very compelling case for building a LArTPC at depth, which is of the scale of 40 kt.

2.5 Path to building DUNE - The 35 ton prototype

One extremely important aspect of DUNE which has not yet been addressed, is the need for prototypes. The DUNE FD modules represent an increase in size by more than an order of magnitude, when compared to existing LArTPCs. It is therefore necessary for a robust

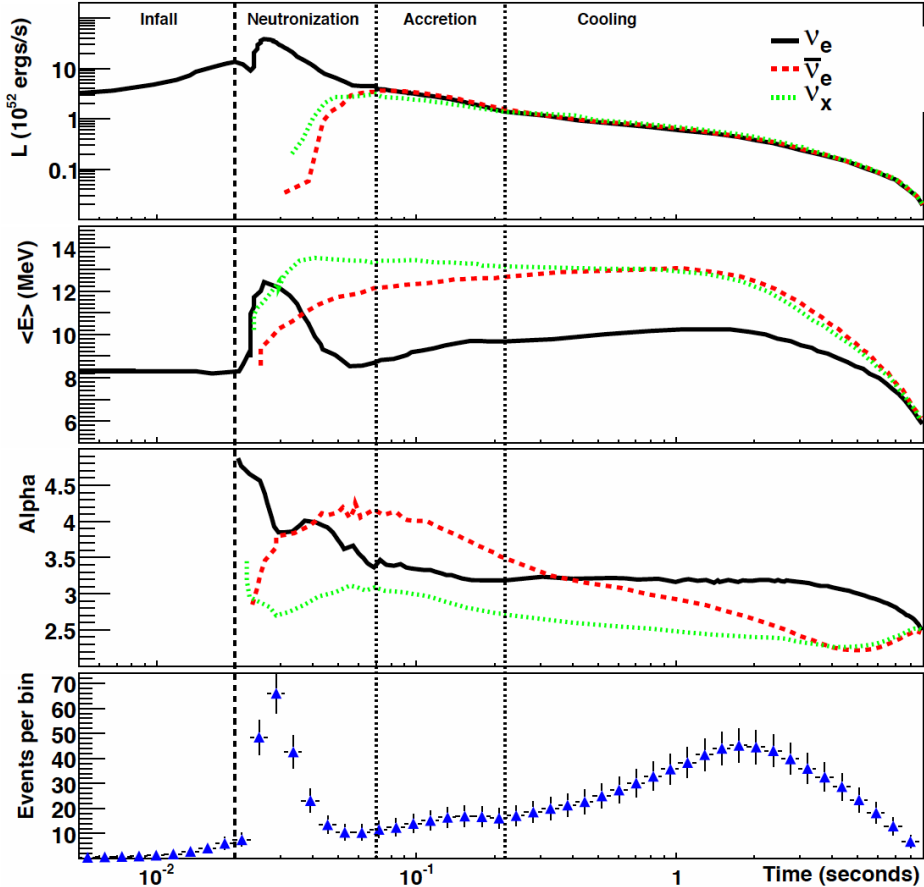


Fig. 2.19 The predicted time-dependant signal, for an electron-capture supernova, at a distance of 10 kpc from Earth [64]. It is assumed that there are no oscillations after the neutrinos are emitted. Some of the eras which are predicted in the supernova evolution are shown, and are separated by vertical dashed lines. The fluxes of ν_e , $\bar{\nu}_e$, and ν_x are shown. From top to bottom, the luminosity, the neutrino energy, the ‘pinching’ parameter, and the total number of observed events are shown, as a function of time. The figure is taken from [29].

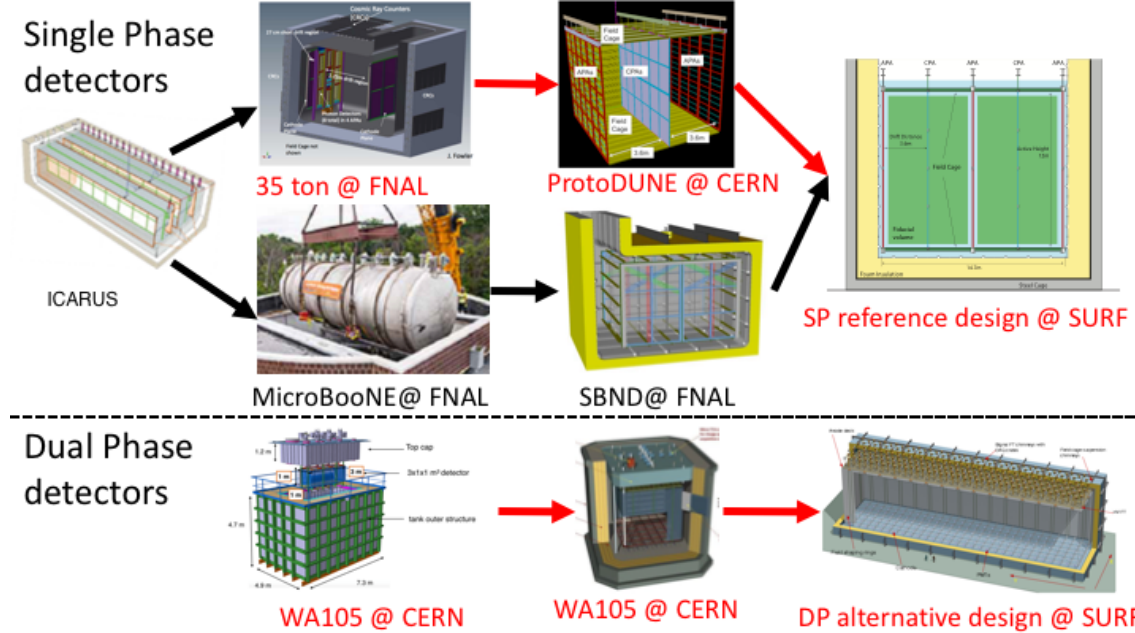


Fig. 2.20 An overview of the DUNE prototyping schedule, including complementary experiments. Top shows the experiments which utilise single phase LArTPC designs, whilst bottom shows experiments which utilise a dual phase design. The experiments which are part of the DUNE prototyping program are shown in red. The figures are taken from [70, 31].

prototyping schedule to be performed. A brief outline of this prototyping effort is shown in Figure 2.20. It should be noted that experiments not associated with DUNE which also use LArTPCs, will also feed into the development of DUNE by improving the technology used in LArTPCs. For this reason MicroBooNE and SBND are shown in Figure 2.20, but experiments not shown in Figure 2.20 such as ArgoNeut and LArIAT, will also feed into the development of DUNE through the improvements which they make to LArTPC technology.

As shown by Figure 2.20, the 35 ton is the first prototype under the umbrella of the DUNE experiment, for the single phase detector design. As such, the 35 ton provides a test bed for many of the novel aspects of the detector design required for the DUNE FDs. This testing was done during two running periods, the Phase 1 run from November 2013 - February 2014, and the Phase 2 run from November 2015 - March 2016. Chapters 3, 4, and 5, will focus on some of the studies performed in preparation for, and during the Phase 2 run.

The primary goal of the Phase 1 run was to verify that a detector with a membrane cryostat could achieve, and maintain, the high levels of LAr purity which are required to perform the physics which DUNE hopes to achieve. It was also designed to show that it was

possible to achieve this high level of purity without the need to fully evacuate the detector prior to filling, but that this could instead be achieved by performing a “piston purge.” This “piston purge” had previously been demonstrated by the Liquid Argon Purity Demonstrator (LAPD) [71], which the 35 ton was built next to, at Fermilab’s PC-4 facility. The process by which the “piston purge” was performed is as follows. Firstly, room temperature argon is pumped into the detector, displacing the air in the detector. Once the purity is no longer seen to improve, a gas/liquid spray is used to slowly cool the detector. The injection of the spray introduces turbulence into the gas in the detector, which causes the entire cryostat to cool, meaning that there are no large temperature differences in the cryostat. Upon the completion of the cooldown, filling of the LAr commences, and LAr purification is performed using the installed recirculation loop. Using this purification method, electron lifetimes of 3 ms were observed, and maintained for many days at a time, demonstrating that membrane cryostat technology is capable of producing and maintaining high purity LAr [72, 73].

A detector similar to ProtoDUNE (outlined below), was originally planned to follow the Phase I run, however, funding constraints meant that this detector (at the time part of LBNE) got cancelled, and so the 35 ton was repurposed to contain a TPC. This repurposed 35 ton detector is the 35 ton Phase II run. The TPC which was installed had many of the features which are present in the single phase reference design, these include:

- Modular APAs with wrapped wires, collecting charge from multiple drift volumes.
- Vertical and horizontal gaps between APAs. The Phase II run must show that it is possible to stitch particle tracks across, and through, APA frames.
- APAs and electronics which are immersed in the LAr.
- Waveguide-style photon detectors, installed inside the APA frames.
- A field cage built using FR4 printed circuit board.
- A DAQ which is capable of taking triggerless operation.

All of these features are central to the single phase DUNE detector design, and so demonstrating the successful operation of a detector with these properties is an important step in realising DUNE. Getting the Liquid Argon Software (LArSoft) framework (outlined in Section 2.6) ready for data taking required extensive simulation work, some of which is presented in Chapter 4.

In total four APAs were installed in the 35 ton cryostat, each collecting charge from two drift volumes, to give a total of 8 TPCs. As the drift volume for the 35 ton was limited to around 2.5 m, it was not possible to use TPCs with the drift length which will be present in the DUNE FD design. As such, it was decided that the TPCs would either have a “long” drift volume of 2.23 m, or a “short” drift volume of 0.27 m. These lengths were chosen so as to represent a reasonable drift distance in the “short” drift volume, whilst also maximising the “long” drift distance. The four APAs which were installed were done so, so as to have two “long” APAs, of roughly the length of proposed the LBNE APA frames, and two “short” APAs, stacked on top of each other, sandwiched between the two “long” APAs. This orientation allowed for both vertical, and horizontal gaps to be produced, over which reconstruction algorithms could attempt to stitch tracks. A total of 8 photon detectors were installed in the APAs, with 3 PDs in each of the “long” APAs, and 1 PD in each of the “short” APAs. A schematic of the 35 ton cryostat, with the TPC installed is shown in Figure 2.21.

Figure 2.21, also shows a system of Cosmic Ray Counters (CRCs) on the outer edges of the cryostat walls. These were installed so as to be able to easily gather a set of cosmic muons which were either parallel, or perpendicular, to the APA frames, as it was envisioned that these muons would be useful for later studies. There was also an additional set of CRCs on top of the cryostat to collect muons which were nearly vertical. The location of the 35 ton was not in a beamline, because, as discussed earlier, it was not originally intended to house a TPC. As such, only cosmic ray data was collected in the Phase II run, and so the muons identified by these CRCs produced a very valuable subset of the data. The locations, and numbering scheme for the CRCs, is shown in Figure 2.22.

The Phase II run would build on the experience gained during the Phase I run, using the same process for the initial cooldown, and LAr recirculation. The run would also serve to show that the electron lifetime which could be achieved would not be limited by the presence of a detector. The operation of the installed TPC would also serve to test many of the novel features if the FD reference design. The results from the Phase II run are shown in Chapter 5.

Following on from the 35 ton Phase II run is the single phase ProtoDUNE detector, which is due to take data in the second half of 2018. The ProtoDUNE detector is a scaled version of the full DUNE single phase reference design, as the APAs, and the drift length, are the same size as those in the reference design. The detector will be in a test beam, and so will be able to fully test the assumptions made in the DUNE CDRs about the detector performance characteristics. The detector will contain two sets of three APAs, 7.2 m apart, with one set of

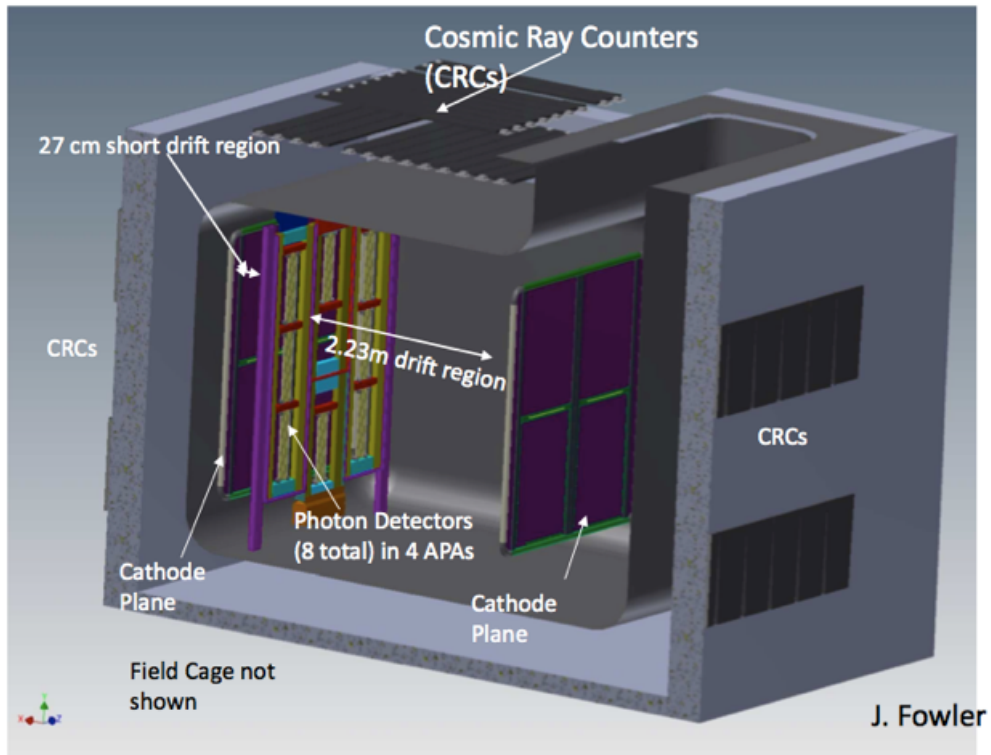


Fig. 2.21 A schematic representation of the TPC installed in 35 ton prototype, for the Phase II run. The cathode planes (purple), photon detectors (yellow), APAs (bounded blue regions), cosmic rays counters (outer black rectangles), and the two drift volumes (2.23 m and 0.27 m) are shown. The 35 ton vessel (spotted grey), and steel contained (black) are also shown. The field cage is not shown. Cryogenic piping for the detector is placed within the cryostat, to the right of the cathode plane associated with the “long” drift. The figure is taken from [31].

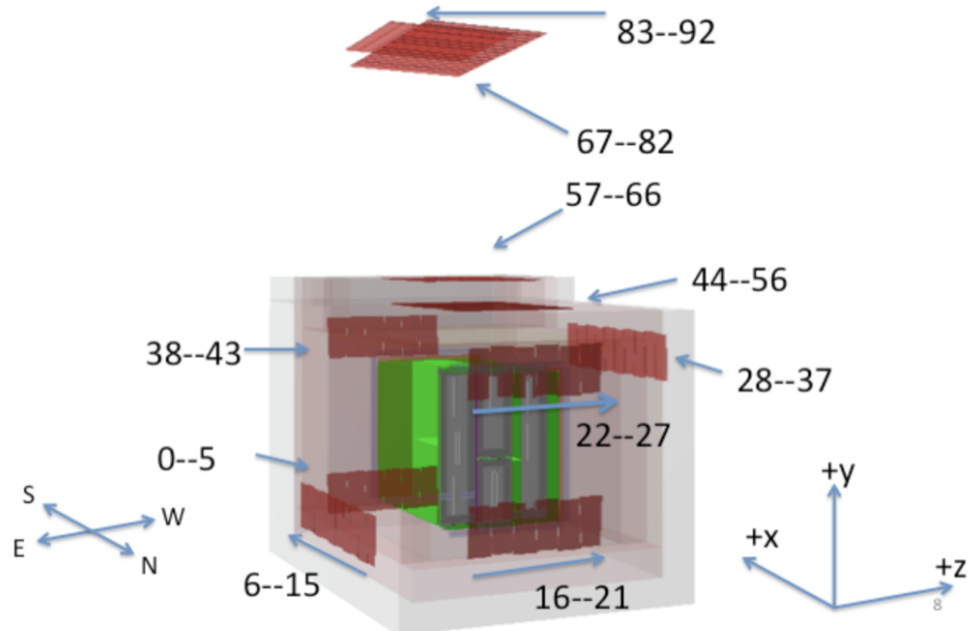


Fig. 2.22 A representation of the counter locations in the 35 ton, with the magnetic, and LArSoft, co-ordinate systems shown. The other detector components can be seen inside the cryostat, such that the counters on the North wall are behind the short drift volume. The East - West counters are numbered 6-15 and 28-37 respectively. The North Lower - South Upper counters are numbered 16-21 and 38 - 43 respectively. The North Upper - South Lower counters are numbered 22-27 and 0-5 respectively. The “telescope” (vertically through-going) counters are numbered 44-92 and are split into four groups.

CPAs between them. This will give a total of 6 TPCs, each with a drift length of 3.6 m.

There is also a series of prototypes for the dual phase design. The WA105 project involves both a small scale demonstrator with an active mass of $1 \times 3 \times 3 \text{ m}^3$, which ran from late 2016 to early 2017, and a larger, scaled version of the dual phase design, the dual phase ProtoDUNE detector, measuring $6 \times 6 \times 6 \text{ m}^3$. As was the case with the single phase prototypes, the demonstrator is not in a beam and so has only taken cosmic data, whilst the larger detector is in a test beam, at the CERN neutrino platform. The larger detector will serve as a full scale demonstration of the dual phase detector design, though the drift distance is half of that in the final DUNE FD. Data-taking for this detector will be during the second half of 2018, at roughly the same time as the single phase ProtoDUNE detector.

2.6 The DUNE software

The software package used by DUNE is called LArSoft [74] [75]. LArSoft is a simulation, reconstruction and analysis package for LArTPCs that is being used by many experiments in the US neutrino program. It has been developed to be detector agnostic, meaning that much of the code is shared between experiments. To this end, it is envisioned that it will be used as a platform for constant development in existing experiments, and those still in the planning phases, such as DUNE. LArSoft is built around the Fermilab-supported *analysis reconstruction framework (art)*. External packages such as ROOT [76] and GEANT4 [77] are incorporated into LArSoft, meaning that the user does not have to coordinate specific versions of the packages.

There are numerous mechanisms by which particles can be generated within the software, as many external packages have been incorporated into the software. One such package is Generates Events for Neutrino Interaction Experiments (GENIE) [78], which is used to study neutrino interactions and nucleon decays. Another package, Nuance [79], is a neutrino interaction generator specifically for LAr. Finally, Cosmic-ray Shower Library (CRY) [80, 81], and COsmic Ray SImulations for KAscade (CORSIKA) [82], are cosmic ray events generators, which are used to simulate the expected event rates for surface detector locations, in the absence of a neutrino beam. Recently the MUon Simulations UNderground (MUSUN) [83, 84] generator, which takes the output of MUon SImulation Code (MUSIC) [83, 85, 86], has also been incorporated, see Section 6.2 for further details. It is also possible to use a single particle generator, where the particle type, initial momenta, initial

positions, and initial directions, can all be set by the user.

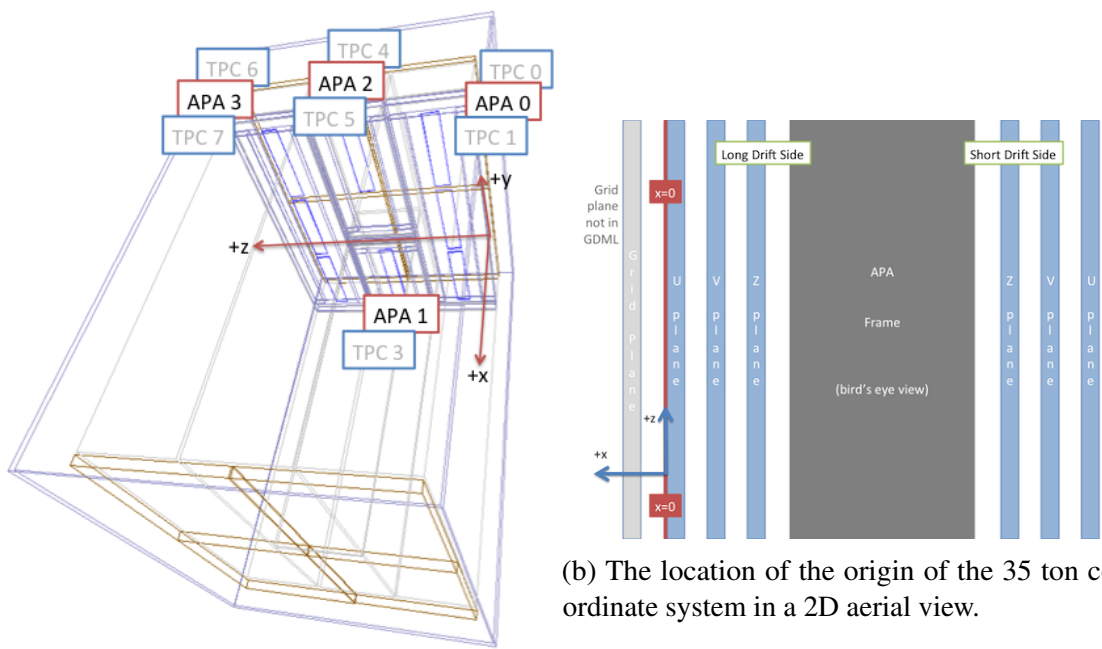
The co-ordinates and angles in LArSoft are defined as follows;

- x - The beam direction, with maximal x being where the beam enters the detector.
 - In the 35 ton prototype where there is no beam, positive x is in the opposite direction to that which electrons drift in the large TPC, where $x = 0$ is the position of the APA frames in the long drift volume.
 - In the far detector geometry $x = 0$ is defined as the midpoint between the two rows of CPAs
- y - The vertical direction, with maximal y being the most highest point.
 - In the 35 ton $y = 0$ is halfway between the gap created by the two centre APAs, which are mounted one above the other.
 - In the far detector $y = 0$ is defined as the midpoint between the two vertical layers of TPCs.
- z - Defined so as to have a right handed co-ordinate system.
 - In both the 35 ton, and the far detector geometries, $z = 0$ is at the edge of the leftmost (when looking down the long drift volume) APA frame.
- θ - The angle that a vector makes from the x axis in the xy plane.
- ϕ - The angle between the z axis and the vector.

Figure 2.23 shows a schematic representations of how the location of the origin appears in the 35 ton prototype.

The simulation of particles is usually split into five processes, to reflect the different area in which development often progresses. These stages are as follows;

- Particle generator.
- Particle transport using GEANT4.
- Full detector simulation, including detector responses.
- Full event reconstruction.



(a) The location of the origin of the 35 ton co-ordinate system in 3D.

(b) The location of the origin of the 35 ton co-ordinate system in a 2D aerial view.

Fig. 2.23 The LArSoft co-ordinate system as it is represented in the 35 ton. Left shows the location of the origin, relative to the TPC detector components. The four APAs, and eight TPCs are shown, where the even numbered TPCs are on the “short” drift side, 27 cm drift, and the odd numbered TPCs are on the “long” drift side, 223 cm drift. The CPAs (objects with a brown outline) are also shown. Right shows the location of the origin with respect to the APAs, and also shows the wire planes. It can be seen that $x = 0$ is defined as the location of the U plane in the “long” drift volume. The figure is taken from [87].

- Analysis.

The advantage of separating the computational processes in this way, is that improvements can be easily applied to a file without rerunning the entire simulation/reconstruction chain. This is especially important when large Monte Carlo, or data, samples are produced for general use within the collaboration, because it allows users to concentrate on improving a specific part of the computational process. When these all-purpose samples are produced a very general analysis is performed, which provides users with all of the Monte Carlo truth information, along with all of the reconstructed quantities. This general analysis produces a file which can be used outside of the LArSoft framework, so that users can perform analyses independently of LArSoft, should they wish to.

Later significant focus will be given to the reconstruction of TPC data, and so it is necessary to briefly illustrate the mechanisms by which TPC data is reconstructed in LArSoft. Much of the information presented below is summarised in [75, 88]. The data collected by an experiment will have detector effects such as, an electronics response function, and a pedestal offset, present in the data. The full detector simulation also introduces these detector effects into simulated data, so that the reconstruction process does not treat simulated, and collected data, differently. The first step of the reconstruction algorithms is therefore, the removal of these detector effects. Once these effects are removed, the signal is estimated using the value of *signal/noise* which would produce the measured signal. This process, called deconvolution, does not conserve pulse height, and is not guaranteed to preserve the normalisation. The deconvoluted signals are all unipolar distributions, which means that Gaussian distributions can be fitted to them, when trying to reconstruct hits. This is shown in Figure 2.24, and explained further below.

The deconvoluted signals are reconstructed into hits by identifying regions that are above a threshold value, and then attempting to replicate the signal in these regions by introducing Gaussian distributions. For isolated hits, this is typically achieved using only one Gaussian distribution, however, for large energy depositions, over a large period time, where many particles are involved, multiple Gaussian distributions are often required. Large energy depositions are also possible when the direction of the particle aligns with the inclination of a wire plane, this means that all of the deposited energy may be deposited on a single wire. Examples of reconstructed hits are shown in Figure 2.24. These figures are taken from separate CRY simulated events, and so do not correspond to a continuous simulated event. They have been selected only as a demonstration of the process of hit reconstruction. Figures 2.24a, and 2.24b, show multiple time-separated energy depositions on a collection

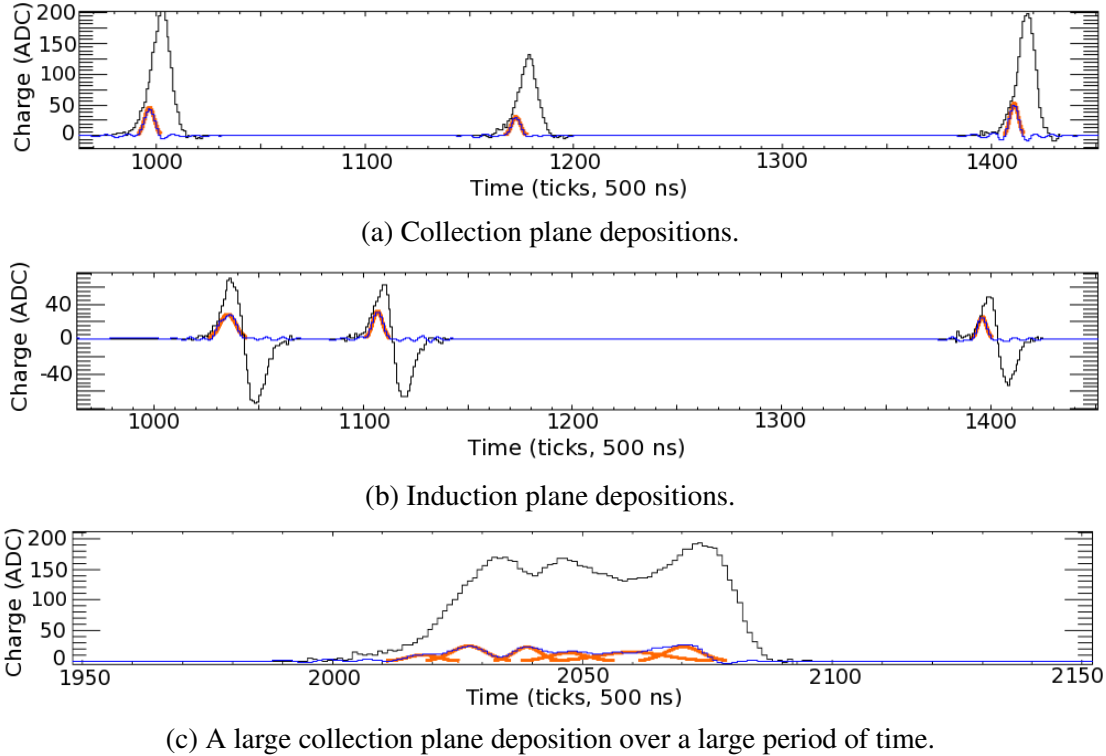


Fig. 2.24 The raw and deconvoluted signals, with reconstructed hits, for simulated energy depositions. The depositions, from particles generated by CRY, are not from a single event, and have been selected for demonstration purposes only. The plots are shown with increasing charge (ADC) on the y axis, and increasing time (ticks, 500 ns) on the x axis. The black lines represent the raw signals, the blue lines represent the deconvoluted signals, and the orange lines represent the reconstructed hits. Top shows depositions on a collection plane wire, it can be seen that the raw signal is unipolar. Middle shows depositions on an induction plane wire, it can be seen that the raw signal is bi-polar, whilst the deconvoluted signal, and reconstructed hits, are unipolar. Bottom shows a complex deposition on a collection plane wire, where multiple reconstructed hits are required to reproduce the deconvoluted signal.

plane wire, and an induction plane wire, respectively. A more complex energy deposition on a collection plane wire is shown in Figure 2.24c, where energy depositions from many particles, at similar times, have created a complicated energy deposition, which requires many reconstructed hits to explain.

As noted in Section 2.3, and Section 2.5, the DUNE FD, and the 35 ton, both have wrapped wires on the induction planes. A result of this, is that the location of the reconstructed hit on an induction wire is ambiguous, as a single wire has many wire segments, as shown in Figure 2.6. An important feature of this ambiguity, is that the TPC in which the hit occurred cannot be identified, unless it is combined with another hit. These ambiguities do not extend to the collection plane wires, as they are not wrapped, and so consist of only a single wire segment, in a single TPC. Hits are combined across the three planes by identifying wire segments on each plane which intersect, and have hits at common times. In the traditional reconstruction process only hits that make these so-called ‘triple points’ are considered disambiguated, with other hits being identified as noise hits, causing them to be discarded.

The inclination of the wire planes has to be carefully chosen so as to minimise both the number of wires required, and the number of times that wire triplets intersect. This is shown in Figure 2.25, where the wire inclinations used in the 35 ton detector are compared to those in the DUNE FD reference design. The inclination of wires in the 35 ton was $45^\circ \pm 0.7^\circ$, meaning that many wire triplets cross twice, and some wire pairs cross three times. When wire triplets cross multiple times, the triplet which has the smallest distance between the common intersection point, and the two-wire intersection points, is chosen as the location of the hit. This is shown as the ‘Good intersection’ on the right panel in Figure 2.25. The different wire pitches are necessary so that one of the triple points can be evaluated to be a better candidate for the hit location, as with a wire pitch of 45° it can be impossible to distinguish between different triple points. The inclination of wires in the FD was chosen to be 36° to remove the possibility of multiple intersection points, as given the geometry of the APAs, multiple intersection points are impossible, and so disambiguation is much simpler. The lower inclination results in more induction wires being required though, making it more expensive to instrument the detector. It is also important that all wires on a given APA are either read out at the top, or base, of the APA. This is because there must be minimal space between TPCs in the DUNE FD to reduce the internal dead space. As a result of this, APAs at the top of the cryostat are read out from the top of the APA, whilst APAs at the bottom of the cryostat are read out from the bottom of the APA. The APAs are never read out from the

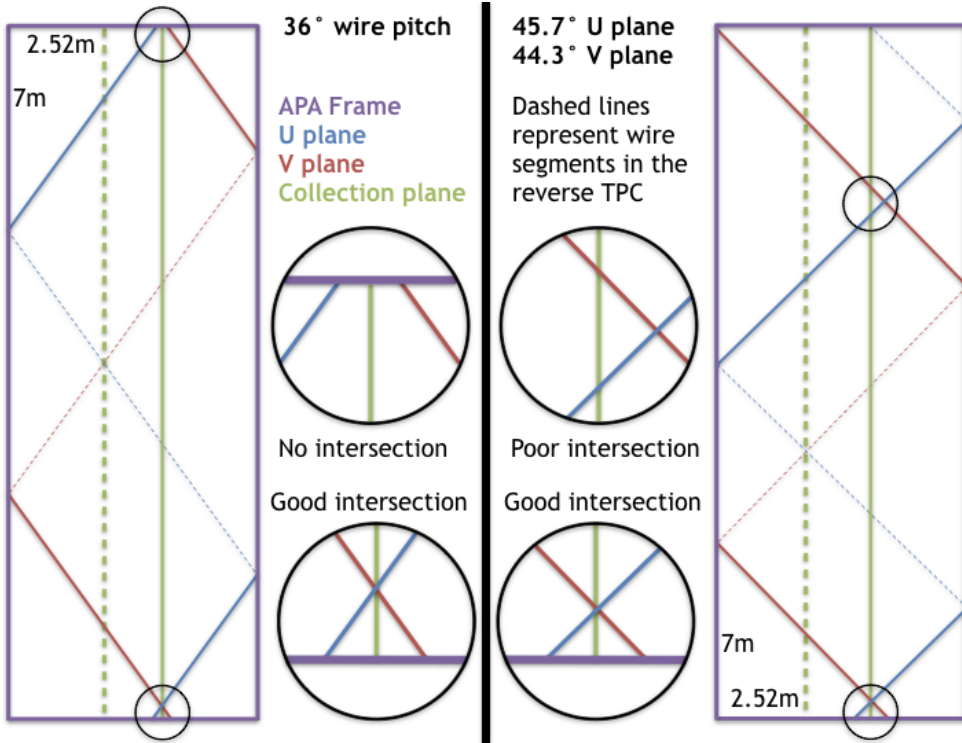


Fig. 2.25 The effect that different wire pitches have on the ability to perform disambiguation in APAs with the far detector geometry. The left panel shows a wire pitch of 36° , which is the reference design for the far detector, whilst the right panel shows wire pitches of $45^\circ \pm 0.7^\circ$, as was used in the 35 ton. The left panel shows that only one 'triple point' can be made with the three wires shown, and so disambiguation is trivial. The right panel shows that two 'triple points' can be made with the three wires shown. The 'triple point' where the three wires have a common intersection point is labelled as a 'good intersection,' and it is this intersection point which would be chosen for the disambiguated hit.

sides of the APAs, as the amount of cabling which would be required to do this, would cause a large amount of dead space between adjacent APAs.

Once the hits have been disambiguated they are combined to make clusters in each of the three planes. The clustering process is usually performed in wire-tick space on each plane separately, where all the hits from a single track or shower, should make a single cluster in each plane. It is possible to seed the start of clusters by using imaging techniques such as a Harris transform [89], or to identify straight lines by using Hough transforms [90]. As hits from a physical entity are unlikely to remain on a single channel, or all come at identical times, clusters are often spread out over many channels, for a range of times, especially when performing clustering for showers.

Once clusters have been identified in each plane, they can then be merged into 3-dimensional tracks and showers. The two most common tracking algorithms are PM-Track [55] and Pandora [91], and the most common showering algorithm is EMShower [92]. Once 3D objects have been reconstructed, the calorimetric quantities need to be determined, this is often done separately for each plane. Two models exist for calculating $\frac{dE}{dx}$ in LArSoft, Birks model [93] and a modified Box model [94]. The modified Box model uses a correction to the Box model [95] at low values of $\frac{dE}{dx}$. Normally the modified Box model is used, as it holds for both large and small ionisation's, whereas Birks model experiences difficulties at large ionisation's, and the traditional Box model struggles at low $\frac{dE}{dx}$. Both models incorporated in LArSoft calculate the $\frac{dE}{dx}$ of a hit using the deposited charge (dQ), and the track pitch (dx) of the hit, as well as the conversion of ADC value to number of electrons ($C_{GeV \rightarrow e^-}$), a correction due to electron lifetime ($C_{lifetime}$), the LAr density (ρ), the electric field (E_{field}), and the tuneable electron recombination factors ($Recomb_X$). The series of equations used in Birks model are shown in Equation 2.1, whilst those used in the modified Box model are shown in Equation 2.2.

$$\frac{dE}{dx} = \frac{dQdx}{\alpha - (\beta \times dQdx)} \quad (2.1a)$$

$$dQdx = \frac{dQ \times C_{lifetime}}{dx \times C_{ADC \rightarrow e^-}} \quad (2.1b)$$

$$\alpha = Recomb_A \times C_{GeV \rightarrow e^-} \times 10^{-3} \quad (2.1c)$$

$$\beta = \frac{Recomb_B}{\rho \times E_{field}} \quad (2.1d)$$

$$\frac{dE}{dx} = \frac{e^\alpha - Recomb_A}{\beta} \quad (2.2a)$$

$$\alpha = \frac{10^3 \times \beta}{C_{GeV \rightarrow e^-}} \times \frac{dQ}{dx} \quad (2.2b)$$

$$dQdx = \frac{dQ \times C_{lifetime}}{dx \times C_{ADC \rightarrow e^-}} \quad (2.2c)$$

$$\beta = \frac{Recomb_B}{\rho \times E_{field}} \quad (2.2d)$$

When performing calorimetry, it is also important that the interaction time is known, so that the x positions of hits can be corrected, as they will be reconstructed assuming an

interaction time of 0 s. This assumption is made, because when using beam events, the beam trigger is placed at a time of $T = 0$. An unknown interaction time causes the hit and track positions to be calculated incorrectly, and will also skew the calorimetric corrections, as recombination is a drift dependant effect.

Chapter 3

The 35 ton camera system

As noted in Section 2.5, a camera system which was designed and built by the University of Sheffield, was installed in Run II of the 35 ton prototype. The reason for this was to monitor the cryostat for any potential high voltage (HV) breakdowns. The occurrence of a HV breakdown in liquid Argon (LAr) is possible due to the large electric fields which are required for experiments such as DUNE. For example, when the drift field of 500 V cm^{-1} will be applied to the DUNE far detector (FD), it will require a bias voltage of -180 kV [31] on the cathode plane. As the breakdown field has recently been measured to be much lower than this, at around 40 kV cm^{-1} [96], some form of monitoring is required.

To this end, a Complementary Metal-Oxide Semiconductor (CMOS) camera is used within the LAr to observe any potential HV breakdowns in the 35 ton cryostat. Charge-Coupled Device (CCD), and CMOS cameras have previously been used to do this. This has never been done before using cameras which are immersed in LAr. Previously, cameras have either used viewing ports which were built into the detector, or were inside enclosures which had a raised temperature [96, 97, 71, 98, 99]. As well as looking for HV breakdowns, the cameras also visually monitored the TPC and cryogenic components as filling occurred. The information contained in this section is a summary of the paper detailing the performance of the cameras in the 35 ton prototype [100]. The author was responsible for the fabrication of, initial setup, and maintainence of all equipment which was used at Fermilab, including ensuring that the camera system met all safety standards. The author was not responsible for the studies which were performed to select the cameras used, or in the design and construction of the camera mounting modules.

3.1 The selection and characterisation of cameras

As the cameras in the 35 ton are submerged in LAr, they are required to work at cryogenic temperatures. The cameras are also required to be sensitive enough to visible light, that they can observe the sparks created by the HV breakdowns, this means that the cameras must have low thermal noise. CMOS cameras are used as there are many cameras which are rated to work down to temperatures of -40 °C. CMOS cameras are also found to have lower leakage currents, improved mobility, and lower thermal noise, at temperatures around 100K [101, 102].

When a shock test, consisting of submersion in LAr, is performed on a range of CMOS cameras, it is found that the most reliable camera is a *Floureon* car reversing camera. It is believed that the simplicity of this camera allows it to be relatively unaffected when operating at low temperatures. This is because it has a simple internal circuit consisting of resistors, capacitors, a crystal oscillator, and a flash memory chip.

It is important to determine the effect which operation at cryogenic temperatures has on the performance of the cameras. To do this, the frame rate, and resolutions in both time and space, whilst submerged in LAr, are compared with a complementary set of measurements made at room temperature in air. It is found that the frame rate, and resolution in time, are both unaffected at 50 Hz, and 20 ns, respectively. The timing resolution of the cameras was determined using LED's in a dark box, which were connected to a pulse generator that generated pulses of variable widths. It was found that in both air and LAr, the cameras were able to trigger on pulses once they were longer than 20 ns. The spatial resolution, which was also found to be unaffected within systematic errors, was measured by varying the distance between two optical fibres, connected to a single LED, until the light from both optical fibres could no longer be resolved.

When attempting to use the cameras to locate HV breakdowns, it is necessary to develop a triggering mechanism. The camera signals are read out using a digital video recorder (DVR), which is remotely accessible using SwannView Link, a commercially available surveillance program. The SwannView Link software detects movement between successive frames, and so in normal use will begin recording if, for example, a person enters the field of view. The length of time for which a video is recorded, and the number of frames which are recorded before the trigger, can be configured by the user. The monitoring for HV breakdowns is remarkably similar to this application, as when a breakdown occurs the field of view would be illuminated by a large flash of light, which was not present in the previous frame. When

determining if a breakdown has occurred, a threshold in the number of pixels which change between consecutive frames is used. It is also possible to select only a limited number of pixels, if for example, some regions of the cameras field of view are rapidly changing, or if the expected change would only be in a very precise location. This was the case with some of the cameras in the 35 ton, where there was elevated thermal noise in some regions of the camera pictures.

The ability of the cameras to measure HV breakdowns, using the above triggering system, was tested prior to installation in the 35 ton. In the tests, a high voltage was applied across a printed circuit board, until breakdown was observed. When breakdowns occurred, the triggers which the cameras recorded showed sparks which were highly localised and lasted over multiple frames.

3.2 The design of the camera system

As will be noted at the start of Chapter 5, the 35 ton detector was filled with LAr for over 3 months, and so the shock tests performed with liquid nitrogen were not sufficient to guarantee continuous running of the cameras during the entire 35 ton run. It is also necessary to protect against the prospect of a power failure, which could cause the cameras to be turned off for a large period of time. Should this occur, the cameras would have to be able to be turned on at cryogenic temperatures. During testing, it was found that whilst some of the *Floureon* cameras were able to do this, this was not the case for all cameras. Only cameras which were found to be able to be turned off and on again in the cold were used in the 35 ton. The process of turning a camera off and on again is referred to here as a camera being “power cycled.”

As the failure rate of the cameras was non-zero, and because the 35 ton run was scheduled to be much longer than any cameras had been tested in the cold, it was decided that it was prudent to build a self-contained module to house the cameras. A heater, consisting of two resistors placed either side of the camera, was installed inside the camera module. This is because it was found that some of the cameras which failed the shock tests, could be power cycled when they were exposed to an elevated, though still cryogenic, temperature. A temperature sensor was also placed in the modules, so that the increase in temperature during normal operation, and also during heating, could be measured. It was found that the cameras caused the internal temperature of the module to rise by roughly 15 K, though the temperature of the glass viewing panel, and the external camera module, were unchanged. It

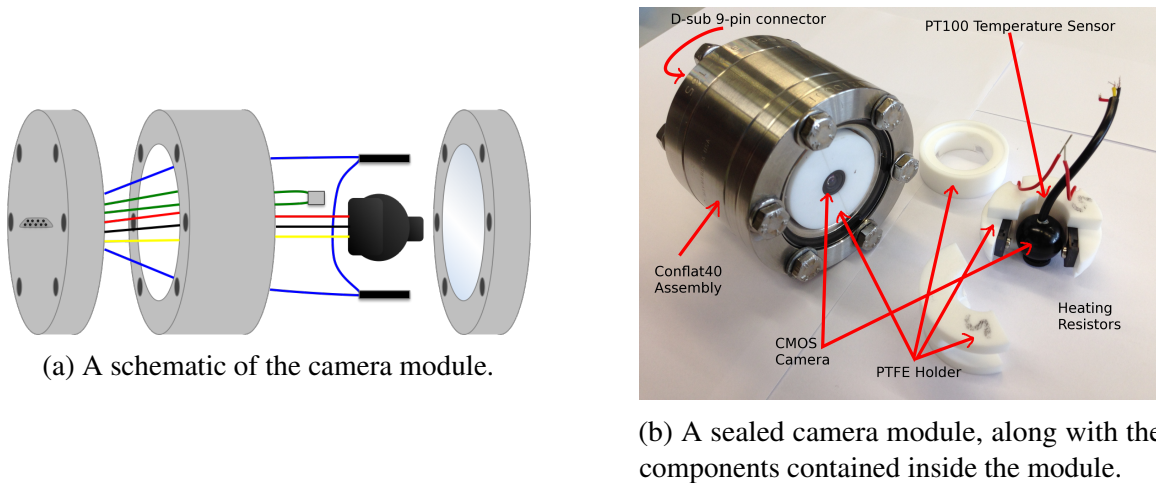


Fig. 3.1 The components which made up a camera module used in the 35 ton camera system. Left: a schematic representation of the components in the camera modules, with wires from the PT100 temperature sensor (green), the heating resistors (blue) and camera (red, blue, yellow), connected to a 9-pin D-sub feed through, shown on the left of the image. Right: the physical components, both inside and outside, a module. A camera, a heater and a temperature sensor, can all be seen. A PTFE holder is used to ensure that the components remain in the desired locations, with the camera pressed up to the glass viewing panel. Bolts are used to ensure that the camera modules are leak tight.

was also found that with the heater operational, the internal temperature of the module could rise by as much as 80 K after 17 minutes. During operation, the heaters and power supply to the cameras were controlled using a custom-built, remotely controllable device, built by Bob Bridgeland, at the University of Warwick. The temperature from the PT100 sensor was processed by another custom-made device, the output of which was read into a computer, using a NI USB-6009 device.

A schematic of a camera module is shown in Figure 3.1a. Figure 3.1b shows a picture of a sealed camera module, with the individual components inside a module next to it.

It was necessary to mount the camera modules inside the 35 ton. This was achieved using a custom-designed mounting bracket, an example of which is shown in Figure 3.2. The mounts were fixed to existing cryogenic pipework, and could be freely rotated, so that the cameras could be pointed towards specific regions of interest. This meant that the camera mounts had two degrees of freedom, as well as being able to freely placed on the cryogenic pipes.



Fig. 3.2 Two camera modules which are mounted in the 35 ton prototype detector. The mounts are affixed to a 3" SCH cryogenic pipe. The multi-coloured ribbon cables which were used to carry the camera signals outside of the cryostat can be seen in the picture.

However, before the cameras could be installed in the 35 ton cryostat, several safety reviews had to be completed, in order to comply with safety standards set out by Fermilab, the host lab for the 35 ton prototype. These consisted of a review of the cable rack which was used during operations, plus individual reviews for the components which were custom-built. There was also a further review covering the camera system as a whole when it was operational. Only after the successful completion of all of these reviews was the camera system allowed to be installed, and ran unsupervised, inside the 35 ton cryostat.

In order to satisfy the safety requirements, adequate grounding of the rack, and all of its components, had to be displayed. This requirement extended to ensuring that the cables used in the system, which were assembled at Fermilab, would not introduce any potential ground loops into the 35 ton system. This meant that detailed diagrams of the individual components, and how they linked together to form the camera system, had to be produced. The detailed diagram which was produced representing the entire camera system is shown in Figure 3.3.

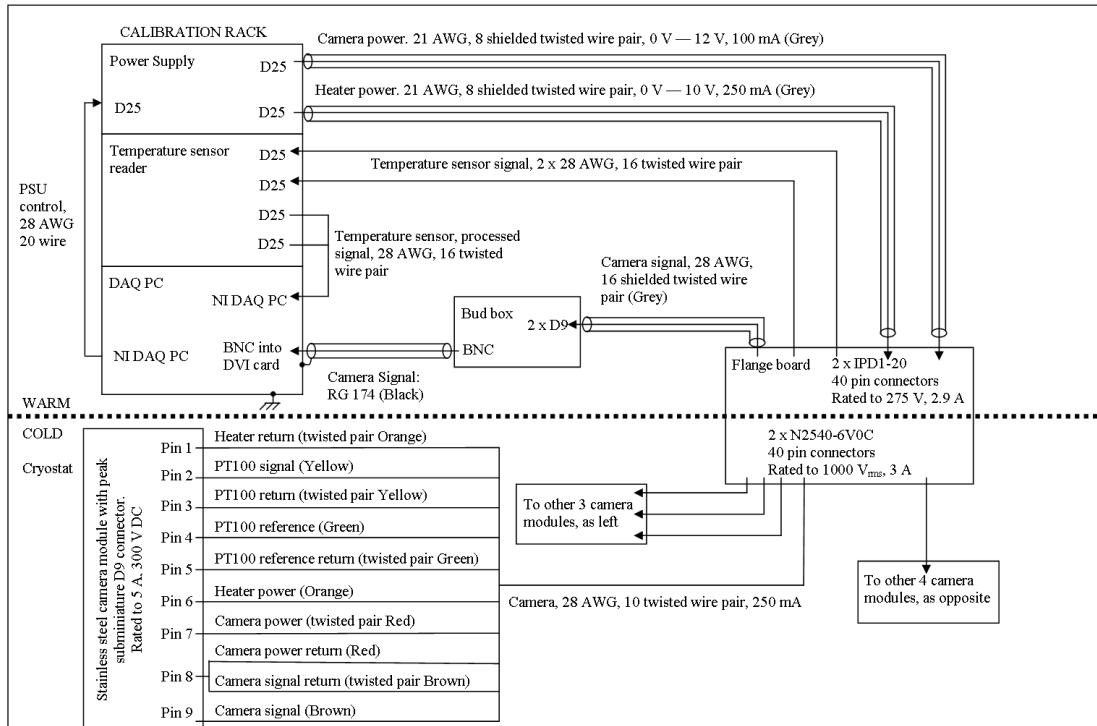


Fig. 3.3 The system diagram for the 35 ton camera system. The contents of the rack which was used in the camera system (top left), the wires which were terminated at the flange board (right), and the signals that each of the wires connected to the cameras carried (bottom left), are shown. In addition to this, the wire gauge (in units of American Wire Gauge), along with the voltages and currents which they carried, and the number of wires which were bound together, are shown for the connections between each subsystem and the flange board. Shielded wires are shown as wires with cylindrical covers around them, such as the wire labelled "Camera power." In total there were eight camera modules installed in the cryostat, connected in two groups of four cameras, to the flange board by two 40 pin connectors.

3.3 Performance in the 35 ton

In total eight cameras were installed inside the 35 ton cryostat, the locations of which were selected to maximise the potential of observing any HV breakdowns which may occur. It was decided that the cameras would be focused on the following parts of the detector;

- The top right hand corner of the cathode.
- The bottom right hand corner of the cathode.
- The top left hand corner of the cathode.
- The bottom left hand corner of the cathode.
- The location of the high voltage feedthrough.
- The ullage - the gap between the top of the TPC, and the roof of the cryostat
- The cool down sprayers - this was only for use during cool down, to check that they were operating as expected.
- The phase separator - this was for use during operation to ensure that it was running as expected.

Upon installation in the cryostat, some calibration images were taken for each camera, these are shown in Figure 3.4.

As previously mentioned, the cameras used were car reversing cameras, and so this is why there are distance lines on some of the images in Figure 3.4. From Figure 3.4, it also evident that there is a large variation in the picture quality of the different cameras. This is attributed to aspects of the cabling, as some cables were slightly longer than others, or had less reliable electrical connections. It could also be due to differences in the cameras, because, as discussed in Section 3.2, the stability of the cameras which were tested was not uniform. This variability in the camera stability, also manifested itself in the amount of signal degradation which was observed over time. The signal degradation over the course of the run, for two cameras, is shown in Figure 3.5.

From Figure 3.5, it can be seen over the course of the run, the fields-of-view for both cameras became more pixelated, and that there was an increase in the number of pixels which were either saturated, or dead. The large number of saturated pixels was particularly evident when the cryostat was not illuminated, and meant that the region which could be

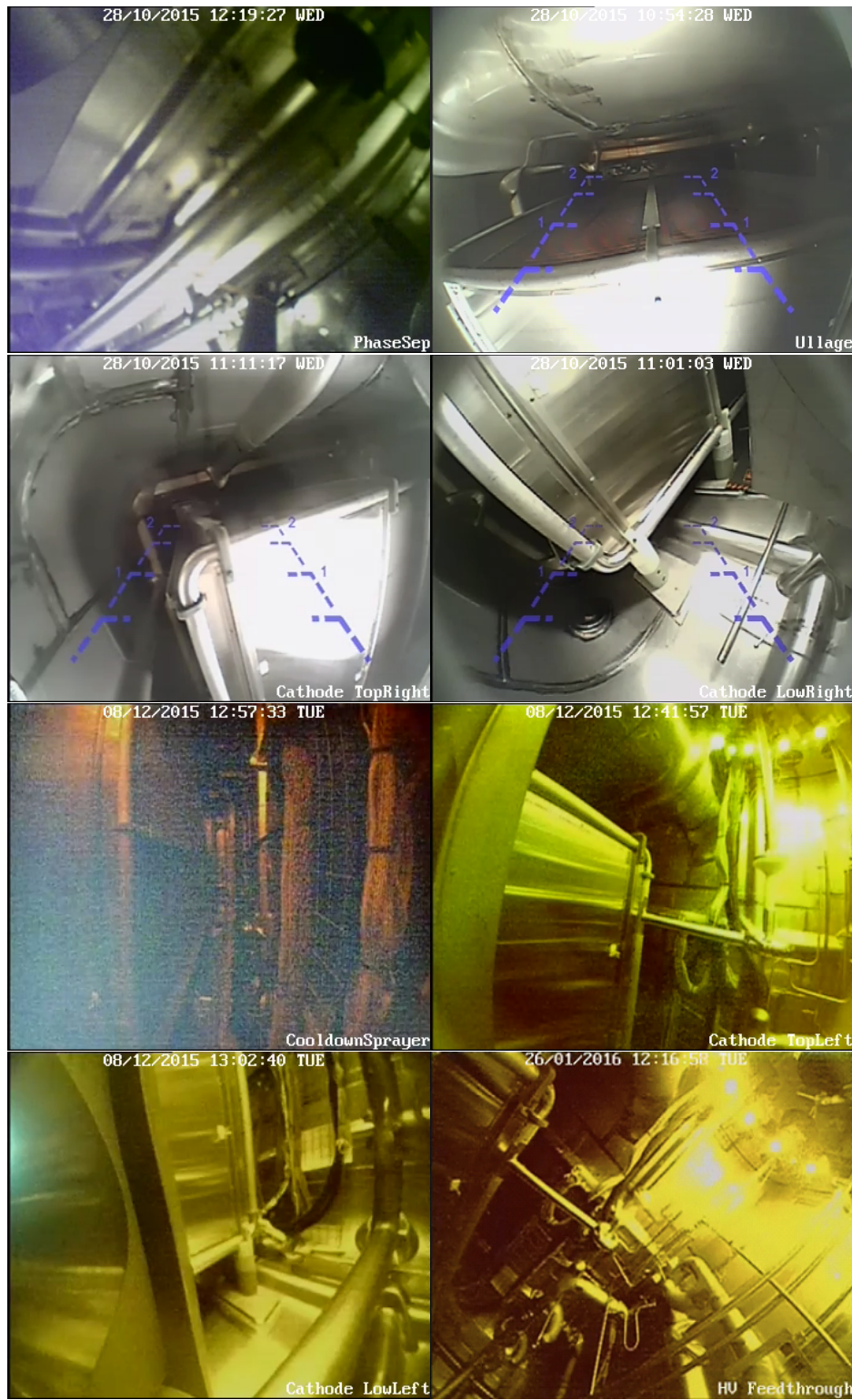


Fig. 3.4 The calibration images for the 8 cameras used in the 35 ton camera system. The images from left to right, top to bottom, show the following: phase separator, ullage, cathode top right, cathode bottom right, cool down sprayers, cathode top left, cathode bottom left, and high voltage feed through. The upper four images were taken with a halogen light illuminating the cryostat, prior to it being sealed up. The lower four images were taken after the cryostat was sealed, and was illuminated by a ring of LEDs. All images are left-right inverted due to software.



(a) The degradation in signal quality of the camera focused on the ullage.



(b) The degradation in signal quality of the camera focused on the lower left corner of the cathode.

Fig. 3.5 The signal degradation over time for two cameras in the 35 ton camera system. Top shows the signal degradation observed for the camera focused on the ullage. Bottom shows the signal degradation for the camera focused on the lower left corner of the cathode. For both cameras, left shows the field-of-view prior to cool down, centre shows the field-of-view immediately after cool down, and right shows the field-view after 10 weeks of operation. These are full colour images, as recorded by the DVR, and so no post-processing has been performed on the images.

used to trigger on HV breakdowns was severely limited for some cameras. As shown, this degradation was highly camera specific, with the resolution of the ullage camera deteriorating severely, whilst the camera focusing on the lower left corner of the cathode is relatively unchanged over the course of the run. A striking difference between the left-most images, and the central and right-most images, in Figure 3.5, is the loss of colour in the images which are produced. This is attributed to a partial failure of the on-board encoding circuits, which resulted in the colour signal streams not being functional when exposed to cryogenic temperatures. This loss of colour was seen as soon as the cameras were exposed to cryogenic temperatures, and was also observed in the initial tests performed in Sheffield.

It is important to note that the cameras were able to operate safely within their modules, and did not impinge on any other systems in the cryostat. They were also found to be able to be power cycled after large periods of time in the cold, including after not being operational for a large period of time. One such period, which lasted for 9 days, was when the cameras were powered off whilst extensive noise hunting was performed. Upon being power cycled, all 8 cameras were immediately brought back online, without the need for the inbuilt heaters.

During normal operation of the 35 ton system, the high voltage operated stably at 60 kV, and so no breakdowns were observed. However, after the cathode was raised to 135 kV in low-purity argon, three of four breakdowns were detected by the camera system, and data was written to disk as expected. Unfortunately, the cameras were not able to pinpoint the exact locations of the breakdowns, and so their effectiveness at discerning the locations of HV breakdowns is still largely untested. Despite this, however, the cameras proved to be a very valuable monitoring tool in the 35 ton cryostat, and there has been interest in including analogous systems in future LArTPCs, such as SBND [103].

Chapter 4

Simulations of the 35 ton prototype

4.1 Determination of interaction times

As outlined at the end of Section 2.6, it is important to know the interaction time of a track when performing calorimetric reconstruction. When performing simulations, the simplest interaction time to assign to a reconstructed object is the Monte Carlo truth time of when the particle was created. The generation time can be used, as the time taken to travel the distances considered in simulations (less than 100 ns), is small when compared to the resolution of the detector (500 ns). When matching a reconstructed object, with a GEANT4 particle, the particle which contributed the most overall deposited charge to the whole track is chosen. In order to calculate this, the energy contribution of each particle, to the total energy for each hit on the track is calculated. The particle which contributed the most overall charge to the track, is then calculated by the summing the energy contributions for all particles, over all hits, in the track. The ability to calculate the true interaction times of 3D objects, such as tracks, is vital when wanting to benchmark how well other algorithms estimate interaction times, or to determine the efficiency of the tracking algorithms, as described in Section 4.3.

It was envisioned that there would be at least two ways in which interaction times could be assigned to tracks in the 35 ton detector, one using the external cosmic ray counters, and another using reconstructed scintillation light collected by the photon detectors. The cosmic ray counters were used extensively in the 35 ton data, as described in Section 5.4. However, in simulations the scintillation light was used, as this would have been more powerful during continuous running. This is because not all particles entering the detector would pass through the counters, but one would expect almost all of them to produce reconstructable scintillation light. The flashes of light are reconstructed using a pre-built library, which models the expected number of photoelectrons that would be measured on

each photon detector, given the 3D position of the source of the flash. Using the library it is then possible to reconstruct the location of a flash in three dimensions, given the relative amounts of light that each photon detector collects. For example, less scintillation light will be collected for a flash that originated further away from the photon detectors. This library also takes into account the expected quantum efficiencies of each photon detector.

When trying to produce an association metric, a sample of 10,000 isolated positive muons generated with CRY at $T = 0$ is used. Isolated positive muons are used, as then the events should only contain one muon track, and one reconstructed flash. This should mean that matching the track and flash is trivial. The positive muons are generated outside of the detector with a constant y position, above the uppermost scintillation counters, and flat distributions in x and z . Upon simulation, it was clear that the photon detector reconstruction, using the pre-built libraries, worked well, as the reconstructed flash source normally lay very close to the track which caused it. It was found that a Point of Closest Approach (PoCA) calculation, between points on the reconstructed track, and the reconstructed flash centre, gave an effective metric by which the flash and track could be associated. Other metrics, such as the distance between the flash and track centres, and the perpendicular distance between the flash centre, and the line joining the start and end of track were investigated, but found to provide less reliable metrics. The latter of these metrics is less effective because the reconstructed tracks are rarely straight lines, due to particles scattering as they travel through the LAr. Therefore, calculating the separation between the track and the flash for each point along the track, will result in a smaller minimum separation being calculated. A comparison of these metrics is shown in Figure 4.1.

Another metric by which flashes could be assigned to reconstructed tracks, is by utilising the relationship between the number of measured photoelectrons in the simulation, and the distance from the APAs at which they were produced. When considering two flashes of scintillation light that are produced at different distances from the APAs, it would be expected that more photoelectrons would be collected when the photons were produced closer to the APAs. This relationship is shown in Figure 4.2, where it can be seen that, as drift distance increases, the number of measured photoelectrons decays exponentially. This relationship means that the distance between the APAs and the source of the flash, can be predicted from the number of measured photoelectrons. The predicted separation of the flash source and the APAs, can then be compared to the expected x position of a reconstructed track, given the difference in flash time and hit times (Figure 4.3). The difference in these two quantities can then be used as a second metric, as it gives a measure of how well matched the reconstructed

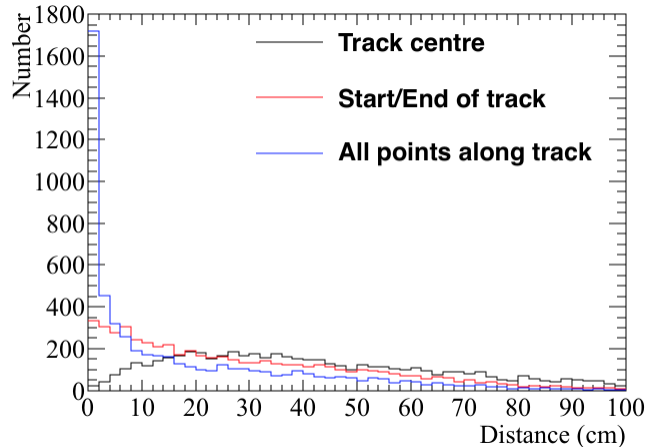


Fig. 4.1 The number of events as a function of the calculated distance between a reconstructed track, and a reconstructed flash, for various metrics. Black: the distance between the track centre and the flash centre. Red: the perpendicular distance between the flash centre, and the line joining the start and end of the track. Blue: the point of closest approach between the flash centre, and all hits along the track.

flash and track are. The number of flash/track combinations which are “well matched,” can be by the collection of points around the $y = x$ line in Figure 4.3. These points correspond to flash/track combinations where the predicted and reconstructed x positions are identical, and so the metric has very accurately predicted the interaction time of the flash.

Using these metrics, it is possible to attempt to assign reconstructed flashes to reconstructed tracks. Only flashes which are within one drift window of a given track are considered, as flashes outside of this time window cannot have been caused by the reconstructed track. Once a flash has been assigned to a track, it is possible to determine how well the matching has performed, by comparing the Monte Carlo truth interaction time with the photon detector interaction time. When doing this, it is more useful to use a CRY sample which spans multiple drift windows, as then incoming particles will create scintillation flashes at random times, as opposed to all at $T = 0$ as in the positive muon sample initially considered. The sample generated using CRY contains many particles, over a wide range of times, and is not limited to only producing positive muons. This means that it better represents the cosmic flux which will be observed by the 35 ton detector. The comparison between the Monte Carlo truth interaction time, and the photon detector interaction time, is shown in Figure 4.4.

Figure 4.4a shows a clear peak at a time difference of 0 ms between the Monte Carlo truth and photon detector times, showing that the interaction time which is calculated by the

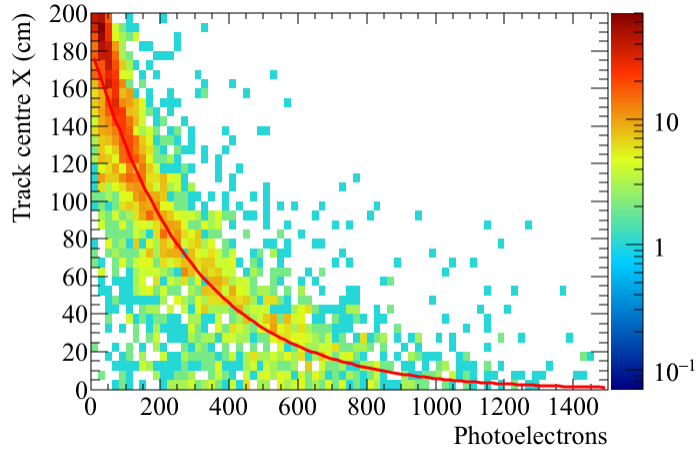


Fig. 4.2 The central x position of a reconstructed track versus the number of detected photoelectrons. The red line corresponds to a parameterisation of the distribution, which is used to predict the distance between the APAs and the flash source, given the number of measured photoelectrons in the flash. Using this parameterisation, the flash can be matched with a reconstructed track, whose centre is the same distance from the APAs.

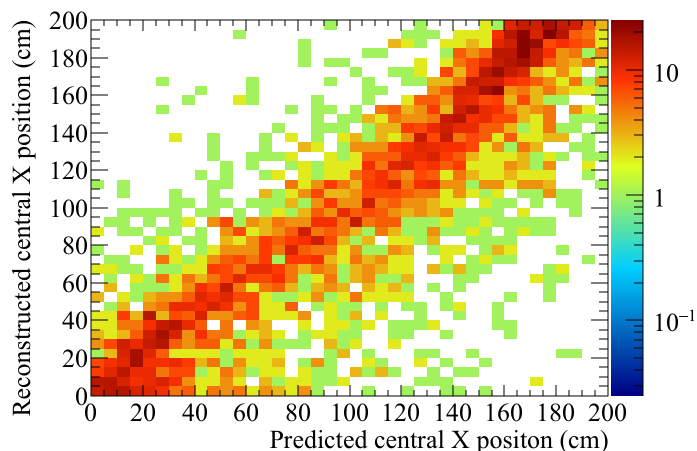
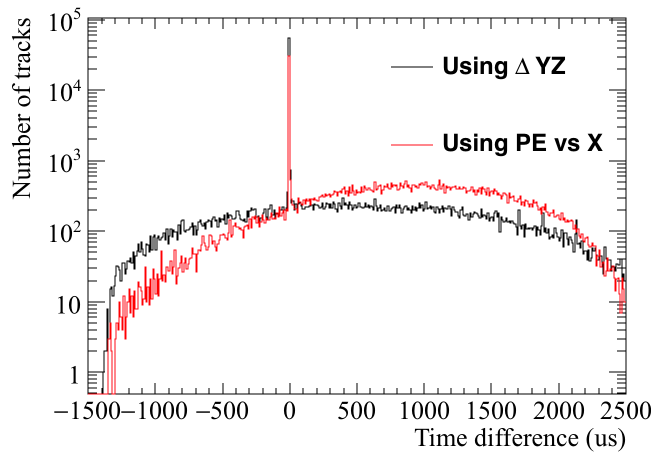
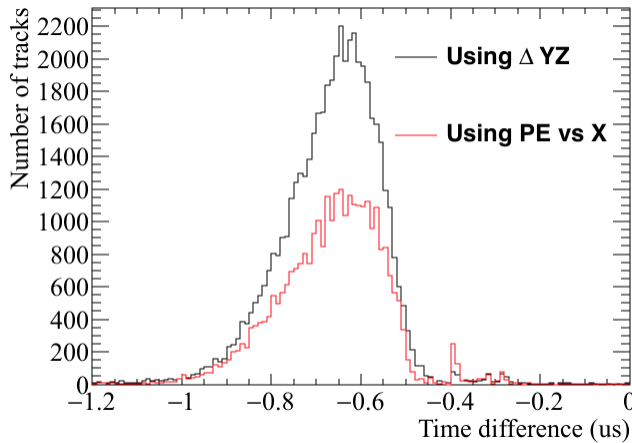


Fig. 4.3 A comparison of the x position predicted using the relationship in Fig 4.2, and the x position predicted using the difference in flash and hit times.



(a) The difference in interaction times.



(b) Zoomed in at low time differences.

Fig. 4.4 The number of events as a function of the difference between Monte Carlo and photon detector times. Top: the difference in interaction times over a large range of times. Bottom: the peak at a time difference of 0 is expanded, showing a systematic offset of $0.6 \mu\text{s}$ due to an electronics offset in the simulation.

photon detectors is often very accurate. However, there is also a significant number of tracks for which the photon interaction time does not match the Monte Carlo truth interaction time. This is due to, for example, the broad width of the distribution shown in Figure 4.2, meaning that the number of photoelectrons cannot necessarily accurately predict the distance between the APAs and the flash source. Improving the accuracy of the photon detector interaction time is required, as applying an incorrect interaction time correction will result in the x position of hits being incorrect. The peak seen at a time difference of 0 ms has been expanded in Figure 4.4b, where it can be seen that there is a systematic offset of 0.6 μs , this is due to an electronics offset applied in the simulation to the photon detector system.

From Figure 4.4 it can be seen that the metric using the proximity of the flash centre to the track trajectory, yields the best track/flash matches. This is likely caused by the large spread in the number of photoelectrons collected at fixed drift distances, as shown by Figure 4.2, which causes a large degeneracy between the number of measured photoelectrons, and the distance between the APAs and the flash source. The two metrics can be combined to give a prediction for the interaction time, though given the increased sensitivity from the proximity metric, this should be given greater weighting. In physics data, the metric using the number of collected photoelectrons is particularly sensitive to the absolute light level in the detector. This is because a high residual light level in the detector would reduce the proportional change in the number of photoelectrons collected for increasing drift distances. This metric also relies on the existence of a sample of tracks with known x positions, upon which to calibrate the change in the number of photoelectrons collected for increasing drift distances. It may be difficult to obtain this dataset in a real detector, though the cosmic ray counters around the 35 ton may be able to provide such a sample.

4.2 Calibrating calorimetric constants

Having the correct calorimetric responses is vital when trying to calculate $\frac{dE}{dx}$, as the measured change in charge, has to be correctly converted to the change in energy. The parameter which has to be tuned in order to ensure that this is done correctly, is the number of electrons that each ADC corresponds to. This was presented in Equations 2.1 and 2.2, as $C_{ADC \rightarrow e^-}$. Each plane will have a different response function, and so each plane has to be treated separately. These parameters have to be tuned in such a way as to make a known particle energy deposition have the correct $\frac{dE}{dx}$, the easiest deposition to tune against is the minimally ionising particle (MIP) peak, which in LAr should have a value of 1.8 MeV cm^{-1} . To do

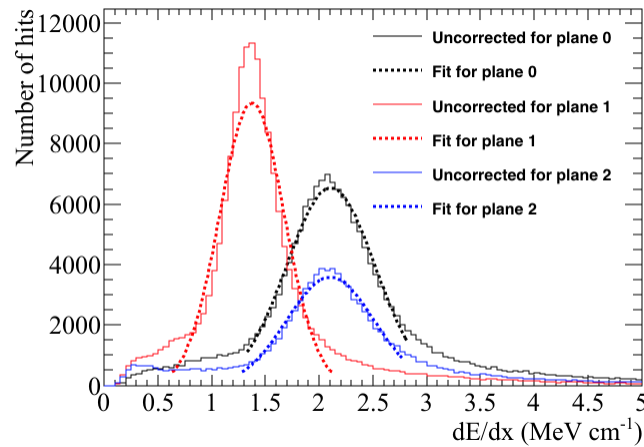
this, the sample of 10,000 positive muons made to calibrate the photon detector track/flash assignment will be used, as many of these particles will be MIPs.

To select the MIPs in the sample, only tracks caused by through-going muons are used. The $\frac{dE}{dx}$ value for all hits, in all tracks, is then calculated, and the different planes are considered separately. A Gaussian distribution is fitted around the peaks for each of the planes, to discern the Most Probable Value (MPV) of $\frac{dE}{dx}$ for that plane. If the MPVs are not equal to 1.8 MeV cm^{-1} , the ADC to electron parameters are scaled by the factor between the measured MPV, and the MIP peak. As the relationship between $\frac{dE}{dx}$ and $C_{ADC \rightarrow e^-}$ is not linear, an element of trial and error is required to find the correct ADC to electron parameters. An example of the calibration being applied is shown in Figure 4.5. Calibration of the response functions is required whenever the electronics gains, or signal shaping functions, are changed.

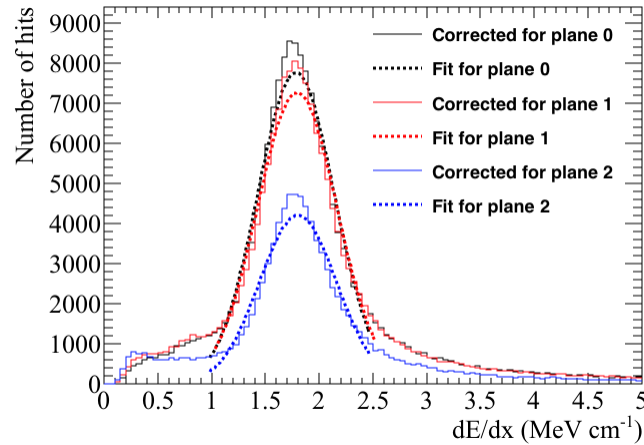
4.3 Discerning reconstruction efficiencies

Knowledge of the strengths and weaknesses of different tracking algorithms is vital when using them for physics analyses. To this end, it is useful to develop a metric by which they can be compared. In order to do this, a series of conditions have to be applied to the reconstructed tracks from a large set of simulated particles, which are reconstructed using different tracking algorithms. It is interesting to observe the effect that event complexity has on the reconstruction algorithms, and so efficiencies will be calculated for the positive muon sample, and the CRY sample, which were used in Section 4.1. The sample referred to as the positive muon sample contains single positive muons generated at $T = 0$, with a constant y position above the scintillation panels, and flat distributions in x and z . The sample referred to as the CRY sample, contains multiple particles, of multiple particle types, generated at times spanning multiple drift windows, and at an altitude above sea level of 0 m.

The criteria upon which to determine whether a particle is well reconstructed has to be carefully chosen, as every definition will have limitations. For example, consider a particle that travels 100 cm in the active volume of the detector, but is reconstructed as 2 separate tracks (tracks 1 and 2), with lengths 77 cm and 23 cm respectively. Firstly, should these tracks be merged, or left separate? If the reconstruction algorithms have found them to be separate tracks, then it is likely that it would be difficult to ascertain that they are from the same particle in real data, and so in considerations here they are not merged. Secondly, one has to determine what the definition of a well reconstructed track should be. One definition



(a) Before calibration is performed.



(b) After calibration is performed.

Fig. 4.5 The number of hits as a function the hit $\frac{dE}{dx}$, before and after calibration of the response functions, for the conversion of ADC to number of electrons, for each plane is performed. Top: the distribution of hit $\frac{dE}{dx}$ and the MPV of $\frac{dE}{dx}$ before calibration. Bottom: the distribution of hit $\frac{dE}{dx}$ and the MPV of $\frac{dE}{dx}$ after calibration.

of a well reconstructed track, would be that the reconstructed track length is between 75% and 125% of the track length in the detector from Monte Carlo truth, in which case track 1 would be considered well reconstructed. Another definition to consider however, would be whether the track length in the detector from Monte Carlo truth is between 75% and 125% of the reconstructed track length, in which case neither track would be considered well reconstructed. These definitions have used exactly the same tracks, and seemingly identical definitions of what constitutes a well reconstructed track, but they have got very different results. As such, it is wrong to say which definition gives the correct result, but instead the result of each should be considered equally. It should also be noted, that these are just two of a wide range of definitions one could use to quantify whether a track is well reconstructed. In the discussions presented here, the former definition of a well reconstructed track is used, such that a track is considered well reconstructed if:

- Reconstructed track length is more than or equal to 75% of the Monte Carlo track length.
- Reconstructed track length is less than or equal to 125% of the Monte Carlo track length.
- Only one reconstructed track can be matched per Monte Carlo particle.

When calculating the reconstruction efficiencies, the number of well reconstructed tracks, is divided by the total number of particles in the active volume, from Monte Carlo truth. When calculating these efficiencies, it is important to consider much more than just the ratio of reconstructed to true track length. To this end, efficiencies with regards to many aspects of the tracks are calculated:

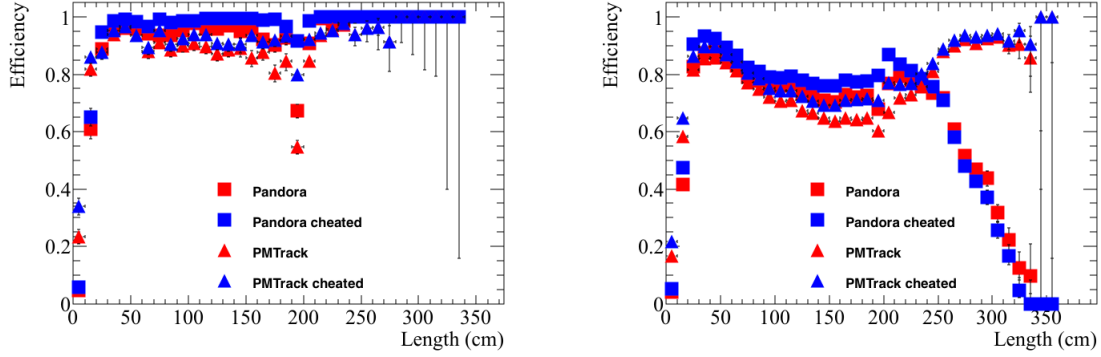
- Track length,
- Energy deposited in the active volume of the detector,
- The angle θ of the track, defined as the angle that a vector makes from the x axis in the xy plane,
- The angle ϕ of the track, defined as the angle between the z axis and the vector.

In all efficiency plots, the Monte Carlo truth quantity, not the reconstructed quantity, is shown, so as to reflect how the change in these quantities affects the reconstruction efficiency. It is also useful to observe the effect that failed disambiguation, and incorrect interaction time determination, has on the reconstruction efficiency. To show this, two reconstruction paths are ran on the particles. One reconstruction path uses no Monte Carlo information, and

so the disambiguation is performed as outlined in Section 2.6, and the interaction time is determined using the simulated photon detectors, as described in Section 4.1. The second reconstruction path uses cheated disambiguation, whereby Monte Carlo truth information is used to select the wire segments which hits occurred on, and Monte Carlo truth information is also used when calculating the interaction time of the track.

The calculation of reconstruction efficiencies also serves as an effective method upon which reconstruction algorithms can be further developed, as it identifies aspects which do not work as expected. For example, when the reconstruction efficiencies for the CRY sample were initially calculated, they were significantly lower than for the positive muon sample, but only when disambiguation was not cheated. It transpired that this was because the disambiguation was only selecting the largest collection of hits on each plane, for each TPC. This is not a problem when only 1 particle is simulated, as one would expect that there only be one particle on a given plane, in each TPC. However, when considering a CRY sample which lasts of the order of 10 ms, there will almost certainly be multiple particles on each plane, in each TPC. Removing the hits from all but one of these multiple particles, will cause them to have no reconstructed track, and thus cause the efficiency to drop significantly. Upon making the disambiguation algorithm no longer have this restriction, the reconstruction efficiencies of the positive muon and CRY samples were observed to become much more similar, as presented here.

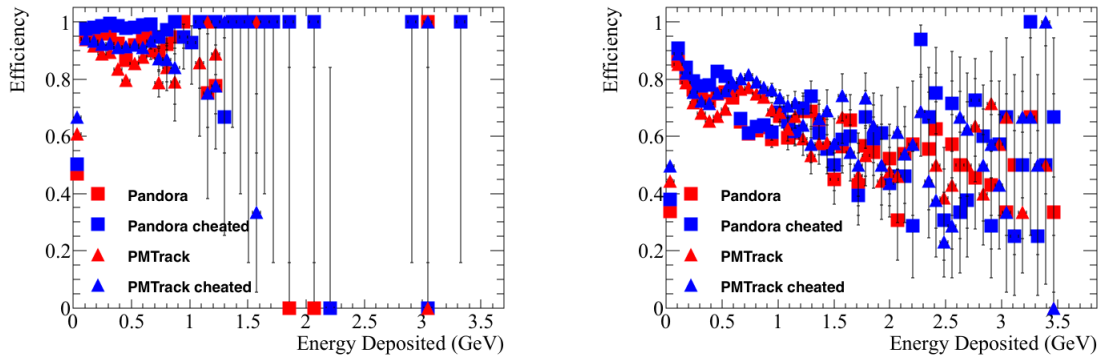
The reconstruction efficiencies given the current state of the most commonly used reconstruction algorithms, Pandora [91] and PMTrack [55], are shown in Figures 4.6, 4.7, 4.8, 4.9 and 4.10. Efficiencies are shown for both the positive muon and CRY samples, where it can be seen that the efficiency tends to be lower for the CRY sample. It is thought that this is due to the more complex event structure in the CRY sample, as multiple primary particles will be present in the detector at any given time. The relatively slow drift velocity of LAr may mean that these tracks cross in wire-tick space. Tracks crossing in wire-tick space could cause reconstruction errors, as the overlaps may be mistaken for interactions, which would cause the tracks to be split, resulting in the interaction time calculated from the photon detectors to be incorrect. This error, in the calculation of interaction time using the photon detectors, was seen in Figure 4.4. The reconstruction efficiencies for the CRY sample are more realistic, as events will rarely be isolated in the 35 ton detector, due to the large flux of cosmic particles on the Earth's surface.



(a) Reconstruction efficiencies for the positive muon sample.

(b) Reconstruction efficiencies for the CRY sample.

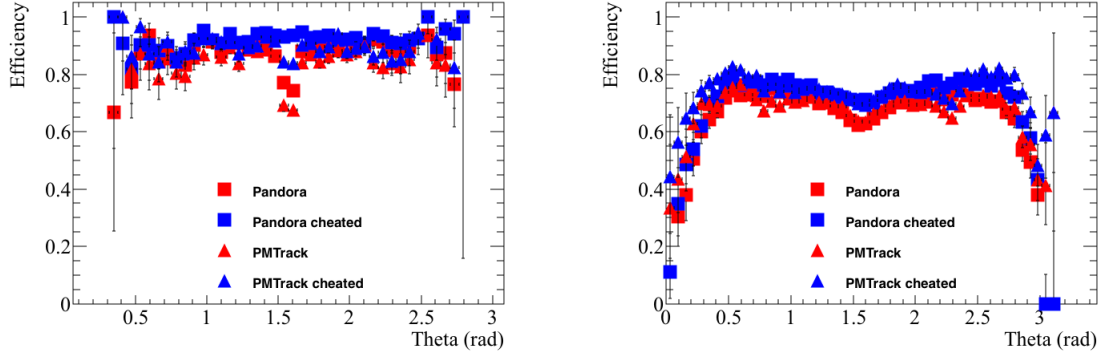
Fig. 4.6 The reconstruction efficiencies for simulated events as a function of the track length in the detector from Monte Carlo truth. The efficiencies are shown for 'non-cheated' reconstruction (red), and 'cheated' reconstruction (blue), for both Pandora [91] (triangles) and PMTrack [55] (squares).



(a) Reconstruction efficiencies for the positive muon sample.

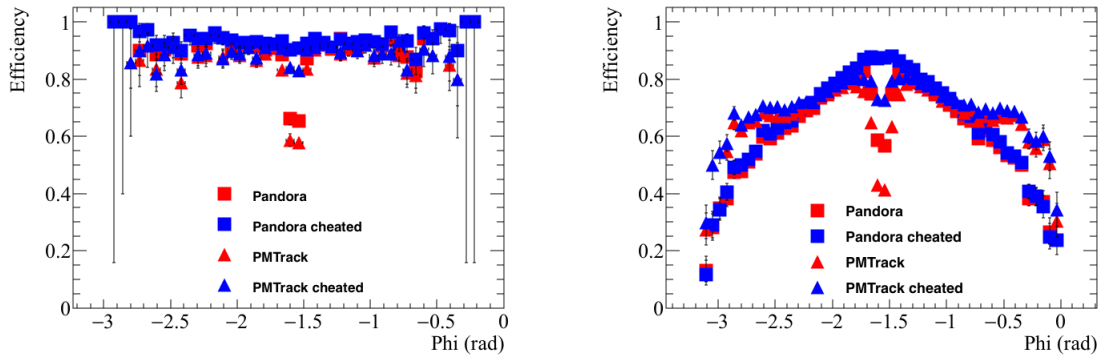
(b) Reconstruction efficiencies for the CRY sample.

Fig. 4.7 The reconstruction efficiencies for simulated events as a function of the deposited energy from Monte Carlo truth. The efficiencies are shown for 'non-cheated' reconstruction (red), and 'cheated' reconstruction (blue), for both Pandora [91] (triangles) and PMTrack [55] (squares).



(a) Reconstruction efficiencies for the positive muon sample. (b) Reconstruction efficiencies for the CRY sample.

Fig. 4.8 The reconstruction efficiencies for simulated events as a function of the θ track angle from Monte Carlo truth track. The efficiencies are shown for 'non-cheated' reconstruction (red), and 'cheated' reconstruction (blue), for both Pandora [91] (triangles) and PMTrack [55] (squares).



(a) Reconstruction efficiencies for the positive muon sample. (b) Reconstruction efficiencies for the CRY sample.

Fig. 4.9 The reconstruction efficiencies for simulated events as a function of the ϕ track angle from Monte Carlo truth track. The efficiencies are shown for 'non-cheated' reconstruction (red), and 'cheated' reconstruction (blue), for both Pandora [91] (triangles) and PMTrack [55] (squares).

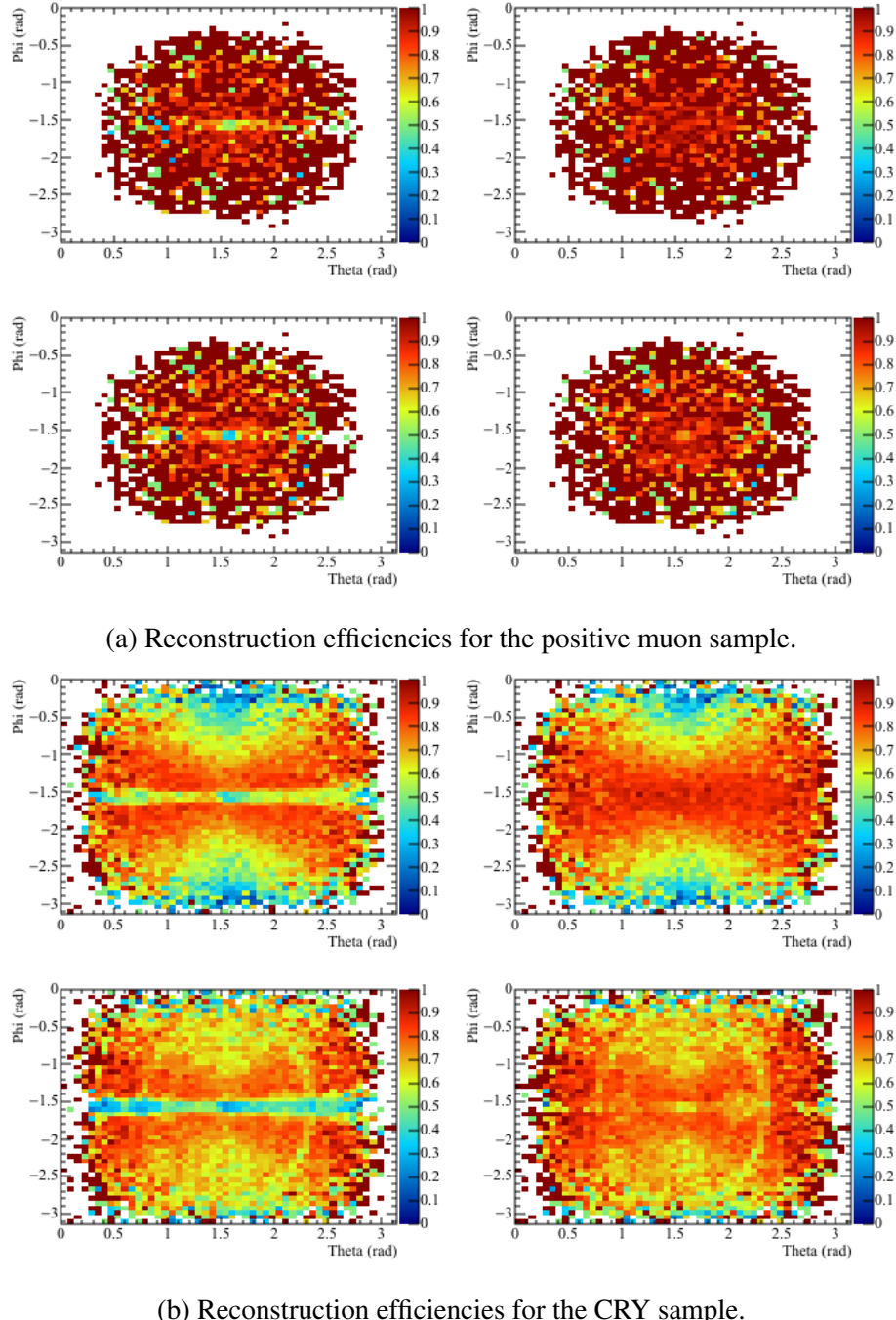


Fig. 4.10 The reconstruction efficiencies for simulated events as a function of the θ and ϕ track angles from Monte Carlo truth track. The track angle θ is shown on the x axis, and the track angle ϕ is shown on the y axis. The colour z axis shows the reconstruction efficiency. The efficiencies are shown for 'non-cheated' reconstruction (red), and 'cheated' reconstruction (blue), for both Pandora [91] (triangles) and PMTrack [55] (squares).

A striking feature of Figure 4.6 is the rapid decrease in reconstruction efficiency seen in the CRY sample, when using Pandora, for particles with track lengths in the detector of more than 250 cm from Monte Carlo truth. The cause of this, is that tracks are reconstructed separately in the long, and short drift volumes, before being merged when they are found to be co-linear in the yz plane. This is not a problem in the positive muon sample, as the x position of the hits calculated using Equation 4.1 will be correct.

$$x_{Hit} = T_{Hit} \times v_{Drift} \quad (4.1)$$

In Equation 4.1, x_{Hit} is the calculated x position of the hit, T_{Hit} is the measured time of the hit, and v_{Drift} is the electron drift velocity. An electron, in an electric field of 500 V cm^{-1} , in LAr, drifts at a speed of $0.160563 \text{ cm } \mu\text{s}^{-1}$. However, when the same is done for hits in the CRY sample, using particles with large interaction times, the x positions will have offsets proportional to the interaction time of the particle, unless the hit time is corrected by Equation 4.2.

$$T_{Hit} = T_{Measured} - T_{Interaction} \quad (4.2)$$

In Equation 4.2, T_{Hit} is the corrected hit time, $T_{Measured}$ is the measured time of the hit, and $T_{Interaction}$ is the calculated interaction of the particle which caused the hit.

The scale of these offsets in x positions can be seen by considering a particle which is generated at a time of $T = 12.5 \text{ ms}$, as then the offset in the reconstructed x position calculated by Equation 4.1, would be more than 20 m! Obviously the hits could not have occurred at these positions, as the drift distances are roughly 30 cm in the 'short' drift volume, and 225 cm in the 'long' drift volume. However, as track segments are reconstructed separately in the 'short' and 'long' drift volumes, before later being merged, it is possible for there to be a discontinuity in x of more than 40 m, if these x offsets are not corrected for. As the interaction time of the track is calculated using the output of the tracking algorithms, it is not possible to prevent this by using the interaction time at present. It is however, possible to subtract this discontinuity in x from the total reconstructed track length when the stitched track is stored in the event. This will give the correct track length, though the user will still have to correct the positions of individual hits, using the calculated interaction times. This is what is done by PMTrack, hence it not exhibiting this rapid decrease in reconstruction efficiency for long tracks. The interaction time can be found from, among other things, the Monte Carlo truth generation time, or the photon detectors, as discussed in Section 4.1.

It is clear from Figure 4.6 that particles with track lengths in the detector of less than 30 cm are poorly reconstructed. The extremely low efficiency for particles with track lengths of less than 10 cm, can be partially attributed to particles with track lengths of less than 1 cm in the active volume of the detector. These particles, which represent 30% of the particles with active volume track lengths of less than 10 cm, are too short to be reconstructed using the current reconstruction process. These particles will need to be reconstructed when looking for supernovae bursts, though special algorithms will be written to do this, as the traditional hit finding and clustering algorithms may discard them due to the isolated nature of the hits. Another issue, is that the low energies of these particles may mean that the signals that they produce are below threshold, and so will not even be reconstructed, or, if hits are reconstructed, they may be too close to a more energetic track and get absorbed into them. The reconstruction of tracks is affected by the number of wires which they cross, though this should not matter for particles with track lengths of more than 5 cm in the active volume, as they will have crossed roughly 10 wires in each plane, which should produce enough unique hits for a cluster to be reliably reconstructed. This can be seen to be the case for PMTrack when considering the positive muon sample, as the efficiency for particle track lengths between 10 and 20 cm, is roughly the same as that for track lengths between 20 and 30 cm. However, when considering the CRY sample, there is still a significant decrease in efficiency. This is attributed to secondary particles which are produced in hadronic interactions with the concrete surrounding the detector. Many of these particles will travel only very short distances in the active volume, though those that travel slightly larger distances are likely to cause energy depositions that will be confined to the detector edges. The tracking algorithms may struggle to accurately reconstruct these tracks, as significant portions of the track will be close to the detector edge, where the field is poorly modelled, and hits may be more difficult to disambiguate.

The trend of increasing efficiency for longer track lengths, which was seen in Figure 4.6, can also be seen in Figure 4.7, where the reconstruction efficiency increases as the amount of deposited energy increases. This is because particles which deposit more energy, will tend to have travelled further in the detector. The amount of energy that particles deposit is limited by the size of the detector, as particles with an energy of more than 1 GeV are energetic enough to be MIPs. This results in few particles depositing more than 1 GeV in the detector, and is why the uncertainty in the reconstruction efficiency increases for energy depositions in the detector volume of more than 1 GeV. The larger range in the amount of energy deposited seen in Figure 4.7b, is due to the larger number of muons in the CRY sample which create

large electromagnetic showers upon entering the LAr.

It is also interesting to note the pronounced decreases in reconstruction efficiencies for particular angles, shown in Figures 4.8 and 4.9. The decrease in efficiency at $\phi = \frac{\pi}{2}$, seen in Figure 4.9, can be attributed to the drop in efficiency for particles with track lengths between 190 cm and 200 cm, seen in Figure 4.6. This is because the vertical height of the detector is approximately 195 cm, and near vertical tracks will hit few collection wires, meaning that determining the triple points needed by the disambiguation is very difficult. This is verified by the large increase in efficiency achieved by cheating the disambiguation, as seen in Figure 4.8a, where the reduction in reconstruction efficiency is seen to become much less pronounced. Similarly, the decrease in efficiency at $\theta = \frac{\pi}{2}$ can be attributed to particles which are perpendicular to the collection plane wires, as this track orientation also results in few collection wires being hit.

The information from Figures 4.8 and 4.9 is combined in Figure 4.10, where the sharp drop in efficiency at $\phi = \frac{\pi}{2}$ for the 'non-cheated' CRY sample is particularly visible. The effect of cheated disambiguation is clear in Figure 4.10b, where the dip in efficiency as a function of θ at fixed $\phi = \frac{\pi}{2}$ is completely removed. The same is not true however, for the dip in efficiency as a function ϕ at fixed $\theta = \frac{\pi}{2}$, though the reduction in efficiency was not as severe as that seen for fixed values of $\phi = \frac{\pi}{2}$. The effect of 'cheated disambiguation' can still be seen though, as the reconstruction efficiency in Figure 4.10b can be seen to improve for values of ϕ . There are still however, noticeable decreases in the reconstruction efficiency for values of ϕ close to 0 or π , when using Pandora. The improvement in the performance of the reconstruction algorithms that comes from 'cheating' the reconstruction, is part of the motivation for the wire pitches in the DUNE FD being 36° , as opposed to the $45 \pm 0.7^\circ$ used in the 35 ton. This is because, as discussed in Section 2.6, the shallower wire pitch makes disambiguation easier. Though disambiguation will be easier in the different geometry, further efforts to improve disambiguation are still required, as are continued efforts to reconstruct the shortest tracks.

4.4 Performing particle identification

Being able to perform reliable Particle IDentification (PID) is a key requirement for the DUNE experiment, and so efforts have been made to establish a procedure by which this can be achieved. The predominant method of performing PID in LAr is to use the relationship

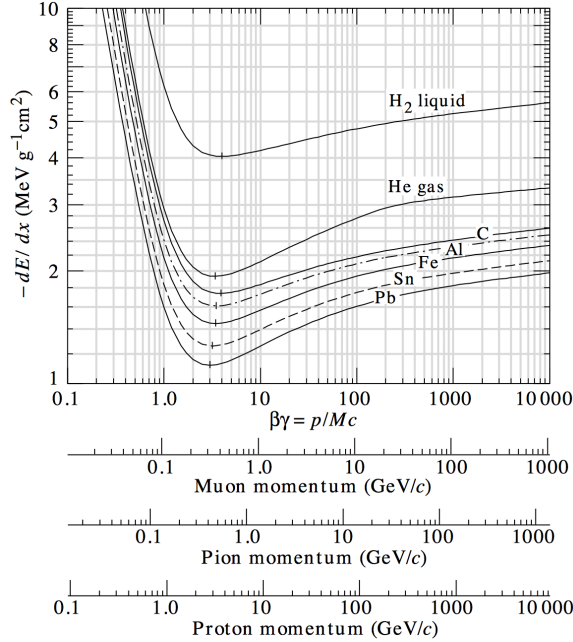


Fig. 4.11 The mean energy loss per unit track length of different particle masses in different materials [57]. The $\frac{Z}{A}$ of liquid argon is slightly less than that of carbon.

between $\frac{dE}{dx}$, and the residual range of the track. The residual range of a track is defined as, the distance between a point on the track, and the stopping point of the track. This relationship is observed to be dependent on particle mass, and is quantified by the Bethe-Bloch equation [104, 105] which is shown in Figure 4.11, and presented in Equation 4.3.

$$-\frac{dE}{dx} = Kz^2 \frac{Z}{A} \rho \frac{1}{\beta^2} \left[\frac{1}{2} \ln \frac{2m_e c^2 \beta^2 \gamma^2 T_{max}}{I^2} - \beta^2 - \frac{\delta(\beta\gamma)}{2} \right] \quad (4.3)$$

The sharp increase in energy loss per unit length can be seen to occur at different momenta for different particle masses, meaning that the peak value of $\frac{dE}{dx}$ changes significantly for particles of different masses. For example, it can be seen that the momenta at which the increase in $\frac{dE}{dx}$ occurs is very different for muons and protons. However, it can be seen the momenta at which this increase in $\frac{dE}{dx}$ occurs is very similar when considering muons and pions. For this reason, it should be relatively simple to discern a proton and a muon track, though it may be difficult to discern a muon and a pion track.

The particle mass dependence can be seen by plotting the $\frac{dE}{dx}$ against the residual range of the particle on a log-log plot, as shown in Figure 4.12. A power law dependence is found

Table 4.1 Stopping power parameterisation for various particle types in liquid argon. The table is taken from [94].

Particle	A (MeV cm ^{b-1})	b
Pion	8	-0.37
Kaon	14	-0.41
Proton	17	-0.42
Deuteron	25	-0.43

to describe the relationship [94], as shown in Equation 4.4.

$$\frac{dE}{dx} = AR^b \quad (4.4)$$

The dependence on b is found to be weak, and so can be set to -0.42 for all particle masses. This means that the main discriminant used is the A parameter, which has a strong dependence on particle mass. The values for A and b calculated from Figure 4.12, are shown in Table 4.1. It is found that the error introduced by fixing the b parameter is small compared to the error from ionisation fluctuations [94].

Once the b parameter is set to be constant for all particle types, it is possible to calculate a value for the A parameter for each hit on the track using Equation 4.5, where R_i is the residual range of the track at that point.

$$A_i = \left(\frac{dE}{dx} \right)_i \times (R_i)^{0.42} \quad (4.5)$$

The particle type discriminant, called PIDA, can then be calculated for a track by finding the average value of A_i for the track. As the particle mass dependant increase in $\frac{dE}{dx}$ only occurs near the end of the track, the PIDA variable can only be calculated for particles which stop in the detector, as all other particles will have MIP-like $\frac{dE}{dx}$ distributions, and so cannot be identified in this way. As shown by the plotted range of Figure 4.12, the average value of A is normally calculated for the last 30 cm of the track.

The PIDA method was tested in [94], where the PIDA values were calculated for simulated particles which stopped in the detector, using Monte Carlo truth information over the last 30 cm of the particle tracks. This is shown in Figure 4.13, where a clear separation can be seen between the peaks for muons, pions, kaons, and protons. Though the muon and pion peaks are relatively close together, they can still be resolved in the plot due to little overlap.

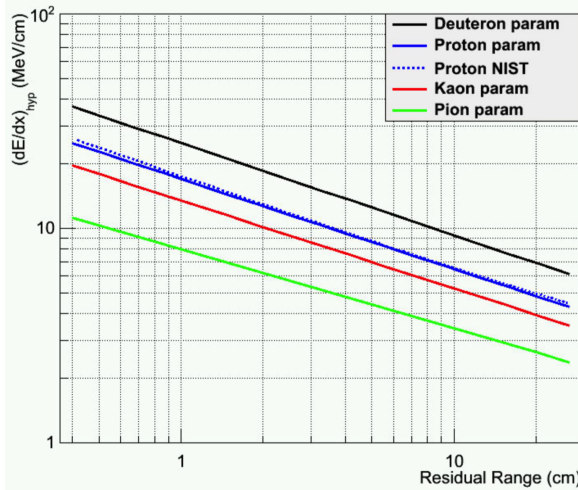


Fig. 4.12 Stopping power for different particle masses as a function of residual range in liquid argon. The figure is taken from [94].

It is interesting to note how tight the PIDA distributions found in the paper are, which allows the different particles types to cleanly separated in the truth study. The author notes that an incorrect tuning of the electron recombination effects will cause the distributions in Figure 4.13 to become broader. The dependence of $\frac{dE}{dx}$ on the recombination effects ($Recomb_X$) were presented in Equations 2.1, 2.2. The author also notes that an incorrect calibration of the detector will introduce a systematic shift in the expected values of PIDA, this is why the work presented in Section 4.2 is important.

From Figure 4.13, it can be seen that the most distinct PIDA distributions are that of muons and protons, these are also two of the most common particle types in cosmic rays. For these reasons, particle identification using the PIDA variable, will be attempted in simulations of the 35 ton detector. As outlined in Sections 4.1 and 4.2, in order to do this the interaction times of particles have to be well known, and the calibration constants must be tuned, so as to ensure that the effects of recombination are properly accounted for. It is also useful to use the information found in Section 4.3 about the efficiency with which tracks are reconstructed. In this regard, it is useful to produce additional figures showing the reconstruction efficiencies of protons in the CRY sample (Figure 4.14).

Figure 4.14 shows that the average reconstruction efficiency for PMTrack is higher than that for Pandora when considering protons. This can be easily seen in Figure 4.14c, where the efficiency for PMTrack is roughly 10% higher than that of Pandora, for all values of θ . The reconstruction efficiency is still much lower than the overall efficiency shown in

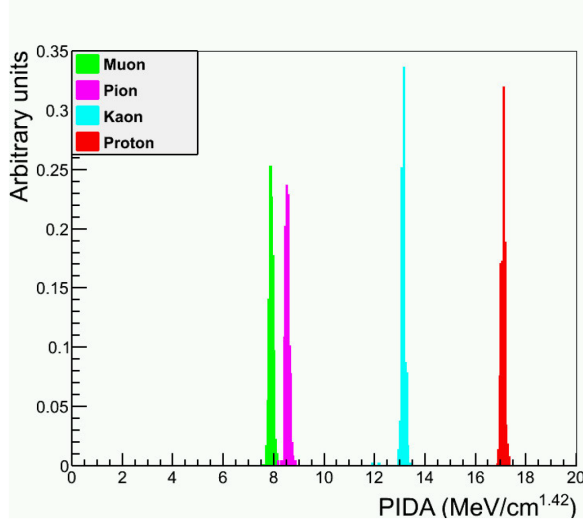


Fig. 4.13 The distribution of PIDA values, calculated using Monte Carlo truth, for different particle masses. The figure is taken from [94].

Figure 4.8, for both the positive muon and CRY samples though. This shows that the overall reconstruction efficiency for protons is quite low. Comparing Figures 4.6b, and 4.14a, it is evident that the reconstruction efficiency for protons with track lengths of more than 10 cm is reasonably similar to that of the overall reconstruction efficiency for the CRY sample, when using PMTrack. However, the reconstruction efficiency is significantly lower for protons with tracks of less than 10 cm. When using Pandora to reconstruct protons, the reconstruction efficiency is lower for all track lengths. It is found that 60% of simulated protons have track lengths of less than 1 cm, and that none of these particles are reconstructed. It is this large number of very short particles which causes the overall reconstruction efficiency to be relatively low. When particles with track lengths of less than 1 cm (10 cm) are removed, the average reconstruction efficiency for PMTrack rises to 37% (58%). This shows that, when the shortest tracks are not counted, the reconstruction performs reasonably well.

It is also useful to produce samples where the primary particle is a single muon, or proton, located in the active volume of the detector. This allows for a sample of isolated tracks to be made, upon which the capabilities of the PIDA metric can be tested. It also allows the reconstruction efficiency to be found for particles in isolation. The properties of the generated particles are illustrated in Table 4.2. The values of the simulated quantities were found by changing the given parameters by an amount taken from a random sampling of a Gaussian distribution of width equal to the error listed. These simulation parameters were chosen to produce samples which would contain both exiting, and stopping particles, whilst generating the particles in the LAr would ensure that there should always be a reconstructable track in

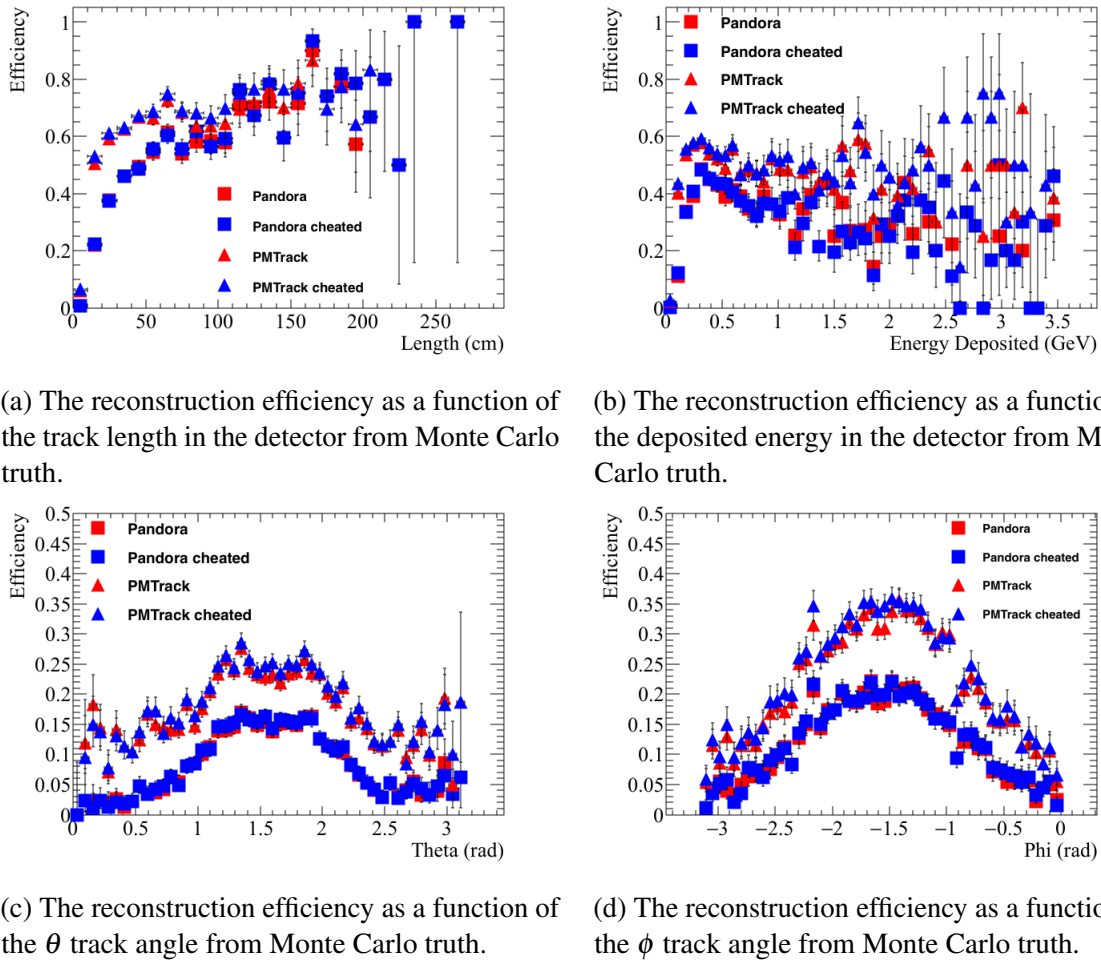


Fig. 4.14 The reconstruction efficiencies for protons in a sample generated using CRY. Top left: the efficiencies as a function of the track length in the detector from Monte Carlo truth. Top right: the efficiencies as a function of the deposited energy from Monte Carlo truth. Bottom left: the efficiencies as a function of the θ track angle from Monte Carlo truth. Bottom right: the efficiencies as a function of the ϕ track angle from Monte Carlo truth. The efficiencies are shown for 'non-cheated' reconstruction (red), and 'cheated' reconstruction (blue), for both Pandora [91] (triangles) and PMTrack [55] (squares).

Table 4.2 The properties of initial particles simulated in the muon and proton samples. The angles θ_{xz} , and θ_{yz} , are defined as the angle that a vector makes in the xz , and yz planes, respectively.

	Muon properties	Proton properties
Initial position (cm)	$(100 \pm 50, 0 \pm 30, 80 \pm 20)$	$(100 \pm 50, 0 \pm 30, 80 \pm 20)$
Initial momentum (GeV)	0.3 ± 0.1	0.8 ± 0.5
Initial θ_{xz} ($^{\circ}$)	0 ± 180	0 ± 180
Initial θ_{yz} ($^{\circ}$)	-45 ± 45	-45 ± 45

the detector. The reconstruction efficiencies when using the PMTrack reconstruction method are shown for the simulated particles in Figure 4.15.

Particles with track lengths of less than 1 cm have been excluded from these plots, which is why the angular reconstruction efficiencies for protons in Figures 4.15c and 4.15d, are higher than those seen in Figures 4.14c and 4.14d. This was done as none of these particles were reconstructed, due to the very short distances which they travel. After discounting these very short particles, the efficiencies generally follow similar patterns observed in the earlier efficiency plots, though there is a decrease in efficiencies for the longest track lengths which is not observed in other samples. This is attributed to the initial positions of the particles being within the detector volume, as this means that any particle travelling over 100 cm would have a very peculiar trajectory, as the edge of the detector should never be more than 100 cm away from the starting position. The only exception to this, is if a particle travelled along the x axis to the other end of the detector. As discussed earlier, this is a very problematic orientation to reconstruct, as all of the charge would be deposited over a large range of time, on very few collection plane wires.

As the increase in $\frac{dE}{dx}$ is only visible when the particle stops in the detector, it is necessary to remove exiting particles from the sample. This is done by applying a fiducial cut on the end point of the reconstructed track. It is important to only place this on the end point of the track, as one does not want to remove particles which enter the detector and then stop. When calorimetry is performed, the end point of the track is determined using, among other metrics, the increase in $\frac{dE}{dx}$, and so the residual range of the track (a stored data member of the track object), should always refer to the distance to the end of the particles trajectory. For this study, a fiducial cut of 5 cm is used. This means that any track with hits within 5 cm of the edge of the detector volume is discarded, and counted as an exiting particle. This should mean that very few tracks due to exiting particles are identified as stopping in the detector,

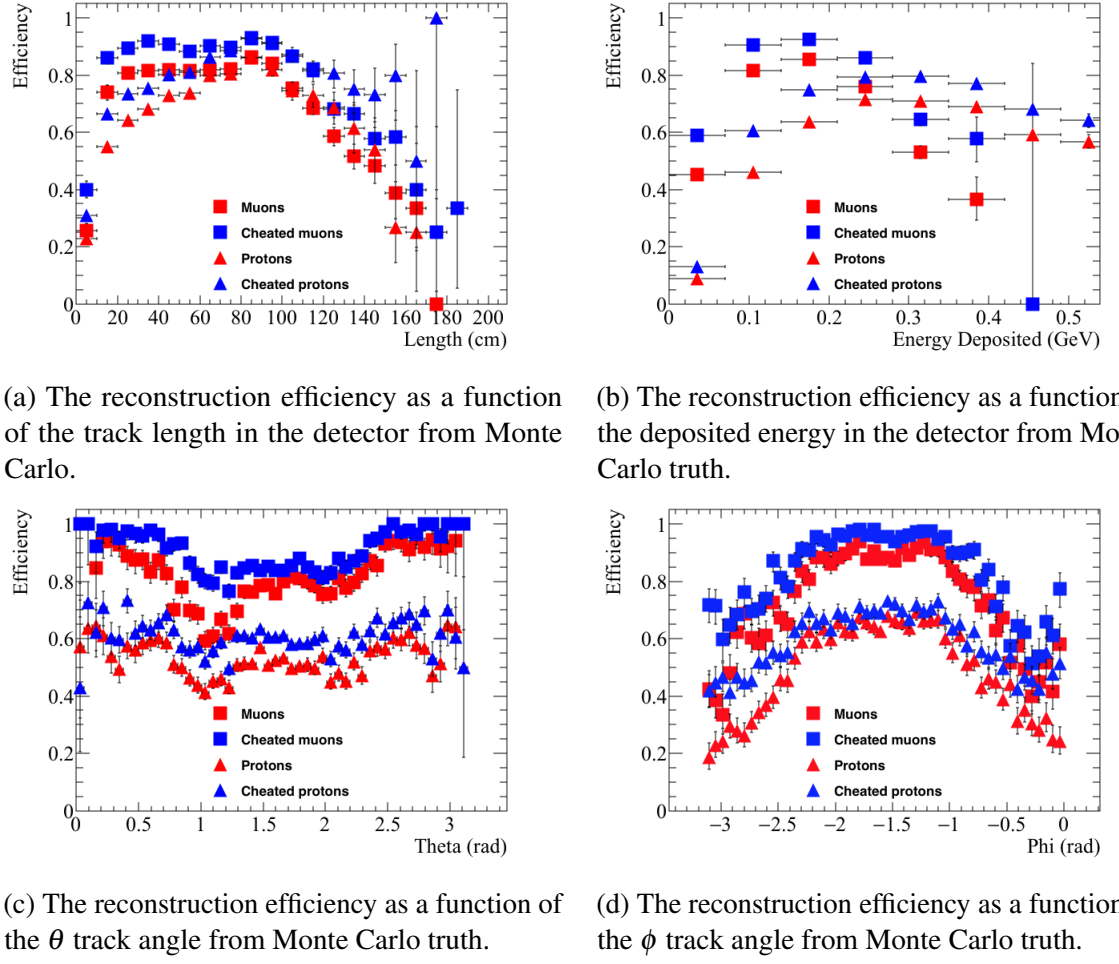


Fig. 4.15 The reconstruction efficiencies for the simulated isolated muon and proton samples in the 35 ton detector. Top left: the efficiencies as a function of the track length in the detector from Monte Carlo truth. Top right: the efficiencies as a function of the deposited energy from Monte Carlo truth. Bottom left: the efficiencies as a function of the θ track angle from Monte Carlo truth. Bottom right: the efficiencies as a function of the ϕ track angle from Monte Carlo truth. The efficiencies are shown for 'non-cheated' reconstruction (red), and 'cheated' reconstruction (blue), for both Pandora [91] (triangles) and PMTrack [55] (squares).

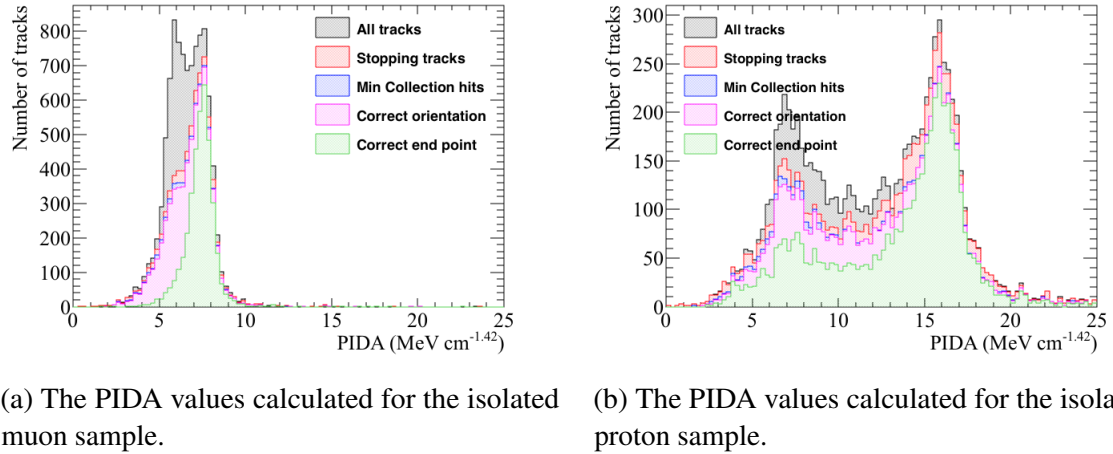
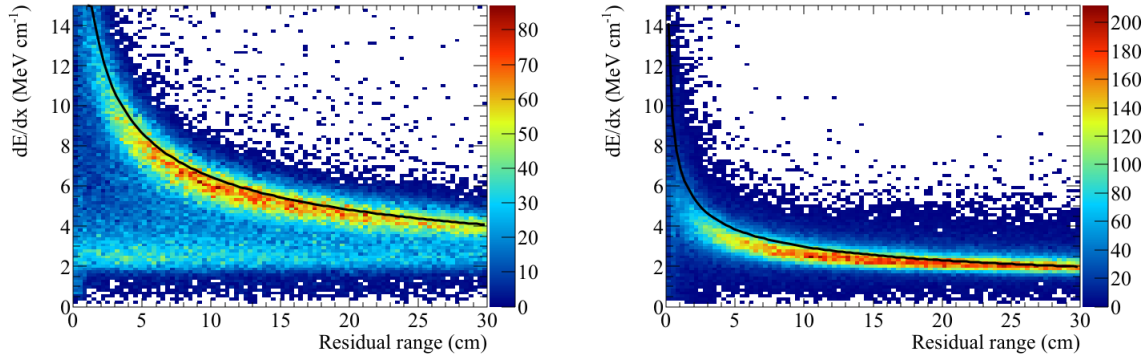


Fig. 4.16 The calculated PIDA values for the simulated isolated muon (left) and proton (right) samples in the 35 ton detector. A series of criteria designed to select only tracks due to stopping particles which have a required number of collection plane hits is applied. The tracks are then further refined using truth information such as the true end point of the particle.

as it would require the reconstruction algorithms to miss large section of the track. This will mean that some stopping particles are incorrectly assigned as exiting particles, causing the identification efficiency to drop, but it is necessary to ensure that exiting particles are not included in the final distributions. A further cut that is applied, is the requirement that there are a minimum of 5 collection plane hits, this is to ensure that an adequate number of points are taken upon which to find an average value of PIDA for the track. Similar cuts are described in [94], and the resulting distributions of PIDA values for the isolated muon, and isolated proton samples, are shown in Figure 4.16.

As can be seen from Figure 4.16, using Monte Carlo truth information can make the distributions much cleaner, particularly when discounting particles for which the reconstruction algorithms do not track to their end point. A track is identified as having a correctly reconstructed end point, if the reconstructed end point is within 2.5 cm of the end point of the particle from Monte Carlo truth. It is reassuring to see that few tracks are reconstructed backwards, as if this were not the case then performing particle identification would be very difficult. This is because, it would indicate that the calorimetry, and tracking algorithms, are not performing well. However, improvements can still be made, as both plots in Figure 4.16 contain many tracks which do not extend to the end points of the particles from Monte Carlo truth. This can be seen as when the requirement that the reconstructed track end point is consistent with the end point from Monte Carlo truth, the low tails of the PIDA distributions



(a) The $\frac{dE}{dx}$ versus residual range plot for the simulated isolated proton sample.

(b) The $\frac{dE}{dx}$ versus residual range plot for the simulated isolated muon sample.

Fig. 4.17 The measured relationship between $\frac{dE}{dx}$ and residual range for the simulated isolated muon (left) and proton (right) samples in the 35 ton detector. These plots are made after applying all of the cuts outlined in Figure 4.16, meaning that only hits from tracks whose end points are consistent with the end points from Monte Carlo truth are plotted.

are significantly reduced. This is most noticeably the case in Figure 4.16a, where the peak at low values of PIDA is significantly reduced. It is observed that the PIDA distributions are cleaner when information from all three wire planes are used, as opposed to only using the collection plane, and so this is presented here. This shows how important it is to calibrate the electronics responses of all three wire planes, and how additional wire planes can improve calorimetry, as well as the accuracy of reconstruction algorithms [106].

The relationship between the $\frac{dE}{dx}$ and residual range of a track, is shown in Figure 4.17, for both protons and muons. The much steeper increase in $\frac{dE}{dx}$ at low residual ranges for protons compared to muons is clearly visible, when comparing Figures 4.17a and 4.17b. The contamination in the proton sample at low PIDA can be seen in Figure 4.17a, where there is a clear sample of tracks for which the $\frac{dE}{dx}$ does not increase for low residual ranges. These plots are filled after tracks whose end points do not correlate with the end points from Monte Carlo truth are removed, and so the tail of low $\frac{dE}{dx}$ values is due to particles for which the simulated detector did not find increased energy depositions as the particle stopped. It is therefore possible that at least some of these protons do not in fact stop, but interact inelastically when they still have a significant amount of kinetic energy meaning, that GEANT4, and the tracking algorithms, will create a new particle, or track, after this interaction.

It is useful to summarise the information shown in Figure 4.16 in a table, so that an efficiency of identifying stopping particles can be found. This is shown in Table 4.3 for

protons, and in Table 4.4 for muons. The efficiency shown in these tables is defined as the number of tracks in the PIDA range, divided by the total number of stopping particles. This means that it is possible to have an efficiency of more than 100% if more reconstructed tracks have PIDA values within the PIDA range, than there are stopping particles from Monte Carlo truth. This is the case in Table 4.4, where there are initially more reconstructed tracks than stopping particles within the PIDA range. The purity shown in these tables is defined as the percentage of tracks in the PIDA range associated with particles that stop in the detector from Monte Carlo truth. As many of the tracks shown in the 'reconstructed tracks' row in Table 4.4 are not due to stopping particles, the initial purity is low, though this increases markedly after the fiducial cut is applied. The PIDA ranges referred to are $14\text{-}18 \text{ MeV cm}^{-1.42}$, and $5\text{-}9 \text{ MeV cm}^{-1.42}$, for protons and muons respectively, as these ranges cover the peaks of the distributions shown in Figure 4.17, and are centred on the peaks in Figure 4.13.

As can be seen in Table 4.3, the efficiency upon which protons can be identified does not change significantly as the sequential criteria are applied, but, as shown in Figure 4.16a, the peak at low values of PIDA decreases significantly. The same cannot be said for the muon sample however, as when the criteria that the tracking end point matches the end point from Monte Carlo truth is applied, a significant section of the tail within the PIDA range is removed, significantly reducing the PIDA efficiency. However, the resulting distribution is more similar to that shown in Figure 4.13, showing that the particles which survive the cut are those that are very well reconstructed. The cut to remove tracks that do not have the correct end points from Monte Carlo truth reduces both sets of efficiencies, but, if all particles were reconstructed with the correct end points, then one can imagine that the number of tracks within the PIDA ranges would increase, and the distributions would become more symmetrical, as shown in Figure 4.16b. Both tables also exhibit high purities, which shows that the fiducial cut, designed to removing exiting particles, is effective, with only 2 exiting protons being mis-identified in the proton sample.

From Table 4.3, it can be seen that there are more stopping protons than primary protons, as only 10,000 primary protons were generated. The effectiveness of the PIDA algorithm at identifying only primary protons is shown in Table 4.5. Comparing both tables, it can be seen that the efficiency with which the primary protons can be identified is larger than the secondary protons, as the efficiencies shown in Table 4.3 are lower than those in Table 4.5. It is thought that this is due to the low reconstruction efficiency for particles with the shortest track lengths, as many of the secondary protons will have short track lengths in detector from Monte Carlo truth, as discussed in Section 4.3. A similar table is not produced for primary

Table 4.3 A summary of the PIDA values calculated for the simulated isolated proton sample, as sequential cuts are applied.

Applied cut	Proton sample			
	Tracks	In PIDA range	Efficiency	Purity
Total stopping particles	13295			
Reconstructed tracks	8761	3009	22.6%	98.7%
Survives 5 cm fiducial cut	7552	2894	21.8%	99.9%
Minimum of 10 collection plane hits	6186	2507	18.9%	99.9%
Correct track orientation	6022	2491	18.7%	99.9%
Correct tracking end point	4588	2327	17.5%	100%

Table 4.4 A summary of the PIDA values calculated for the simulated isolated muon sample, as sequential cuts are applied.

Applied cut	Muon sample			
	Tracks	In PIDA range	Efficiency	Purity
Total stopping particles	6880			
Reconstructed tracks	9883	8907	129%	67.4%
Survives 5 cm fiducial cut	7126	6259	90.9%	90.2%
Minimum of 10 collection plane hits	6580	5876	85.4%	89.9%
Correct track orientation	6436	5767	83.8%	90.1%
Correct tracking end point	3832	3699	53.8%	100%

Table 4.5 A summary of the PIDA values calculated for the primary particles in the simulated isolated proton sample, as sequential cuts are applied.

Applied cut	Proton sample			
	Tracks	In PIDA range	Efficiency	Purity
Total stopping particles	7798			
Reconstructed tracks	5920	1937	24.8%	98.9%
Survives 5 cm fiducial cut	5044	1878	24.1%	99.9%
Minimum of 10 collection plane hits	4485	1711	21.9%	99.9%
Correct track orientation	4363	1707	21.9%	99.9%
Correct tracking end point	3246	1595	20.4%	100%

muons, as there were no secondary muons produced in the isolated muon sample, and so Table 4.4 is itself the efficiency with which the primary muons can be identified.

Upon verifying that the PIDA metric can reliably determine particle type when they are simulated in isolation, the next step is to observe the accuracy with which particles can be identified in a CRY sample. The sample used here differs from the CRY sample used earlier, in that only events which contain a proton track in the detector from Monte Carlo truth are reconstructed. This is done to reduce simulation time and storage space, as this cut will still provide a substantial number of muons, whilst ensuring that a large proton sample can be reconstructed. This sample is thus called the “proton enriched CRY sample”.

The process of calculating PIDA values for tracks is identical in all samples, though, as discussed in Section 4.3, the much more complicated event structure in the CRY sample affects the reconstruction efficiency, and so will likely also affect the accuracy of the calorimetry. The calorimetry will be affected in two ways, firstly, the reduced performance of the reconstruction algorithms will mean that some particles are not reconstructed at all, whilst those that are reconstructed may be more likely to have missing hits, and so the end points may be reconstructed less accurately. This will cause the tail of low $\frac{dE}{dx}$ values, seen in Figure 4.17a, to be more pronounced. Secondly, though the photon detector time determination is very accurate for a large number of tracks, it is also incorrect for a number of tracks, as shown in Figure 4.4. This will cause the recombination correction to be miscalculated, which will in turn increase the calculated $\frac{dE}{dx}$, and hence PIDA values. For this reason, it is also useful to present the PID efficiency when using cheated reconstruction, so that the effect of incorrectly determining the interaction time, and performing incorrect disambiguation, can be seen.

The PIDA values calculated for protons and muons in the proton enriched CRY sample are shown in Figure 4.18. The PIDA distributions when the reconstruction is both “cheated,” and not “cheated” are shown.

From Figure 4.18, it can be seen that the proton tracks which are reconstructed in the proton enriched sample, look very similar to the proton tracks which were reconstructed in the isolated proton sample, shown in Figure 4.16a. This is reassuring, as it shows that even when protons are surrounded by multiple cosmic rays, the reconstruction algorithms are still able to accurately reconstruct proton tracks. The benefit of performing “cheated” reconstruction can be seen by comparing Figures 4.18a, and 4.18c, where the number of proton tracks that survive the application of all cuts is seen to increase. When the reconstruction is performed using non-cheated disambiguation, and a cheated interaction time determination, the distribution of events surviving the application of all cuts is seen to be very similar to Figure 4.18c. This implies that the increase in the number of potentially identifiable proton tracks seen in Figure 4.18c, is largely due to the increased accuracy of interaction time determination.

Though the plots shown in Figure 4.18 concerning the identification of protons are encouraging, the complementary plots concerning the identification of muons are much less encouraging. This is because, though there is quite a large peak at a PIDA value of around 8 MeV cm^{-1} after the application of all cuts, this cannot be seen before the last cut is applied. This is because of two large peaks with PIDA values of around 3 and 6 MeV cm^{-1} . A large peak at a PIDA value of 6 MeV cm^{-1} was observed in Figure 4.16b, though this was largely removed by requiring that the muon track stopped in the detector. Unfortunately, this is not seen to be the case when considering muons in the enriched proton sample, though the size of the peak is significantly reduced by requiring that the track stops in the detector. Therefore, it is thought that the tracks which make up the peak of PIDA values at 6 MeV cm^{-1} , are partially reconstructed muon tracks. Effectively removing these partially reconstructed tracks is difficult, though if some degree of supplemental track stitching is performed during the analysis stage, they may be able to be removed. Evidence that this may work is presented in Figure 4.22, where through-going particles from Monte Carlo truth have been removed.

A feature of Figures 4.18b, and 4.18d, which was not present in Figure 4.16b, is the presence of a large peak at PIDA values of 3 MeV cm^{-1} . It is thought that this is due to very short delta rays coming off the high energy muon track, as it passes through the detector. These tracks are considered to be due to the muon in the current framework, as the delta rays

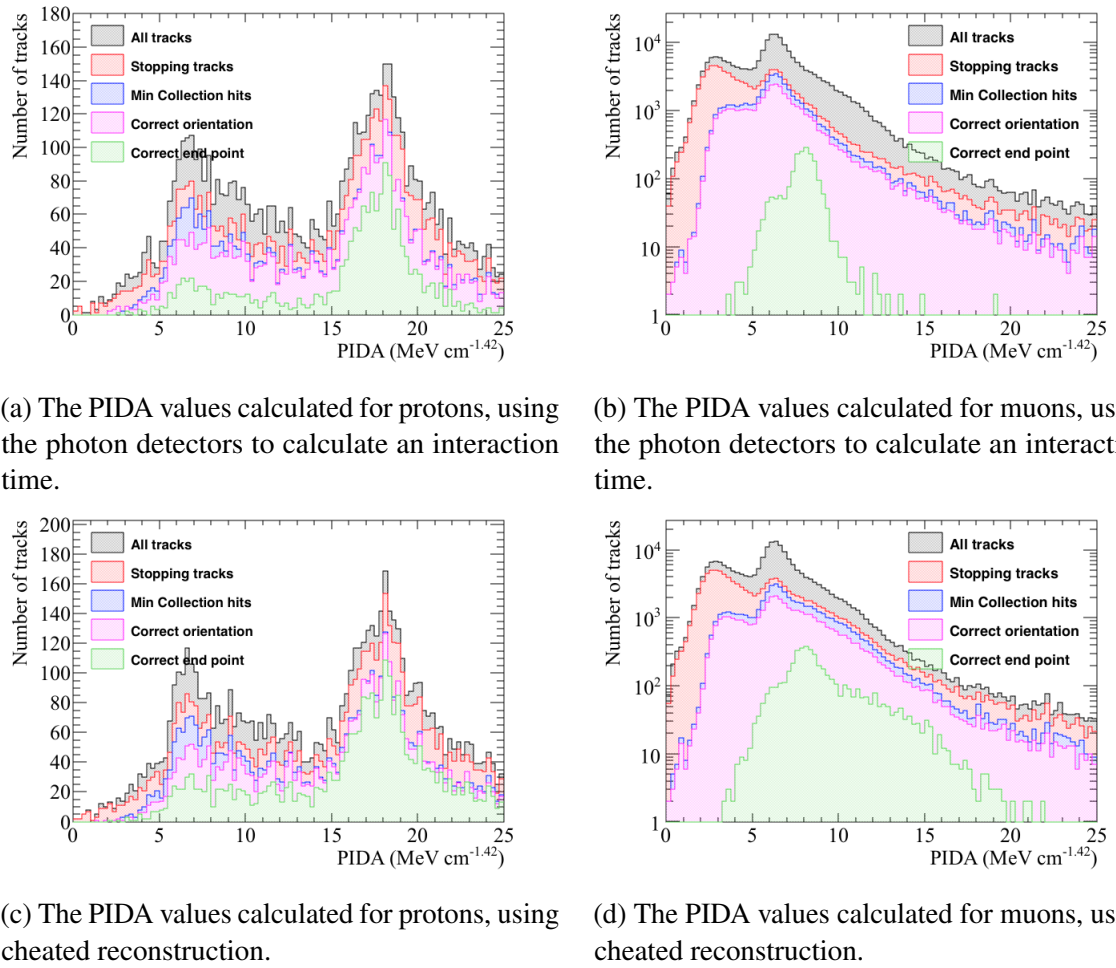


Fig. 4.18 The calculated PIDA values for the simulated proton enriched sample in the 35 ton detector. Top left: the PIDA values calculated for muons using the photon detectors to measure the interaction time. Top right: the PIDA values calculated for protons using the photon detectors to measure the interaction time. Bottom left: PIDA values calculated for muons using a cheated interaction time determination. Bottom right: the PIDA values calculated for protons using a cheated interaction time determination. A series of criteria designed to select only tracks due to stopping particles which have a required number of collection plane hits is applied. The tracks are then further refined using truth information such as the true end point of the particle.

are not saved by GEANT4, and so LArSoft assigns any tracks which they produce to the parent of the electron, which in this case is the muon. Figures 4.19a, 4.20a, and 4.20b support this assessment. From Figure 4.19a, it can be seen that many of the tracks with very low values of PIDA have track lengths below 10 cm, which is much shorter than one would expect for a cosmic ray muon. This is conclusively shown by Figures 4.20a, and 4.20b, as it can be seen that the muon tracks which have low PIDA values have very short reconstructed track lengths, compared to the track length in the detector from Monte Carlo truth. Figure 4.20b, then shows that many of the shortest reconstructed tracks, are associated with particles which have track lengths in the detector from Monte Carlo truth, which are much longer than themselves. It can be seen that many of these very short tracks have reconstructed track lengths of less than 10 cm. Placing a cut at a minimum track length of 10 cm will also remove some of the muon tracks which contaminate the range of PIDA values expected for protons. However, it can be seen from Figures 4.19c, and 4.19d, that though some of the proton tracks which have PIDA values within the expected range will also be removed. It may therefore be necessary to develop a more sophisticated cut to remove these delta rays, should the identification of protons be attempted in the cosmic ray data collected by the 35 ton detector. Neither the development of such a cut, or the attempt to identify protons from cosmic ray data collected by the 35 ton detector, is presented here though.

Figure 4.21, shows the distribution of calculated PIDA values for protons and muons in the proton enriched CRY sample, after a cut on the minimum reconstructed track length of 10 cm is applied.

When comparing Figures 4.18, and 4.21, the removal of muon tracks with PIDA values of 3 MeV cm^{-1} is very apparent, and shows that the cut on minimum reconstructed track was successful. It can also be seen that the number of muon tracks which have PIDA values consistent with a proton has also decreased, by around a factor of 2. However, as noted above, this has come at the cost of some of the proton tracks which could have been correctly identified as protons being removed, due to their short track lengths. This is unfortunate, but some loss is unavoidable, as the significantly more numerous muons would overwhelm any proton tracks, should the identification be attempted in cosmic ray data collected by the 35 ton detector. The peak around PIDA values of 8 MeV cm^{-1} for muon tracks, is however, only identifiable once the requirement that the end point of the reconstructed track is close to the end point of the particle from Monte Carlo truth. Therefore, a more robust system of cuts is required in order to produce a sample of muon tracks which can reliably identified as such.

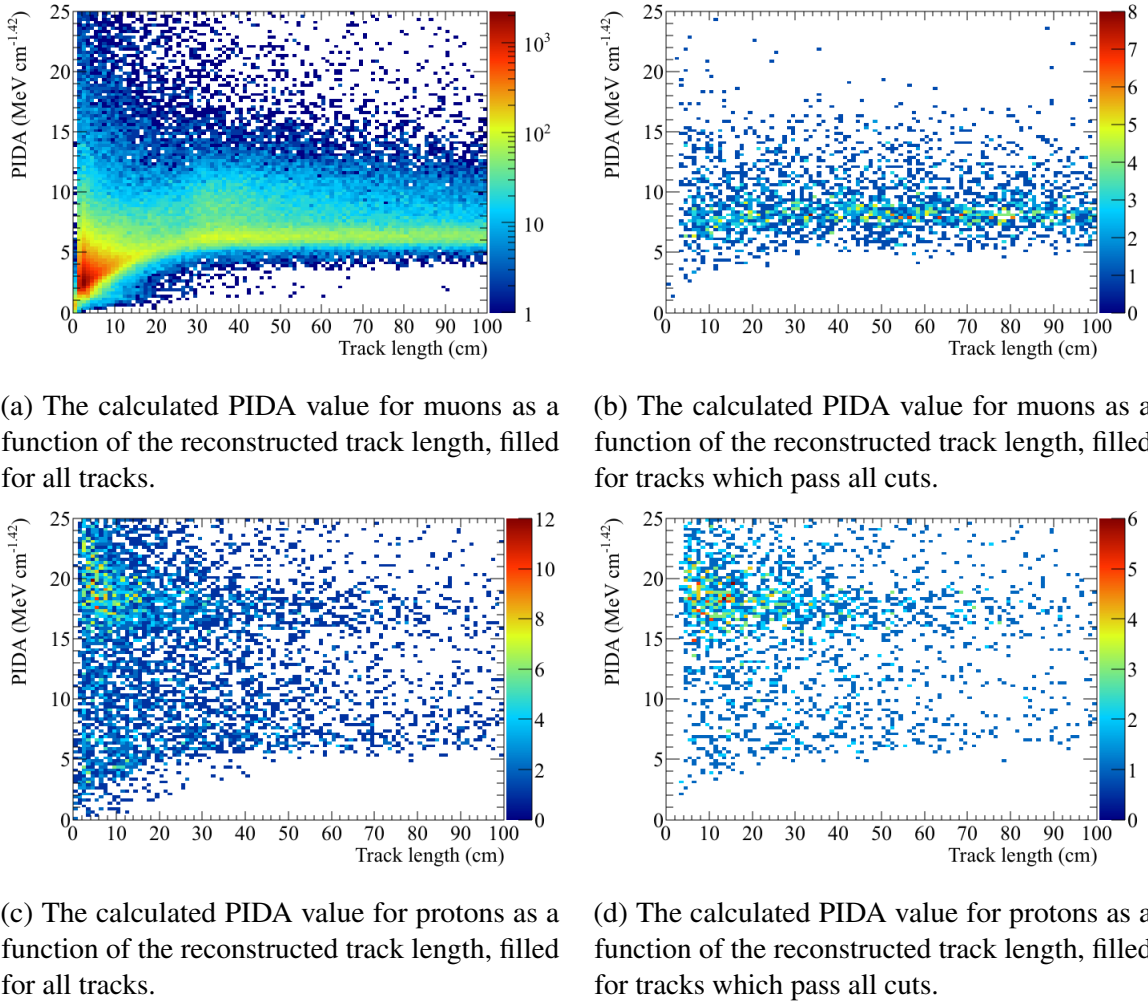
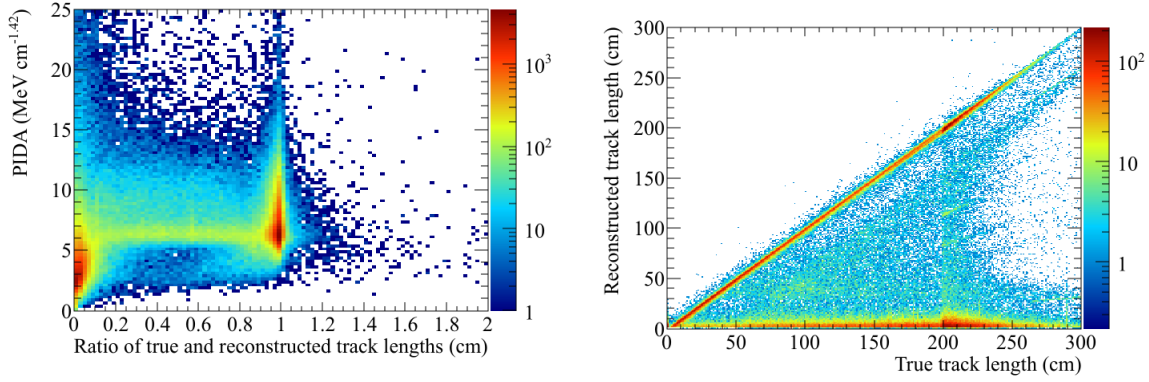


Fig. 4.19 The calculated PIDA values, as a function of the reconstructed track length, for the simulated proton enriched sample in the 35 ton detector. Left: the PIDA values, as a function of the reconstructed track length, when filled for all tracks. Right, the PIDA values, as a function of the reconstructed track, filled for tracks which pass all cuts. Top: The PIDA values calculated for muons. Right: the PIDA values calculated for protons. All plots are made for tracks which have been reconstructed using a cheated interaction time determination.



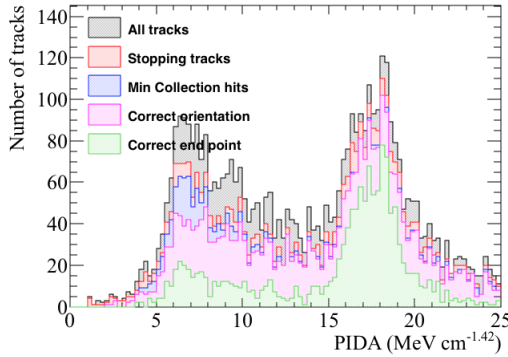
(a) The calculated PIDA value for muons, as a function of the ratio between reconstructed track length and the track length from Monte Carlo truth, filled for all tracks.

(b) The relationship between reconstructed track length, and the track length from Monte Carlo truth, filled for all tracks.

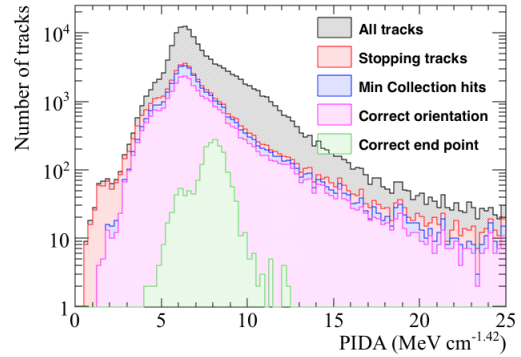
Fig. 4.20 The calculated PIDA values, as a function of the reconstructed track length, for the simulated proton enriched sample in the 35 ton detector. Left: the PIDA values, as a function of the ratio between reconstructed track length, and the track length from Monte Carlo. Right, the relationship between reconstructed track length, and the track length from Monte Carlo truth. All plots are made for tracks which have been reconstructed using a cheated interaction time determination, and are shown for muons.

As outlined above, partially reconstructed muon tracks have PIDA values of 6 MeV cm^{-1} , and so in order to remove the large peak of these tracks still seen in Figure 4.21, some form of track stitching is required in order to remove these tracks. It is possible that a large number of these tracks are due to muons which pass through the detector, as many cosmic muons will do, but have been reconstructed as at least two separate tracks. Should this be the case, at least one of the tracks would be considered to “stop” in the detector. The effect of removing these split tracks can be seen in Figure 4.22, where all particle which do not stop in the detector, from Monte Carlo truth, have been removed. This effectively “cheats” the stitching which is required to remove the majority of split muon tracks, though any muons which stop in the detector, but have been split into two or more tracks by the reconstruction, will still be present in Figure 4.22. It can be seen that these tracks are still present, as there is still a peak in PIDA values of 6 MeV cm^{-1} , though these tracks are now overshadowed by tracks with PIDA values of 8 MeV cm^{-1} .

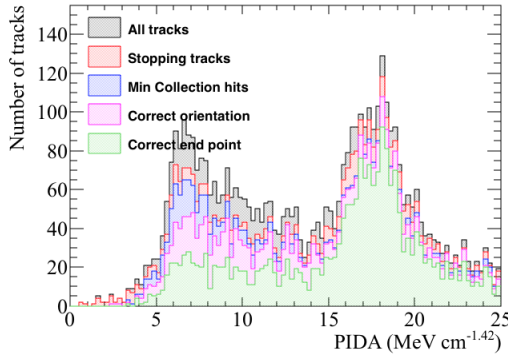
The number of muon tracks with high PIDA values in all plots is concerning, though this is particularly true for those shown in Figure 4.22, as these tracks are due to particles which stop in the detector, and are accurately reconstructed. This is because the contamination caused by these tracks, would mean that it would be difficult to ascertain whether a track



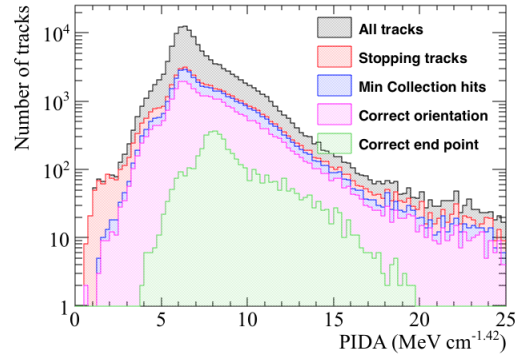
(a) The PIDA values calculated for protons, using the photon detectors to calculate an interaction time.



(b) The PIDA values calculated for muons, using the photon detectors to calculate an interaction time.

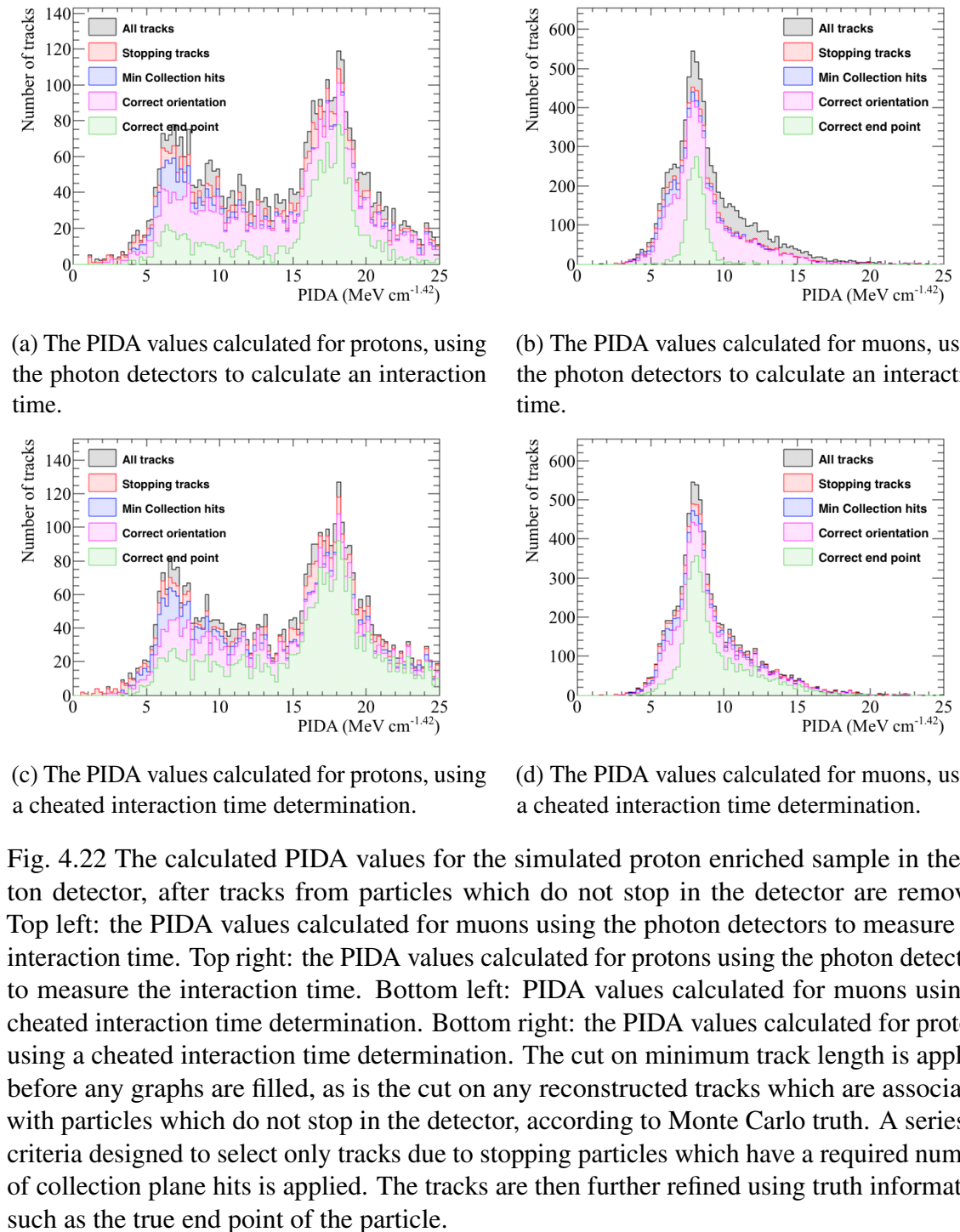


(c) The PIDA values calculated for protons, using a cheated interaction time determination.



(d) The PIDA values calculated for muons, using a cheated interaction time determination.

Fig. 4.21 The calculated PIDA values for the simulated proton enriched sample in the 35 ton detector, after a cut on the minimum reconstructed track length is applied. Top left: the PIDA values calculated for muons using the photon detectors to measure the interaction time. Top right: the PIDA values calculated for protons using the photon detectors to measure the interaction time. Bottom left: PIDA values calculated for muons using a cheated interaction time determination. Bottom right: the PIDA values calculated for protons using a cheated interaction time determination. The cut on minimum track length is applied before any graphs are filled. A series of criteria designed to select only tracks due to stopping particles which have a required number of collection plane hits is applied. The tracks are then further refined using truth information such as the true end point of the particle.



with a PIDA value of around 18 is actually a proton.

However, the basic framework by which PID can occur has been outlined here, and shown to be very effective when particles are simulated in isolation. It has also been shown that a clear separation between muons and protons can be seen in cosmic rays, though there is a non-negligible contamination of the proton track ROI, by muon tracks. This separation was only possible when using information from Monte Carlo truth though, and so a more sophisticated method of identifying through-going muons is required, should the analysis be performed on the cosmic ray data collected by the 35 ton detector.

Chapter 5

The 35 ton data sample

The data taking period for the 35 ton prototype was from November 2015 until March 2016. This included an extensive commissioning period before the detector was filled with LAr, and the electric field was turned on. During this time many of the features of the data discussed below were first noticed, and attempts to rectify these were pursued. A long commissioning period was also required because many of the DAQ sub-systems were still under active development in November.

A total of 22 days worth of data was collected with the electric field set at 250 V cm^{-1} , the breakdown of when these periods occurred is shown in Figure 5.1. It is clear that the analysable data is interspersed with data where the electric field was not turned on, this is both due to extenuating circumstances such as a site wide power outage in early March, and a dedicated two week noise hunting exercise in February. The physics data taking period ended at 3am on 19th March 2016, when a filtration pump broke causing an unrecoverable loss of purity as air was pumped into the detector. Following this studies to understand the electronics noise and to test the high voltage systems continued, but it was deemed too costly to acquire any more physics data. During this time the electric field was raised to the nominal value of 500 V cm^{-1} , and some of the causes of the higher than expected noise levels were discerned.

5.1 Organisation of the data structure

As previously noted the 35 ton consisted of three detector sub-systems: RCEs collecting TPC data, SSPs collecting photon detector data, and CRCs tagging cosmic rays. The DAQ combined these three data streams into synchronous events in time and saved them as LArSoft

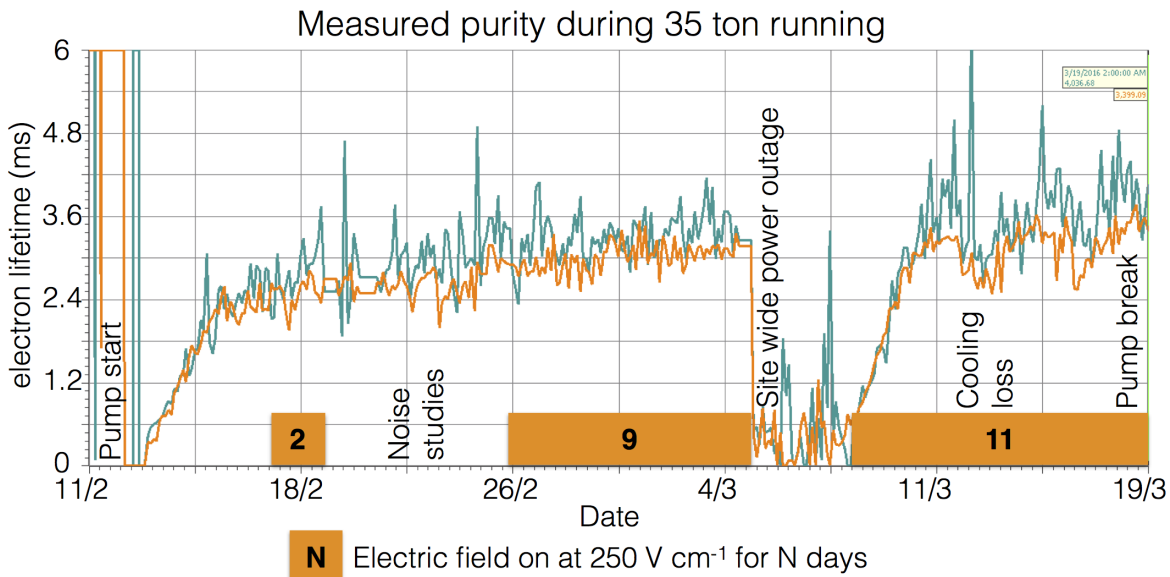


Fig. 5.1 Timeline showing the data collected during the 35 ton Phase II run once the purification pumps were turned on.

data objects. These data objects would later have to be converted to the offline data products, which the reconstruction tools developed on simulation used, this is discussed in Section 5.2. This section describes the structure of the data objects in the raw form.

During operations the DAQ was configured to maximise data throughput and physics potential. This meant recording different lengths of times for each of the three sub-systems, as the data volumes and length of physics information were significantly different. For example, due to the emission of prompt light, the physics information from the SSPs is of a much shorter length of time than the physics information from the RCEs, where data has to be recorded whilst the electrons drift through the LAr. During the running period the recorded data was triggered by through-going muons which produced coincidences on the CRCs on opposite sides of the cryostat. A coincidence is defined as two CRC modules recording a hit within 32 ns. The system used to collect the CRC data was also responsible for generating the triggers, and so this meant that the trigger rate could be suppressed to approximately 1 Hz, by only producing triggers every N times a coincidence occurred, where N was a tuneable variable. A trigger rate of 1 Hz was used as the maximum speed at which data could be written to disk was approximately 60 MB s^{-1} , which is roughly equal to the size of each triggered event when the entire detector is read-out in the configuration discussed below. The rate at which events were recorded could have been increased if zero-suppression

of the TPC data had been used, however the noise level meant that this was not feasible.

With an electric field of 250 V cm^{-1} , and a drift of 2.25 m, the drift time for electrons at the long drift CPA was roughly 2.6 ms or 5200 ticks (where 1 tick is 500 ns). It was decided that in order for a track causing a counter coincidence to be separated from other tracks, it was necessary to have roughly one drift window both before, and after, the drift window around the coincidence. This means that data was recorded for 7.5 ms, or 15,000 ticks, around each coincidence. The SSPs only collected the prompt light from through-going particles, and so only $200 \mu\text{s}$ of SSP data was recorded for each event. The CRCs produced the least volume of data, and so were able to be read out constantly.

As the run mode required accessing buffered data, it had to be discretised inside the components before being sent to the event builders in the DAQ. In the discussion of how this worked, focus will be given on the RCE data where some new terms need to be introduced. The smallest unit of data, called a nanoslice, is the data from one RCE for one tick, where each RCE controls 128 channels meaning that there were a total of 16 RCEs in the 35 ton. A microslice is then made by combining $1000 \times N$ nanoslices such that it contains 0.5 ms (1,000 ticks) of data across all channels, where N is the number of RCEs that are recorded in the run. Microslices are then combined to make millislices, the length of which was configurable. Once produced, these millislices were sent by the DAQ to the event builders, to be stored as time synchronous LArSoft data objects.

The time synchronous events produced by the DAQ, did not, however, correspond to the physics events. This is because the DAQ was originally designed to produce a continuous data stream. This meant that the DAQ was configured to pad events with headers when a sub-system provided no physics information, such as nanoslices in the case of the RCEs. Removing these padded header objects was a remit of the online to offline converter discussed in Section 5.2. As the length of the millislices was configurable, it was chosen to be 10 ms (20,000 ticks), in order to best attempt to fully contain physics events, and reduce the need for the online to offline converter to stitch DAQ events together. The padding of millislices with headers between physics events introduced some peculiarities in the recorded data, such as millislices containing two parts of non-continuous data. This is shown in Figure 5.2, where the second millislice has no information for the time between the end of physics event 2, and the start of physics event 3.

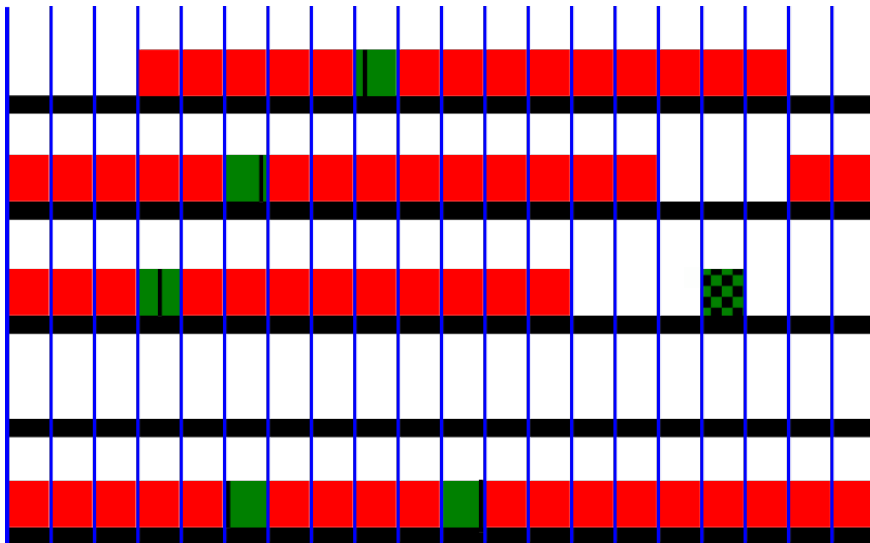


Fig. 5.2 A diagram of possible millislice structures for the TPC data recorded by the 35 ton. Each row represents a millislice, whilst each box represents a microslice. The vertical blue lines delineate each microslice, giving 20 microslices per millislice. Solid red and green boxes represent microslices with TPC data in them. A group of 15 continuous red and green boxes are the recorded “physics events”. Green boxes represent triggers which were used, with the black lines showing the time in the millislice at which the trigger occurred. Green and black patterned boxes represent coincidences of CRCs which were not issued as triggers. A possible reason for these triggers not being issued, is their proximity to a previous coincidence trigger which was issued.

During normal data taking, the last N microslices are buffered in the RCEs so that if a trigger is issued, the previous millislices can be accessed before they are deleted. As the data is buffered in the form of microslices, previous microslices may only be accessed in whole. This means that a whole number of microslices must be loaded before the trigger, so when a trigger is issued part way through a microslice, the previous X microslices are sent to the event builders. As a result, there are always a minimum number of ticks both before (5,000 ticks), and after (9,000 ticks), the trigger, but the exact numbers can change by up to 1,000 ticks for a given event, depending on where in the microslice the trigger came. The result of this is that it is impossible to know the number of ticks before/after a given counter coincidence. This is shown in Figure 5.2 where the black lines representing triggers, are seen to occur at different points within the microslices. For example, physics event 1 will have more data after the trigger than physics event 2 as the trigger occurs earlier in the triggered microslice.

5.2 Reformatting the data to the offline structure

Conversion of the data objects stored in the raw data to the data objects used in simulation required a suite of unpacking services to be written, the specifics of which are not discussed here. These all required a common interface through which to access the data and check that the timing of each component was consistent, so that a final LArSoft file for downstream use could be produced. This interface had the added role of producing complete physics events, meaning that it had to be able to combine multiple millislices and extract only the data containing the continuous physics events.

Following the unpacking of each of the sub-systems, the data reformatter would loop through the TPC ticks to see if a user defined set of conditions could be satisfied at that time. These conditions were usually whether an East-West or North-South counter coincidence occurred at that time, or if this millislice contained TPC data whilst the previous one did not. The latter was the default configuration as this gave the option of preserving all of the data gathered, for reasons discussed at the end of Section 5.1. Other conditions were available, though rarely used, such as if the SSPs observed a large flash of flight, or if there was a large change in the average TPC ADC value. Once a set of conditions are satisfied a user defined number of pre-condition ticks are gathered. No pre-condition ticks are gathered when the previous millislice contains no TPC data, as there is no previous data to load which would not have a gap in time, see Figure 5.2. In the case of using a counter coincidence to make an event, a value of 300 pre-condition ticks is normally used,

with a maximum of 5000 ticks being able to reliably collected. Once the pre-conditions ticks are gathered, a further N post-condition ticks are gathered, where N is defined by the user. Usually 15,000 ticks are gathered when the previous millislice is empty, and 5,200 ticks are gathered when there is a coincidence, though a maximum of 9,000 ticks could be reliably gathered. Data from the other components is added to the event if its timestamp is within the timestamps of the first and last ticks in the event, when no more TPC data is required, or at the end of a millislice if stitching is required. All timestamps are corrected such that the event began at $t=0$ as the reconstruction assumes this, and the timestamp of the start of the event is stored in the event record, so that it can be accessed later if required.

At all points in this process it is important to integrate flexibility so that the user can choose the length of events, which sub-systems are in the events, and what the conditions are for making events. It is also important for users to be able to run the service on already formatted events, as the unpacking services are the major overhead in running the interface. It is also conceivable that users would want to reformat Monte Carlo events so as to centre them around their chosen conditions, and so the use of the unpacking was determined by the interface depending on the format of the input file.

5.3 Observations on data quality and noise mitigation

Reformatting the online data to the offline format was an important step in maintaining data quality, as subsequently there was no access to the raw data due to the framework of the 35 ton software. Some of the important checks which are performed are outlined in Figure 5.3. If any of these issues are present in a given physics event then it is discarded, as the integrity of the data cannot be guaranteed. It was decided that these events would be discarded as non-synchronous events would lead to hits in the detector being at incorrect times, and padding empty events with pedestals could mean that tracks seem to disappear and later reappear as they travel through the detector.

Another example of inconsistent events is when the sub-systems are not synchronised with each other. This is normally caused by one of the sub-systems missing a clock increment from the master timing unit, due to the data trigger being issued close to an increment from the master unit. This misalignment causes an incorrect time sample being read out, and so the data from each sub-system within a millislice is not consistent. The result of this is that the event will fail the timestamp check, and so won't be added to the event record. To avoid

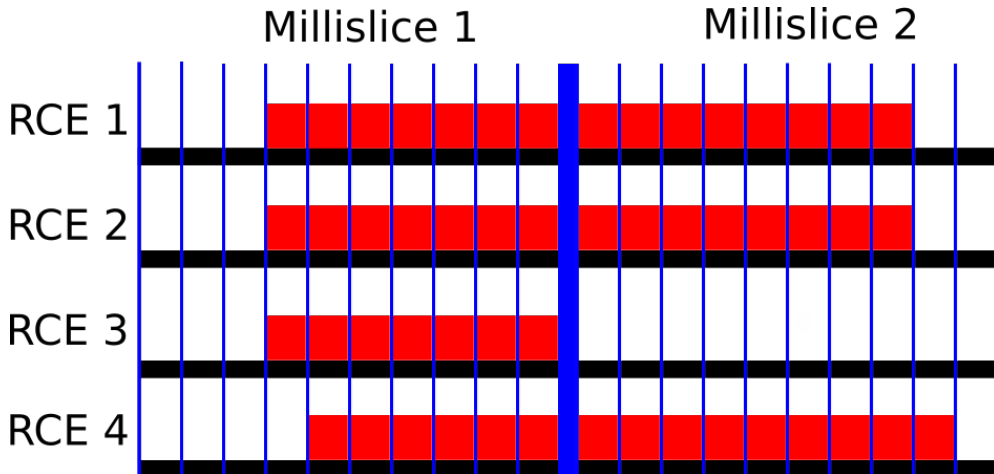


Fig. 5.3 A diagram of TPC microslices within millislices in the 35 ton data stream. Two millislices are shown, each containing 10 microslices. One physics event straddling the millislice boundaries is shown, and 4 RCEs representing each row are read out. The vertical blue lines delineate each microslice (0.5 ms, 1,000 ticks), with the thick blue line showing the millislice boundary. Solid red boxes represent micro slices with TPC data in them. It can be seen that RCEs 1 and 2 contain data for the same interval, whilst the data from RCE 3 in millislice 2 has been “Dropped,” and the data from RCE 4 is shifted by 1 microslice from RCEs 1 and 2 and is thus “Inconsistent.” As a result of these issues this physics event would be discarded as data integrity cannot be guaranteed.

incomplete events these physics events are also discarded when observed.

The electronic noise in the 35 ton was higher than anticipated, with the RMS of the RCE ADC being approximately 30 counts compared to an expected thermal noise of around 2.5 ADC counts. Many sources contributed to this elevated noise, some of which are explained below.

Though not directly affecting the noise issues “stuck ADC codes” were a feature of the data which had to removed. “Stuck ADC codes” were caused by bit level corruption where lowest 6 bits in the ADC became frozen to either 0x0 or 0x3f. This was observed during the first stages of commissioning and an algorithm to remove them was developed and tested on Monte Carlo [107]. In simulations it was observed that the signal could be recovered with minimal losses, as shown in Figure 5.4, where the blue lines (after removal) are seen to closely match the black lines (before adding stuck codes).

A significant portion of the noise was correlated between groups of 32 channels, where the ADCs would coherently oscillate. To remove these coherent shifts, ADC baselines

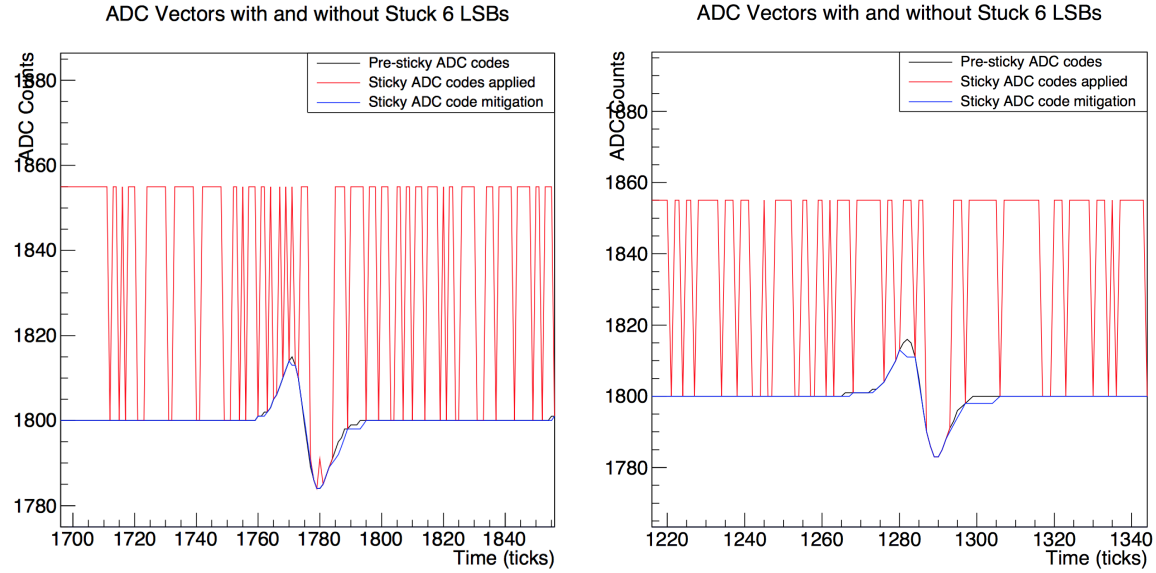


Fig. 5.4 Two Monte Carlo spectra showing the effect of the introduction and removal of stuck bits on a simulated signal. The black line shows the simulated signal on a wire, which is then modified by adding the effects of “stuck ADC codes,” shown by the red line. The “stuck ADC codes” are then removed, and the resulting signal is given by the blue line. It can be seen that the signal loss is minimal after the “stuck ADC codes” are removed. The figures were taken from [107].

were calculated for these groups of 32 channels at each tick, and then subtracted from the measured ADC values. This was found to be an effective method of removing coherent noise in MicroBooNE [108]. The effect of removing coherent noise is shown in Figure 5.5, where the signal peak becomes much easier to discern after noise removal, and a coherent noise peak around tick 6030 is removed. An issue with removing coherent noise in this way is that events which are parallel to the APAs will produce signals at common times across adjacent wires, and these signals may be removed along with the coherent noise. This will cause a reduction in the hit reconstruction efficiency. The only way to prevent this is to “protect” potential signal regions from the coherent noise removal, as is done in MicroBooNE [108].

When a Fast Fourier Transform (FFT) [109] is performed on the coherent noise subtracted waveforms, it can be seen that signals occur with specific frequencies. Some of these frequencies are caused by real energy depositions, whilst others are due to the electronics noise. It is possible to remove the noise frequencies by applying Wiener filters [110]. Frequency spectra are taken for each of the three planes, and a clear signal is both preserved and suppressed. The raw signal spectra, are then divided by the signal suppressed spectra, to produce *signal/noise* frequency spaces. The regions of frequency space to be conserved, given by regions of

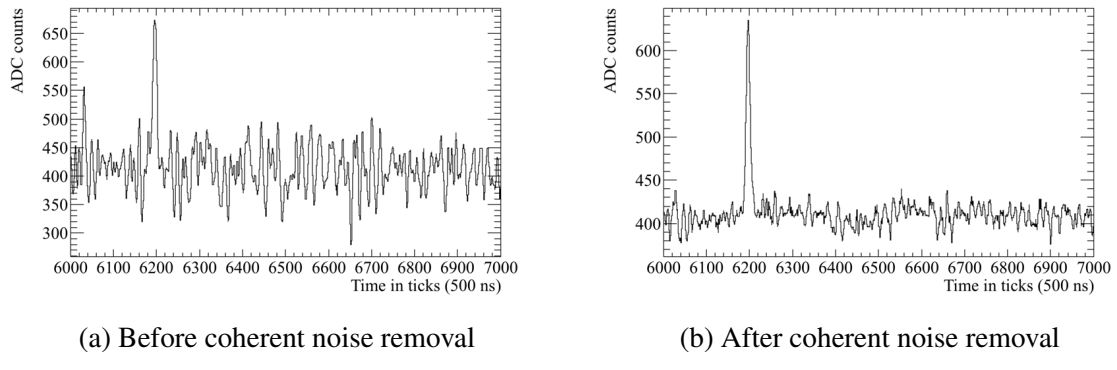
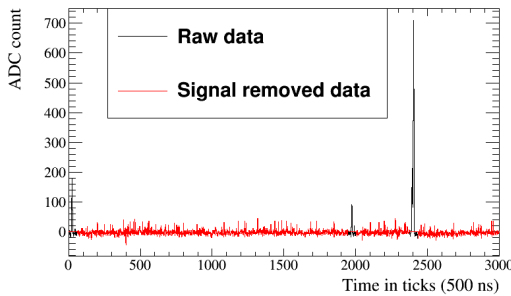


Fig. 5.5 The effect of coherent noise removal on a 35 ton signal event. Left shows the signal before coherent noise is removed, and right shows the signal after the coherent is removed. The signal peak around tick 6200 is much clearer after coherent noise removal, meaning that hit reconstruction becomes much simpler.

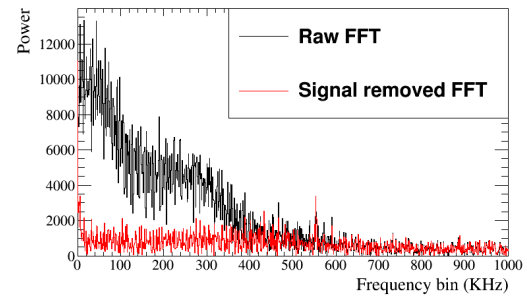
high *signal/noise*, can then be found by fitting a combination of sigmoid functions to the frequency spaces. A demonstration of how this was applied is shown in Figure 5.6. It is also possible to remove specific frequencies which are not removed by the filters, this was necessary for a 54 KHz noise component, which was introduced by the fluorescent lights in the detector hall. After the run ended it was found that some of the high frequency noise components were introduced by a short on a warm power cable. The techniques used to find this cable will be used when commissioning future detectors [111].

An example of the effect of the noise mitigation steps is shown in Figure 5.7. The left side shows the raw data and the right side shows the data after the stuck code unsticker, coherent noise removal and Wiener filter algorithms have been applied. The effect of noise removal is clear, as the signals from the tracks become much more pronounced, particularly on the bottom induction plane. However, it can also be seen that the noise removal algorithms also remove signals from tracks, as the depositions shown on the collection plane (top plot) around tick 10,000 becomes much less pronounced.

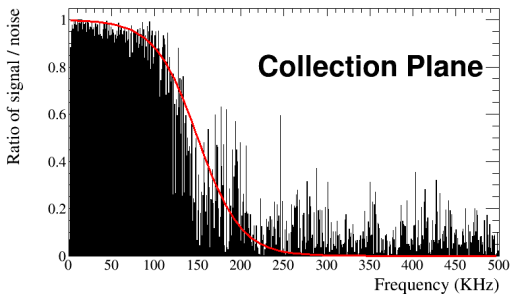
Transitions to a higher noise state associated with strong signals at high frequencies, between 400 and 650 KHz, were observed after cool down. The transitions would occur approximately every 2 hours, and were occasionally observed to happen shortly after a saturation event across the whole detector [111]. Once the state was induced the only way to stop it was to power cycle the low voltage supplies. It was found that power cycling APA3 could both stop, and induce the higher noise state. Importantly, this was the only APA with electronics located at the base of the TPC. The data taken during the elevated noise state



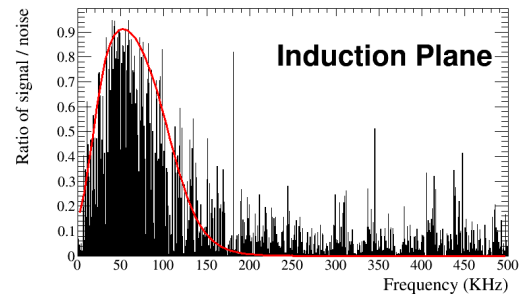
(a) A raw and signal subtracted waveform for a collection plane wire.



(b) The FFT of the raw and signal subtracted waveform for a collection plane wire.



(c) The *signal/noise* ratio for a collection plane wire, the red line shows the fraction of frequency power which passes the filter.



(d) The *signal/noise* ratio for an induction plane wire, the red line shows the fraction of frequency power which passes the filter.

Fig. 5.6 The application of Wiener filters to the 35 ton data. Top left shows a waveform from a collection plane wire which is then signal suppressed. The FFT of both the raw and signal suppressed waveforms are shown top right. The *signal/noise* ratio for this waveform is shown bottom left, where a sigmoid function has been overlaid to preserve only the areas of high *signal/noise*. The *signal/noise* frequency space ratio, and an overlaid sigmoid function, for an induction wire, is shown bottom right.

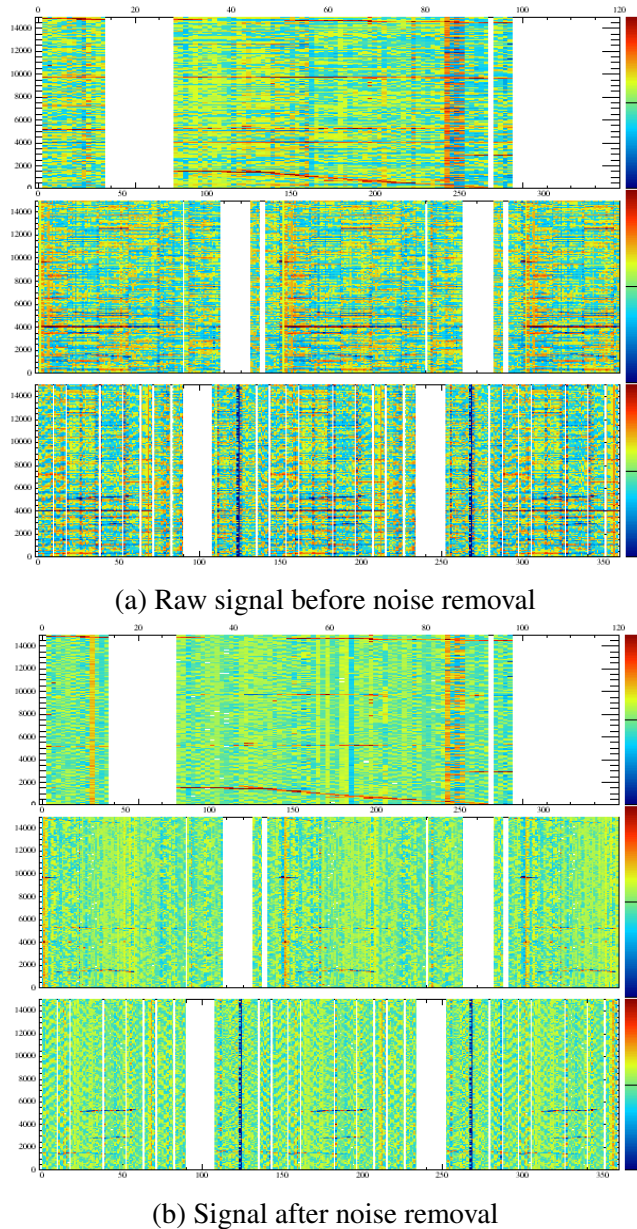


Fig. 5.7 Event displays showing the effect of the noise removal algorithms on data in the 35 ton. The event displays show the signals in the collection, U and V planes respectively. The plots show wire number, time in ticks and charge in ADC counts on the x, y and z axes respectively. The effect of the noise removal algorithms can clearly be seen, as large changes in charge due to the noise, are no longer present after they have been applied. The application of the noise removal algorithms does however also remove real signals, as depositions across many channels at the same time which were present before their application, can no longer be seen after they are applied.

was unrecoverable as the electronics noise was too large, and so upon the observation of a transition the low voltage supplies were power cycled. It was observed that the transitions occurred much less frequently when APA3 was not powered, and so it was not used for significant portions of the data taking period. Despite efforts to study the transitions during warm testing they were unable to be induced, and have not been observed in other experiments such as MicroBooNE, despite other experiments using the same low voltage supplies. It is thought that the cause of the transitions is a feedback loop in the low voltage cable, which was much longer in the 35 ton than in MicroBooNE. This would explain why APA3 was more susceptible to the feedback loop, as the cable is routed past its electronics [112].

5.4 Performance of reconstruction algorithms

Following the noise removal outlined above, hit and track finding was still more difficult than in simulations, due to the still elevated noise level. In order for a reasonable number of hits to be reconstructed the hit finding threshold had to be substantially increased in data, as compared to Monte Carlo. This meant that many of the low energy hits would not be reconstructed.

A potential solution to not reconstructing the low energy hits, is to use the counter positions to select only hits which could have caused coincidences. When determining whether a reconstructed hit could have caused the counter coincidence, a two-dimensional window around the counter edges in the yz plane is constructed, and timing information is used to extend this to three dimensions. The x position of the hit can be calculated using the hit time, and electron drift velocity using Equation 4.1.

Determining whether collection plane hits are within the counter window is trivial as they have a constant z position, and either cover the full detector height (tall APAs), or roughly half of the detector height (short APAs). The wrapping of the induction planes, however, means that each wire segment has to be considered individually, and that multiple segments of a given wire could lie within the counter shadow. The 3-dimensional volume that is enclosed by connecting the edges of the counters which were hit in the counter coincidence, is called the “counter shadow.” Only those wires which lie within the 2-dimensional projection of this volume onto the yz plane, are considered here. Choosing between these potential wire segments is done by iterating through the following steps. If at any point only one segment satisfies the condition then that segment is chosen:

- Does the wire segment intersect any collection plane wires which record hits?

- This is because when there is a signal on an induction plane there should also be signals on the collection wires.
- Are there adjacent wires which have hits at a similar time?
 - This is because one would expect a track to deposit energy on multiple adjacent wire segments.
- Which hit lies closest to the line defined by unique collection plane hits in the xz plane?
 - This follows identical logic to the first criterion, but selects the hit which best matches the collection plane hits, and attempts to remove the effect of noisy collection plane wires by only using wires which have one hit within the counter shadow. This would also hopefully improve the quality of the fit, as there will not be numerous outlying hits.
 - This can be changed to consider the line defined by previously selected hits in the given TPC and plane where the hit choices are.

Following a re-optimisation of the clustering algorithms, it was observed that the standard reconstruction could achieve track reconstruction to a similar efficiency as the counter shadowing, and so the standard reconstruction has been used in the discussions to follow [113]. There has since been an effort to improve the counter shadowing hit disambiguation to remove the outlying collection plane hits using the MLESAC method [114], whereby points which are far away from a best fit are ignored. These studies are still on-going [115].

A symptom of the elevated noise state is that signals are often dropped on one of the induction planes, this means that the tracking algorithms often have to combine clusters in only two of the three planes. Reconstruction using two planes was shown to be effective by the ArgoNeuT collaboration [116], so the loss of signal in one of the three planes is not prohibitive to track reconstruction. Another consequence of the elevated noise level is that even when the counters are used to seed hit finding, the hit finding threshold is too high to reconstruct the very lowest hits. This causes the plot of dQ/dx for muons, shown in Figure 5.8, to look flat, due to a cutoff at 100 ADC cm^{-1} , below which no hits are reconstructed. The inability to reconstruct the lowest energy hits means that calorimetry is all but impossible on the 35 ton dataset, even though the tracking algorithms perform relatively well. The inability to perform reliable calorimetry en masse means that the only particles which can be assuredly identified are the muons which triggered the counter coincidences, making the analysis proposed in Section 4.4 extremely difficult, if not impossible.

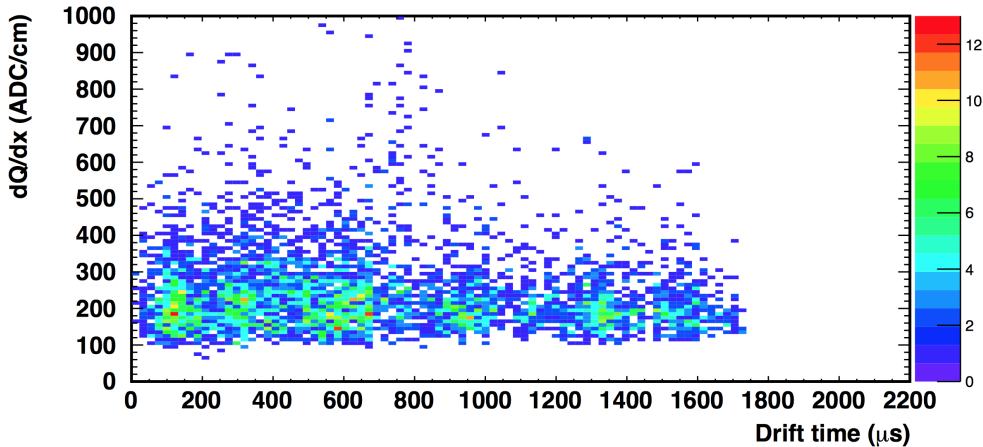


Fig. 5.8 The dQ/dx values for a sample of muon collection plane hits, note the cutoff at 100 ADC cm^{-1} due to the hit finding threshold. Figure taken from [117].

The muons in the triggered sample will all traverse the detector, but their orientations can be carefully selected by the user. For example, one could easily select a sample of muons which cross the APAs at increasing angles, or are parallel to the wire planes at increasing drift distances. This is done by matching through-going muons with counter coincidences. The process by which this is done is identical for both North-South and East-West coincidences, though more focus will be given to the later, as it is with muons of this orientation that the study shown in Section 5.5 was performed. The same matching technique would also have been applied to vertical muons had the telescope trigger been utilised. For a reference as to the locations of the counters around the cryostat, see Figure 2.22, and for a representation of only the East-West counters, see Figure 5.9.

It is possible to construct a line in the yz plane joining the centres of the two counters which were hit when a coincidence occurred, shown by the dashed line in Figure 5.9. This can then be compared with the trajectory of a track in the yz plane and a dot product of the two vectors calculated. A reconstructed track is assigned to a given counter coincidence if the dot product of the track and the coincidence is more than 0.98, and the hit times are consistent with the x positions of the counters. The results of the dot product calculation are shown in Figure 5.10. Matching only tracks which are well aligned with a counter coincidence should produce a pure sample of tracks, as parallel muons are unlikely to be highly correlated in time, and any tracks reconstructed from the noise will have random directions. This is shown in data where if multiple tracks pass the dot product cut they are co-linear and are not randomly orientated, as shown in Figure 5.11.

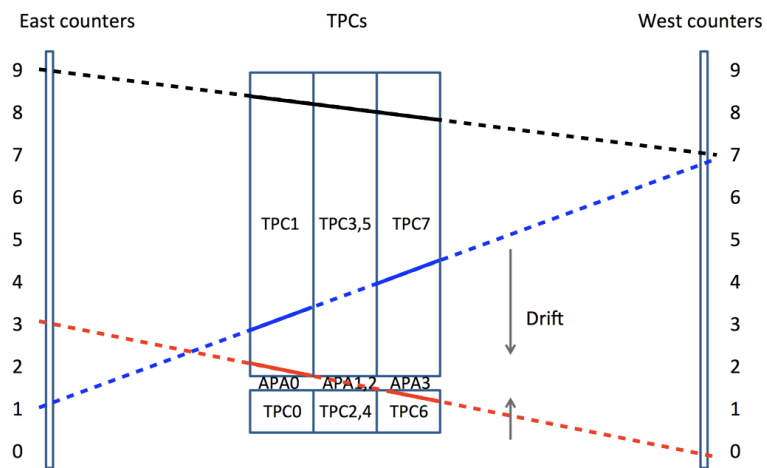


Fig. 5.9 The numbering scheme for the East - West counters in the 35 ton. The counters have been numbered from 0 to 10 depending on their position from the end of the short drift volume. This is different to the LArSoft numbering scheme shown in Figure 2.22 where they go from 6-15 and 28-37 for the East and West counters respectively. Three hypothetical muons which would have caused coincidence triggers are shown as dashed lines, and the hypothetical reconstructed tracks they produce are shown as solid lines. The red track is an APA crossing event, and would produce tracks in TPCs 1 and 6. The black muon is fully reconstructed as one continuous track, however the blue particle is not reconstructed in the middle TPCs and so is reconstructed as two separate tracks.

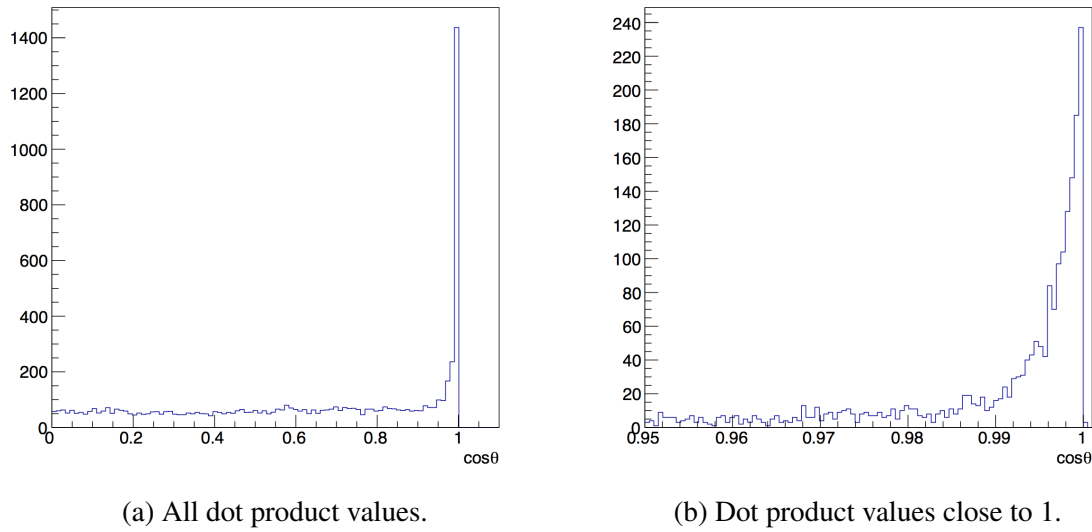


Fig. 5.10 The dot product of the track and vector joining the centres of the coincidence counters in the yz plane. A threshold value of 0.98 is required for a track to be considered to be due to the counter coincidence. It can be seen that many tracks are well aligned with counter coincidences, having dot products of more than 0.99.

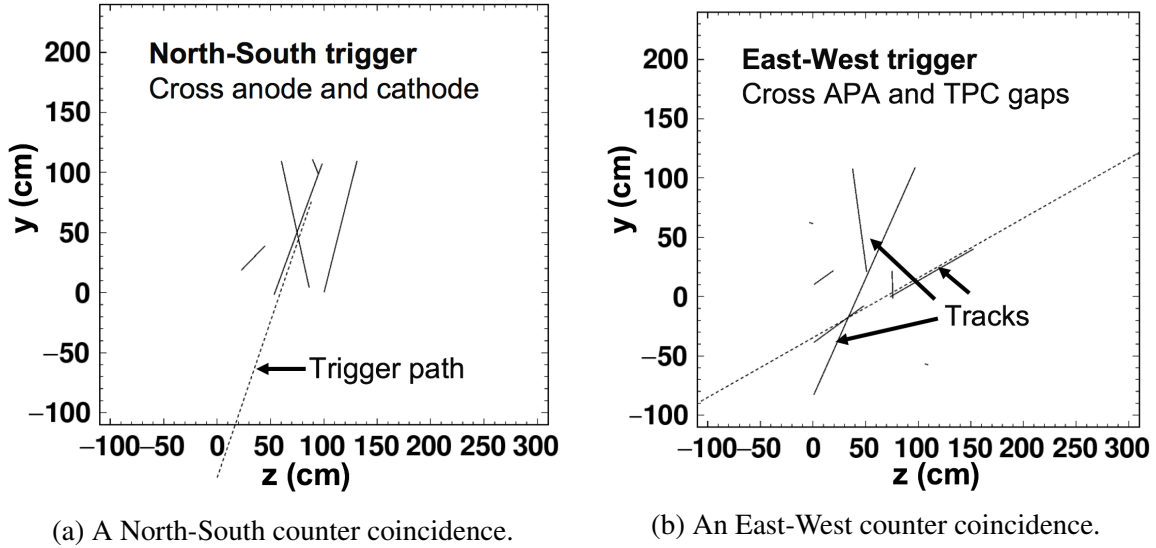


Fig. 5.11 The alignment of reconstructed tracks with the vectors joining the centres of the coincidence counters. The dashed lines show the vectors joining the centres of counters hit in the coincidence, whilst the solid lines show the reconstructed tracks. Left shows the alignment of tracks with a North-South coincidence, whilst right shows the alignment of tracks with an East-West coincidence. The z positions of the tracks are shown on the x axis, and the y positions of the tracks are shown on the y axis. Figures taken from [113].

By matching tracks in this way it is possible to evaluate the reconstruction efficiencies for these muons, at increasing drift distances and track angles. If multiple tracks are aligned with the coincidence, and are within the expected time region, then their track lengths are summed when calculating reconstruction efficiencies. This is because, it is expected that the track was split by a region of the detector either being turned off, or being too noisy to reconstruct a track. If these tracks have a combined track length of more than 50 cm, then the coincidence is identified as having been successfully reconstructed. This threshold is much lower than the true track length which should be reconstructed (more than 150 cm), but few particles are fully reconstructed in the data, and so a compromise is made to achieve a large enough sample of tracks upon which analyses can be performed. A reconstructed track that is 50 cm long is likely to have a large number of hits on collection plane wires that are not noisy, and it is these hits which are required when calculating purity or measuring the effect of diffusion, as discussed in Section 5.5. A track with length more than 50 cm is also likely to have been stitched between TPCs, due to the geometry of the 35 ton and track trajectories. The demonstration of stitching tracks between TPCs was a design goal of the 35 ton, and so identifying tracks where this was achieved satisfies that goal.

An important concept that must be introduced before these reconstruction efficiencies can be described is that of a “counter difference.” The “counter difference” of a coincidence and its associated tracks, is defined as the absolute difference between the counter numbers of the East and West counters that were hit. As such, the “counter differences” of the coincidences shown in Figure 5.10, are 2, 3 and 6 for the black, red and blue coincidences respectively. Given the orientation of the counters, the rarest counter difference will be 9, as only particles which hit counters (E_0 and W_9) and (E_9 and W_0) will have a counter difference of 9. In contrast to this, the most common value for the counter difference is 1, as there are many possible combinations of East and West counters being hit to give this counter difference. In the discussions below “counter difference” is occasionally referred to as “delta counter” or “ Δ counter.” The approximate angles which tracks, with given counter differences, have relative to the APA frames, is shown in Table 5.1.

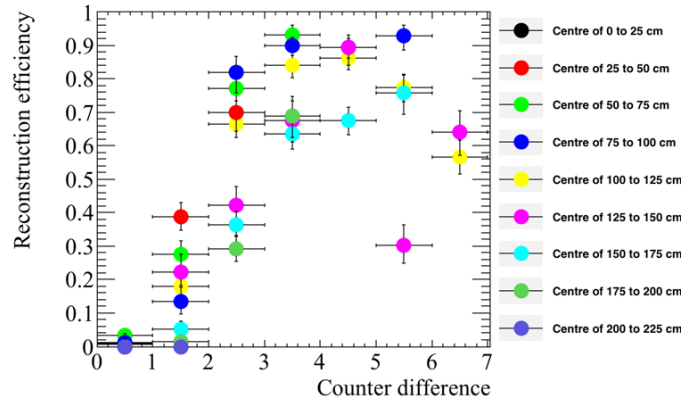
Figure 5.12 shows a range of reconstruction efficiency plots for combinations of different counter differences, and different drift distances. As the counter coincidences with large counter differences will have large variations in drift positions, the drift distance plotted here is the average x position of the counter centres that were hit. For example, if the two counters that produced the coincidence are at $x = 10$ cm and $x = 230$ cm respectively, then the drift distance plotted would be 120s cm. This distance is called the “coincidence centre” in the

Table 5.1 The angles which tracks, with given counter differences have, relative to the APA frames. Though the East and West counters have a width in the y (vertical) direction, this is much less than their extent in the z direction. The depth of the counters, their extent in x , is negligible compared to the separation of the East-West counters. The counters have identical widths in both the y and z directions. The angles are calculated using the difference in the centres of the counters in the z direction divided by the separation of the East and West counters in z .

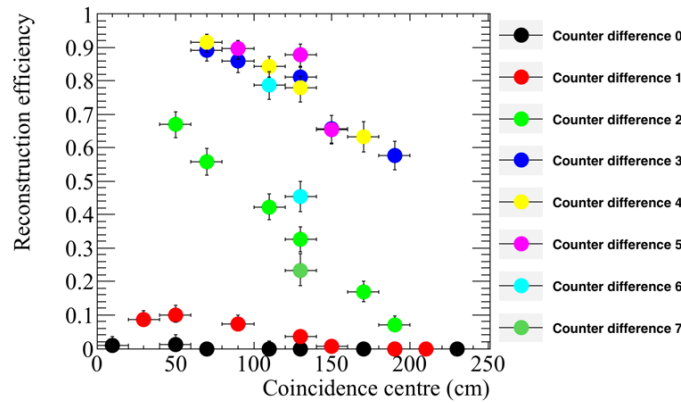
Absolute counter difference	Approximate angle ($^{\circ}$)
0	0 ± 2.1
1	4.2 ± 2.1
2	8.4 ± 2.0
3	12.5 ± 2.0
4	16.5 ± 2.0
5	20.3 ± 1.9
6	23.9 ± 1.8
7	27.3 ± 1.7
8	30.7 ± 1.6
9	33.5 ± 1.5

following discussion. Only coincidences which would produce tracks that are contained within the long drift volume are considered here, hence there being no negative x positions.

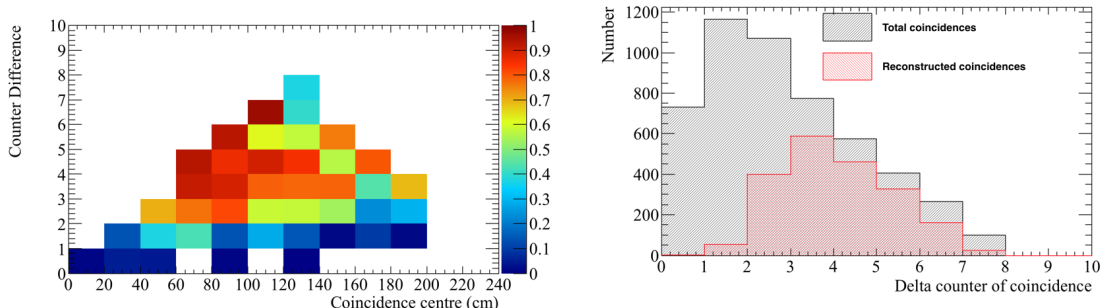
From Figure 5.12a, it is evident that the reconstruction efficiency for tracks with shallow angles relative to the APAs is extremely poor, with the efficiency for tracks aligned with counter differences of 0 or 1 never rising above 10%. This is due to the coherent noise removal, where hits which are correlated in time will be removed as they will be perceived as being noise, as opposed to real signals. As the difference in counter number increases, the efficiency is seen to increase, though the rate of this increase is seen to depend on the “coincidence centre”. The effect of increasing “coincidence centre” can be seen more clearly in Figure 5.12b, where the efficiency for each counter difference as a function of “coincidence centre” is plotted. Here, it can be seen that the reconstruction efficiency decreases for coincidences that are centred further away from the APAs. This is due to the fact that when an energy deposition has further to drift, it will induce a smaller pulse on the wires, meaning that it is more likely to be below the hit threshold. Figure 5.12c combines Figures 5.12a and 5.12b, to show how the reconstruction efficiency for increasing “coincidence centre” changes, with increasing counter difference. It can be seen that tracks with counter differences of between 3 and 5, where the “coincidence centre” is between 60 cm and 140 cm away from the APAs, are the best reconstructed coincidences. Finally,



(a) The reconstruction efficiency as a function of counter difference for different coincidence centres.



(b) The reconstruction efficiency as a function of coincidence centres for different counter differences.



(c) How the reconstruction efficiency changes for increasing coincidence centres and counter differences.

(d) The number of events for each counter difference that were recorded in the data and the number of those which were successfully reconstructed.

Fig. 5.12 The reconstruction efficiencies for coincidences that trigger an East-West coincidence in the 35 ton data over a 2 day running period.

Figure 5.12d shows how the frequency of coincidences of a given counter difference occurs, compared to how many events contain reconstructed tracks which are aligned with the coincidence. It can be seen that, as stated earlier, the most common counter difference is 1, with the least common being a counter difference of 9. However, given the low reconstruction efficiency seen for the lowest counter differences, few tracks are reconstructed. This means that when considering the reconstructed tracks, most are due to coincidences with counter differences of either 3, 4 or 5.

5.5 Measuring interaction times using electron diffusion

As electrons drift from the interaction point to the wire planes they become spread out in both time and space, this effect is known as diffusion, and is an important property of electron transport in LAr, which must be well understood. The mechanism by which diffusion occurs in LAr was first discussed in [118–121], and has since been developed to consist of a complete set of measurements for electric fields between 100 and 2000 V cm⁻¹ [122]. The diffusion of electrons is rarely isotropic, and so the component that is transverse to the drift field, and the component that is parallel to the drift field, are normally measured separately. Diffusion parallel to the drift field is called longitudinal diffusion, and is generally smaller than the component of diffusion that is transverse to the drift field. Figure 5.13 shows how diffusion can smear the electrons collected on a set of wires when the electrons are initially highly correlated in time and space.

Longitudinal diffusion has the effect of spreading the drifting electrons out in time, causing signals to become wider in time, and smaller in height, as the total charge is conserved. The increasing hit width can be measured for increasing drift times (distances), provided the hits do not fall below a hit finding threshold. Transverse diffusion causes drifting electrons to spread out in space, changing the amount of charge deposited on a wire, and reducing the charge resolution of the detector. Transverse diffusion is measured by discerning how the width of the hit charge distribution changes for increasing drift distances [122].

Through-going particles make ideal tracks to study diffusion as they are minimally ionising, and so have roughly constant energy depositions along their tracks. The tracks that they produce can also cover a wide range of drift distances, if they are not parallel to the APAs. The drift distances of hits within a track can be determined by matching the track with a counter coincidence as discussed at the end of Section 5.4. The *x* positions of the hits can

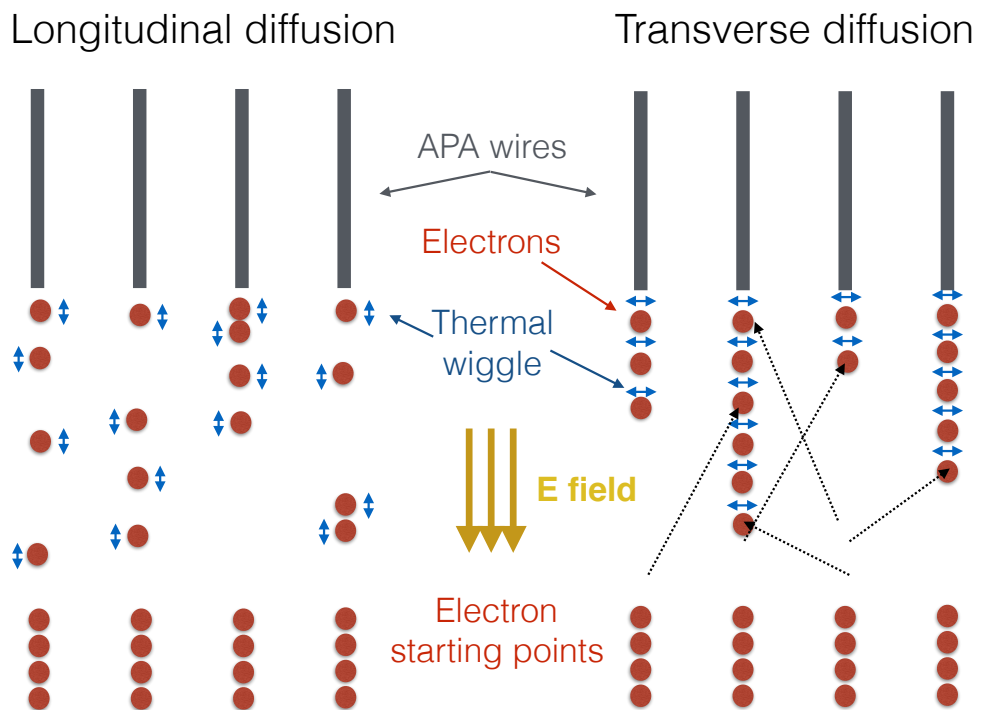


Fig. 5.13 A schematic showing the longitudinal diffusion (left), and the transverse diffusion (right), of electrons. In both cases, four electrons are initially shown below four wires, and are allowed to diffuse in either the drift direction, or perpendicular to the drift direction, in the longitudinal and transverse cases respectively. It can be seen that the effect of diffusion is to make the electrons spread out in time, in the case of longitudinal diffusion, and to spread out in space, in the case of transverse diffusion. Figure taken from [123].

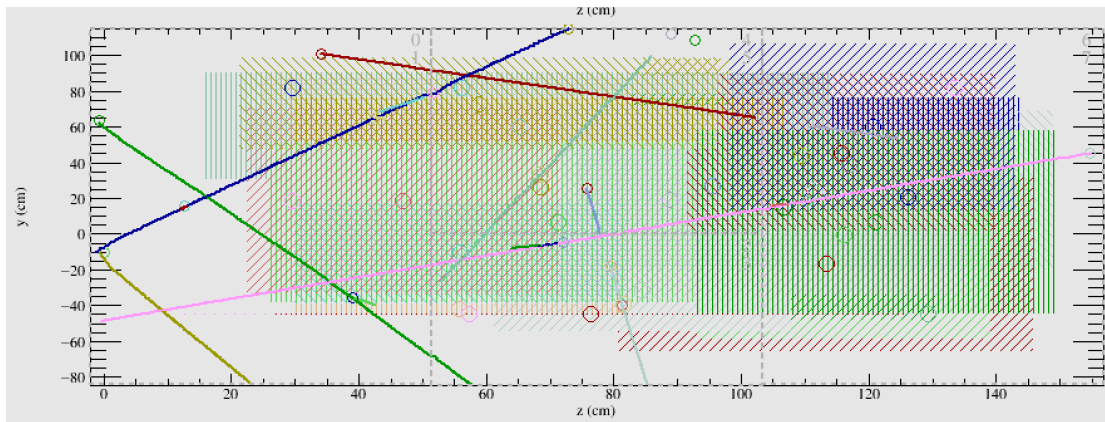


Fig. 5.14 A simulated event display showing multiple tracks and flashes to be assigned to each other in the 35 ton, in the yz plane. The coloured lines represent reconstructed tracks, whilst the coloured dashed boxes represent flashes.

then be corrected using the result of Equation 4.2, in Equation 4.1.

Traditionally the only way to determine an interaction time for a track is to either match it to an external calibration source, such as whether it aligns with an external counter coincidence, or to match it to a flash of scintillation light, as in Section 4.1. These techniques are particularly crucial for neutrino detectors on the Earth's surface, such as MicroBooNE, where each neutrino interaction usually has a background of at least one cosmic muon. The reconstructed tracks from this muon background have to be distinguished, from those due to the neutrino interactions, in order correctly assign a scintillation flash to the reconstructed tracks. An event where scintillation flashes and cosmic muons need to be correctly distinguished is shown in Figure 5.14. However, it may be possible that the change in hit width due to diffusion, as a particle travels through the detector, could be used to determine the interaction time; though this has not been attempted before. To study whether this is possible, the effects of diffusion would have to be measured for a sample of tracks with known interaction times and orientations.

The 35 ton dataset is ideal for testing this hypothesis, as the counters are able to provide a sample of tracks with known angles and interaction times, which can be used to tune interaction time determination metrics. These metrics can then be applied to another sample of tracks, where the interaction time is known but not used, so that the accuracy of the calculated interaction times can be found. As longitudinal diffusion is the dominant effect that increases the hit width, transverse diffusion will not be directly considered further. However, as noted in Section 5.4, the noise level in the 35 ton data causes reconstruction

issues, and so it is also useful to compare the method against a low noise detector. Monte Carlo can provide this sample, and this comparison is shown in Section 5.5.2. It is also useful to observe the effects that different detector conditions such as, the electric field, the electron lifetime, the noise level and the rate of diffusion, have on the method. This is shown in Section 5.5.3. First though, the method is performed on the 35 ton dataset.

5.5.1 Determining interaction times in 35 ton data

When calculating the determination metrics, only hits on wires which are not noisy want to be considered. This is because wires with a high level of correlated noise observe hits with a wider RMS. This is shown in Figure 5.15, where, when a baseline noise of 10 ADC counts is added to a simulated hit, with a peak value of 50 ADC counts, and an RMS of 10 ticks, the width increases by over 10%. Hits with delta rays also need to be removed, as the deposited energy will be larger and over a longer period of time than hits from the main track. This will make the RMS of the individual hit wider, and also increase the width of the charge distribution for the track. To remove these hits only hits which satisfy the following cuts are used:

- No hit on the same wire within 50 ticks of the hit in question. This removes delta rays.
- No more than 10 hits on the same wire in the whole 15,000 tick data sample. This removes clearly noisy wires.

These cuts will clearly become much more restrictive as the noise level in the detector increases, but they are essential in order to produce a dataset which is not overpowered by noise. Only collection plane hits are used, as the charge resolution is better, and the signals are unipolar as opposed to bipolar, meaning that a Gaussian function can be easily fitted to the signals. Additionally the *signal/noise* ratio on the collection planes was much higher than on the induction planes for the 35 ton dataset, and so the hits could be much more reliably reconstructed.

Diffusion is a track angle dependent property, and so track angle ranges have to be considered independently. To minimise the number of figures presented, when graphs are made for all counter differences separately, only graphs made for tracks which have a counter difference of 4 are shown. However, the procedure for predicting interaction times is identical for tracks of all counter differences. Tracks with a counter difference of 4 were chosen as they were one of the angles for which tracks were well reconstructed in the data, see Figure 5.12. Tracks are considered en masse, and so the hits for every track are separated into 10 cm

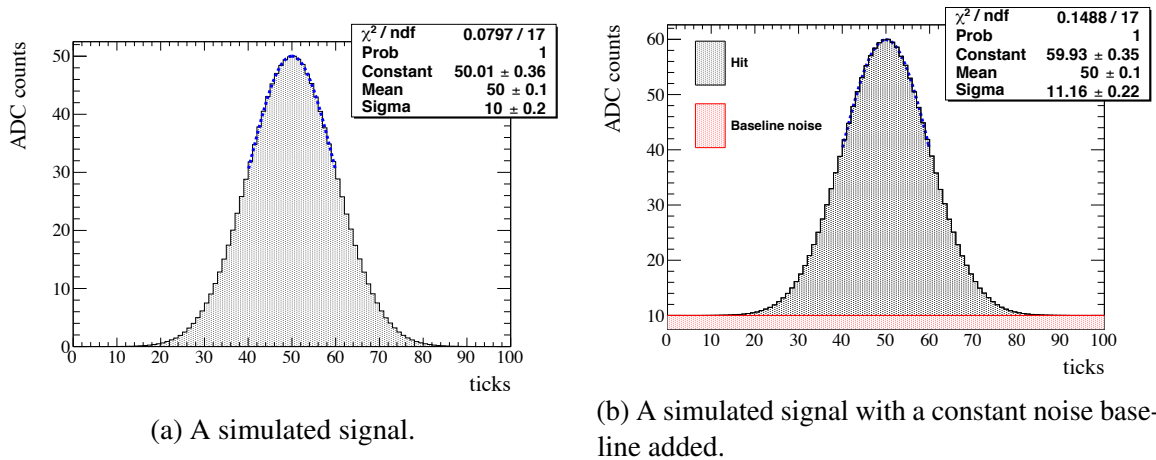


Fig. 5.15 ADC counts as a function of time for simulated signal with a width of 10 ticks, and an amplitude of 50 ADC counts, both before and after, a constant noise baseline of 10 ADC counts is added. The simulated ADC value is shown on the y axis, and the time, in ticks, is shown on the x axis. In reality the noise would fluctuate with time. When a Gaussian function is fitted to each signal, it is seen to be more than 10% larger for the signal where the noise baseline is added. This shows that noise can cause the measured width of a hit to increase. Figure taken from [123].

regions of increasing drift distance from the APAs. The following quantities are calculated for each 10 cm drift region:

- The hit *RMS* - the most direct way to measure transverse diffusion.
- The hit *RMS/Charge* - an attempt to incorporate the effect of impurities in the LAr for relatively low purity data which will have a drift distance dependence.
 - The charge of a hit is calculated by integrating the ADCs of the reconstructed hit over time.

Fitting Gaussian functions around the peaks of the distributions will yield the most probable values for the drift regions, as is shown in Figure 5.16.

From Figure 5.16 it is clear the the width of the hit *RMS* distribution increases for hits which are further from the APAs. However, the width of the hit *RMS/Charge* is seen to decrease, though this is due to a sharp cut-off at a hit *RMS/Charge* equal to roughly $0.038 \text{ ticks ADC}^{-1}$. The reason for this cut off was shown in Figure 5.8. It can also be seen that the most probable values of both the hit *RMS* and hit *RMS/Charge* increases with drift distance.

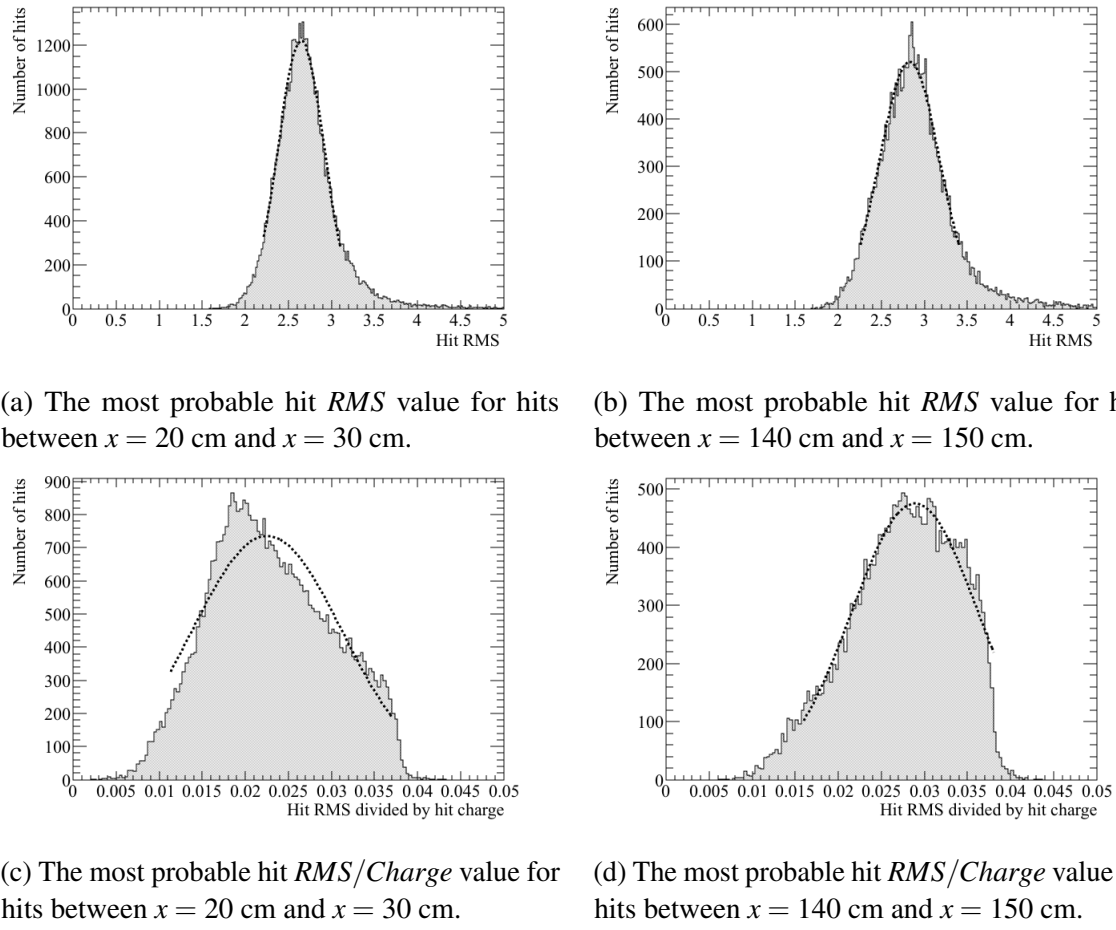


Fig. 5.16 The distributions of hit RMS (top), and hit $RMS/Charge$ (bottom), for points between 20 and 30 cm from the APAs (left), and points between 140 and 150 cm from the APAs (right), for tracks associated with coincidences that have a counter differences of 4. The most probable values hit RMS and hit $RMS/Charge$ are determined by fitting Gaussian functions around the peaks of the distributions. These fits are shown as dashed lines.

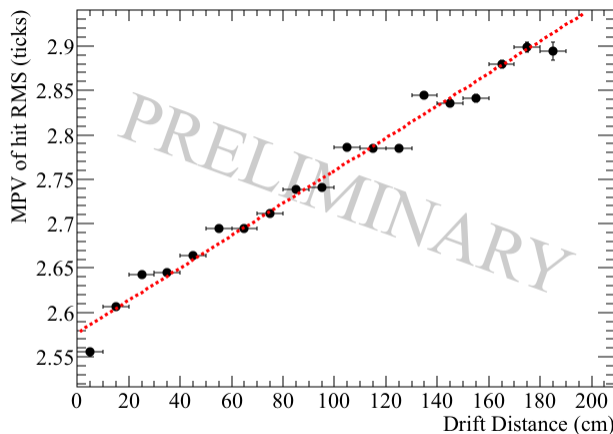


Fig. 5.17 The most probable values of hit RMS as a function of drift distance, for the hits within a track, associated with a coincidence that had a counter difference of 4.

This drift distance effect can be observed by plotting the most probable values of hit RMS and hit $RMS/Charge$, as drift distance increases, for fixed counter differences. This drift distance dependence on hit RMS is shown in Figure 5.17, for tracks that are associated with a coincidence which had a counter difference of 4. A drift distance dependence can clearly be seen in the data, as the most probable hit RMS is seen to increase for hits which originate further from the APAs.

The angular dependence can then be shown by observing how the most probable fit values at a drift distance of 0 cm changes for increasing angles, this is shown in Figure 5.18. It is clear that there is an angular dependence on the hit width, as the most probable hit widths next to the APAs is seen to rise for tracks associated with coincidences with large counter differences. This angular dependence, along with the drift distance dependence show that when considering a large sample, diffusion can be separated into distance and angular dependencies. However, whether this can be observed for individual tracks, has not yet been considered.

To consider single tracks, the best line fits for the counter differences for a large sample of tracks, such as in Figure 5.17, are required. These best line fits can then be used to predict the position you would expect a hit to originate from, given values for the hit RMS and hit $RMS/Charge$, and the angle of the track to which it belongs. The predicted positions can then be compared to the known position from the counter coincidence to determine the accuracy of the prediction.

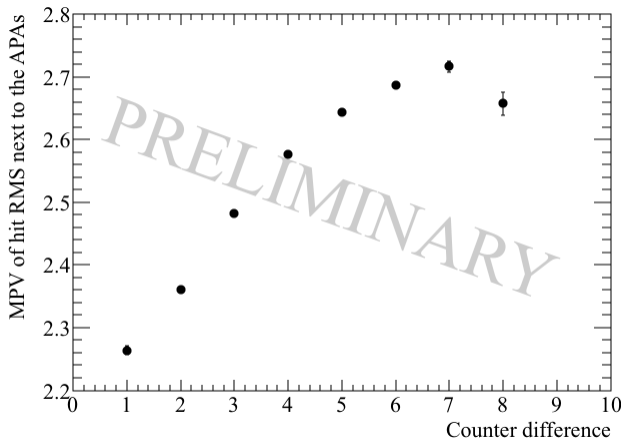


Fig. 5.18 The most probable values of hit *RMS* within 10 cm of the APAs, as a function of the counter difference of the coincidence, that the track, to which the hits belong, was associated with.

The distributions shown in Figure 5.16 are asymmetric due to some hits having large values of hit *RMS* or hit *Charge*. Asymmetry is also introduced due to the thresholding of the hits with the lowest hit charges, this comes about as a result of the elevated hit threshold, required to minimise the number of reconstructed noise hits, as shown in Figure 5.8. Whilst nothing can be done retrospectively concerning the omission of the lowest charge hits, the highest charge hits, which cause the tails at low hit *RMS/Charge*, can be removed. This can be done by not using hits which are in the tails of the hit *Charge* distribution. The tails of the distributions are removed by considering a plot of normalised hit charge, whereby the most probable hit charge has a value of 1. A conservative cut on normalised hit charges of 0.25 is made, so that it can be guaranteed that the tails are removed. This is shown in Figure 5.19, and means that any hits with charges less than ~ 65 ADC, and any hits with charges more than ~ 170 ADC are not used. This will have the effect of removing some of the low charge hits which were reconstructed, but the main effect will be the removal of the significant number of high charge hits, which introduce the tail at low hit *RMS/Charge*. This is shown in Figure 5.16. The difference in the predicted and reconstructed hit times should then be centred around the interaction time, and be distributed much more uniformly. This will mean that the interaction time can be determined much more accurately.

An intrinsic assumption in this method is that the track has a large number of collection plane hits, which do not contain delta rays, and are on wires which would not be identified as noisy. The tracks being considered here will have crossed all *z* values in the detector, meaning that a total of 336 collection hits could potentially be reconstructed. Given the reconstruction

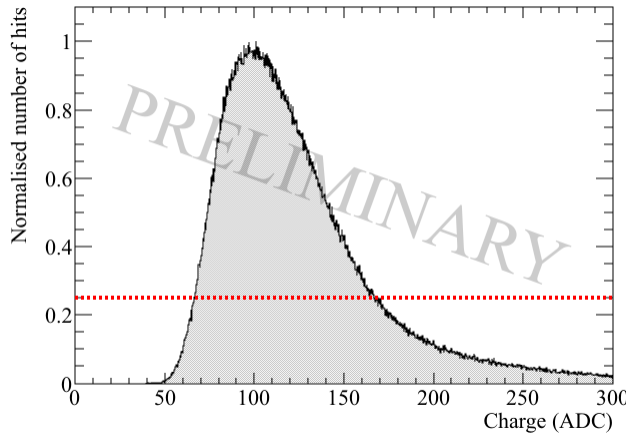


Fig. 5.19 The distribution of normalised hit charge, shown in units of ADC, in the 35 ton dataset. The number of hits with the most probable hit charge has been normalised to a value of 1. A cut on the normalised number of hits being greater than 0.25 is shown, the aim of this cut is to remove the tails of the hit charge distribution.

problems in the 35 ton detector, very few tracks will have hits on all of these collection wires. However, requiring at least 100 collection plane hits is not unreasonable, and would correspond to a reconstructed track length of at least 50 cm. The difference between the predicted and reconstructed hit time for each hit is shown in Figure 5.20, for both the hit *RMS* and hit *RMS/Charge* metrics.

Figure 5.20 shows that both distributions are centred around a time difference of 0 μs in the 35 ton dataset. This is encouraging as it shows that the method has potential. The width of the distribution for the *RMS/Charge* metric is smaller, and the peak larger, so it is expected that this will provide the more robust metric. This is because these features show that the predicted hit times are likely to be close to the reconstructed hit times. The peaks are centred around a time difference of 0, as the hit times had previously been corrected using the measured interaction time from the counter coincidence. This was done so as to avoid the uncertainty which would arise from allowing the coincidences to remain at random times between ticks 5000 and 6000, in the 15000 tick event. For an explanation as to why this occurs, see the discussion concerning Figure 5.2.

When evaluating interaction times the average difference in reconstructed and predicted hit times across every hit on the track must be considered. This is shown in Figures 5.21 and 5.22, where, as expected from Figure 5.20, the *RMS/Charge* metric provides a better estimation of the interaction time. The reason for this is that by utilising the charge informa-

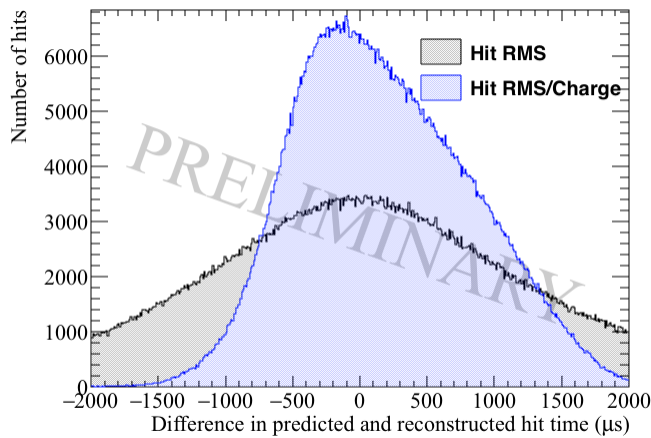
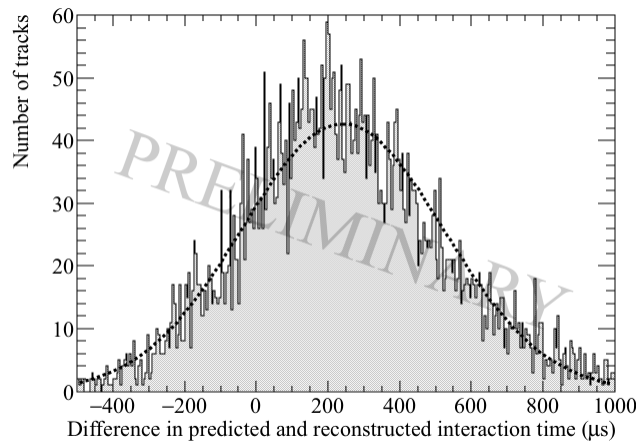


Fig. 5.20 The difference between the predicted and reconstructed hit times in the 35 ton dataset. The differences in time when the hit *RMS* metric is used are shown in black, whilst the differences in time when the hit *RMS/Charge* metric is used are shown in blue.

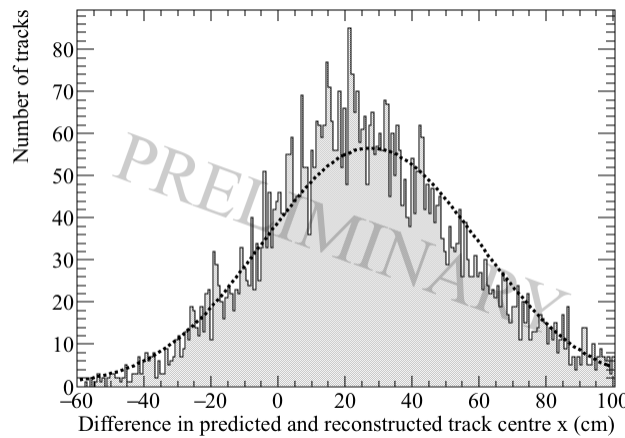
tion due to losses from impurities, this metric gains an extra handle on the drift distance, and hence the reconstructed time of the hits. The losses due to impurities are difficult to measure in high-purity LAr environments, as the decrease in collected charge with increasing drift distances is small [124]. The effect of increasing LAr purity is shown in Section 5.5.3. Using the change in hit charge in the 35 ton may have a drawback though, because, as shown in Figure 5.8, there is a threshold effect for hits with large drift times. However, as the same threshold effect is present in all 35 ton data samples, the limitation it introduces is mainly in the efficiency with which 'good' collection plane hits will be reconstructed, and so this information can be confidently used.

Figure 5.21 shows that using the effects of diffusion, and the hit *RMS*, the interaction time and central *x* position of a track, can be reliably predicted in the 35 ton dataset. The accuracy in determining the interaction time is found to be 240 μ s, where the distribution has a FWHM of 281 μ s. When this is converted into the difference in central *x* position of the track, the accuracy is found to be 27.7 cm, with a FWHM of 32.1 cm.

Figure 5.22 shows that using the effects of diffusion, and the hit *RMS/Charge*, the interaction time and central *x* position of a track, can be reliably predicted in the 35 ton dataset. The accuracy in determining the interaction time is found to be 171 μ s, where the distribution has a FWHM of 210 μ s. When this is converted into the difference in central *x* position of the track, the accuracy is found to be 18.5 cm, with a FWHM of 23.0 cm.

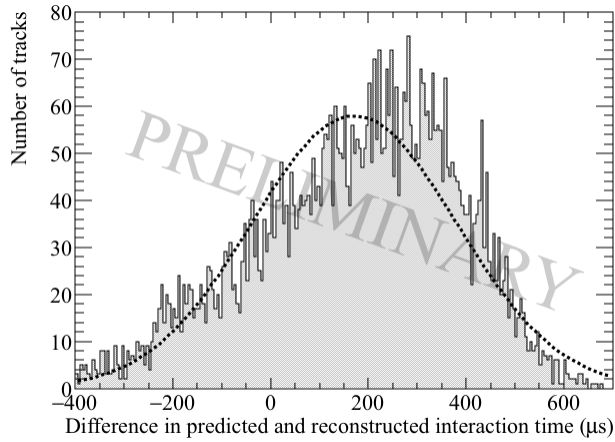


(a) The average difference in interaction times using the hit *RMS* metric.

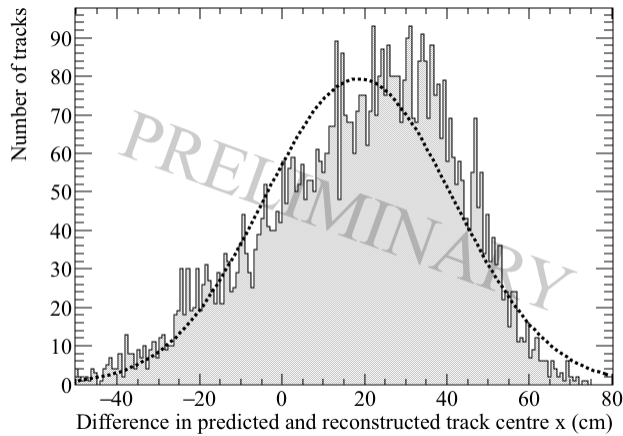


(b) The average difference in the central x position of a track using the hit *RMS* metric.

Fig. 5.21 The accuracy of the hit *RMS* method in the 35 ton dataset. Top shows the accuracy to which interaction times can be determined in μs . Bottom shows the accuracy to which the central x position of a track can be determined. Gaussian functions are fitted to the distributions so that any offset in the predicted times or positions can be discerned.



(a) The average difference in interaction times using the hit *RMS/Charge* metric.



(b) The average difference in the central x position of a track using the hit *RMS/Charge* metric.

Fig. 5.22 The accuracy of the hit *RMS/Charge* method in the 35 ton dataset. Top shows the accuracy to which interaction times can be determined in μs . Bottom shows the accuracy to which the central x position of a track can be determined. Gaussian functions are fitted to the distributions so that any offset in the predicted times or positions can be discerned.

The resolutions found are quite impressive, as given that the total drift time for electrons through the whole 35 ton detector volume of 250 cm is roughly 5200 ticks, it means that tracks can be cleanly distinguished throughout the detector volume. Though the resolution of the interaction time determination is impressive, it is concerning that there appears to be a systematic offset which has been introduced. This is seen by the distributions not being centred around a difference in predicted and reconstructed times of 0 μs , as would be expected from the discussion concerning Figure 5.20. As discussed earlier, the issues with noise in the 35 ton dataset affect the accuracy with which tracking and calorimetry can be performed, and so it is reasonable to expect that the effectiveness of the interaction time determination was also affected. Therefore, it is prudent to repeat the study on a Monte Carlo sample, with the same detector conditions, but a much lower level of detector noise. This is presented in Section 5.5.2.

5.5.2 Determining interaction times in a low-noise detector using Monte Carlo, and differences with data

When determining interaction times in Monte Carlo simulations, exactly the same criteria are applied to the hits. This is because δ -rays would still change the measured hit width, and will be present in any sample. In a low noise detector it is expected that few wires would be removed due to being noisy, but for consistency there is no danger in applying this cut. Imposing a minimum number of collection plane hits is again important to ensure that the distribution of predicted hit times is centred on the interaction time. In addition to the same criteria being imposed on which wires are used, the same metrics are calculated. In all plots shown below the Monte Carlo dataset has been normalised to the size of the 35 ton dataset. This was done so that the area of the plots shown was the same, enabling easier comparison between the two datasets.

Figure 5.23 shows both the hit *RMS* and hit *RMS/Charge* distributions, for hits from tracks that are associated with a coincidence that has a counter difference of 4, and are between 20 cm and 30 cm away from the APAs, or between 140 cm and 150 cm from the APAs. It can be seen that there is a large difference in the distributions for hits which are relatively close to the APAs, at distances between 20 cm and 30 cm. The distributions are also much more tightly distributed in the Monte Carlo sample, showing that the variation between hits is much smaller. However, the difference between the Monte Carlo and 35 ton data samples are much smaller at large drift distances, showing that at large distances the

distributions become much more varied. An important feature of the 35 ton data sample, which is not present in the Monte Carlo sample, is the sudden cut off in values of high hit *RMS/Charge*. This was briefly discussed in the consideration of Figure 5.16, but it is much clearer in Figure 5.23d, where the rapid decrease in the number of hits with values of hit *RMS/Charge* which are more than 0.038 ticks ADC^{-1} seen in the 35 ton dataset, is not repeated in the Monte Carlo sample. This, along with Figure 5.8, shows clear evidence that the hits with low values of hit *charge* are not reconstructed in the 35 ton data sample.

The most probable values of hit *RMS* at increasing drift distance are shown in Figure 5.24, where the Monte Carlo simulation is again shown with the values from the data. As was seen when considering the distributions at specific distances and counter differences, the most probable values of hit *RMS* in the Monte Carlo simulation is systematically lower than in the data. This is attributed to the elevated noise level seen in the data, because, as seen in Figure 5.15, when a noise base-line is added to a signal, the width of the signal increases. Another difference between the Monte Carlo and the data, is that the gradient of the most probable values of hit *RMS* in data is roughly half of that in the Monte Carlo. This could be due to an overestimation of the effect of longitudinal diffusion in the Monte Carlo sample, or, it could be due to the larger hit widths seen in the dataset at low drift distances, causing the effects of diffusion to be less apparent. Evidence for the latter can be seen in the stark differences between the figures in Figure 5.23 at relatively short drift distances, compared to the similarities seen at large drift distances, where it appears that the Monte Carlo accurately simulates the distributions seen in the 35 ton dataset.

The most probable value of hit *RMS* at a drift distance of 0 cm for a range of counter differences is shown in Figure 5.25. The change in MPV of hit *RMS* can be seen to increase for both the Monte Carlo and 35 ton data samples, which again shows that the effects of diffusion can be seen to be track angle dependant. However, the way in which the MPV of hit *RMS* increases is different in the two samples. The increased MPVs of hit *RMS* seen in the 35 ton dataset, is again prescribed to the increase in hit width caused by the elevated noise level.

Upon calculating the fit metrics in the low-noise Monte Carlo dataset it is then possible to use these to predict track interaction times. However, it is first necessary to calculate the normalised hit charge distributions as was done for the 35 ton dataset. This is shown in Figure 5.26. It can be seen that there are hits with lower values of hit *charge* in the Monte Carlo sample, supporting the idea that there is a thresholding effect in the 35 ton dataset.

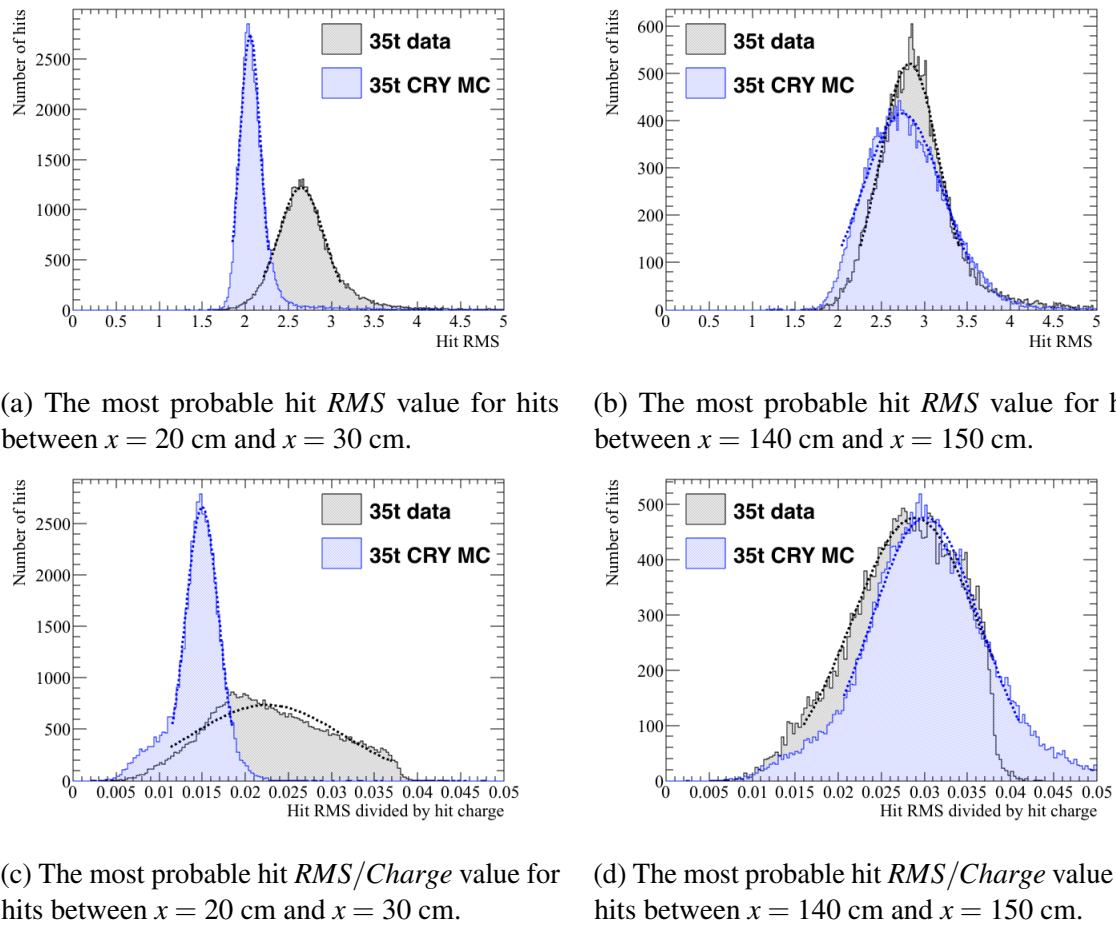


Fig. 5.23 The distribution of hit RMS (top), and hit $RMS/Charge$ (bottom), for points between 20 and 30 cm from the APAs (left), and points between 140 and 150 cm from the APAs (right), for tracks associated with coincidences that have a counter differences of 4. The most probable values hit RMS and hit $RMS/Charge$ are determined by fitting Gaussian functions around the peaks of the distributions. These fits are shown as dashed lines. The distributions for the 35 ton dataset are shown in black, whilst the distributions for the Monte Carlo simulation are shown in blue.

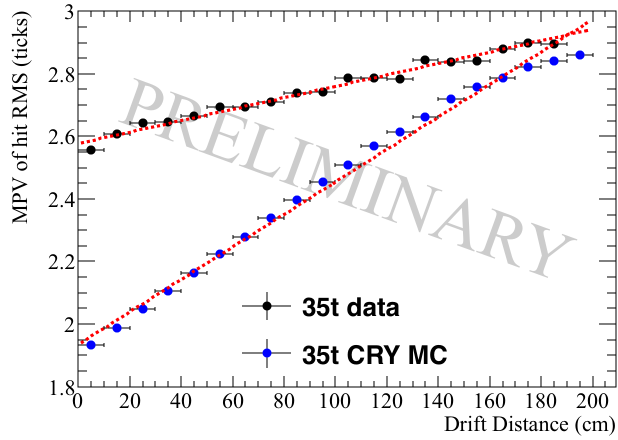


Fig. 5.24 The most probable values of hit *RMS* as a function of drift distance, for tracks associated with a coincidence that had a counter difference of 4. The distribution for the 35 ton dataset is shown in black, whilst the distribution for the Monte Carlo simulation is shown in blue.

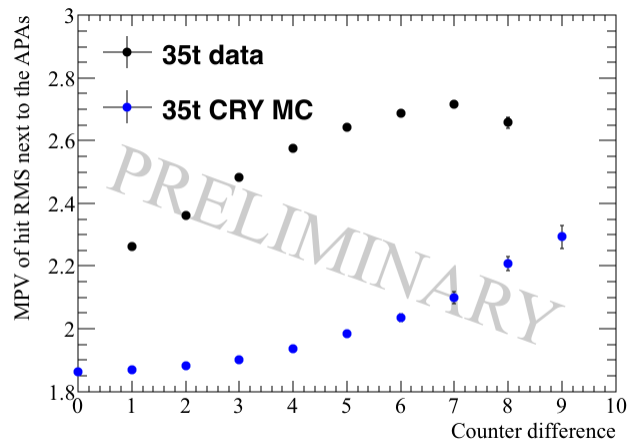


Fig. 5.25 The most probable values of hit *RMS* within 10 cm of the APAs, as a function of the counter difference of the coincidence, that the track was associated with. The distribution for the 35 ton dataset is shown in black, whilst the distribution for the Monte Carlo simulation is shown in blue.

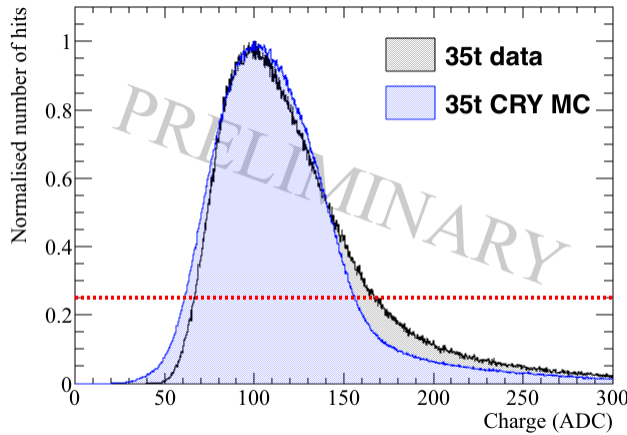
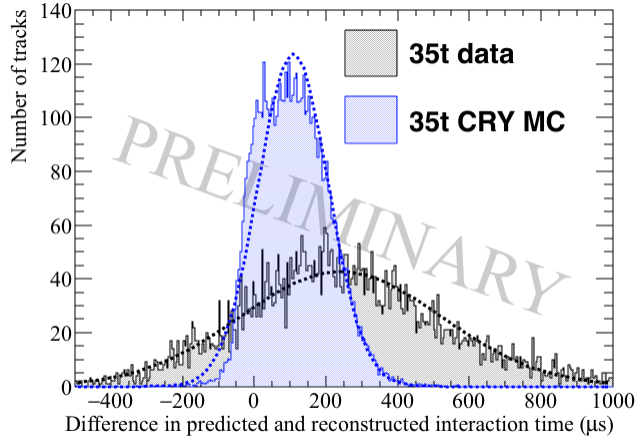


Fig. 5.26 The distribution of normalised hit charge, shown in units of ADC, in the 35 ton dataset and Monte Carlo sample. The number of hits with the most probable hit charge has been normalised to a value of 1. A cut on the normalised number of hits being greater than 0.25 is shown, the aim of this cut is to remove the tails of the hit charge distribution. The distribution for the 35 ton dataset is shown in black, whilst the distribution for the Monte Carlo simulation is shown in blue.

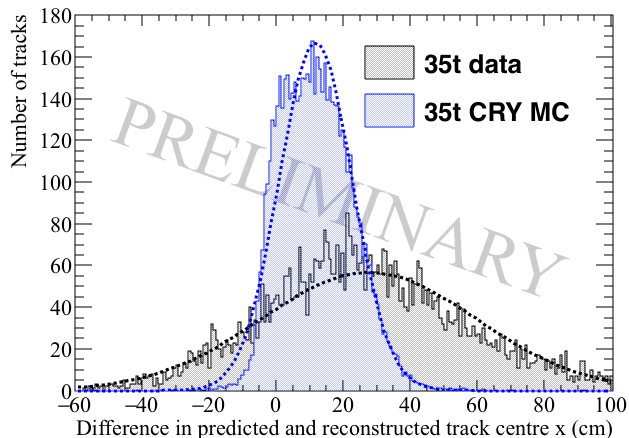
Importantly however, the aim of the cut to remove the tails of the hit *charge* distributions can be seen to be successful in both the 35 ton dataset and Monte Carlo sample, as hits with large value of hit *charge* are removed in both samples. The result of this will be that, the difference in predicted and reconstructed hit times, for a given track, will be centred on the interaction time of the track, as was presented in the discussion of Figure 5.19. The Monte Carlo hit times have been corrected using the time of the counter coincidence, as was the case for the 35 ton dataset.

Figure 5.27 compares how reliably the interaction time, and central *x* position of a track, can be predicted using the effect that diffusion has on the hit *RMS*, in the 35 ton dataset and a low-noise Monte Carlo sample. The accuracy in determining the interaction time in Monte Carlo (data) is found to be, 108 (240) μs , where the distribution has a FWHM of 98 (281) μs . When this is converted into the difference in central *x* position of the track, the accuracy is found to be, 11.8 (27.7) cm with a FWHM of 10.9 (32.1) cm.

Figure 5.28 compares how reliably the interaction time, and central *x* position, of a track can be predicted using the effect that diffusion has on the hit *RMS/Charge*, in the 35 ton dataset and a low-noise Monte Carlo sample. The accuracy in determining the interaction time in Monte Carlo (data) is found to be, -3 (171) μs , where the distribution has a FWHM



(a) The average difference in interaction times using the hit *RMS* metric.



(b) The average difference in the central x position of a track using the hit *RMS* metric.

Fig. 5.27 The accuracy of the hit *RMS* method in the 35 ton dataset and a Monte Carlo simulation. Top shows the accuracy to which interaction times can be determined in μs . Bottom shows the accuracy to which the central x position of a track can be determined. Gaussian functions are fitted to the distributions so that any offset in the predicted times or positions can be discerned. The distributions for the 35 ton dataset are shown in black, whilst the distributions for the Monte Carlo simulation are shown in blue

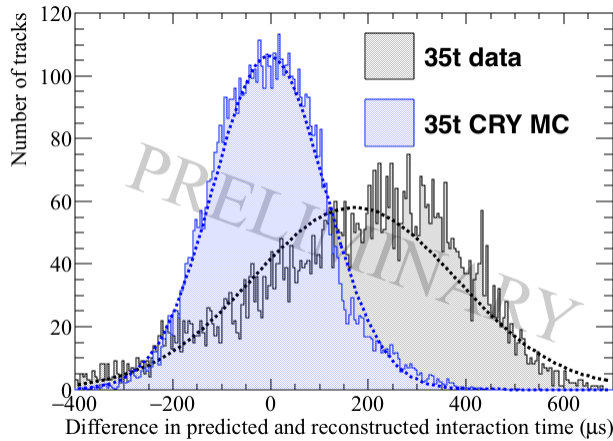
of 114 (210) μs . When this is converted into the difference in central x position of the track, the accuracy is found to be, -0.4 (18.5) cm with a FWHM of 12.6 (23.0) cm.

The hit $RMS/Charge$ metric appears to be able to more accurately predict interaction times, as was seen in when considering the only 35 ton dataset. This is again due to the ability to incorporate information about losses due to impurities, which increase with drift distance. Also, as expected from the previous figures and the lower noise state in the Monte Carlo, it is seen that the interaction times predicted in the Monte Carlo sample more closely match the true interaction times, than was the case with the predictions made in the dataset. An important feature to observe is that, as well as more accurately predicting the interaction times, the widths of the distributions in Monte Carlo are less than half of that in the data, particularly when using the hit RMS , as shown in Figure 5.27. This means that the resolution with which tracks can be distinguished in the Monte Carlo sample is much better than in the 35 ton dataset, again this is attributed to the lower noise level in the Monte Carlo.

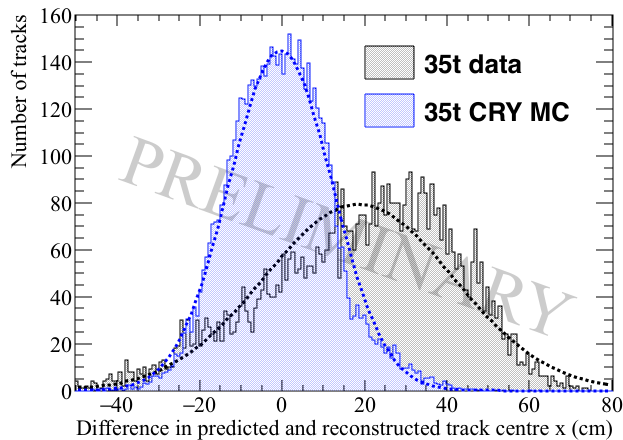
The calculation of interaction times is clearly much better in the low-noise Monte Carlo dataset, than in the 35 ton dataset. However, the distributions when using the hit RMS are still not centred around 0, implying that there is a systematic error in the method, which has not been removed when considering a low-noise environment. The cut applied on the normalised hit *charge* distribution was applied in order to remove the tails of the hit $RMS/Charge$ distribution, as seen in Figure 5.26. Given that Figure 5.28 shows that when using this metric, the predicted interaction times are centred on the reconstructed interaction times, this appears to have been successful. However, the analogous cut is not performed on the hit RMS distribution, and so this could explain the decreased accuracy using this metric.

It is also possible that some δ -rays have not been removed. This is because the only way to remove hits containing unseparated δ -rays, is to look for the slight dip in the raw signal, which is associated with the δ -ray beginning to separate from the main track. This would be almost impossible in the 35 ton dataset given the oscillatory nature of the noise. Were a cut on hit RMS to be applied, then these indistinguishable δ -rays would likely be removed. This is because hits with delta rays would lie in the high value tails of the hit RMS distribution, which the cut would remove.

The 35 ton dataset as a whole overestimates the interaction times though, and it is thought that this is due to elevated noise level. Justification for this assertion is discussed in Section 5.5.3 where the detector conditions of a simulated detector are varied. One of the detector



(a) The average difference in interaction times using the hit *RMS/Charge* metric.



(b) The average difference in the central x position of a track using the hit *RMS/Charge* metric.

Fig. 5.28 The accuracy of the hit *RMS/Charge* method in the 35 ton dataset and a Monte Carlo simulation. Top shows the accuracy to which interaction times can be determined in μs . Bottom shows the accuracy to which the central x position of a track can be determined. Gaussian functions are fitted to the distributions so that any offset in the predicted times or positions can be discerned. The distributions for the 35 ton dataset are shown in black, whilst the distributions for the Monte Carlo simulation are shown in blue

conditions which is varied is the noise level in the detector.

5.5.3 Discerning the impact of changing detector properties using Monte Carlo samples

Much has been made of the difficulty that the noise level in the 35 ton dataset introduces, when performing reconstruction and analysis of the data. It is necessary to verify this claim, and so a sample of Monte Carlo events with increasing noise levels is produced, and analysed below. The noise level in the Monte Carlo samples is increased from the low-noise state used in the previous section, to a level more similar to that which is seen in the 35 ton dataset. If the claim that the noise level made reconstruction more difficult is correct, then the accuracy with which the interaction time can be determined should be seen to anti-correlate with the noise level of the simulated detector. In addition to varying noise levels, the electron lifetime, the electric field, and the constant of longitudinal diffusion are varied. All samples have used the same initial muons, this is done so that the only difference between the different samples are the detector conditions. Only one detector condition is varied at a time, so that the effect of each detector condition can be studied in isolation. As only one detector property is changed between samples, there is one sample that is consistent to all sample sets. This is when the RMS of the noise is 2.5 ADCs, the electron lifetime is 3 ms, the electric field is 500 V cm^{-1} , and the coefficient of longitudinal diffusion is $6.2 \times 10^9 \text{ cm}^2 \text{ ns}^{-1}$. When presenting the studies with changing detector conditions, only the accuracy with which the interaction time, and central x position of a track, can be predicted is shown here. A more robust collection of figures can be seen in Appendix A.

Figures 5.29 and 5.30 show the effect that the increase in the noise level has on the accuracy to which the interaction time, and central x position of a track, can be determined.

Figures 5.31 and 5.32 show the effect that different electron lifetimes have on the accuracy to which the interaction time, and central x position of a track, can be determined.

Figures 5.33 and 5.34 show the effect that different electric fields have on the accuracy to which the interaction time, and central x position of a track, can be determined.

Figures 5.35 and 5.36 show the effect that different constants of longitudinal diffusion have on the accuracy to which the interaction time, and central x position of a track, can be

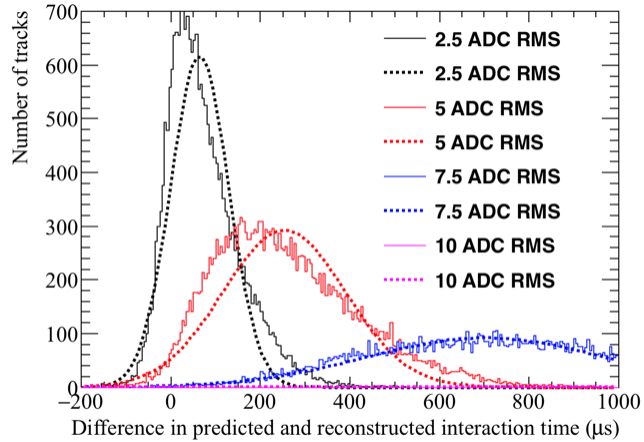
determined.

Figures 5.29 and 5.30 show the accuracy to which the interaction time, and central x position of a track, can be determined using the effect that diffusion has on the hit *RMS* and hit *RMS/Charge*, as the noise level in the detector changes. Figures 5.29 and 5.30 both show that the accuracy of the fits decrease with increasing noise levels, but they show this decrease in accuracy is manifested in different ways. As discussed in Section 5.3, the 35 ton data had significant amounts of coherent noise which was not expected, and so this had not previously been simulated. As this level of coherent noise is not expected in future detectors, coherent noise has not been simulated in these increased noise level samples. Instead, the electronics noise, or 'thermal noise,' has been varied. The lowest noise level was the design noise level for the 35 ton, and is what is used in the 'baseline' sample in the plots to follow. This level of thermal noise is very minimal, and so only noise levels which are more than this have been simulated. This is because the *signal/noise* ratio which one gets with such a low ADC RMS is large, and so a decrease in this noise level is unlikely to make a significant difference in the accuracy of the method. However, as can be seen in the 35 ton data, and the following plots, increasing the noise level has serious consequences.

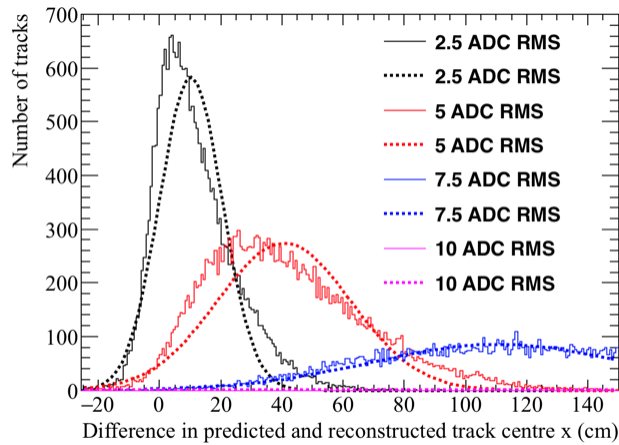
No noise mitigation algorithms have been applied to the increased noise samples shown here. Instead, the threshold that the hit finder uses has been increased to the level that was necessary for a reasonable number of hits to be reconstructed. A reasonable number of hits simply means, not reconstructing such a large number of noise hits that they outweigh the number of true signals from tracks. The hit threshold which was required was determined by looking at the deconvoluted signal, and choosing a threshold which was above the majority of the noise signals. The hit threshold used for each level are summarised below:

- Noise level of 2.5 ADC RMS - hit threshold of 6 ADC
- Noise level of 5 ADC RMS - hit threshold of 10 ADC
- Noise level of 7.5 ADC RMS - hit threshold of 15 ADC
- Noise level of 10 ADC RMS - hit threshold of 20 ADC

This means that the main effect of increasing the noise level is to remove the low charge hits, as they will fall below the hit threshold, as it is increased to compensate for the increased noise level.

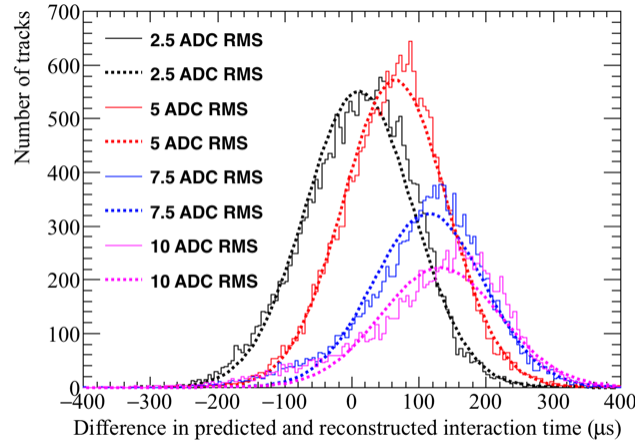


(a) The average difference in interaction times using the hit *RMS* metric.

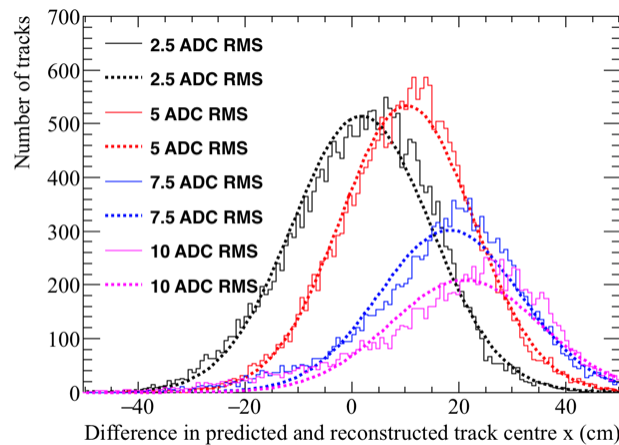


(b) The average difference in the central x position of a track using the hit *RMS* metric.

Fig. 5.29 The accuracy of the hit *RMS* method, for different electronic noise levels. Top shows the accuracy to which interaction times can be determined in μs . Bottom shows the accuracy to which the central x position of a track can be determined. Gaussian functions are fitted to the distributions so that any offset in the predicted times or positions can be discerned.

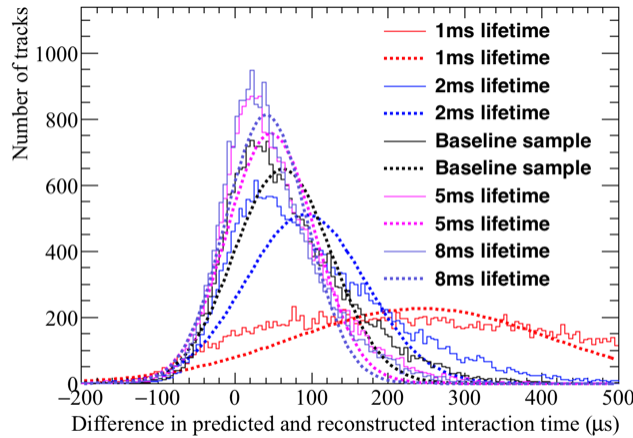


(a) The average difference in interaction times using the hit *RMS/Charge* metric.

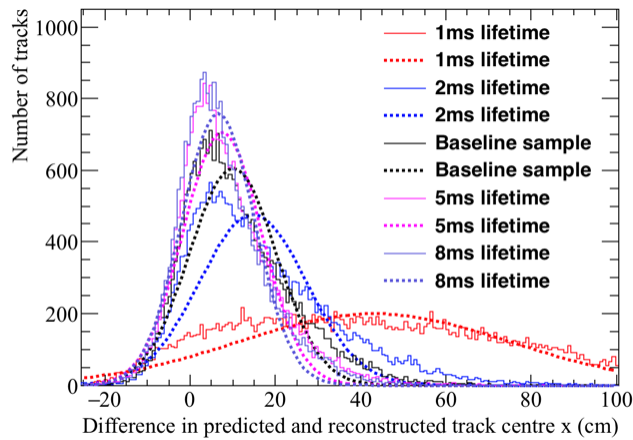


(b) The average difference in the central x position of a track using the hit *RMS/Charge* metric.

Fig. 5.30 The accuracy of the hit *RMS/Charge* method, for different electronic noise levels. Top shows the accuracy to which interaction times can be determined in μs . Bottom shows the accuracy to which the central x position of a track can be determined. Gaussian functions are fitted to the distributions so that any offset in the predicted times or positions can be discerned.

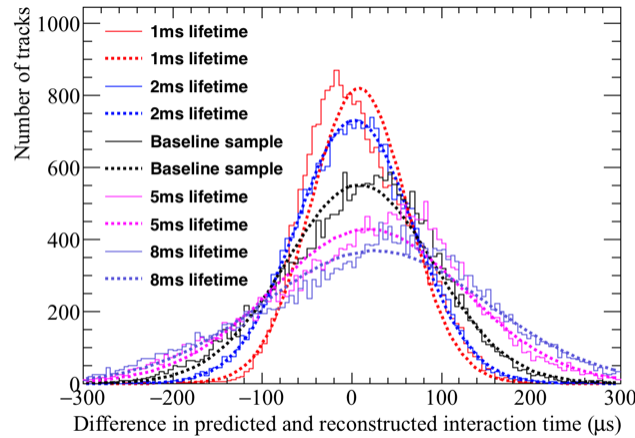


(a) The average difference in interaction times using the hit *RMS* metric.

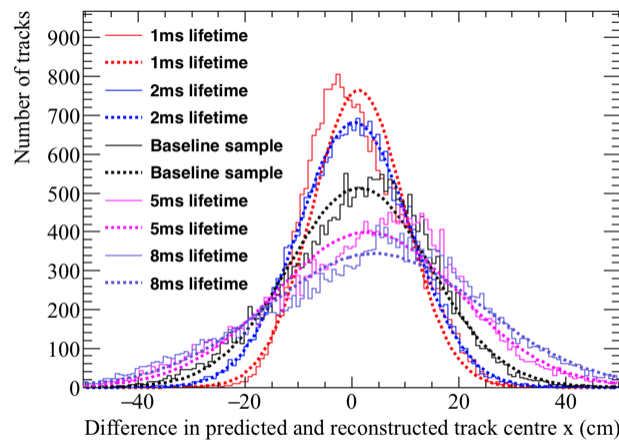


(b) The average difference in the central *x* position of a track using the hit *RMS* metric.

Fig. 5.31 The accuracy of the hit *RMS* method, for changing values of the electron lifetime. Top shows the accuracy to which interaction times can be determined in μs . Bottom shows the accuracy to which the central *x* position of a track can be determined. Gaussian functions are fitted to the distributions so that any offset in the predicted times or positions can be discerned.

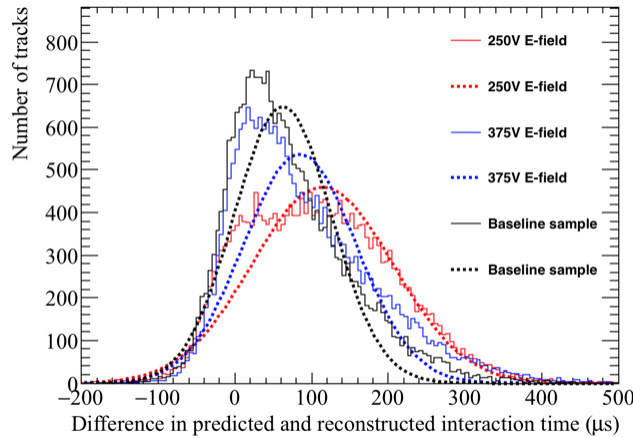


(a) The average difference in interaction times using the hit *RMS/Charge* metric.

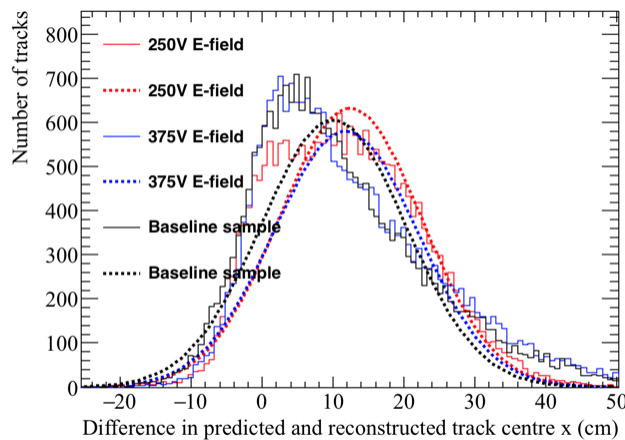


(b) The average difference in the central x position of a track using the hit *RMS/Charge* metric.

Fig. 5.32 The accuracy of the hit *RMS/Charge* method, for changing values of the electron lifetime. Top shows the accuracy to which interaction times can be determined in μs . Bottom shows the accuracy to which the central x position of a track can be determined. Gaussian functions are fitted to the distributions so that any offset in the predicted times or positions can be discerned.

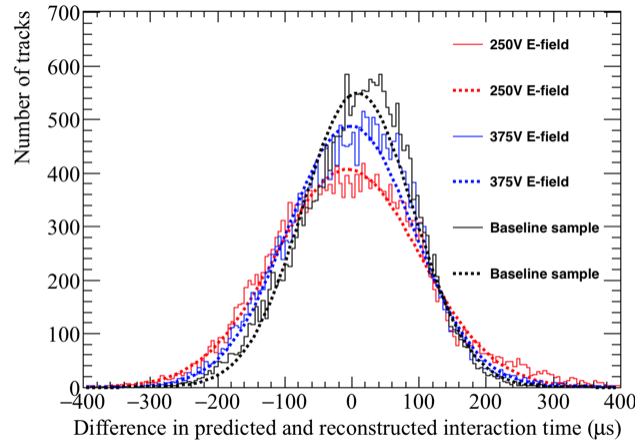


(a) The average difference in interaction times using the hit *RMS* metric.

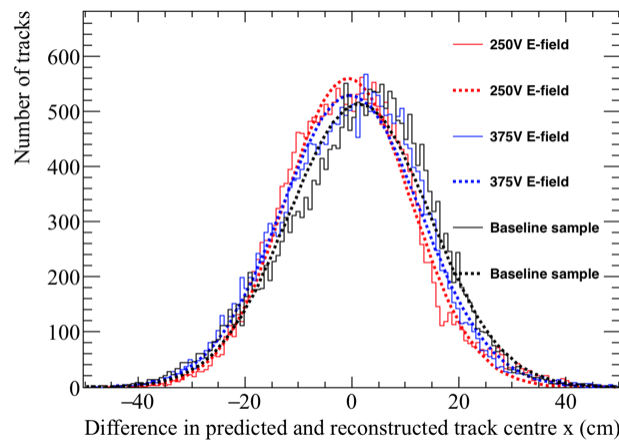


(b) The average difference in the central x position of a track using the hit *RMS* metric.

Fig. 5.33 The accuracy of the hit *RMS* method, for changing values of the electric field. Top shows the accuracy to which interaction times can be determined in μs . Bottom shows the accuracy to which the central x position of a track can be determined. Gaussian functions are fitted to the distributions so that any offset in the predicted times or positions can be discerned.

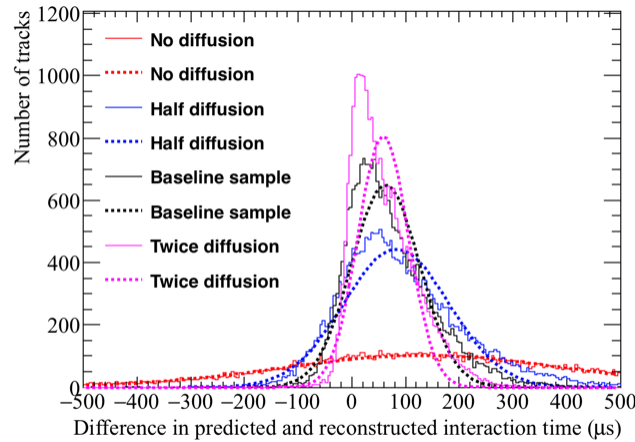


(a) The average difference in interaction times using the hit *RMS/Charge* metric.

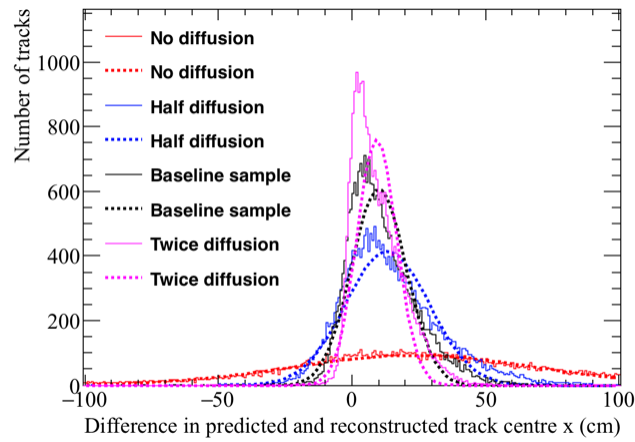


(b) The average difference in the central x position of a track using the hit *RMS/Charge* metric.

Fig. 5.34 The accuracy of the hit *RMS/Charge* method, for changing values of the electric field. Top shows the accuracy to which interaction times can be determined in μs . Bottom shows the accuracy to which the central x position of a track can be determined. Gaussian functions are fitted to the distributions so that any offset in the predicted times or positions can be discerned.

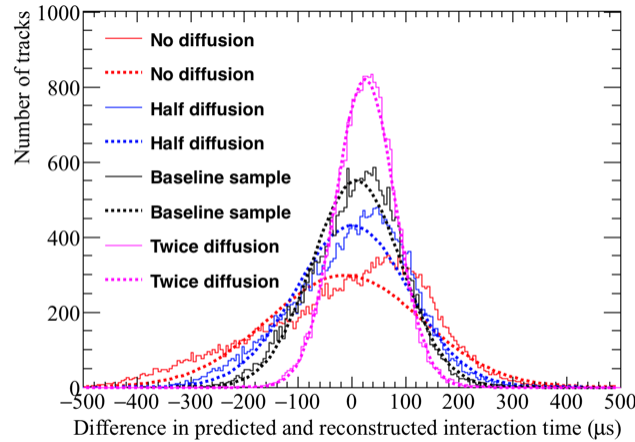


(a) The average difference in interaction times using the hit *RMS* metric.

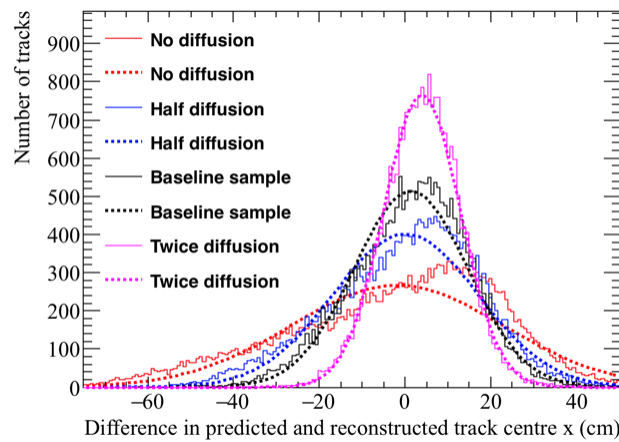


(b) The average difference in the central x position of a track using the hit *RMS* metric.

Fig. 5.35 The accuracy of the hit *RMS* method, for changing values of the constant of longitudinal diffusion. Top shows the accuracy to which interaction times can be determined in μs . Bottom shows the accuracy to which the central x position of a track can be determined. Gaussian functions are fitted to the distributions so that any offset in the predicted times or positions can be discerned.



(a) The average difference in interaction times using the hit *RMS/Charge* metric.



(b) The average difference in the central x position of a track using the hit *RMS/Charge* metric.

Fig. 5.36 The accuracy of the hit *RMS/Charge* method, for changing values of the constant of longitudinal diffusion. Top shows the accuracy to which interaction times can be determined in μs . Bottom shows the accuracy to which the central x position of a track can be determined. Gaussian functions are fitted to the distributions so that any offset in the predicted times or positions can be discerned.

Firstly, considering Figure 5.29, it can be seen that the accuracy to which interaction times can be determined rapidly decreases as the noise level increases. This is partly due to the fits used to make the prediction metrics not converging for counter differences of 1, 2, 3 and 4, where the MPV of hit *RMS* is not seen to increase for increasing drift distances. For evidence of this, see the Figures in Appendix A. Though this is the extreme case, it can be seen that the validity of the hit *RMS* for increasing drift distances becomes less predictable as the noise is increased. The result of this is a less accurate prediction metric, which leads to the large offsets and widths of the distributions that are shown in Figure 5.29.

The most striking feature of Figure 5.30 is the decrease in statistics seen for the increasing noise levels. This shows the effect that increasing the noise level, and hence hit threshold has. This is because fewer tracks in total are reconstructed, and those that are reconstructed are less likely to meet the criteria about the number of collection hits required to make predictions.

Figures 5.31 and 5.32, show the accuracy to which the interaction time, and central x position of a track, can be determined using the effect that diffusion has on the hit *RMS* and hit *RMS/Charge*, for changing electron lifetimes. Figure 5.31 shows that with an electron lifetime of 1 ms, the hit *RMS* metric is very inaccurate, this is likely due to hits which are a large distance away from the APAs being very difficult to reconstruct, due to the extremely poor lifetime. For this reason, the accuracy to which the hit *RMS* metric predicts the interaction time improves as the electron lifetime increases, though this increase is small between the 3 ms, 5 ms and 8 ms samples. Figure 5.32 shows the opposite effect, the accuracy to which the interaction time can be determined decreases with increasing electron lifetime for the hit *RMS/Charge* metric. This is shown by the widths of the distribution increasing as the electron lifetime increases. This happens because the decrease in hit charge is much greater when the electron lifetime is lower, and this dependence is the corner stone of this metric. The large decrease in hit charge for low electron lifetimes is why this metric performs so well for low electron lifetimes, and so the decrease in its accuracy is an unavoidable consequence of increasing electron lifetime.

Figures 5.33 and 5.34, show the accuracy to which the interaction time, and central x position of a track, can be determined using the effect that diffusion has on the hit *RMS* and hit *RMS/Charge*, for changing electric field values. Figure 5.33 shows that the accuracy to which the interaction time can be predicted, decreases with increasing electric field. This is shown by the introduction of an offset in the predicted interaction time for lower values of electric field strength. However, when these interaction times are converted to the central x

position of a track, the accuracy is relatively unaffected by electric field strength, due to the slower drift velocities at low electric field strengths. The opposite is shown in Figure 5.34, as the accuracy to which interaction time can be predicted does not see the introduction of an offset, and is better for the samples with lower electric field strengths. As the interaction times are accurately predicted, there is no offset seen in the predicted central x position. This shows that the hit $RMS/Charge$ method is unaffected by electric field strength.

Figures 5.35 and 5.36, show the accuracy to which the interaction time, and central x position of a track, can be determined using the effect that diffusion has on the hit RMS and hit $RMS/Charge$, for changing values of the longitudinal diffusion constant. As would be expected, both figures show that the accuracy to which the interaction time and central x position can be predicted are highly dependant on the longitudinal diffusion constant. This is seen by the distributions becoming much narrower, and more closely centred around the true interaction time, or central x position, as the constant of longitudinal diffusion increases. It is interesting to note that the extremely poor resolution seen in Figure 5.35 when there is no longitudinal diffusion, is not present in Figure 5.36. It is thought that this is due to the effect of charge attenuation, which will still occur because of the finite electron lifetime.

5.5.4 The limitations of and future improvements to the method of interaction time determination using diffusion

The comparison of the 35 ton data and Monte Carlo samples, as well as the Monte Carlo samples with differing detector conditions, show that there is potential in the ability to determine interaction times using the effects of diffusion. However, there are still some issues which need to be overcome. These will be discussed briefly below.

Many of the figures shown still have slight offsets even though the tails of the hit charge distributions have been removed. However, these offsets are generally confined to detector conditions which would not be considered optimal, such as very low electron lifetimes (1 ms) or high detector noise. The latter is seen to be the case when considering the 35 ton dataset, where the high noise scale can be seen to affect the accuracy to which the interaction time, and central x position, can be determined. A potential solution to reduce these offsets, and also to reduce the width of the distributions, is to perform the interaction time determination twice. The result of the first run, which is what was shown earlier, would then be used to select only hits which lie within the expected regions of hit RMS and hit $RMS/Charge$. This would be possible as the initial interaction time determination could be used to work out the

rough x positions of hits, and then only hits which lie within $N \sigma$ of the MPV would be used to determine the interaction time from the second pass. When performing the second pass of interaction time determination, N would be a user defined parameter, but would likely be less than 2, so as to exclude the beginnings of the tails of the hit RMS , and hit $RMS/Charge$, distributions.

An important improvement to the method would be to expand it to include the induction plane wires, as this will greatly increase both the number of wires which can be used, and the range of track angles whose interaction times can be predicted. The angular range of the method would increase, as when using only collection plane wires it is impossible to reconstruct enough hits for nearly vertical muons, as very few wires would be hit. This was discussed in Section 4.3. This was not attempted here, as the electronics noise in the 35 ton data was too large to able to reliably reconstruct all hits on the induction planes, without reconstructing many noise hits. This meant that the hit threshold on the induction planes was very high.

Chapter 6

Simulations of the DUNE Far Detector

Work presented in previous work has been done concerning the 35 ton prototype, however the following simulations have been performed with respect to the DUNE Far Detector (FD). Simulations in the FD have concentrated on cosmogenic background to neutrino oscillations, discussed in Section 6.1, and the muon background to nucleon decay, discussed in Section 6.3. The simulations shown in Section 6.1 are discussed in [125], and were performed for the Long Baseline Neutrino Experiment (LBNE), which along with the Long Baseline Neutrino Observatory (LBNO) experiment, formed the basis for DUNE, and so are included here for completeness. The author contributed by incorporating the *complex* detector geometry, and the accurate surface profile, into the simulations, though the main body of work was performed by the author of [125]. The other work presented was performed for the DUNE collaboration, in conjunction with work done by Vitaly Kudryavtsev and Matthew Robinson, both of the University of Sheffield. This work was performed with the aim of producing muon-induced background limits to nucleon decay in the DUNE FD.

6.1 Simulations of the LBNE surface detector

A preliminary design of the LBNE experiment had a 10 kt LAr detector on the surface, with a 3 m rock overburden [126]. Due to the large flux of cosmic rays at such a shallow depth, and the relative scarcity of neutrino events, it is necessary to establish whether the cosmic background can be sufficiently removed to allow neutrino interactions to be discerned. In order to show this, a series of simulations using both a simplified, and a more detailed detector design are performed. The cosmogenic backgrounds due to muons, protons and neutrons, are considered. These simulations, unlike other work presented in this thesis, were performed using a stand-alone version of GEANT4, and not in LArSoft. For a more thorough

review of the simulations, see [125].

Simulations have been built using GEANT4 versions 9.4 and 9.6. Initial simulations were performed using version 9.4, before being rebuilt to use version 9.6. A study showing that the background rate did not change with the newer version of GEANT4 was performed, in order to verify that the two sets of simulations were consistent. In all simulations the physics list “Shielding” was used [127]. Shielding allows particles to undergo Compton scattering, inelastic scattering with nuclei and nucleons, and includes all electromagnetic (EM) processes for all charged particles.

The authors work built on initial simulations which were performed using a simplified geometry, referred to as the *simple* geometry, which consisted of a single box of LAr measuring $30 \times 15 \times 16 \text{ m}^3$. This detector was enclosed in rock measuring $5 \times 10^3 \times 5 \times 10^3 \times 22 \text{ m}^3$, in the x , y , and z coordinates respectively. The detector was positioned in the rock so as to have a 3 m overburden of rock. As simulations were not performed in LArSoft, the co-ordinate system used was defined as follows;

- x - parallel to the beam direction.
- y - perpendicular to the beam direction.
- z - vertical direction.
- The co-ordinate system is centred on the middle of the detector volume in x and y , and on the surface of the rock which was above the detector in z .

The results of these initial simulations, discussed in detail in [125], are not shown here, but will be summarised in Table 6.2.

The improvements which the author made to these initial simulations were two fold. Firstly a more detailed geometry, referred to as the *complex* geometry, was included, this had a much more realistic detector design [128]. The *complex* geometry had two identical cryostats, each containing 120 TPC cells measuring $2.52 \times 2.28 \times 7.00 \text{ m}^3$. These cells each contain an active volume of LAr which measures $2.27 \times 2.25 \times 6.30 \text{ m}^3$. The TPC cells are arranged such that are 10, 6 and 2 TPC cells in the x , y and z directions, respectively. This gives a total volume of LAr in each cryostat which measures $28.20 \times 13.95 \times 15.0 \text{ m}^3$, and has a mass of 10.7 active mass. Running vertically between the TPC cells are anode plane assemblies (APAs) and cathode plane assemblies (CPA’s), all of which are embedded within the larger blocks of LAr. These blocks of LAr are further housed inside

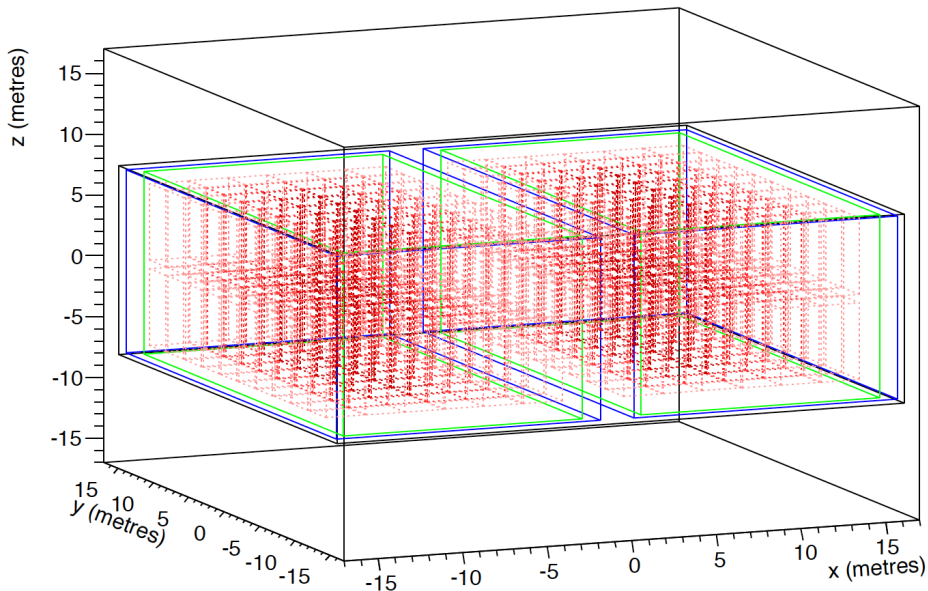


Fig. 6.1 The *complex* detector geometry used in the LBNE surface detector simulations. The TPC cells are shown in red, and are orientated such that there are 10, 6, and 2 in the x , y , z coordinates respectively, in each cryostat. The steel walls of the cryostats are green, whilst the outer edges of polyurethane are blue, and the concrete enclosures are black. Figure taken from [125].

stainless steel containers, which are insulated by 0.8 m of polyurethane. The two cryostats are surrounded by 0.5 m of concrete on all sides, with 3 m of concrete separating them. This gives a total fiducial mass of 10.7 kton of active LAr, which is surrounded by additional LAr. A representation of the detector, produced by the GEANT4 visualisation tool, is shown in Figure 6.1.

Secondly, an accurate surface profile, including the hills surrounding the far detector site was incorporated into the simulations. The proposed location of the LBNE detector was the same as the proposed DUNE detector location, though it was on the surface, and not in the mine. A satellite generated map, centred on SURF, which encompasses an area of 20×20 km 2 is used to generate the accurate surface profile. The map is sampled in bins measuring 5 \times 5 m 2 . To include the effects that the surrounding hills would have on the muon flux, muons are initially sampled 600 m above the surface, and are then stepped through the surface profile, until they reach a box surrounding the detector, which measures 80 \times 80 \times 36 m 3 . The amount of rock that a muon passes through is calculated, and the energy losses which this will cause are then taken into account before subsequent simulations. By taking the surface profile into account in this way, simulation time can be reduced, by not having to

simulate the surface profile for every new set of muons. The surface profile is modified so as to have a flat surface above the detector location of $100 \times 100 \text{ m}^2$, as it is envisioned that there will be detector out buildings around the detector site. The accurate surface profile is shown in Figure 6.3a, where it is presented in the context of the producing muons for the DUNE FD location.

It should be emphasised that all work presented here has been done using Monte Carlo truth, and so no reconstruction has performed. It also means that at all times only Monte Carlo truth information is used. Therefore, any positions or trajectories which are referred to are those which are recorded by GEANT4 [77]. This information saved by GEANT4 is “smeared” before analysis is performed, in attempt to take into account of some of the detector effects which were not simulated. This smearing is particle type, and energy dependant, and is performed on the particles position, trajectory, and energy [125, 129].

6.1.1 Classifying signal and background events

Before the simulations can be described in detail, it is neccessary to classify what quantifies as a background event. In the LBNE and DUNE FD, a ν_e appearance signal event would occur when a ν_e undergoes inelastic scattering with either an electron or nucleon. This interaction will produce an electron, which will in turn produce an EM shower. It is this EM shower which will be identified as a neutrino appearance signal. The electron track which is produced in these interactions will not necessarily be isolated, and may be accompanied by hadronic debris.

However, cosmic ray particles are able to produce signal which mimic this signal. These signal mimicking events can come from a large variety of sources, including, but not limited to, knock-on electrons from muons, bremsstrahlung photons, hadron decays to photons, and EM showers which originate outside of the active volume of the detector but then enter it. A background event is then defined as the initial photon in an EM shower. The first generation photon was used as this will contain the total energy of the shower, and removes the need to record every particle produced in the shower. The final position (point of pair production) of the photon was used in all calculations where the position was required, as the photon will not be observed in the actual detector, only the electrons and positrons it produces. Background showers which start with an electron from Compton scattering are not counted, as pair production is the major source of photons at the energies considered here.

6.1.2 Description of cuts used

As noted above, the event rate due to cosmic backgrounds will be much larger than the neutrino event rate, and so a series of cuts, designed to remove cosmic background, whilst preserving signal events, have to be developed. This section will briefly outline the cuts which were developed to achieve this, for a more rigorous definition of the cuts used see [125].

The simplest cut considers the energy of the electromagnetic (EM) cascade which is induced. As is the case for DUNE, the LBNE beamline was a broadband neutrino beam, and had an energy range of between 0.25 and 5.0 GeV. This means that any EM cascade which deposited more than 5 GeV of energy into the detector could not be due to the interaction of a neutrino. A lower limit of 250 MeV is also applied, as the analyses of neutrinos in the beam will not go to energies below this.

As charged particles which enter the detector will produce tracks, it is possible to calculate the minimum separation of these charged tracks, and the point at which a photon pair produces. This Point of Closest Approach (PoCA), is calculated by extrapolating the trajectory of the photon backwards from the location at which it pair produces, towards the charged particle tracks. The charged particle tracks are also extrapolated backwards, and so the smallest separations may be outside of the active volume of the detector. A photon is identified as being due to the charged particle track if the PoCA is below a certain threshold. Should a photon be due to a charged particle track, then it is identified as being a background event. Thresholds of 30 cm and 10 cm are used when considering the initial charged muon, and all charged particles respectively. The latter threshold is smaller to avoid removing signal events, and also has a lower limit of 2 cm, meaning that any photons which have PoCAs of less than 2 cm are not identified as background events. This is because it is possible that charged hadrons are produced at the neutrino interaction vertex, and so the electron produced would have a charged particle very close to it, meaning that were this lower limit not in place, it would fail the all charged PoCA cut.

It has been found that the angle of a neutrino event, with respect to the neutrino beam, is highly correlated to the energy of the neutrino [130]. This means that it is possible to use the angle of a shower, with respect to the beam, to distinguish between signal, and backgrounds events. The effectiveness of this constraint is highly energy dependant, as any high energy photons which are not tightly correlated to the beam axis will be identified as backgrounds, though few low energy photons will be [131]. An example of how the PoCA, and angle of a

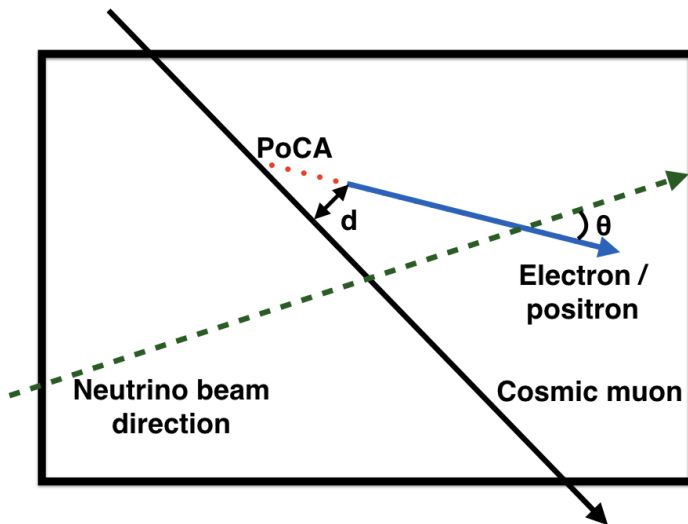


Fig. 6.2 A diagram of the PoCA, and the angle w.r.t the beam, calculations in the LBNE surface detector simulations. A cosmic muon which passes through the detector is shown as a black line, whilst an electron/positron that is produced is shown as a blue line. The minimum distance between the muon and electron/positron is shown (d), as well as the point of closest approach (PoCA) when the electron/positron track is extrapolated backwards. The extrapolated track is shown as a dotted red line. The neutrino beam direction is shown as a dashed green line, and the angle that the electron/positron makes with respect to this is shown (θ). Figure is modified from [125].

photon with respect to the beam axis are calculated is shown in Figure 6.2.

It is envisioned that not all of the instrumented LAr will be able to be used to identify neutrino events. This is because, a fiducial cut will be applied around the detector edges, in order to ensure that the entire track is contained within the active volume of the detector. For the *complex* detector, this fiducial cut is applied to the outward facing edges of the active volumes. This is because it is assumed that tracks passing between cells, within a given cryostat, will be able to be stitched, as is done in LArSoft.

Additionally, signal events should be able to be distinguished from background events based on the energy deposition measurements. These will come from identifying the start of an EM shower as coming from either an electron, or a photon, in the case of a signal, and background event, respectively. Studies have shown that the failure rate of this separation tails off at 10% for showers with energies above 0.5 GeV [132]. Therefore, a flat reduction of 1/10 is applied to all surviving simulated background events.

Finally, it is envisioned that an efficient photon detection system will be used, which uses the scintillation light emitted by excited argon [133]. This efficient photon detection system should be able to provide information on individual events, and so identify whether a candidate event occurred within the beam spill. If this is used, then the effective drift time of the detector can be reduced from 1400 μs to only 10 μs , a reduction by a factor of 140. This is also applied as a flat reduction to all surviving background events.

6.1.3 Generating particles for background studies

When simulating the cosmogenic background for a detector on the surface it is necessary to simulate the backgrounds due to muons, protons, neutrons and photons. It was found that the background due to cosmic photons was negligible [125], and so they are not discussed here.

The muons used in the simulations are generated using a Gaisser's parameterisation [134], which has been modified for large zenith angles, and muon decay [135]. The differential muon intensity at sea level ($\frac{dI_\mu}{dE_\mu d\Omega}(E_\mu, \theta)$), in units of $\text{cm}^{-2} \text{ s}^{-1} \text{ sr}^{-1} \text{ GeV}^{-1}$, is shown in Equation 6.1.

$$\begin{aligned} \frac{dI_\mu}{dE_\mu d\Omega}(E_\mu, \theta) = & A \times 0.14 \times (E_\mu + \Delta)^{-\gamma} \times p_d \\ & \times \left[\frac{1}{1 + \frac{1.1(E_\mu + \Delta)\cos\theta^*}{115\text{GeV}}} + \frac{0.054}{1 + \frac{1.1(E_\mu + \Delta)\cos\theta^*}{850\text{GeV}}} + R_c \right] \end{aligned} \quad (6.1)$$

where E_μ is the muon energy in GeV at the surface, θ is zenith angle at the height of muon production, $\cos\theta^* = \sqrt{1 - 0.99(1 - \cos^2\theta)}$, Δ is the muon energy loss in the atmosphere and is equal to $\frac{1030 \times 2.06 \times 10^{-3}}{\cos\theta - 120}$, R_c is the ratio of prompt muons to pions, and p_d is the probability for a muon to not decay in the atmosphere [136]. There are also a normalisation constant A , and a spectral index γ , which can both be chosen to fit experimental data. When considering shallow depths, or surface locations, values of $A = 0.1$ and $\gamma = 2.7$ are used [134]. When considering larger depths, as will be done in Sections 6.2 and 6.3 where MUSUN [83, 84] is used to simulate the muon flux at depth, values of $A = 1.84$ and $\gamma = 2.77$ are used.

The protons and neutrons used in the simulations are generated using CRY [80, 81], on a plane measuring $50 \times 50 \text{ m}^2$ area in the xy plane. It is not necessary to generate protons and neutrons over a large area as their interaction lengths are much shorter than muons, and so

Table 6.1 The minimum energies of simulated particles, when determining the cosmogenic background for the LBNE surface detector. The percentage of background events which are caused by particles of these energies, or above, is shown. The percentage of the particle flux above this energy, is also shown. It can be seen that, with appropriate minimum energy constraints, it is possible to avoid simulating over 80% of the muon flux, 99% of the proton flux, and 95% of the neutron flux. Table taken from [125].

Primary particle	Min. energy simulated (GeV)	Background (%)	Particle flux (%)
Muons	10	92.3	19.6
Proton	10	92.7	0.76
Neutrons	1	95.6	6.5

protons and neutrons at large angles which pass through large amounts of rock will not be a serious concern. The particles are generated at an altitude of 2100 m above sea level. However, the LBNE surface detector would have had an altitude of 1505 m above sea level, and so the particle fluxes generated by CRY have to be corrected to the particle fluxes expected at 1505 m above sea level [125]. The fluxes generated by CRY are also subject to a further correction, as CRY underestimates the cosmic ray flux by as much as 70% [137]. This is because CRY only considering protons striking the Earth's atmosphere. As the muon flux is calculated at sea level, this flux also has to be corrected so as to be the flux at 1505 m above sea level [125].

To reduce simulation time, only particles which will cause background events are simulated. For example, it is found that 92.7% of the proton induced background events are due to protons with energies of 10 GeV or more, yet these particles represent only 0.76% of the total proton flux. This means that by not simulating protons with energies below 10 GeV, the vast majority of background events will be simulated, but this will require less than 1% of the simulation time. The background events which are not simulated, can be accounted for by correcting the background seen from simulations, by the proportion of background events which were not simulated [125]. The minimum energies of the simulated muons, protons, and neutrons, along with the percentage of background events which they cause, and the percentage of the particle fluxes above this energy, are shown in Table 6.1.

From Table 6.1 it can be seen that in the case of only simulating protons above 10 GeV, 7.3% of the background were not simulated, and so the background rate from simulations should be scaled by a factor of 1.0787 ($\frac{1}{0.927}$).

Table 6.2 The normalised annual background rate for the *simple* detector geometry, separated by particle species, using the flat surface profile. The rates for muons entering the detector, muons missing the detector, proton induced events, and neutron induced events are shown. The annual background for muons entering the detector is only an approximate value, as initial simulations were performed without saving proton hit information, the inclusion of which greatly increases the accuracy of the all charge PoCA cut. Table is taken from [125].

Primary particle	Annual background rate
Muons entering	≈ 1.18
Muons missing	0.11 ± 0.02
Protons	2.57 ± 0.08
Neutrons	1.23 ± 0.07
Total	≈ 5

6.1.4 Results from background simulations

Before the results of the simulations involving the *complex* geometry, and accurate surface profile are discussed, it is useful to briefly summarise the results of the simulations using the *simple* geometry, and flat profile. This is shown in Table 6.2.

It can be seen from Table 6.2 that the overall background rate is dominated by hadronic components of the cosmic flux. It is expected that the additional shielding in the *complex* geometry will suppress these components significantly. The annual background induced by cosmic muons has been split into events where the muon enters the detector and events where it does not. This is because when a muon does not enter the detector, the PoCA with respect to the initial muon cannot be calculated. It will also instructive to observe how the background from each case changes, as the detector geometry is made more accurate. The *complex* geometry, has a larger surface area, and a larger volume of active LAr, and so it is expected that the muon fluxes will increase. This increase may be quite large for muons which miss the active volume of the detector, as muons may pass through the vertical gaps between TPC volumes, and produce secondaries which enter the active volume of the detector. Events like this would, at first glance at least, appear very similar to a neutrino event, as they will be isolated in the centre of the detector.

Only results for the *complex* geometry and accurate surface profile are shown. A separate set of simulations where the annual background when using the *complex* geometry and simple surface profile are shown in [125]. However, as discussed below and in [125], these background rates were found to be consistent with the background rates for the *complex*

Table 6.3 The normalised annual background rate, for events where a primary muon enters the active volume of the detector, for the *complex* geometry and accurate surface profile. A total of 2×10^8 muons with energies greater than 10 GeV are generated, representing 0.1003 years worth of detector live time. The background rate is separated into different first generation photon ancestries. The application of the cuts outlined in Section 6.1.2 is shown, where E_γ is the 0.25 - 5.0 GeV cut, $PoCA_\mu$ is the PoCA w.r.t. the initial muon cut, $\theta_{beam}(E)$ is the energy dependant cut on the angle between the beam and photon trajectory, $PoCA_{all}$ is the PoCA w.r.t. all charged particles cut, $D > 30$ is the 30 cm fiducial cut. Following this, two scaling factors of 1/10 and 1/140, representing the e- γ separation, and the use of an efficient photon detection system respectively, are applied. The errors quoted are Gaussian, unless the simulated annual background rate drops to 0, in which case an upper limit at 90% confidence level [138] is used, with any scaling factors applied to this limit. No errors are quoted if the error is less than 1% of the simulated annual background rate. Table is taken from [125].

	E_γ	$PoCA_\mu$	$\theta_{beam}(E)$	$PoCA_{all}$	$D > 30$ cm	$e - \gamma(E)$	γ detection
<i>Total</i>	1.32×10^7	$(6.38 \pm 0.09) \times 10^4$	$(2.87 \pm 0.06) \times 10^4$	3796 ± 229	2854 ± 199	285 ± 20	2.03 ± 0.14
$\pi^0 \rightarrow \gamma$	2.24×10^6	$(5.82 \pm 0.09) \times 10^4$	$(2.62 \pm 0.06) \times 10^4$	3339 ± 215	2743 ± 195	274 ± 20	1.96 ± 0.14
$Ext \rightarrow \gamma$	4.48×10^6	5237 ± 270	2425 ± 183	457 ± 80	111 ± 39	11.1 ± 3.9	0.08 ± 0.03
$\mu \rightarrow \gamma$	6.36×10^6	0 - 34	0 - 15.20	0 - 2.01	0 - 1.51	0 - 0.15	0 - 0.001
$Other \rightarrow \gamma$	7.87×10^4	333 ± 68	97 ± 37	0 - 15.20	0 - 11.43	0 - 0.11	0 - 0.002

geometry and accurate surface profile.

Table 6.3 shows the background rate for muons which enter the active volume of detector, as sequential cuts are applied, for the *complex* geometry, and accurate surface profile. A total of 2×10^8 muons with energies greater than 10 GeV are generated, representing 0.1003 years worth of detector live time. The overall number of background mimicking events is seen to increase when using the *complex* detector geometry, and the accurate surface profile, as opposed to using the *simple* detector geometry, and simple surface profile. It is observed that the expected annual background rates for the *complex* detector geometry in the flat, and accurate surface profiles, are consistent. This means that including the accurate surface profile does not have a significant effect on the background rate.

The effectiveness of the PoCA cut with respect to the initial muon is obvious, as the annual background event rate is reduced by over 99%. In the simulated event sample, this background rate is observed to be 100% when considering the $\mu \rightarrow \gamma$ photon ancestry. The rejection rate is seen to approach 100% in the $Ext \rightarrow \gamma$ photon ancestry too, where, when the photons trajectories are extrapolated they are seen to be very close to the muon track outside the detector, and so are identified as background events. The remaining background is dominated by photons with π^0 parents. Around half of the surviving events are removed

Table 6.4 The normalised annual background rate, for events where a primary muon misses the active volume of the detector, for the *complex* geometry and accurate surface profile. A total of 2×10^8 muons with energies greater than 10 GeV are generated, representing 0.1003 years worth of detector live time. The background rate is separated into different first generation photon ancestries. The application of the cuts outlined in Section 6.1.2 is shown.

	E_γ	$D > 30\text{ cm}$	$\theta_{beam}(E)$	$PoCA_{all}$	$e - \gamma(E)$	$\gamma detection$
<i>Total</i>	19800 ± 500	4004 ± 235	1551 ± 147	914 ± 113	91 ± 11	0.65 ± 0.08
$\pi^0 \rightarrow \gamma$	3284 ± 213	1108 ± 123	526 ± 85	166 ± 48	16.63 ± 4.80	0.12 ± 0.03
$Ext \rightarrow \gamma$	16500 ± 500	2858 ± 199	998 ± 118	748 ± 102	75 ± 10	0.53 ± 0.07
<i>Other</i> $\rightarrow \gamma$	28 ± 5	28 ± 5	28 ± 5	$0 - 20$	$0 - 2.01$	$0 - 0.01$

by the application of the angular cut, but more than 80% of these events are removed by the application of the all charged PoCA cut. This again shows how powerful the use of the PoCA cut is when rejecting background events. Whilst the fiducial cut is seen to be effective at removing the remaining $Ext \rightarrow \gamma$ events, this is not the case for the $\pi^0 \rightarrow \gamma$ events. Therefore, the development of efficient methods of e- γ separation, and the use of an efficient photon detection system are critical in reducing the annual background to a rate which would not be prohibitive to observing neutrino interactions.

The background rate for the *complex* detector geometry, and accurate surface profile, for muons which miss the active volume of the detector, is shown in Table 6.4. The same muons used in Table 6.3, are used here, meaning that a detector live time of 0.1003 years is been simulated. The overall number of background mimicking events is seen to increase substantially when using the *complex* detector geometry, and the accurate surface profile, as opposed to using the *simple* detector geometry, and simple surface profile. This is to be expected, as there is a much larger external surface area, and the vertical gaps produce internal gaps between the TPCs. It is observed that the expected annual background rates for the *complex* detector geometry in the flat, and accurate surface profiles, are consistent, though the total number of background events is less when the accurate surface profile is used.

Table 6.4 shows that muons which miss the active volume of the detector cause much fewer background events than those which strike the active volume of the detector. However, the events which they do cause, are much more likely to survive the application of all cuts. This is due to a combination of both the fiducial cut being less effective, and there being more external photons. Both of these differences are caused by muons which pass through gaps between TPCs, and produce secondaries which are far away from the detector walls. These events will produce photons which are not removed by the fiducial cut, and are identified as external photons, as the muon in these events did not produce a track. There will also be more external photons, as the surface area of the detector has been substantially in-

Table 6.5 The normalised annual background rate, for proton induced events, for the *complex* geometry. A total of 1×10^7 protons with energies greater than 10 GeV are generated, representing 2.482 years worth of detector live time. The background rate is separated into different first generation photon ancestries. The application of the cuts outlined in Section 6.1.2 is shown.

	E_γ	$D > 30$ cm	$\theta_{beam}(E)$	PoCA _{all}	$e - \gamma(E)$	γ detection
<i>Total</i>	1.55×10^4	$10559 \pm$	3475 ± 39	319 ± 12	31.9 ± 1.2	0.23 ± 0.01
$\pi^0 \rightarrow \gamma$	1.18×10^4	9277 ± 63	3098 ± 36	297 ± 11	29.7 ± 1.1	0.21 ± 0.01
$Ext \rightarrow \gamma$	3120 ± 37	858 ± 19	279 ± 11	22 ± 3	2.2 ± 0.3	0.016 ± 0.002
$Other \rightarrow \gamma$	524 ± 15	424 ± 15	97 ± 6	$0 - 1.04$	$0 - 0.10$	$0 - 0.001$

creased as it is now divided into two identical cryostats, as opposed to in a single block of LAr.

Table 6.5 shows the background rate for protons, as sequential cuts are applied, for the *complex* geometry, and accurate surface profile. A total of 1×10^7 protons with energies greater than 10 GeV are generated, representing 2.482 years worth of detector live time. As the protons are generated on a plane which measures 50×50 m², and the accurate surface profile was modified to have a flat area above the detector measuring 100×100 m², it is not necessary to propagate protons through the accurate surface profile. As discussed earlier, protons are generated on a plane measuring 50×50 m² as protons will not induce background events at the high inclinations which muons do. The overall number of background mimicking events is seen to decrease substantially when using the *complex* detector geometry, as opposed to using the *simple* detector geometry.

It can be seen from Table 6.5 that the cut with respect to the beam angle, and the PoCA calculation with respect to all charged particles, are very effective as they remove 67% and 90% of all remaining background events respectively. That the all charged PoCA cut is so effective is not surprising, as many of the photons produced will be close to the initial proton that was simulated. After all cuts are applied, the annual number of background events is seen to decrease by over a factor of 10 when using the *complex* geometry. This decrease is attributed to the additional shielding which is present in the *complex* geometry, as concrete, insulations and inactive regions of LAr have been added.

Table 6.6 shows the background rate for neutrons, as sequential cuts are applied, for the *complex* geometry, and accurate surface profile. A total of 1.1×10^8 neutrons with energies greater than 1 GeV are generated, representing 0.653 years worth of detector live time. The neutrons are generated on a plane which measures 50×50 m², and so as seen with the protons, it is unnecessary to propagate neutrons through the accurate surface profile. The overall number of background mimicking events is seen to decrease substantially when using

Table 6.6 The normalised annual background rate, for neutron induced events, for the *complex* geometry. A total of 1.1×10^8 neutrons with energies greater than 1 GeV are generated, representing 0.653 years worth of detector live time. The background rate is separated into different first generation photon ancestries. The application of the cuts outlined in Section 6.1.2 is shown.

	E_γ	$D > 30$ cm	$\theta_{beam}(E)$	$PoCA_{all}$	$e - \gamma(E)$	γ detection
<i>Total</i>	8405 ± 113	5697 ± 93	1949 ± 54	225 ± 18	22.5 ± 1.8	0.16 ± 0.01
$\pi^0 \rightarrow \gamma$	6397 ± 98	5050 ± 87	1744 ± 51	194 ± 17	19.4 ± 1.7	0.14 ± 0.01
$Ext \rightarrow \gamma$	1796 ± 52	470 ± 26	169 ± 16	30.1 ± 6.7	3.01 ± 0.67	0.021 ± 0.005
$Other \rightarrow \gamma$	209 ± 18	175 ± 16	36.2 ± 7.4	$0 - 3.68$	$0 - 0.37$	$0 - 0.003$

the *complex* detector geometry, as opposed to using the *simple* detector geometry.

From Table 6.6 it can be seen that as was the case with the protons, the cut with respect to the beam angle, and the PoCA calculation with respect to all charged particles, are very effective. Upon the application of all cuts, the annual expected background from neutrons in the *complex* geometry is seen to decrease by almost an order of magnitude. Whilst this is not as dramatic as the reduction seen when considering proton induced backgrounds, it still represents a significant reduction in the background rate. This reduction is again attributed to the extra shielding which is present in the *complex* geometry.

6.1.5 Summary of simulations for the LBNE surface detector

Summing the expected background from Tables 6.3, 6.4, 6.5 and 6.6 gives an expected cosmogenic background after cuts for the *complex* detector geometry, and accurate surface profile, of 3.07 ± 0.25 events per year. This compares with an expected background rate of ≈ 5 events per year, for the *simple* detector geometry, and flat surface profile. The reduction in background rate is due to the additional shielding present in the *complex* geometry which reduces the hadronic background component from 3.80 ± 0.11 to 0.39 ± 0.01 , a decrease of roughly an order of magnitude. However, the increase in surface area of the detector is found to cause the number of background events caused by muons which both enter and miss the active volume of the detector to increase. This increase is very substantial when considering muons which miss the active volume of the detector. This is summarised in Table 6.7.

Following the simulation of large samples of muons, protons, and neutrons, with a *complex* detector geometry, the expected background for the LBNE surface detector is found when considering an accurate, surface profile. This is compared to the expected background

Table 6.7 The normalised annual background rate for the *simple* and *complex* detector geometries, separated by particle species, using the flat and accurate surface profiles respectively. The rates for muons entering the detector, muons missing the detector, proton induced events, and neutron induced events are shown. The annual background for muons entering the detector when using the *simple* detector geometry and flat surface profile is only an approximate value, as initial simulations were performed without saving proton hit information. The inclusion of proton hits greatly increases the accuracy of the all charge PoCA cut, however this was only seen in a small sample. Table is taken from [125].

Primary particle	<i>simp.</i> geom. & flat surf. prof.	<i>comp.</i> geom. & acc. surf. prof.
Muons entering	≈ 1.18	2.03 ± 0.24
Muons missing	0.11 ± 0.02	0.65 ± 0.08
Protons	2.57 ± 0.08	0.23 ± 0.01
Neutrons	1.23 ± 0.07	0.16 ± 0.01
Total	≈ 5	3.07 ± 0.25

rate when using a *simple* detector geometry and flat surface profile [125]. It is observed that the effect of the *complex* detector geometry is to reduce the overall background rate, primarily due to the additional shielding which it provides. This additional shielding causes the proton and neutron induced backgrounds to decrease substantially, as was shown in Table 6.7. It is however found that there will be a significant source of backgrounds from muons which do not enter the active volume of the detector. This is due to the presence of vertical gaps between the TPC cells. The effect of incorporating the accurate surface profile is found to be negligible, as the hills only offer minimal amounts of shielding. These simulations provide relatively accurate estimate of the expected background for the LBNE surface design, although it must be stressed that these studies have been performed using Monte Carlo truth information, and so have not used reconstruction.

6.2 The use of MUSUN in LArSoft

The primary muons in the following discussions are all generated using MUSIC [83] [85] [86] and MUSUN [83] [84], and so a brief overview of them is required. MUSIC first propagates muons through a medium, defined by the user, for given initial energies, positions, and direction cosines. A range of energies between 10^2 and 10^7 GeV are considered, and their energy distributions are stored at depths of between 100 and 15,000 m w.e. Energy losses due to four processes are considered; ionisation, bremsstrahlung, electron-positron pair production and muon-nucleus inelastic scattering. The output of MUSIC is then used by

Table 6.8 Muon flux parameters as calculated with MUSIC/MUSUN.

Total flux ($\text{cm}^{-2} \text{s}^{-1}$)	Mean E_μ (GeV)	Mean slant depth (m w.e)	Mean θ ($^\circ$)
5.66×10^{-9}	283	4532	26

MUSUN to generate a muon energy spectrum and angular distribution, for a given detector location. MUSUN is able to use information about the local surface profile to make these distributions more accurate.

The location of the DUNE far detector, near the Ross shaft at SURF, has global coordinates of, $44^\circ 20' 45.21''$ North, $103^\circ 45' 16.13''$ West. The rock composition is assumed to be, $\langle Z \rangle = 12.09$ and $\langle A \rangle = 24.17$. The density is assumed to be 2.70 g cm^{-3} [139]. The flux calculated by MUSIC/MUSUN of $5.18 \times 10^{-9} \text{ cm}^{-2} \text{s}^{-1} \text{sr}^{-1}$, is well matched to the flux measured by the active veto system of the Davis' experiment, which was $(5.38 \pm 0.07) \times 10^{-9} \text{ cm}^{-2} \text{s}^{-1} \text{sr}^{-1}$ [140]. Given the small differences in these values, and another measurement by the Majorana demonstrator, the systematic uncertainty in calculating the muon flux is estimated to be 20% [141].

The surface profile around the proposed detector location is shown in Figure 6.3a, where the proposed location is in the centre of the map. Each quadrant on the map has been divided into 4 angles of 22° , to help guide the eye when comparing it to Figure 6.3b, where the distribution of azimuth angles is plotted. The vertical lines in Figure 6.3b show the division of the quadrants when the angle is calculated from East to the North. When moving from East to North it is possible to discern how the peaks and troughs on the surface profile, correspond to troughs and peaks, in the distribution of azimuthal angle.

Given these parameters, the muon flux at the DUNE far detector location, when assuming a spherical detector geometry, and without simulating a detector cavern, is given by Table 6.8.

The muons simulated for DUNE are sampled on the surface of a box surrounding the detector hall, that also encompasses 7 m of rock above the cavern, and 5 m of rock on all other sides. This is to ensure that the simulated muons pass through a sufficient amount of rock to induce cascades, both above, and around, the detector hall. The secondaries produced in these cascades which enter the detector, in the absence of the initial muon, are of particular interest, as they could be mistaken for nucleon decay events. The study of these nucleon decay mimicking events is discussed in Section 6.3. The size of the box which the muons

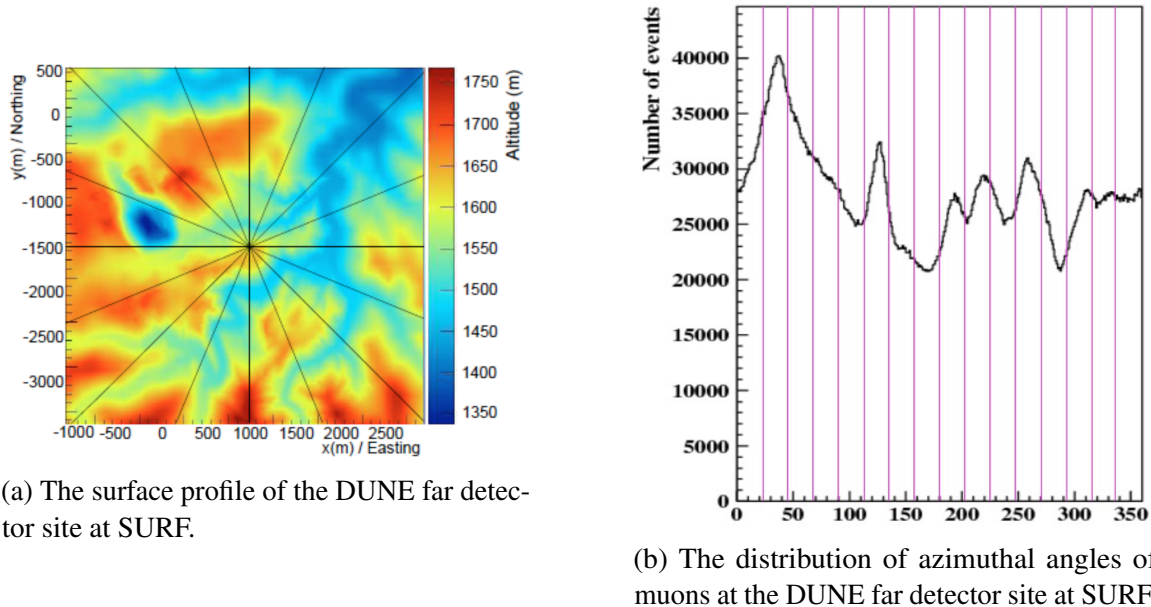


Fig. 6.3 The correlation between the surface profile, and the distribution of azimuthal angles at the DUNE far detector site. The quadrants have been divided into four angles of equal size. The azimuthal angle, calculated as the angle from East (pointing to the right in Fig. 6.3a), and increasing counterclockwise, is seen to follow the contours of the surface profile.

are sampled from is $74.43 \times 29.54 \times 30.18 \text{ m}^3$, compared to the simulated cryostat which has dimensions, $61.62 \times 14.94 \times 13.58 \text{ m}^3$. The dimensions are given as length \times width \times height. The muons are sampled randomly according to their energy spectrum, for a given zenith and azimuthal angle, using the angular distribution obtained with MUSIC.

Before this could be done however, MUSUN had to be incorporated into the DUNE software framework, as it had previously been maintained in FORTRAN, as an external package. This involved building on the work done by the LZ collaboration in porting the code to C++ !!!!citepKareem. The process by which this was done, was to first reproduce the distributions produced by the LZ collaboration using the DUNE software framework. Once the distributions could be reproduced for the Davis shaft at SURF (the proposed location of LZ), the muon distributions produced by the original FORTRAN code for the DUNE detector location were reproduced. The distributions produced by the DUNE software framework are shown in Figure 6.4. These are seen to be consistent with the distributions made for the LBNE collaboration [142]. The initial positions of 10,000 muons, generated in LArSoft around the simulated DUNE 10 kt module, are shown in Figure 6.5. The initial positions of the muons are shown as blue points, whilst the cryostat is a single black box, and each TPC

is a single red box.

It is found that the muon rate through the box upon which the muons are sampled is 0.1579 Hz. This rate is later used to normalise the background event rate in Section 6.3. Roughly a third of the muons which are generated pass through the active volume, to give a muon rate through the active volume of 0.053 Hz.

6.3 Nucleon decay channels in DUNE

When searching for rare processes, where an experiment is unlikely to see more than a few real signatures, an exhaustive study of the potential backgrounds is required. This is so that if a signal is observed, it could provide overwhelming evidence for the process. The search for nucleon decay in DUNE is one such process, and so an exhaustive study of the background to nucleon decay is required. As discussed in Section 1.2.1, cosmogenic muons cause backgrounds to nucleon decay signatures, as the secondary particles produced by their interactions are able to mimic the nucleon decay signatures. For this reason it is necessary to simulate this background, and to develop a series of cuts which can be applied to the energy depositions they produce, to establish that they are not due to nucleon decays. When doing this, it is important to use a simulation that is as accurate as possible to the DUNE far detector. It is for this reason that MUSUN was incorporated into LArSoft, as the muons which it generates are well matched to the observed muon flux, as described in Section 6.2.

To ensure that the background has been properly simulated it is advantageous to simulate many more background events than will be collected by the experiment. As the DUNE detector will run for roughly 20 years, it was decided that an initial sample representing 200 years of detector live time would be simulated. Given that the muon rate through the cavern is 0.1579 Hz, 200 years of detector live time corresponds to roughly 10^9 muons. This only represents one of the DUNE 10 kt modules, and so an even larger dataset will be required to represent the full live time of the 4 10 kt modules. For this reason, muons were generated beyond this initial sample size, with a total of 2×10^9 muons having been currently simulated.

Producing samples of this size requires significant computer power, both in terms of running time, and storage space. As such, many of the simulated events are discarded before being saved to disk. This is done through the application of a filter after GEANT4. It is essential that the events which are discarded could not have been mistaken for nucleon

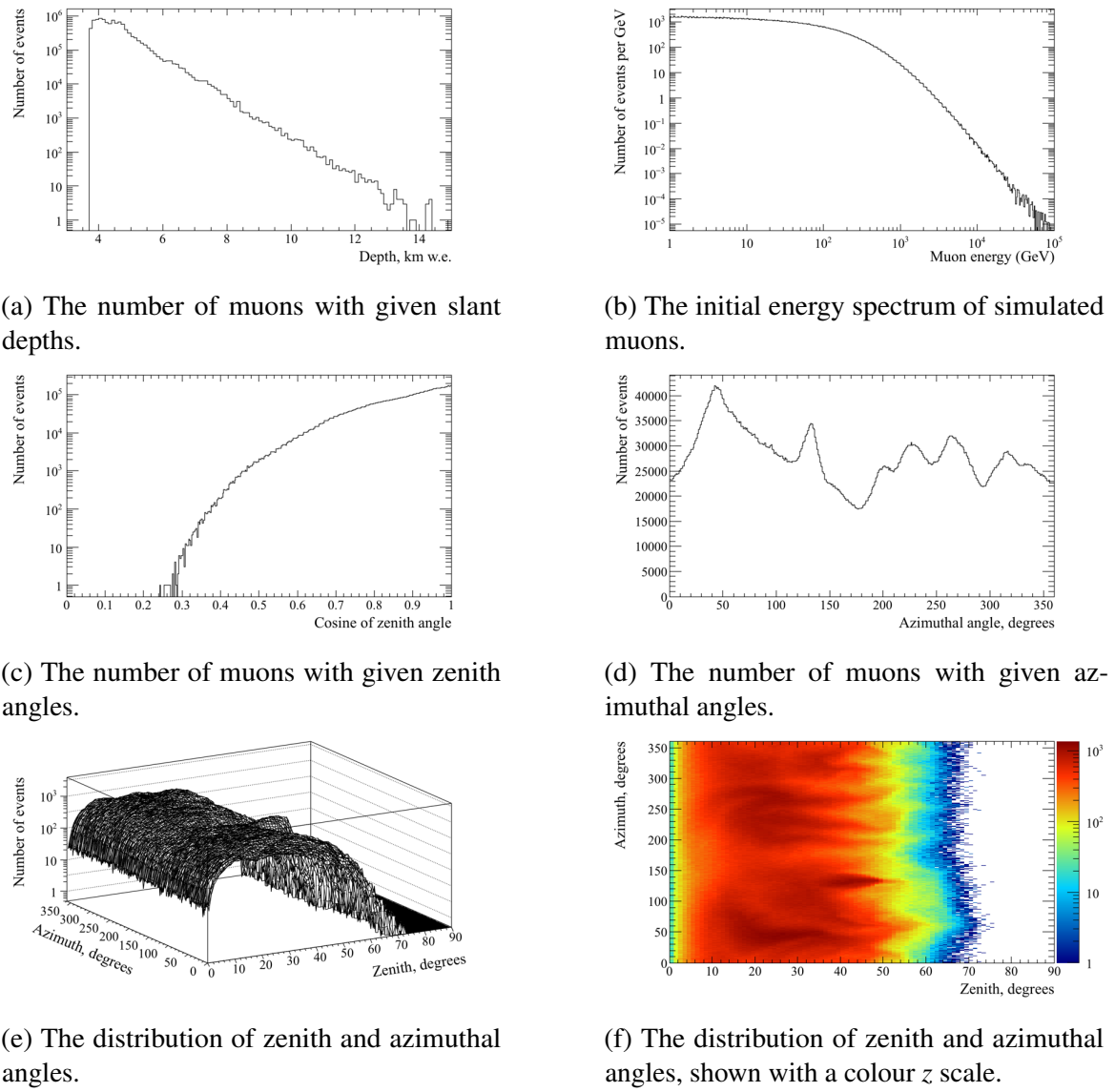


Fig. 6.4 The distributions of some of the important quantities for a sample of 10^6 muons generated by MUSUN, in LArSoft. The slant depths and energies of the simulated muons are shown top. The azimuthal and zenith angles of muons are shown middle. Bottom left shows the profile of zenith angle, against azimuthal angle, whilst bottom right shows this with a colour z axis.

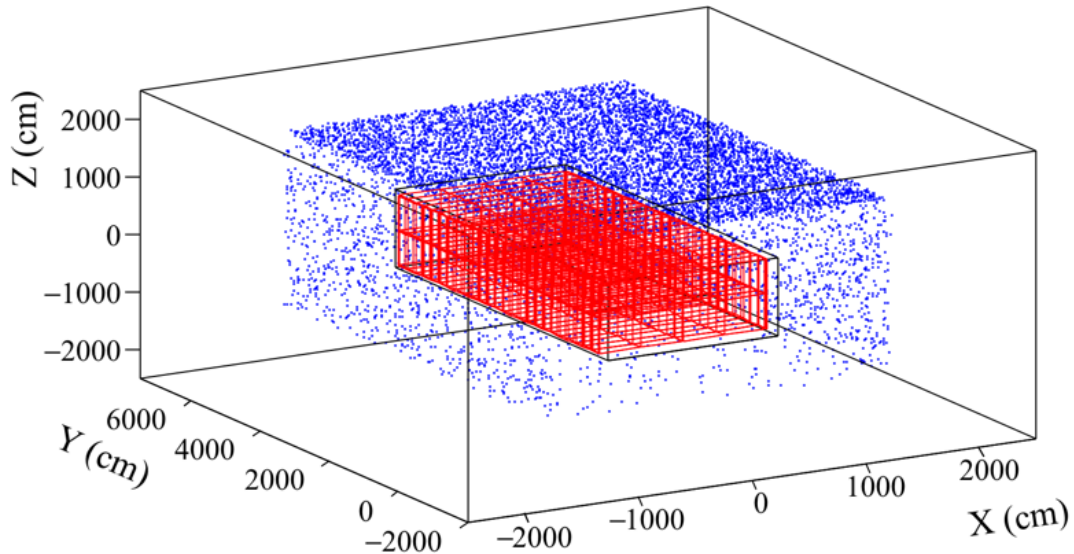


Fig. 6.5 The initial positions of muons generated by MUSUN, around a DUNE 10 kt module. The initial positions of the muons are shown as blue points, whilst the cryostat is a single black box and each TPC is a single red box.

decay events, and so only very generous cuts are applied. Only events satisfying one of the following cuts are discarded;

- Contain a muon track of more than 1 m.
- There are no energy depositions in the entire detector volume.

It is envisioned that a muon track of more than a metre would not be unreconstructed. It is also assumed that any signatures observed within one drift window of such a track would not be studied in a nucleon decay search, as there would be doubt as to the authenticity of the signal. Given that the total rate of muons through the active volume is 0.053 Hz, and that the drift time is a few ms, ignoring all times where any track from a cosmogenic muon is present results in less than 0.1% dead time. The dead time associated with ignoring events with muon tracks of more than 1 m is clearly less than this. This amount of dead time is assumed to be acceptable. Filtering out events where there are no energy depositions in the detector is clearly acceptable, as there are no energy depositions which could mimic a nucleon decay signature.

After applying this series of cuts, the sample of 2×10^9 muons is reduced to $XXXX \times 10^{XXXX}$ muons, which is a much more reasonable sample size to store on tape, and to perform analy-

ses on. It is upon this reduced sample of muons that the cosmogenic background analyses are performed. As discussed in Section 2.4.2, the proton decay channel of $p \rightarrow K^+ + \bar{\nu}^e$ is referred to as the 'Golden Channel' in LAr, this analysis is discussed in [141]. The related decay of channel of $n \rightarrow K^+ + e^-$ is discussed here.

6.3.1 Cosmogenic background to the $n \rightarrow K^+ + e^-$ decay channel

As shown in Table 2.3, the predicted sensitivity that DUNE will have to this channel is much larger than that of Super-K. As a result, it is an interesting decay mode to study as DUNE could easily have the best limit for this decay channel. As discussed in Section 1.2.1, the cosmogenic background to nucleon decay is predominantly caused by neutral particles, such as a K^0 , entering the detector volume, and interacting far away from the detector edges. This is particularly true for the 'Golden Channel,' as shown in Figure 1.1, but it also holds for other channels. This means that it is events such as this which are the main cause for concern when trying to eliminate all cosmogenic backgrounds.

As is the case with the 'Golden Channel,' the final state of the decay contains a single charged kaon, and so events which do not contain a kaon track can be immediately discounted. There is also an electron in the final state of the decay, and so this means that events which do not also contain an electron can be discounted. In a nucleon decay event, the kaon and electron produced in the final state will have a common vertex, and so the requirement that the two particles have a common vertex can also be applied. Other constraints that are applied to eliminate background events are; a cut on external muon length, a cut on depositions near the detector edges, and criteria about the distribution of deposited energy. The criteria about the distribution of deposited energy is found by considering a sample of simulated decay events, and is discussed in Section 6.3.3. These cuts, which are applied sequentially, are outlined below:

- The event contains energy depositions due to kaons and due to electrons.
- The event contains at least one kaon track, and at least one electron track/shower.
- The event contains a single kaon track, and a single electron track/shower.
- No muon travels more than 20 cm in the detector volume.
- The event has no energy depositions within 2 cm of the detector edges.

- This is changed to a maximum of 100 MeV of energy deposited within 2 cm of the detector edge in Section 6.3.2.
- The kaon and electron share a common vertex.
 - The kaon and electron tracks are separated by no more than 5 cm.
 - If the kaon and electron tracks are separated by more than 5 cm, then the point of closest approach between the two extrapolated tracks is less than 2 cm.
- The energy depositions in the event are within the ranges expected from a nucleon decay event. This is explained in Section 6.3.3, but the energies considered are summarised below:
 - The energy directly deposited by the kaon.
 - The energy deposited by the kaon decay products.
 - The energy directly deposited by the electron.
 - The energy deposited near the shared kaon and electron vertex.
 - The energy deposited in the detector which does not fit any of the above criteria.

Inspiration for these cuts were taken from [53], though some of the cuts were relaxed. The cut on muons was relaxed from a cut on any muon being present, to a maximum track length of 20 cm, as this was found to be sufficient. The cuts on the number of pions in the event were relaxed so as to not expect that all particles are perfectly reconstructed. However, as the analysis is performed using Monte Carlo truth information, without position or energy smearing, the kaons and electrons are assumed to be perfectly reconstructed. This means that it is assumed that all deposited charge will be reconstructed, and that the detector characterisation is perfect. This is something which will need to be refined in future analyses, and will be taken into account when the analysis progresses to use reconstructed quantities, as discussed in Section 6.3.4.

When performing the analysis it is important to be able to trace the particle ancestry. This is so that energy depositions in the detector can be properly assigned, and cuts applied, to the relevant particles. For example, a μ^+ is often produced when a K^+ decays at rest, and this muon may travel more than 20 cm. However, the cut on muon length should not be applied to this muon as it was produced by the decay of the kaon. Similarly, as the kaon interacts in the detector secondary particles will be produced, which will be reconstructed as tracks coming off the main kaon track. The initial kinetic energy of the kaon can only be determined by

summing the energy depositions due to these secondary particles, and the energy depositions due to the kaon itself. Correctly calculating the initial kaon kinetic energy is critical when determining if an event is a nucleon decay event. The reason for this is that nucleon decay events have very specific energy spectra, and so being able to correctly assign the ancestry of energy depositions is vitally important. The same is true for the electron energy, which is calculated by tracing the ancestry of the particles produced in the EM shower which it produces back to the electron.

As no reconstruction has been performed, the tracks referred to here are different from those in previous sections. The definition of a track used here, is that the particle in question has energy depositions, on simulated wires, which are directly associated with it. These simulated wires are not the same as the the wires which have been considered in previous Monte Carlo studies, as the signals have not been digitised. This distinction is important, as it allows the energy depositions directly from GEANT4 to be used, whilst also allowing for LArSoft methods concerning whether depositions are within TPC boundaries to be utilised.

The simulated electrons may begin showering immediately, or they may produce a short 'track like' segment before beginning to shower. To ensure that every electron shower can be identified, electrons are not required to produce a short 'track like' segment. This means that all electrons are assumed to begin showering immediately, and it is also assumed that all of the energy in the shower can be identified as coming from a single electron. This definition of shower energy is the one that is used when the showering algorithms are developed in LArSoft. It is hoped that when DUNE begins taking data the showering algorithms will be able to achieve this level of energy reconstruction.

When calculating the distance between the start of the kaon track, and the start of the electron track/shower, the energy depositions whose locations are closest to the Monte Carlo truth start points of the particles are used. For particles which are produced within the active volume, these locations generally correspond to the Monte Carlo truth start positions, though this is not always the case. For example, if a particle is created in the gap between two TPCs, then there will be no charge collected until it enters the active volume. This will result in the measured start position to be shifted from the true generation point. This shift can prove troublesome when considering decay events, as if the decay occurred in the centre of an APA, then it is likely that the kaon and electron would deposit energy on opposite sides of the APA. This would cause the depositions to be separated by over 5 cm, as this is the width of the APAs. However, if the tracks are propagated backwards, towards their true start point,

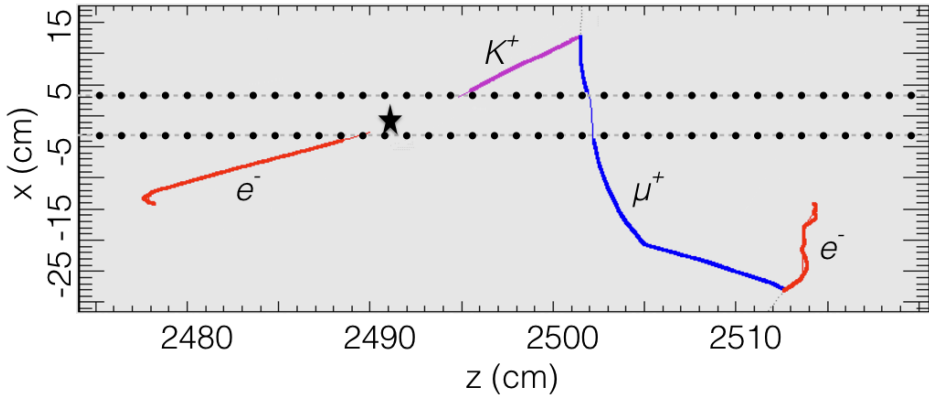


Fig. 6.6 A simulated $n \rightarrow K^+ + e^-$ decay which occurred in a gap between TPCs. The path of the kaon produced in the decay is shown as a purple line. The path of the muon, produced by the decay of the kaon, is shown as a blue line. The paths which the electrons in the event took are shown as red lines. The electron on the left of the figure is the electron produced in the neutron decay, whilst the one on the right of the figure, is produced by the decay of the muon. The thin coloured lines show track segments which were in uninstrumented parts of the detector, such as gaps between TPCs and APAs. The dotted black lines show the edges of the TPCs, and the black star shows the location at which the decay occurred. The distance between the first kaon energy deposition, and the first electron energy deposition, is found to be 10.7 cm. However, when the kaon and electrons tracks are extrapolated towards the true start position, the point of closest approach (PoCA) between the two tracks is found to be 0.67 cm. This shows that they do in fact have a common vertex, despite the large separation of the start points.

it should still be possible to determine that they had a common vertex. An example of a simulated decay event where this happens is shown in Figure 6.6.

In order for a kaon track, and an electron shower, to be considered to share a common vertex, the separation between the start of the kaon track, and the start of the electron shower, must be no more than than 5 cm. A maximum separation of 5 cm is used, as, if the two particles are produced in the centre of a TPC, a gap of 5 cm would require no energy depositions to be collected over approximately 10 collection wires. This is assumed to be unlikely during data taking, and cannot happen in the simulations considered here, as Monte Carlo truth information is used. As shown by Figure 6.6, however, it is possible for the kaon and electron, produced in a signal event, to be separated by more than 5 cm. To prevent events such as this being missed, a second criteria is applied to events with large separations. This criteria is that the “Point of Closest Approach” (PoCA) between the two particles, found by extrapolating the kaon track and the electron shower, forwards and backwards, is less than 2 cm. This is the same PoCA calculation which was made in Section 6.1.2,

and it means that events such as the one shown in Figure 6.6 are still identified as signal events.

The fiducial cut is only applied to the outer edges of the cryostat, as if it were done with respect to the edge of every TPC in the far detector the loss of volume would be prohibitive. This means that the event shown in Figure 6.7 would not fail the fiducial cut, as the decay occurred over 6 m away from the edge of the detector, but happened to be in a gap between two TPCs. The need for a fiducial cut is two fold, firstly the vast majority of cosmically induced events in the detector will have a charged particle, which was produced externally, entering the detector. Performing a fiducial cut will remove all of these events, and will then mean that the only cosmic background events which can mimic a signal event would involve either a significant amount of charge being missed, or a neutral particle entering the detector, and interacting far from the detector walls. Secondly, in order to calculate the kinetic energies of the particles produced in the nucleon decay, and also to perform particle identification, they must be fully contained within the detector. As such, if one of the particles produced in the nucleon decay escapes the detector then its kinetic energy cannot be determined accurately, and if it is the kaon, or its decay products, then the particle cannot be identified using the method discussed in Section 4.4. A fiducial cut of 2 cm is used, as the loss of volume is negligible in a detector which is scale of the DUNE FD. A 2 cm fiducial cut also ensures that a significant amount of charge would have to be missed, for a particle which enters/escapes the detector to be incorrectly identified as being contained within the detector.

Once both the ancestry of energy depositions in the simulation, and the initial kinetic energies, have been correctly accounted for and calculated, it is possible to observe the distribution of background events, as the cuts outlined above are applied. The energy distribution of background events surviving the application of sequential cuts is shown in Figure 6.7. The normalised energy distribution of background events surviving the application of sequential cuts is shown in Figure 6.8. The distribution of normalised energies is found by dividing the number of events by the bin energy.

From Figures 6.7 and 6.8, it can be seen that there are no background events which could mimic a decay signature as there no events which survive the application of all cuts. This corresponds to a limit on the cosmogenic background to the $n \rightarrow K^+ + e^-$ decay channel of $XX \times 10^X X$.

It is interesting to observe the effect that relaxing some of the cuts has on the background rate. For example, the cuts after the presence of at least one kaon track, and at least one

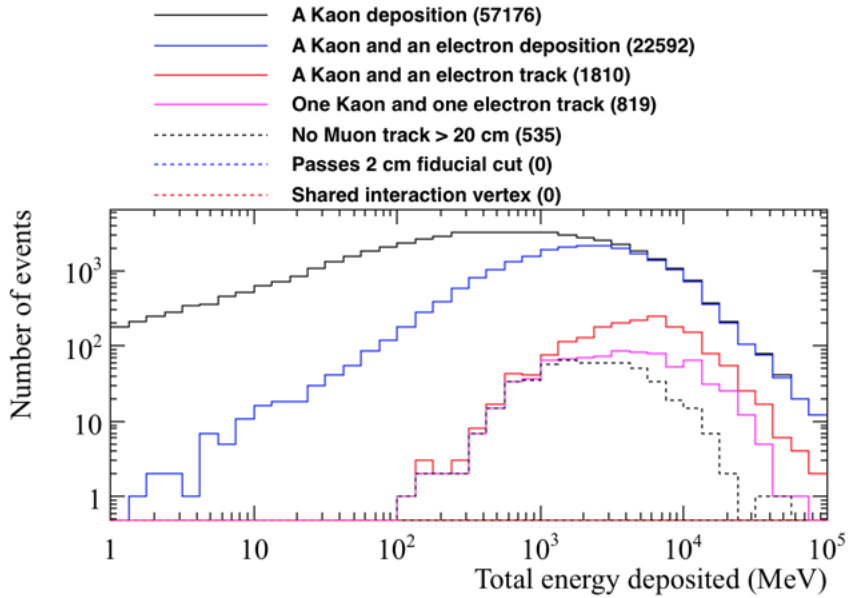


Fig. 6.7 The energy distribution of background events surviving the application of sequential cuts in the $n \rightarrow K^+ + e^-$ channel. The total energy deposited in the detector is plotted on the x axis.

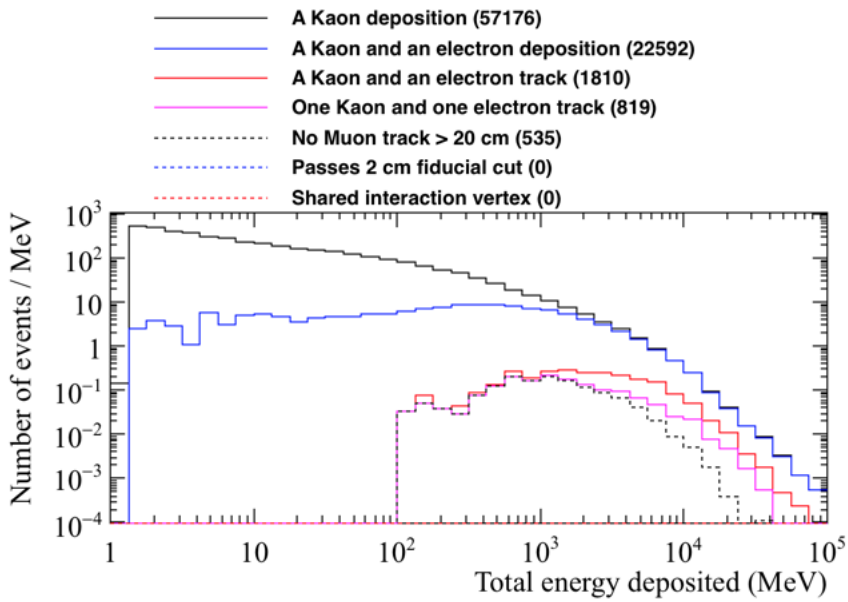


Fig. 6.8 The normalised energy distribution of background events surviving the application of sequential cuts in the $n \rightarrow K^+ + e^-$ channel. The total energy deposited in the detector is plotted on the x axis. The normalised energy distribution has been found by dividing the number of events within a bin by the bin energy.

Table 6.9 The number of events which could mimic a $n \rightarrow K^+ + e^-$ decay, when cuts are applied in isolation. Cuts are applied after it is found that the event contains at least one kaon track, and at least one electron shower. It is found that 1810 events have at least one kaon track, and at least one electron shower, this is shown in the top line of the table. The fiducial cut of 2 cm is seen to remove all of the events considered.

Cut that is applied	Num. events surviving cut
At least one kaon track, and electron shower	1810
Only one kaon track, and only one electron shower	819
No muon track that is longer than 20 cm in length	1303
No energy depositions within 2 cm of detector edge	0
The kaon and electron share a common vertex	137

electrons shower, in the event have been confirmed, could be relaxed. This would allow for the effectiveness of each of the subsequent cuts to be observed. Initially, each of the four subsequent cuts are applied in isolation. The number of events surviving each of the cuts is shown in Table 6.9.

The effectiveness of the fiducial cut is clearly apparent from Table 6.9, as it removes all 1810 events where there is both a kaon track and an electron shower. It is for this reason that the loss in fiducial volume that it causes is accepted. The requirement made on the proximity of the kaon track and electron shower is also seen to be very effective at removing background events. It is found that of the 819 events that have a single kaon track, and a single electron shower, in only 44 of them would the kaon and electron be considered to have a common vertex. When the additional constraint of there not being a muon with a track length of more than 20 cm present in the event is applied, only 14 events would survive the cuts. This shows that the only way to remove all potential background events is to apply the fiducial cut, or to make the some of the other criteria stricter, such as reducing the separation of the kaon track and the electron shower which constitutes a common vertex.

6.3.2 Signal events in the $n \rightarrow K^+ + e^-$ decay channel

It is important to confirm that the cuts developed to reject cosmic backgrounds, do not adversely affect the identification of nucleon decay events. For this reason, a sample of 10,000 neutron decay events in the DUNE far detector were generated using GENIE. Neutron decays are generated at random positions within the detector volume, and so it is possible that the decay occurs in the gaps between TPC volumes, as shown in Figure 6.6, or near the

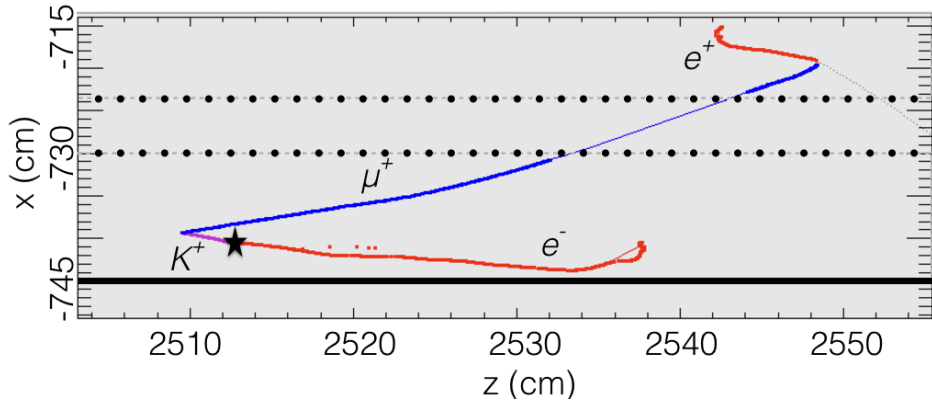


Fig. 6.9 A simulated $n \rightarrow K^+ + e^-$ decay which occurred near the edge of the detector volume. The path of the kaon produced in the decay is shown as a purple line. The path of the muon, produced by the decay of the kaon, is shown as a blue line. The paths which the electrons in the event took are shown as red lines. The electron at the bottom of the figure is the electron produced in the neutron decay, whilst the one at the top of the figure, is produced by the decay of the muon. The thin coloured lines show track segments which were in uninstrumented parts of the detector, such as gaps between TPCs and APAs. The solid black line shows the edge of the detector. The dotted black lines show the edges of the TPCs, and the black star shows the location at which the decay occurred. It can be seen that though the event is contained within the detector it is very close to the edge of the detector due to the location at which the decay occurred.

edge of the detector, as is shown in Figure 6.9.

The analysis performed on the cosmogenic background was primarily designed to reject background events, whilst also attempting to not use cuts which would also affect signal efficiency. Therefore, it is hoped that the loss of signal events will be minimal. When running the analysis on the simulated signal events, the same definitions for tracks, showers, and the ancestry of particles are used, as well as the same cuts that were outlined in Section 6.3.1.

The energy distribution of the signal events surviving the application of the sequential cuts is shown in Figure 6.10, this is the equivalent of Figure 6.7 for the cosmogenic background sample. The normalised energy distribution of signal events surviving the application of sequential cuts is shown in Figure 6.11, this is the equivalent of Figure 6.8 for the cosmogenic background sample. As before, the distribution of normalised energies is found by dividing the number of events by the bin energy.

When comparing Figures 6.10 and 6.11 with Figures 6.7 and 6.8, the most obvious difference is that when considering the nucleon decay events, the total energy deposited in

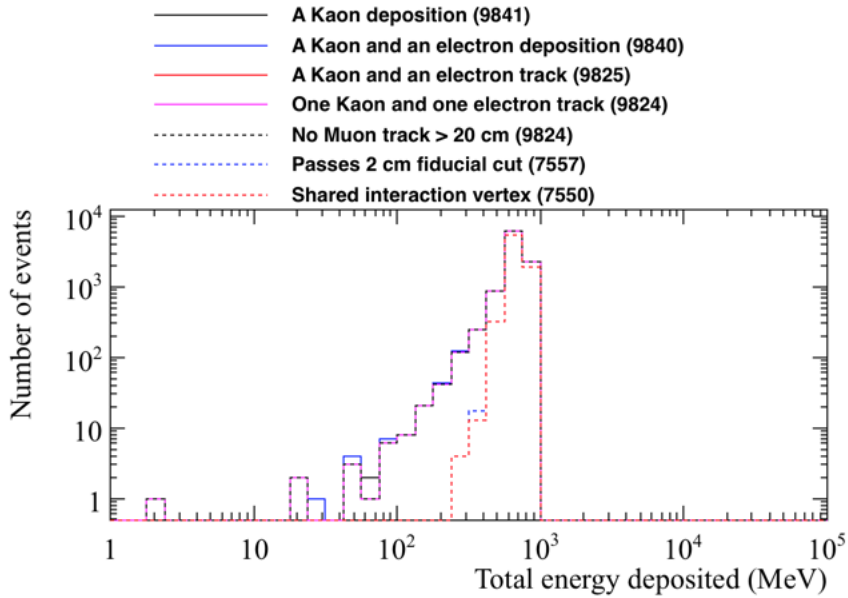


Fig. 6.10 The energy distribution of signal events surviving the application of sequential cuts in the $n \rightarrow K^+ + e^-$ channel. The total energy deposited in the detector is plotted on the x axis.

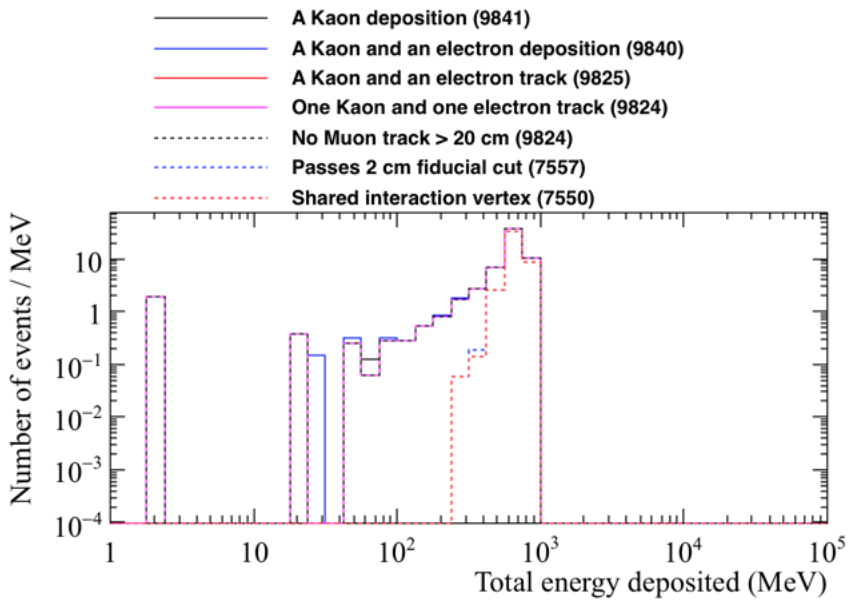


Fig. 6.11 The normalised energy distribution of signal events surviving the application of sequential cuts in the $n \rightarrow K^+ + e^-$ channel. The total energy deposited in the detector is plotted on the x axis. The normalised energy distribution has been found by dividing the number of events within a bin by the bin energy.

the detector never exceeds 1 GeV, whilst in the cosmogenic background sample, the energy deposited in the detector frequently exceeds 1 GeV. This is something which one would expect, as the simulated neutrons decay at rest, and so have a total energy of less than 1 GeV, meaning that there cannot be more than 1 GeV deposited in the detector. This is in stark contrast to the cosmogenic background, where the primary muons being generated have a mean energy of 283 GeV, as shown in Table 6.8. This means that many events will deposit significant amounts of energy in the detector, even if the primary muon narrowly misses the detector volume.

The initial cuts, requiring that both a kaon track and an electron shower are observed in the decay, show that there are occasions when either the kaon, or the electron, do not deposit energy in the detector. This affects very few events, though an example of one such event is shown in Figure 6.12, where it can be seen that the kaon decayed before entering the active volume, and so no track was found for it. It would be very difficult to identify this event as a signal event, as the presence of the kaon could only be inferred from the muon originating from the gap between the APAs, and the energy deposited by the kaon itself will not be reconstructed. Further compounding the identification of this event as a signal event, is the fact that the electron produced in the nucleon decay scatters back into the gap between the APAs. This means that a significant amount of the rest mass energy of the neutron would not be reconstructed.

The number of events which are removed by the fiducial cut is concerning, as when it is considered in conjunction with other cuts it removes almost 23% of events, this rises to almost 25% of events when it is applied in isolation. This suggests that the cut is too strict. The reason for this is that protons and neutrons are emitted from the nucleus in many of the simulated decays. Whilst the protons produced will create relatively short tracks, which are connected to the decay vertex, the neutrons will travel large distances, and cause energy depositions which are far away from the decay vertex. The faint grey dashed lines, which can be seen in Figure 6.12, show the spallation neutrons produced in the decay. None of the figures shown here contain spallation protons, but if they were present, they would be shown as additional purple lines originating from the decay vertex. It is predominantly the energy depositions from the spallation neutrons which are causing events to fail the “no energy depositions within 2 cm of the detector edge” cut. As a result it is likely that this cut needs to be relaxed, to instead be a cut on the amount of energy deposited within 2 cm of the detector edge. Figure 6.13 shows the amount of energy deposited within 2 cm, 5 cm, and 10 cm of the detector edges, for the simulated nucleon decay events (top), and the cosmogenic

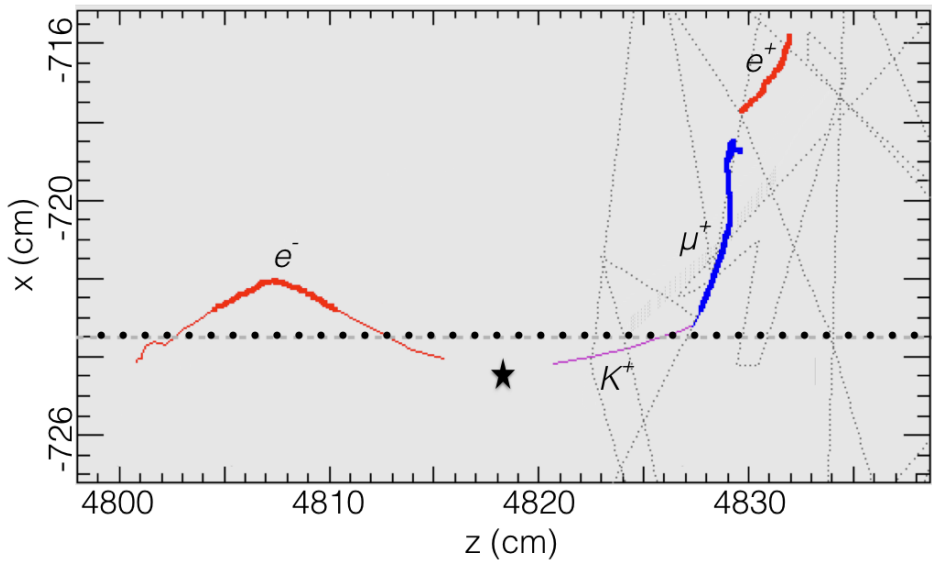


Fig. 6.12 A simulated $n \rightarrow K^+ + e^-$ decay where the kaon did not deposit any energy in the active volume. The path of the kaon produced in the decay is shown as a purple line. The path of the muon, produced by the decay of the kaon, is shown as a blue line. The paths which the electrons in the event took are shown as red lines. The electron on the left of the figure is the electron produced in the neutron decay, whilst the one on the right of the figure, is produced by the decay of the muon. The thin coloured lines show track segments which were in uninstrumented parts of the detector, such as gaps between TPCs and APAs. The dotted black lines show the edges of the TPCs, and the black star shows the location at which the decay occurred. It can be seen that the kaon decayed before it entered the active volume of the detector, and so no track was found for it. A significant portion of the distance which the electron from the decay travelled was also outside the active volume of the detector.

background events (bottom).

As can be seen from Figure 6.13, the amount of energy deposited near the detector edges is very different in the nucleon decay, and cosmogenic background events. As such, they can be relatively cleanly separated. A very conservative cut, designed to preserve as many of the simulated signal events as possible, which demands that there be no more than 100 MeV of energy deposited within 2 cm of the detector edge is used. Requiring that there be no more 100 MeV of energy deposited within 2 cm of the detector edges, removes only 19 of the 9824 signal events, whilst only 171 out of the 535 cosmic background events meet this requirement. Whilst this does mean that the fiducial cut no longer removes every event in the cosmic background sample, it does not cause the huge loss of signal events which was seen when the hard cut, of no energy depositions within 2 cm of the detector edge, was used. It is also important to remember that the requirement that the kaon track and the electron shower share a common vertex, as well as cuts on the energy deposition profiles, will still be applied to these 171 background events. For example, only 2 of the 171 events satisfy the requirement that the kaon track and the electron shower share a common vertex. It will be seen in Section 6.3.3, that the 2 events sharing a common vertex do not satisfy the energy distributions expected from a nucleon decay event.

The definition used to decide if the start of the kaon track, and the start of the electron shower, share a common vertex seems to be a reasonable requirement, as almost all of the signal events satisfy this definition. The distance between the start of the kaon track, and the start of the electron shower is shown in Figure 6.14. It can be seen that the separation between the two particles is very small (<0.1 cm) in most events. However, there are some events where the separations are very large (>10 cm). As discussed earlier, the decays in these events occur in the gaps between TPCs, such as that shown in Figure 6.6. When the requirement that the kaon track and the electron shower have a PoCA of less than 2 cm is then applied to these events, most of them are then seen to have a common interaction vertex. For example, this is found to be the case for the event shown in Figure 6.6. However, in some events the kaon track, and the electron shower, are still not found to have a common interaction vertex. Hand scanning of these events shows that in these events, the particles undergo scattering before entering the active volume, and so by the time that the energy depositions are collected, their trajectories are no longer closely aligned. This causes the calculated values of PoCA to be larger than 2 cm, and so they do meet the requirement that their trajectories are closely aligned.

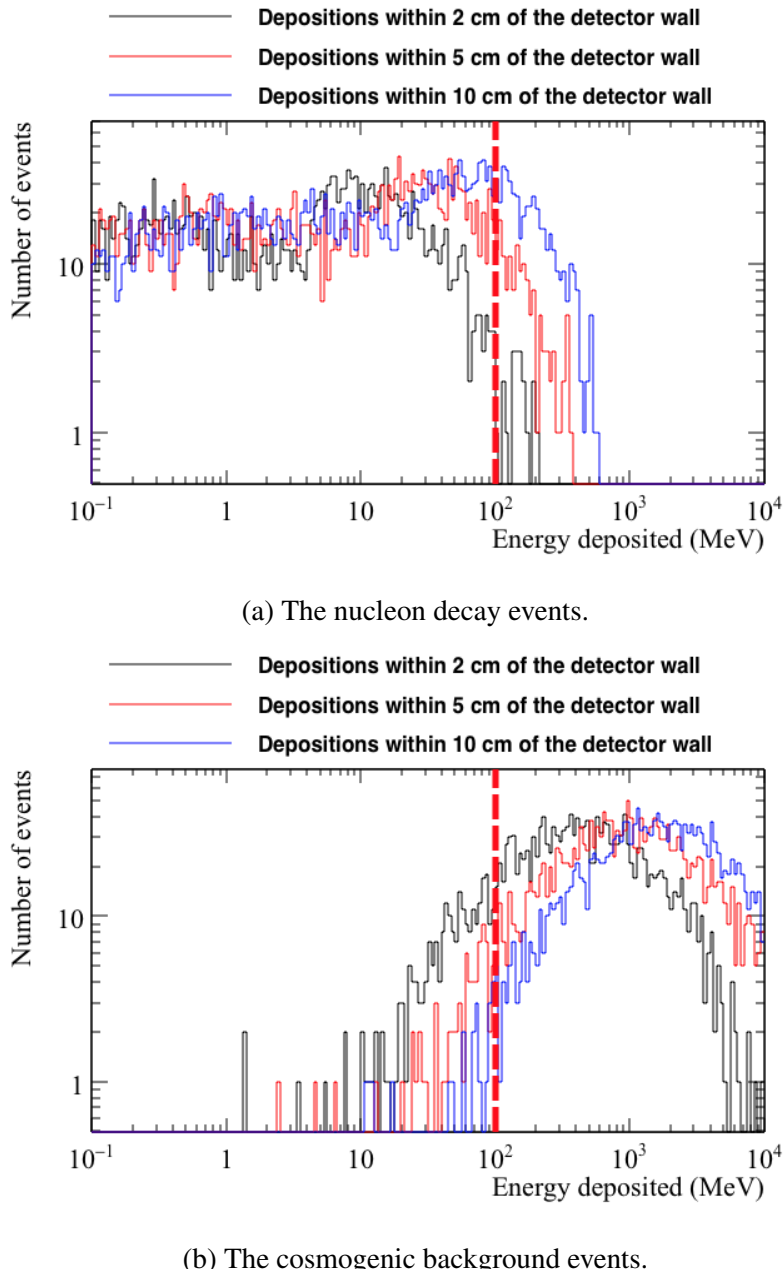


Fig. 6.13 The number of events, as a function of the energy deposited within 2 cm, 5 cm, and 10 cm of the detector edges. Top shows the energies which were deposited for the simulated neutron decay events. Bottom shows the energies which were deposited in the simulated cosmogenic background events. The histograms are filled after the cut requiring that there is at least one kaon track, and at least one electron shower in the event, is applied. As such, the histograms are filled with 9824 and 1810 events for the top and bottom histograms respectively. The dashed red line shows a preliminary cut on the energy deposited of 100 MeV.

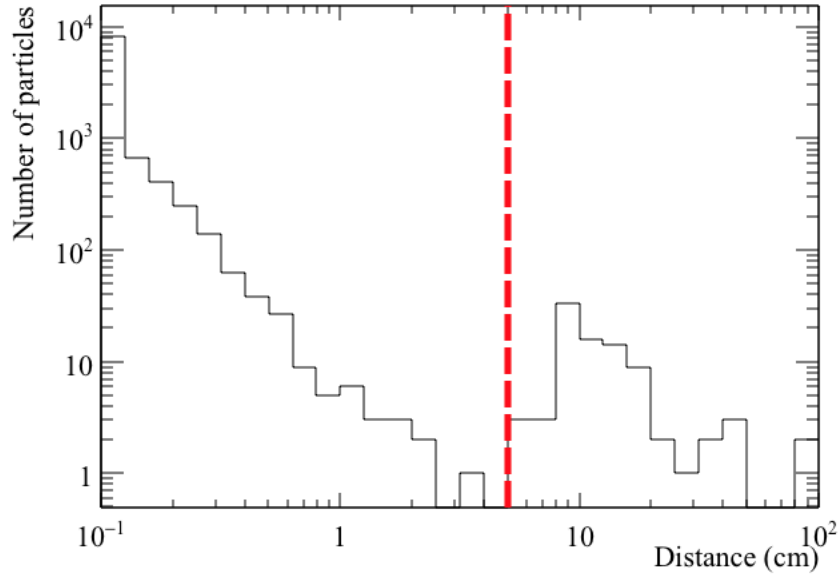
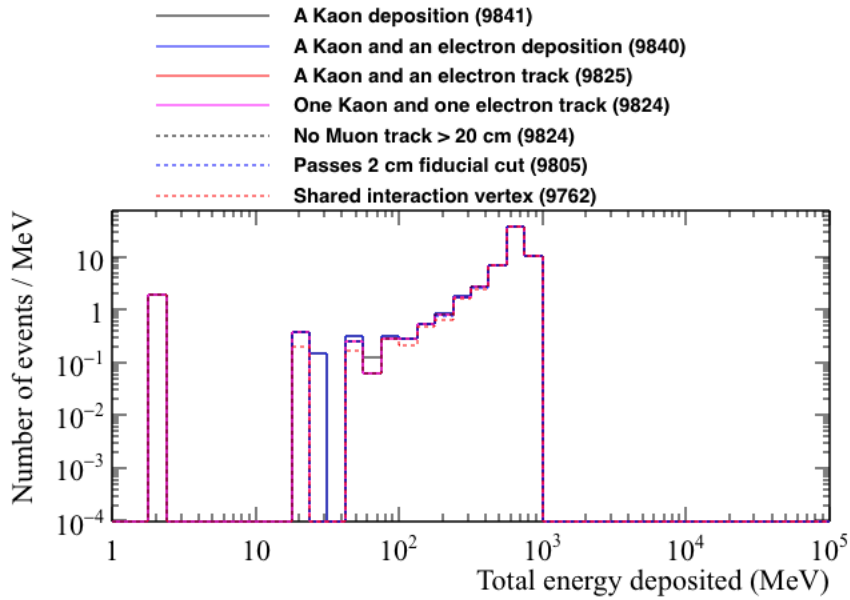


Fig. 6.14 The separation of the kaon and the electron produced in the $n \rightarrow K^+ + e^-$ decay channel. The dashed red line, drawn at a separation of 5 cm, shows the maximum possible separation a kaon and an electron could have, and still be considered to have a common vertex.

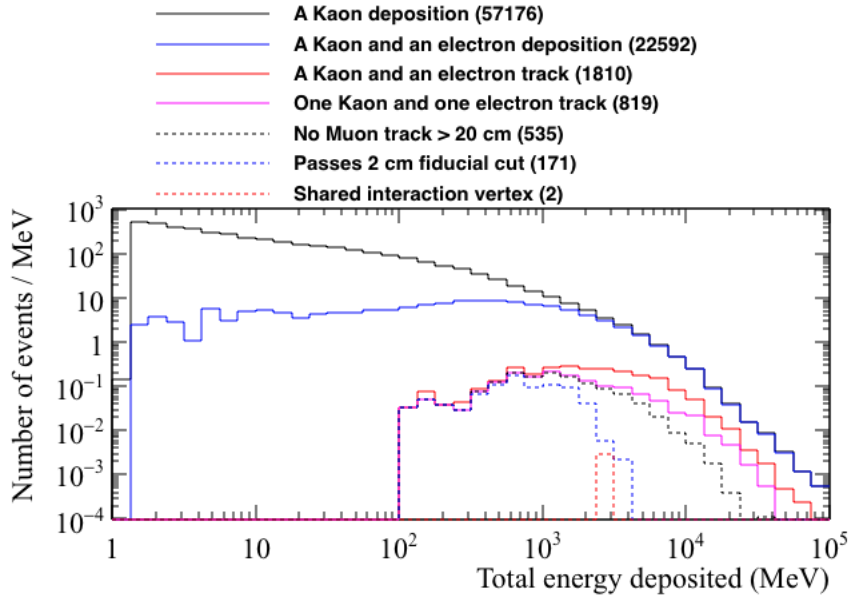
The normalised energy distributions of simulated decay events, and simulated cosmogenic background events, after the fiducial cut is changed to be a limit of 100 MeV of energy deposited within 2 cm of the detector edge, is shown in Figure 6.15. As before, the distribution of normalised energies is found by dividing the number of events by the bin energy.

The number of signal events which are removed by the cuts can be seen to be much more reasonable after the fiducial cut is modified, as less than 2.5% of signal events are removed as cuts are applied. It is seen that in many of the simulated decay events which fail the cuts, at least one of the kaon, or the electron, are not contained in the detector. This means that, either no depositions are found for the particle, or it deposits significant amounts of energy as it leaves the detector.

It can be seen that though 2 of the cosmic background events pass the application of all cuts, the total energy deposited in the detector is not less than 1 GeV in either of these events. This means that the total energy deposited in the detector is more than the rest mass of a neutron, and so the event is not consistent with being from the decay of a neutron at rest.



(a) The normalised energy distribution of signal events.



(b) The normalised energy distribution of cosmic background events.

Fig. 6.15 The normalised energy distribution of signal events, and cosmic background events, surviving the application of sequential cuts, after the fiducial cut is modified. The total energy deposited in the detector is plotted on the x axis. The normalised energy distribution has been found by dividing the number of events within a bin by the bin energy.

However, it is still prudent to determine the expected energy deposition distribution for the signal events, in order to ensure that a clean separation can be observed between the signal, and background events.

6.3.3 Energy constraints on the cosmogenic background to the $n \rightarrow K^+ + e^-$ decay channel

As outlined in Section 6.3.1, it is possible to exclude background events from signal events, using the distribution of how energy is deposited in the detector. The energy criteria which were previously outlined were;

- The energy directly deposited by the kaon.
- The energy deposited by the kaon decay products.
- The energy directly deposited by the electron.
- The energy deposited near the shared kaon and electron vertex.
- The energy deposited in the detector which does not fit any of the above criteria.

Following the earlier discussions in Section 6.3, it should be clear that the energy directly deposited by the kaon corresponds to the sum of all energy depositions, which are due to the kaon or its interaction products. Equivalently, the energy directly deposited by the electron, corresponds to the sum of all energy depositions which are due to the electron as it showers, and any particles created as a result of the shower. The energy deposited by the kaon decay products would include all depositions by the muon and subsequent electron, in the case that the kaon decayed via $K^+ \rightarrow \mu^+ + \nu_\mu$, and then the muon decayed via $\mu^+ \rightarrow e^+ + \nu_e + \nu_\mu$. The energy deposited near the shared kaon and electron vertex, would primarily consist of energy depositions due to spallation products. These depositions would largely be due to protons, though may also include some depositions due to neutrons too, if they deposited energy near the interaction vertex. Any depositions within 5 cm of either, the start of the kaon track, or the start of the electron shower, are considered 'near' to the interaction vertex. It is necessary to consider the energy depositions which are close to the start of both particles, because, as shown in Figure 6.6, occasionally the particles are separated by the APA gaps. When energy depositions are within 5 cm of both, the start of the kaon track, and the electron shower, they are only considered to be near to the start of the kaon track. This is done so as to avoid 'double counting' these energy depositions. As can be seen from Figure 6.14, the

separation between the start of the kaon track, and the start of the electron shower, is normally very small. This means that the sum of the 'near' energy depositions, can be considered to be the energy depositions 'near' the common vertex between the kaon track and the electron shower. The final criteria, of any depositions which do not fit the above description, would largely consist of energy depositions due to the spallation neutrons in the decay sample. However, in the cosmic background sample, this would include all depositions by muons, pions, and any other particles in the detector, which are not associated with either the kaon or the electron. In later discussions these depositions are generally labelled as 'other' energy depositions.

In presenting the separation of simulated cosmic background events, and simulated neutron decay events, the important distributions to consider are as follows:

- The energy directly deposited by the kaon, against the energy directly deposited by the electron. This is shown in Figure 6.16.
- The energy directly deposited by the kaon, plus the energy directly deposited by the electron, against the energy deposited near the shared kaon and electron vertex. This is shown in Figure 6.17.
- The energy deposited by the kaon, including decay products, against the energy deposited in the detector which does not fit any of the other criteria. This is shown in Figure 6.18.
- The energy deposited by the kaon, including decay products, plus the energy directly deposited by the electron, plus the energy deposited near the shared kaon and electron vertex, against the energy deposited in the detector which does not fit any of the other criteria. This is shown in Figure 6.19.

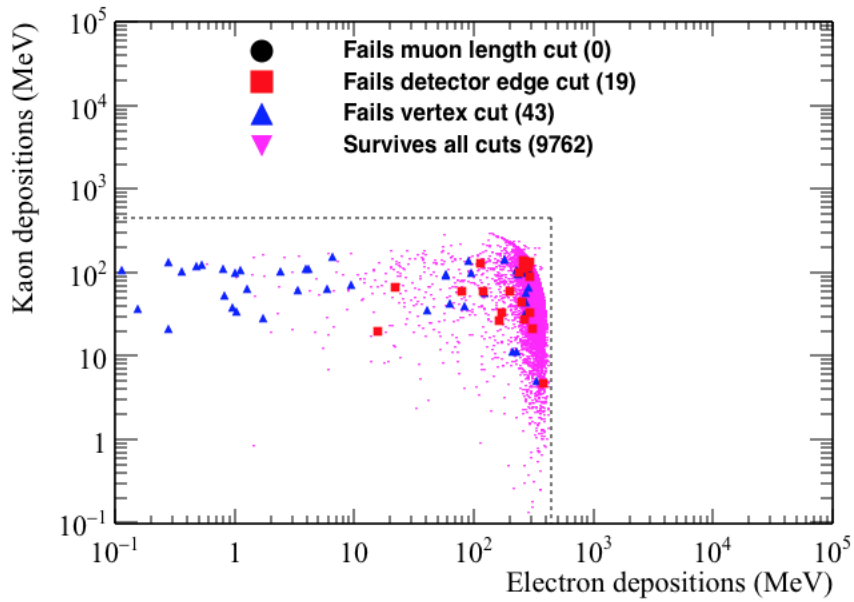
Each of these figures will be discussed in turn below.

When looking at the figures presented, the events which pass all cuts in the simulated decay sample have been plotted with smaller markers. This is to allow the events which fail the cuts to be visible. The markers have also been plotted so as to have the earlier cuts in the foreground in the nucleon decay sample, and the later cuts to be in the foreground in the cosmic background sample. This is done so as to prevent the events which fail (pass) the cuts, from being overwhelmed by the more numerous events which pass (fail) the cuts, in the simulated nucleon decay (cosmic background) sample.

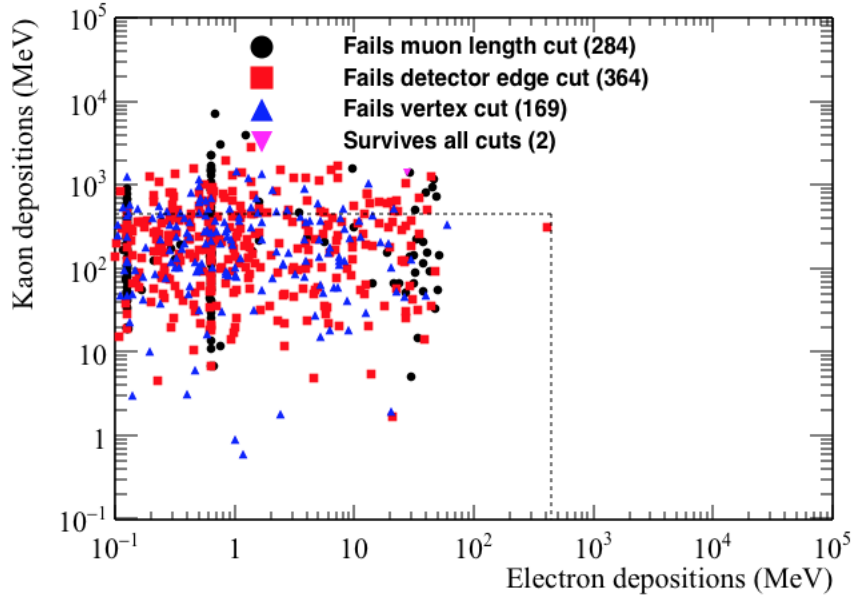
Additionally, in the figures outlined above, there is a box in the lower left corner of the plots, produced by dashed grey lines. This constitutes the expected energy region where a signal event would lie on the graph, and has been drawn so as to contain as many of the simulated signal events as possible. The expected energy regions are propagated down to 0 MeV on both the x and y axis of all figures, and so it is possible for points not drawn here to pass the applied cuts. This is because it is possible for signal events to have either no energy identified as 'near' the common interaction vertex, such as the event shown in Figure 6.6. It is also possible for there to be no energy deposited in the detector which would be classed as 'other' energy depositions.

From Figure 6.16, it can be seen that the electron energy distribution in the cosmic background sample, is very different from the one seen in the simulated neutron decay sample. This is shown by the energies deposited by electrons in the nucleon decay sample being tightly concentrated between ~ 200 and ~ 400 MeV, whilst in the cosmic background sample, the energy deposited by the electron is almost always less than ~ 50 MeV. Many of the electrons in the cosmic background sample deposit less than 1 MeV of energy in the detector, and so are not shown in Figure 6.16b. This is why the events where the kaon and electron share a common vertex are not shown in the cosmic background sample, as the electrons in these events deposit less than 1 MeV of energy in the detector. Realistically, these electrons are unlikely to be reconstructed due to their extremely low energies. From Figure 6.16a, it can be seen that some of the electrons produced in the nucleon decay events also deposit very little energy in the detector, though these events generally fail either the fiducial cut, or the vertex cut. An explanation as to why these events fail the cuts was presented in Section 6.3.2, when considering Figure 6.12.

From Figure 6.17, it can be seen that for the simulated nucleon decay events, as the energy deposited near the kaon and electron vertex increases, the sum of the energy deposited by the kaon and electron decreases. This is reasonable, because, when the spallation protons and neutrons have more energy, the kaon and electron will have less energy. The decrease in the energy deposited by the kaon and the electron, is roughly consistent with the increase in the amount of energy which is deposited near their shared vertex. This means that the sum of the three energies is generally around 450 MeV. This is largely inconsistent with the simulated cosmic background events, where many events have no energy deposited near the shared vertex of the kaon and electron. However, the lack of energy deposited near the shared kaon and electron vertex cannot be used to discriminate against cosmogenic background events, as this is also observed in many simulated nucleon decay events. What can be used to

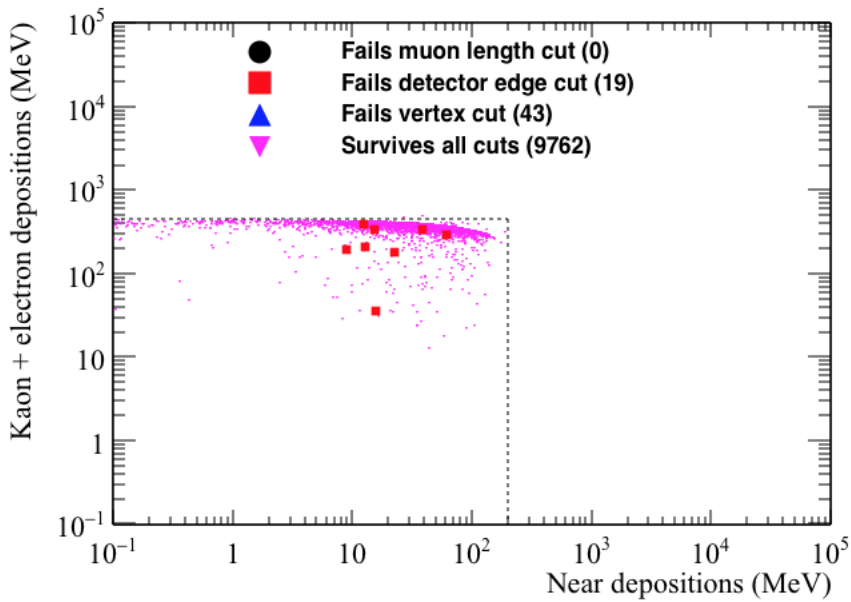


(a) The energy distribution of signal events.

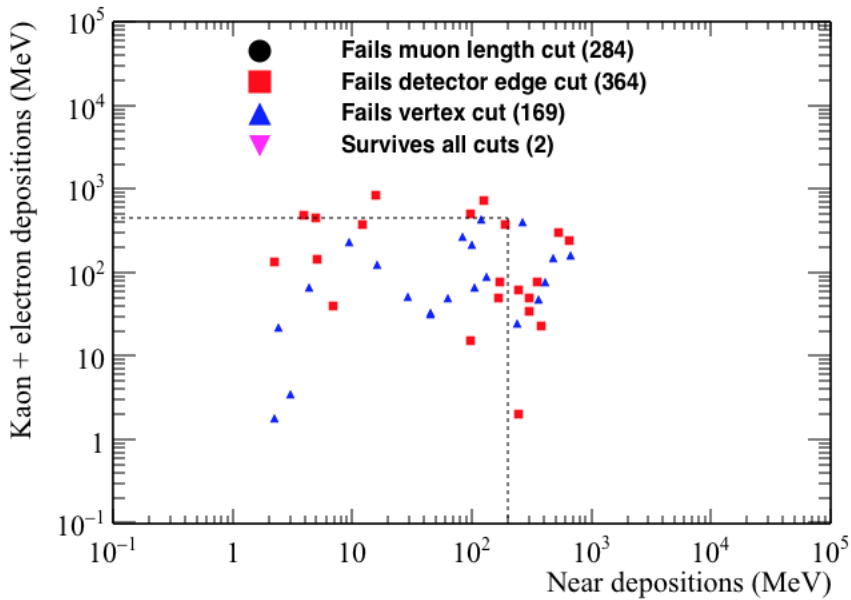


(b) The energy distribution of cosmic background events.

Fig. 6.16 The energy directly deposited by kaons, as a function of the energy directly deposited by electrons, in the simulated nucleon decay, and cosmic background samples. The events failing the application of the muon length (black circle), fiducial (red box) and vertex (blue triangle) cuts, as well as the events passing all cuts (pink triangle) are shown.

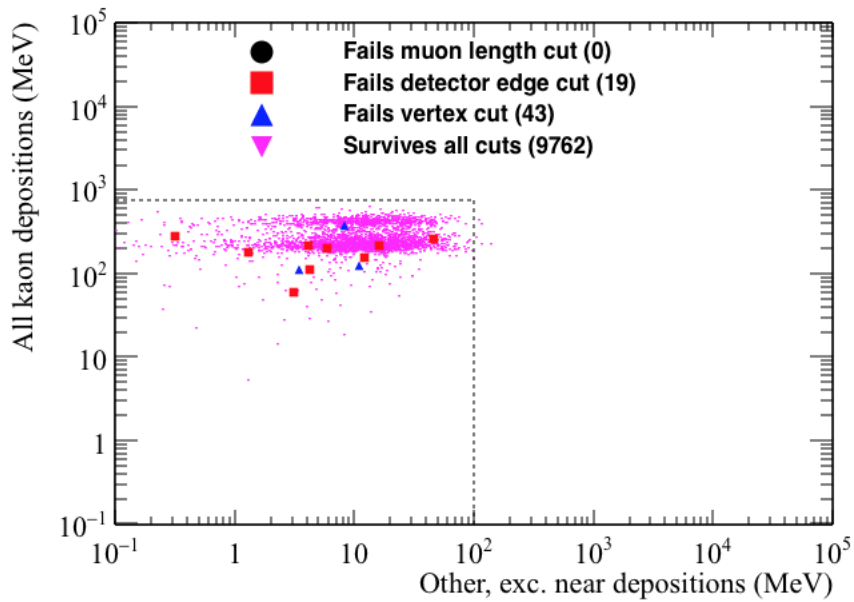


(a) The energy distribution of signal events.

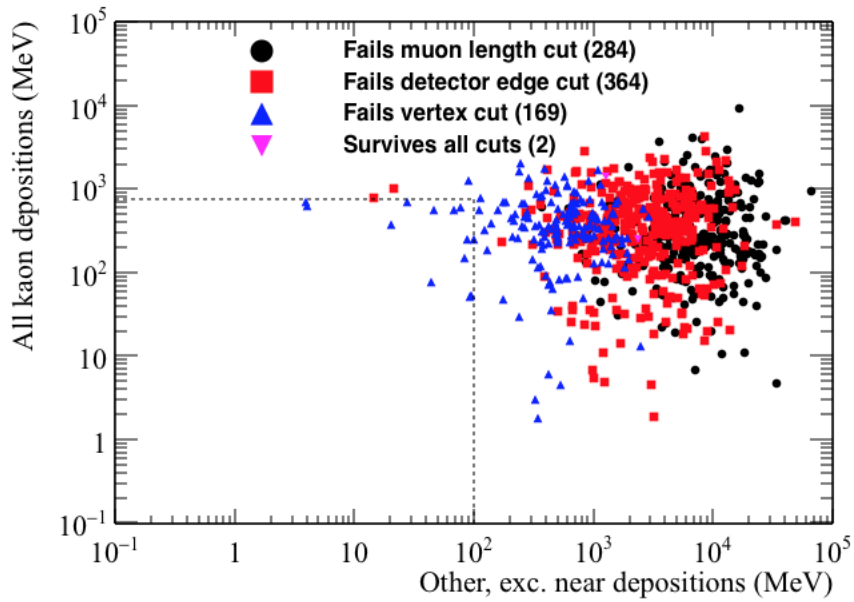


(b) The energy distribution of cosmic background events.

Fig. 6.17 The energy directly deposited by kaons, plus the energy directly deposited by electrons, as a function of the energy deposited near the kaon and electron vertex, in the simulated nucleon decay, and cosmic background samples. The events failing the application of the muon length (black circle), fiducial (red box) and vertex (blue triangle) cuts, as well as the events passing all cuts (pink triangle) are shown.

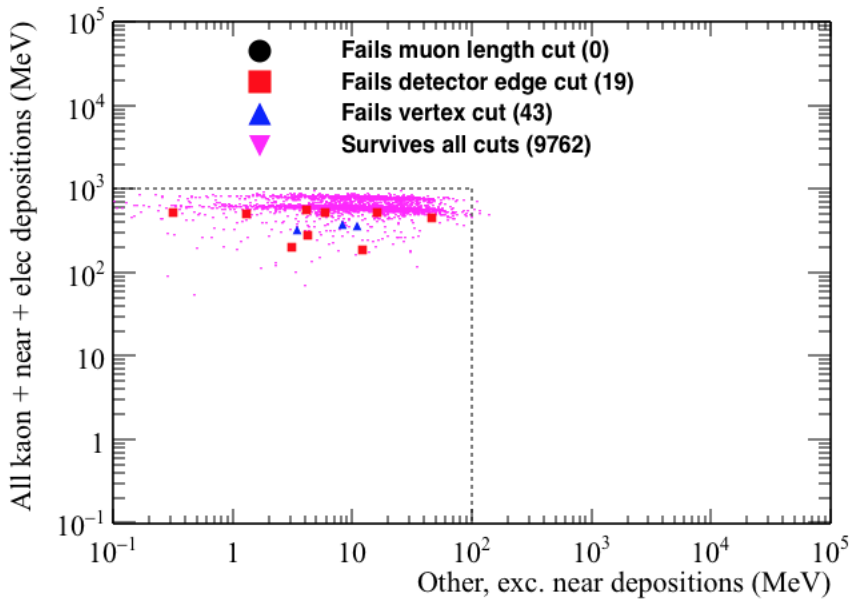


(a) The energy distribution of signal events.

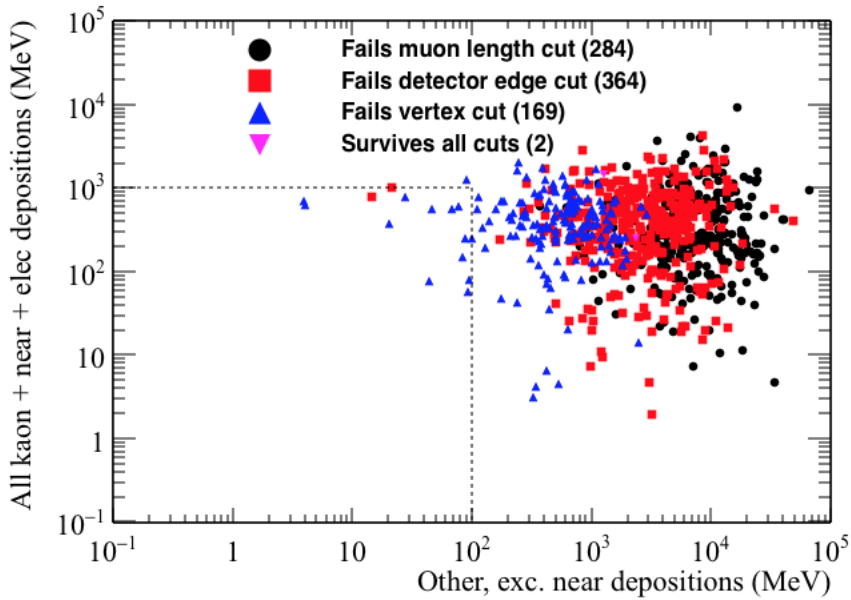


(b) The energy distribution of cosmic background events.

Fig. 6.18 The energy directly deposited by kaons, plus the energy deposited by the kaon decay products, as a function of the energy depositions which do not fit any of the other criteria, in the simulated nucleon decay, and cosmic background samples. The events failing the application of the muon length (black circle), fiducial (red box) and vertex (blue triangle) cuts, as well as the events passing all cuts (pink triangle) are shown.



(a) The energy distribution of signal events.



(b) The energy distribution of cosmic background events.

Fig. 6.19 The energy directly deposited by kaons, plus the energy deposited by the kaon decay products, plus the energy directly deposited by electrons, plus the energy deposited near the kaon and electron vertex, as a function of the energy depositions which do not fit any of the other criteria, in the simulated nucleon decay, and cosmic background samples. The events failing the application of the muon length (black circle), fiducial (red box) and vertex (blue triangle) cuts, as well as the events passing all cuts (pink triangle) are shown.

separate cosmic background events from nucleon decay events though, is the sum of the three energy criteria, as it can be seen that this would rarely be around 450 MeV in the cosmic background sample.

Figure 6.18, shows that the sum of all energy deposits attributed to the kaon, against the sum of all energy depositions which are considered to be 'other' energy depositions, is very different in the two samples. The total energy deposited in the detector which is attributed to the kaon, is found by combining the energy directly deposited by the kaon, with the energy deposited by the kaon decay products. The difference seen in the cosmogenic and signal events, is primarily due to the large amount of 'other' energy depositions which are seen in the cosmogenic background sample. This is expected, as in cosmogenic induced events, many particles may enter the detector, and they will cause energy depositions which are not connected to the kaon track, the electron shower, or their common vertex, should one exist. This gives the most powerful mechanism for the discrimination between signal and background events, as in many background events the 'other' energy deposited in the detector will be very large, and will cause the total energy deposited in the detector to be more than the rest mass of a neutron. Also, the 'other' energy deposited by background events in the detector, will likely be concentrated in track or shower like structures. This is in contrast to signal events, where the 'other' energy depositions are likely to be isolated depositions due to the spallation neutrons interacting in the detector. Classifying the structure of the 'other' energy depositions is not performed here, though it could be included should any cosmic events appear to mimic a signal event. However, given the clear separation in the amount of 'other' energy deposited in the detector, it is not currently required.

A striking feature of Figure 6.18a, is the banded structure of the total energy deposited in the detector which can be attributed to the kaon. This banded structure is due to the amount of energy from the kaon decay which is not reconstructed. The relative strengths of these structural features is due to the various probabilities of the kaon decay modes. Some of the more common decay modes are shown in Table 6.10, along with their probabilities. The amount of energy which is reconstructed from the particles produced by the decay of the kaon is shown in Figure 6.20.

As can be seen in Table 6.10, the most common decay mode for the kaon involves the production of a ν_μ , which will likely leave the detector without interacting. This will mean that a significant proportion of the kaon rest mass energy will not be reconstructed, as the kaon is assumed to decay at rest. It is for this reason that the most likely amount of energy

Table 6.10 The most common decay modes of charged kaons, and their probabilities [57]. The decay modes shown are with reference to K^+ , though the decays of K^- are the charge conjugations of these decays.

Decay mode	Measured probability (%)
$K^+ \rightarrow \mu^+ + \nu_\mu$	63.56 ± 0.11
$K^+ \rightarrow \pi^+ + \pi^0$	20.67 ± 0.08
$K^+ \rightarrow \pi^+ + \pi^+ + \pi^-$	5.583 ± 0.024
$K^+ \rightarrow \pi^0 + e^+ + \nu_e$	5.07 ± 0.04
$K^+ \rightarrow \pi^0 + \mu^+ + \nu_\mu$	3.352 ± 0.033
$K^+ \rightarrow \pi^+ + \pi^0 + \pi^0$	1.760 ± 0.023

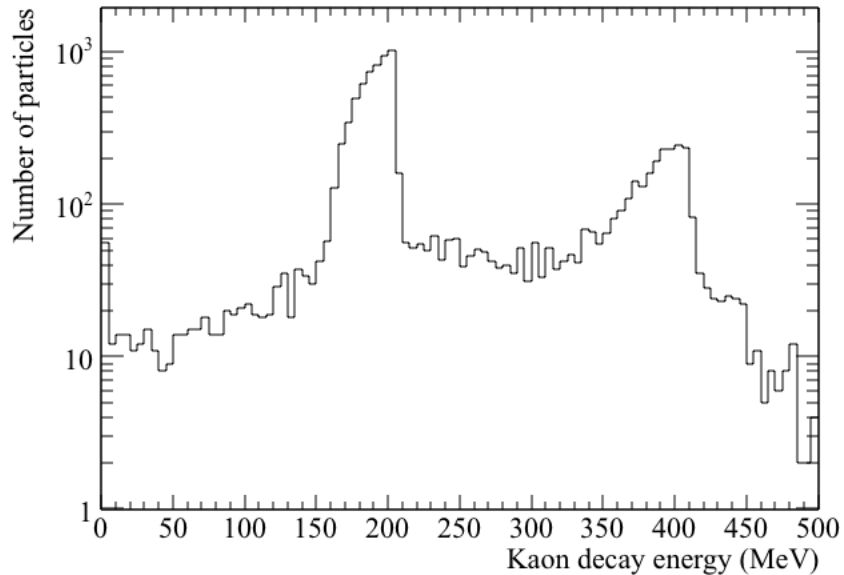


Fig. 6.20 The number of events, as a function of the energy deposited by the kaon decay products. The energies deposited due to the $K^+ \rightarrow \mu^+ + \nu_\mu$ and $K^+ \rightarrow \pi^+ + \pi^0$ decay channels, can be seen in the peaks at roughly 200 MeV, and 400 MeV respectively. The underlying continuous distribution of deposited is caused by the 3-body decays shown in Table 6.10.

deposited by the kaon decay products is around 200 MeV. The second most likely decay mode is also a 2-body decay, and one would expect that the energies from both the π^+ and π^0 would be reconstructed. Evidently some energy is either missed in the APAs gaps, or escapes the detector, as the second peak at 400 MeV, is less than the rest mass of the kaon. This missing energy is likely due to the energy associated with the decay of the π^0 , as when it decays it is likely to produce two EM showers which may escape the detector, or deposit significant amounts of energy in the APA gaps. Neutrinos are also present in many of the other decay modes, and so will also have large amounts of missing energies, whilst the 3-body decay modes will produce particles which have a continuous distribution of energies. These decay modes, along with the missing, and lost energies, in the two most probable decay modes, cause the energy deposited by the kaon decay products to be a continuous distribution, with two large peaks at roughly 200 MeV and 400 MeV. The energy deposited by the kaon decay products in the cosmogenic background sample may not follow this energy profile, as it is likely that the kaon will not decay at rest.

Finally, Figure 6.19 shows the total energy attributed to both the kaon and to the electron, plus any energy deposited near their shared interaction vertex, against any 'other' energy depositions. As the total energy attributed to the kaon is plotted, this includes the energy deposited by the kaon decay products, as was the case in Figure 6.18. As was seen in Figure 6.18, there is a clear separation between the simulated signal events, and the cosmic background events. This is again due to the large amount of 'other' energy depositions observed in the background sample. It is interesting to compare Figures 6.18b and 6.19b, as they are very similar. This is to be expected from Figure 6.16b, where it was seen that the energy deposited by the electron was rarely more than 10 MeV, and only in one event was it more than 100 MeV. This was in stark contrast to Figure 6.16a, where the energy deposited in almost all of the electron showers was more than 100 MeV. It is for this reason that whilst there is a large difference in Figure 6.18a and 6.19a, due to addition of the significant amount of energy deposited by the electron showers, there is relatively little difference between Figures 6.18b and 6.19b. The change, or lack thereof, of the energy plotted between Figures 6.18 and 6.19, thus provides another powerful metric by which to discriminate signal events, from background events.

A significant difference between Figures 6.18a and 6.19a, is the relatively narrow band of energies plotted on the y axis of Figure 6.19a, when compared to Figure 6.18a. This is because of the relationship between the energy deposited by the kaon, the energy deposited by the electron shower, and the energy deposited near their shared interaction vertex.

This was seen in Figure 6.17a, where the sum of the three energies was roughly 450 MeV. This means that for events where the kaon deposited relatively little energy, shown by the population of events at low total kaon energies in Figure 6.18a, the energy deposited by the electron shower, plus the energy deposited near the shared interaction vertex, will be large.

Following the application of all energy cuts, as outlined by the grey dashed boxes in Figures 6.16, 6.17, 6.18, and 6.19, only 17 of the 9762 simulated signal events, which passed all subsequent cuts, are removed. It is found that none of the events survive the application of all cuts. If only the energy cuts, and the requirement that there be at least one kaon track, and at least one electron shower in the event, are applied, it is found that only 12 background candidates would survive the application of cuts. None of these events present serious contenders for signal events though, as all of events fail the vertex cut, and many have electrons which have very little energy (< 10 MeV), and large energy depositions near the edge of the detector.

Many of the signal events which are removed by the energy cuts have large amounts of 'other' energy depositions, though they would no longer be removed if the limit on 'other' depositions were raised to 200 MeV. Though increasing the cut on 'other' energy depositions to 200 MeV would still result in all background events being removed, it would mean that the limit was much closer to the regions of 'other' energy depositions which are populated in Figures 6.18, and 6.19. As a result if a candidate event were to have between 100 and 200 MeV of energy depositions considered to be 'other' energy depositions, its energy distributions would have to be carefully checked in order to verify that it is definitively not due to a background event. It is envisioned that the process by which this would be done, would be to consider how the 'other' energy deposits are distributed in the detector, because, as discussed earlier, in a signal event it is likely that they would be isolated depositions, whereas in a background event, there would likely be 'track-like' objects, which are disconnected from the kaon and electron vertex.

Therefore, the result of a preliminary study on the background rejection for the $n \rightarrow K^+ + e^-$ decay channel, is that one would expect no cosmogenically induced background events in a single 10 kt module, over the course of XXX years of detector live time. In the absence of any candidate events, this would correspond to a partial lifetime of the neutron in the $n \rightarrow K^+ + e^-$ decay channel of $XXX \times 10^{-XX}$ years.

It is also found that using the cuts outlined above, only 2.55% of signal events would not be identified as being from nucleon decay events. However, it would be difficult to identify

many of the events considered here as nucleon decay events. This is because, in many events at least one of the kaon, or electron, leaves the detector. This would mean that accurate particle identification, and the correct calculation of initial kinetic energy, would be very difficult. Therefore, one could argue that the figure of 97.45% nucleon decays being able to be identified as signal events is incorrect. This is because in only 9,216 of the 10,000 simulated decay events, are both the kaon, and the electron, contained in the detector. When only these 9,216 events are considered, it is found that 9,177 events survive the application of all cuts. This represents a signal efficiency of 99.58%. It is found that the events which fail cuts either occur near the edge of the detector, as in Figure 6.13, or scatter whilst outside of the active volume of the detector, as presented when discussing Figure 6.6. As such, one could argue that the signal efficiency, using the cuts presented here is as high as 99.58%. However, given the lack of signal mimicking background events observed in this study, it may be possible to identify many of the signal events where the kaon and/or electron are not contained in the detector, given the rest of the event topology.

6.3.4 Future improvements to nucleon decay studies and conclusions

Thus far, nucleon decay studies have only been performed on Monte Carlo truth information, and so have not used reconstructed objects. The extension of the analyses to include work on tracks is an important next step, as then the full analysis, which would be applied on real data, can be tested. Preliminary studies have begun on hit reconstruction, and involve running a filter on the muons used in the earlier analyses. This is because the number of events which are saved to disk would be prohibitive to running the full reconstruction process. As such, only events which meet the following criteria will be reconstructed [143];

- A minimum of 10 MeV deposited in the detector volume.
- A maximum of 3,000 MeV deposited in the detector volume.
- A maximum of 5 MeV deposited within 10 cm of the detector edge.

These criteria are designed to be broad enough that the full range of nucleon decay modes can be studied, including di-nucleon decay modes. This is why the maximum deposited energy greatly exceeds the rest mass of a single nucleon. This also accounts for the fact that during reconstruction some energy depositions may not be reconstructed, so even though the total energy deposited in the detector is 3 GeV, the total reconstructed energy may be less.

Upon performing reconstruction, and hence energy and position smearing, it is likely that the energy cuts which were outlined above will have to be broadened. This may result in more background events being contained within the expected energy distributions for signal events, however the effectiveness of the cuts to remove background events should be largely unaffected. The reason for this, is that upon performing reconstruction, the separation of the kaon and electron track will not decrease, and so the cut will remain equally as effective. The only cut which may be less effective is the requirement that there only be one kaon track, and only one electron shower in the event. This is because some of the low energy electron showers may not be reconstructed. However, as shown in the discussion of Table 6.9, when this cut is relaxed in the background sample, no events passed all cuts when the strict limit of no energy depositions within 2 cm of the detector wall is used. When this is relaxed to no more than 100 MeV of energy depositions within 2 cm of the detector walls, 10 events are found to pass the requirement that the kaon and electron share a common vertex. However, no events are then found to satisfy the energy requirements, due to large amounts of 'other' energy depositions.

The reduced reconstruction efficiency will also affect the nucleon decay signals and so this, combined with the broader distributions of energies which will be reconstructed, will likely mean that the efficiency with which signal events can be identified will likely decrease. However, it is envisioned that there will still be no background events which survive the application of all cuts, and so the observation of a single event in the DUNE detector would provide a robust indication of nucleon decay.

Chapter 7

Conclusion

References

- [1] G. Aad et al. Observation of a new particle in the search for the Standard Model Higgs boson with the ATLAS detector at the LHC. *Phys. Lett.*, B716:1–29, 2012.
- [2] S. Chatrchyan et al. Observation of a new boson at a mass of 125 GeV with the CMS experiment at the LHC. *Phys. Lett.*, B716:30–61, 2012.
- [3] B. P. Abbott et al. Observation of gravitational waves from a binary black hole merger. *Phys. Rev. Lett.*, 116:061102, Feb 2016.
- [4] Y. Fukuda et al. Evidence for oscillation of atmospheric neutrinos. *Phys. Rev. Lett.*, 81:1562–1567, Aug 1998.
- [5] Q. R. Ahmad et al. Direct evidence for neutrino flavor transformation from neutral-current interactions in the sudbury neutrino observatory. *Phys. Rev. Lett.*, 89:011301, Jun 2002.
- [6] W. Pauli. Open letter to the Gauverein meeting in Tubingen, Dec 1930.
- [7] E. Fermi. An attempt of a theory of beta radiation. 1. *Z. Phys.*, 88:161–177, 1934.
- [8] O. Kofoed-Hansen. Maximum β -energies and the mass of the neutrino. *Phys. Rev.*, 71:451–452, Apr 1947.
- [9] G. C. Hanna and B. Pontecorvo. The β -spectrum of h^3 . *Phys. Rev.*, 75:983–984, Mar 1949.
- [10] L. M. Langer and R. J. D. Moffat. The beta-spectrum of tritium and the mass of the neutrino. *Phys. Rev.*, 88:689–694, Nov 1952.
- [11] C. L. Cowan, F. Reines, F. B. Harrison, H. W. Kruse, and A. D. McGuire. Detection of the free neutrino: A Confirmation. *Science*, 124:103–104, 1956.
- [12] G. Danby, J-M. Gaillard, K. Goulian, L. M. Lederman, N. Mistry, M. Schwartz, and J. Steinberger. Observation of high-energy neutrino reactions and the existence of two kinds of neutrinos. *Phys. Rev. Lett.*, 9:36–44, Jul 1962.
- [13] R. Davis, D. S. Harmer, and K. C. Hoffman. Search for neutrinos from the sun. *Phys. Rev. Lett.*, 20:1205–1209, May 1968.
- [14] B. T. Cleveland et al. Measurement of the solar electron neutrino flux with the Homestake chlorine detector. *Astrophys. J.*, 496:505–526, 1998.

- [15] B. Pontecorvo. Mesonium and anti-mesonium. *Sov. Phys. JETP*, 6:429, 1957. [Zh. Eksp. Teor. Fiz.33,549(1957)].
- [16] K. S. Hirata et al. Observation of ${}^8\text{B}$ solar neutrinos in the kamiokande-ii detector. *Phys. Rev. Lett.*, 63:16–19, Jul 1989.
- [17] M. L. Perl et al. Evidence for anomalous lepton production in $e^+ - e^-$ annihilation. *Phys. Rev. Lett.*, 35:1489–1492, Dec 1975.
- [18] K. Kodama et al. Observation of tau neutrino interactions. *Physics Letters B*, 504(3):218 – 224, 2001.
- [19] Q. R. Ahmad et al. Measurement of the rate of $\nu_e + d \rightarrow p + p + e^-$ interactions produced by ${}^8\text{B}$ solar neutrinos at the Sudbury Neutrino Observatory. *Phys. Rev. Lett.*, 87:071301, 2001.
- [20] S. Ritz et al. Building for Discovery: Strategic Plan for U.S. Particle Physics in the Global Context. 2014.
- [21] LBNE Collaboration. Long-Baseline Neutrino Experiment (LBNE) Project, Volume 1: The LBNE Project. Technical Report LBNE-doc-5235, Oct 2012.
- [22] LBNE Collaboration. Long-Baseline Neutrino Experiment (LBNE) Project, Volume 2: The Beamline at the Near Site. Technical Report LBNE-doc-4317, Oct 2012.
- [23] LBNE Collaboration. Long-Baseline Neutrino Experiment (LBNE) Project, Volume 3: Detectors at the Near Site. Technical Report LBNE-doc-4724, Oct 2012.
- [24] LBNE Collaboration. Long-Baseline Neutrino Experiment (LBNE) Project, Volume 4: The Liquird Argon Detector at the Far Site. Technical Report LBNE-doc-4892, Oct 2012.
- [25] LBNE Collaboration. Long-Baseline Neutrino Experiment (LBNE) Project, Volume 5: Conventional Facilities at the Near Site. Technical Report LBNE-doc-4623, Oct 2012.
- [26] LBNE Collaboration. Long-Baseline Neutrino Experiment (LBNE) Project, Volume 6: Conventional Facilities at the Far Site. Technical Report LBNE-doc-5017, Oct 2012.
- [27] A. Stahl et al. Expression of Interest for a very long baseline neutrino oscillation experiment (LBNO). 2012.
- [28] R. Acciarri et al. Long-Baseline Neutrino Facility (LBNF) and Deep Underground Neutrino Experiment (DUNE), Volume 1: The LBNF and DUNE Projects. 2016.
- [29] R. Acciarri et al. Long-Baseline Neutrino Facility (LBNF) and Deep Underground Neutrino Experiment (DUNE), Volume 2: The Physics Program for DUNE at LBNF. 2015.
- [30] J. Strait et al. Long-Baseline Neutrino Facility (LBNF) and Deep Underground Neutrino Experiment (DUNE), Volume 3: Long-Baseline Neutrino Facility for DUNE. 2016.

- [31] R. Acciarri et al. Long-Baseline Neutrino Facility (LBNF) and Deep Underground Neutrino Experiment (DUNE), Volume 4: The DUNE Detectors at LBNF. 2016.
- [32] DUNE Collaboration. Proposals and Design Reports. [online] <https://web.fnal.gov/project/LBNF/SitePages/Proposals%20and%20Design%20Reports.aspx>.
- [33] S.D. Holmes et al. PIP-II Status and Strategy. *Proc. of IPAC2015*, pages 3982–3985, 2015.
- [34] Y.K. Kim et al. LBNE Reconfiguration: Steering Committee Report, Aug 2012. [online] <https://indico.fnal.gov/getFile.py/access?contribId=2&resId=0&materialId=slides&confId=11627>.
- [35] [online] <http://www.sanfordlab.org>.
- [36] A. Rubbia. Final Report Summary - LAGUNA-LBNO (Design of a pan-European Infrastructure for Large Apparatus studying Grand Unification, Neutrino Astrophysics and Long Baseline Neutrino Oscillations), Dec 2015.
- [37] A. Badertscher et al. First operation and performance of a 200 lt double phase lar lem-tpc with a 40×76 cm² readout. *Journal of Instrumentation*, 8(04):P04012, 2013.
- [38] A. Badertscher et al. First operation and drift field performance of a large area double phase lar electron multiplier time projection chamber with an immersed greinacher high-voltage multiplier. *Journal of Instrumentation*, 7(08):P08026, 2012.
- [39] A. Badertscher et al. First operation of a double phase LAr Large Electron Multiplier Time Projection Chamber with a two-dimensional projective readout anode. *Nucl. Instrum. Meth.*, A641:48–57, 2011.
- [40] J. E. Campagne et al. Pmm²: R&d on triggerless acquisition for next generation neutrino experiments. *Journal of Instrumentation*, 6(01):C01081, 2011.
- [41] B. Genolini et al. PMm²: Large photomultipliers and innovative electronics for the next-generation neutrino experiments. *Nucl. Instrum. Meth.*, A610:249–252, 2009.
- [42] E. Worcester. PRESENTING LONG-BASELINE SENSITIVITIES. Technical Report DUNE-doc-2329, Jan 2017.
- [43] M. Bass et al. Baseline Optimization for the Measurement of CP Violation, Mass Hierarchy, and θ_{23} Octant in a Long-Baseline Neutrino Oscillation Experiment. *Phys. Rev.*, D91(5):052015, 2015.
- [44] Milind V. Diwan. The Case for a super neutrino beam. *Frascati Phys. Ser.*, 35:89–109, 2004. [,89(2004)].
- [45] I. Esteban et al. Updated fit to three neutrino mixing: exploring the accelerator-reactor complementarity. *JHEP*, 01:087, 2017.
- [46] E. Worcester. LBL CPV Sensitivity: Standard Exposures. Technical Report DUNE-doc-2332, Feb 2017.

- [47] E. Worcester. LBL MH Sensitivity: Standard Exposures. Technical Report DUNE-doc-2335, Feb 2017.
- [48] E. Worcester. LBL Sensitivity: Staging Plots. Technical Report DUNE-doc-2377, Feb 2017.
- [49] E. Worcester. LBL CPV Sensitivity: Exposure Plots. Technical Report DUNE-doc-2401, Feb 2017.
- [50] E. Worcester. LBL MH Sensitivity: Exposure Plots. Technical Report DUNE-doc-2407, Feb 2017.
- [51] J. Beringer et al. Review of particle physics. *Phys. Rev. D*, 86:010001, Jul 2012.
- [52] H. Nishino et al. Search for Nucleon Decay into Charged Anti-lepton plus Meson in Super-Kamiokande I and II. *Phys. Rev.*, D85:112001, 2012.
- [53] A. Bueno, Z. Dai, Y. Ge, M. Laffranchi, A. J. Melgarejo, A. Meregaglia, Sergio Navas, and A. Rubbia. Nucleon decay searches with large liquid argon TPC detectors at shallow depths: Atmospheric neutrinos and cosmogenic backgrounds. *JHEP*, 04:041, 2007.
- [54] J. Klinger, V. A. Kudryavtsev, M. Richardson, and N. J. C. Spooner. Muon-induced background to proton decay in the $p \rightarrow K^+ \bar{\nu}$ decay channel with large underground liquid argon TPC detectors. *Phys. Lett.*, B746:44–47, 2015.
- [55] M. Antonello et al. Precise 3D track reconstruction algorithm for the ICARUS T600 liquid argon time projection chamber detector. *Adv. High Energy Phys.*, 2013:260820, 2013.
- [56] L. Lin and M. Goodman. Comprehensive list of nucleon decay modes. Technical Report DUNE-doc-679, Apr 2016.
- [57] C. Patrignani et al. Review of Particle Physics. *Chin. Phys.*, C40(10):100001, 2016.
- [58] C. Adams et al. The Long-Baseline Neutrino Experiment: Exploring Fundamental Symmetries of the Universe. 2013.
- [59] A. Blake. Studying Atmospheric Neutrino Backgrounds to $p \rightarrow K^+ \bar{\nu} e$ Decay. Technical Report LBNE-doc-8836, Apr 2014.
- [60] K. Scholberg. Supernova neutrino detection. *Annual Review of Nuclear and Particle Science*, 62(1):81–103, 2012.
- [61] R. Laha and J. F. Beacom. Gadolinium in water Cherenkov detectors improves detection of supernova ν_e . *Phys. Rev.*, D89:063007, 2014.
- [62] R. M. Bionta et al. Observation of a neutrino burst in coincidence with supernova 1987a in the large magellanic cloud. *Phys. Rev. Lett.*, 58:1494–1496, Apr 1987.
- [63] K. Hirata et al. Observation of a neutrino burst from the supernova sn1987a. *Phys. Rev. Lett.*, 58:1490–1493, Apr 1987.

- [64] L. Hudepohl, B. Muller, H. T. Janka, A. Marek, and G. G. Raffelt. Neutrino Signal of Electron-Capture Supernovae from Core Collapse to Cooling. *Phys. Rev. Lett.*, 104:251101, 2010. [Erratum: Phys. Rev. Lett.105,249901(2010)].
- [65] M. G. Aartsen et al. Search for dark matter annihilations in the Sun with the 79-string IceCube detector. *Phys. Rev. Lett.*, 110(13):131302, 2013.
- [66] K. Choi et al. Search for neutrinos from annihilation of captured low-mass dark matter particles in the Sun by Super-Kamiokande. *Phys. Rev. Lett.*, 114(14):141301, 2015.
- [67] J. F. Beacom. The Diffuse Supernova Neutrino Background. *Ann. Rev. Nucl. Part. Sci.*, 60:439–462, 2010.
- [68] O. L. Caballero, G. C. McLaughlin, and R. Surman. Neutrino Spectra from Accretion Disks: Neutrino General Relativistic Effects and the Consequences for Nucleosynthesis. *Astrophys. J.*, 745:170, 2012.
- [69] O. L. Caballero, G. C. McLaughlin, R. Surman, and R. Surman. Detecting neutrinos from black hole neutron stars mergers. *Phys. Rev.*, D80:123004, 2009.
- [70] M. Thomson. DUNE Collaboration, Strategy and Detector Requirements. Technical Report LBNE-doc-11100, June 2015.
- [71] M. Adamowski et al. The Liquid Argon Purity Demonstrator. *JINST*, 9:P07005, 2014.
- [72] D. Montanari et al. Performance and Results of the LBNE 35 Ton Membrane Cryostat Prototype. *Phys. Procedia*, 67:308–313, 2015.
- [73] A. Hahn et al. The LBNE 35 Ton Prototype Cryostat. In *Proceedings, 21st Symposium on Room-Temperature Semiconductor X-ray and Gamma-ray Detectors (RTSD 2014): Seattle, WA, USA, November 8-15, 2014*, page 7431158, 2016.
- [74] E. D. Church. LArSoft: A Software Package for Liquid Argon Time Projection Drift Chambers. 2013.
- [75] The LArSoft collaboration. Software for LArTPCs, 2017. [online] <http://larsoft.org>.
- [76] R. Brun and F. Rademakers. ROOT: An object oriented data analysis framework. *Nucl. Instrum. Meth.*, A389:81–86, 1997.
- [77] S. Agostinelli et al. Geant4—a simulation toolkit. *Nuclear Instruments and Methods in Physics Research Section A: Accelerators, Spectrometers, Detectors and Associated Equipment*, 506(3):250 – 303, 2003.
- [78] C. Andreopoulos et al. The GENIE neutrino Monte Carlo generator. *Nuclear Instruments and Methods in Physics Research Section A: Accelerators, Spectrometers, Detectors and Associated Equipment*, 614(1):87 – 104, 2010.
- [79] D. Casper. The Nuance neutrino physics simulation, and the future. *Nucl. Phys. Proc. Suppl.*, 112:161–170, 2002. [,161(2002)].
- [80] C. Hagman et al. Cosmic-ray Shower Library CRY, 2012. [online] http://nuclear.llnl.gov/simulation/doc_cry_v1.7/cry.pdf.

- [81] C. Hagmann, D. Lange, and D. Wright. Monte carlo simulation of proton-induced cosmic-ray cascades in the atmosphere. *Lawrence Livermore National Laboratory*, 2007.
- [82] D. Heck, G. Schatz, J. Knapp, T. Thouw, and J.N. Capdevielle. CORSIKA: A Monte Carlo code to simulate extensive air showers. Technical report, 1998.
- [83] V.A. Kudryavtsev. Muon simulation codes MUSIC and MUSUN for underground physics. *Computer Physics Communications*, 180(3):339 – 346, 2009.
- [84] V. A. Kudryavtsev, N. J. C. Spooner, and J. E. McMillan. Simulations of muon induced neutron flux at large depths underground. *Nucl. Instrum. Meth.*, A505:688–698, 2003.
- [85] P. Antonioli, C. Ghetti, E. V. Korolkova, V. A. Kudryavtsev, and G. Sartorelli. A Three-dimensional code for muon propagation through the rock: Music. *Astropart. Phys.*, 7:357–368, 1997.
- [86] V. A. Kudryavtsev, E. V. Korolkova, and N. J. C. Spooner. Narrow muon bundles from muon pair production in rock. *Phys. Lett.*, B471:251–256, 1999.
- [87] T. Alion. LBNE Geometries, Aug 2014. [online] https://cdcvn.fnal.gov/redmine/projects/lbnecode/wiki/LBNE_Geometries.
- [88] J. Asaadi et al. The Current Status of Simulation and Reconstruction for the DUNE Far Detector. Technical Report DUNE-doc-1689, Sept 2016.
- [89] C. Harris and M. Stephens. A combined corner and edge detector. Citeseer, 1988.
- [90] P. V. C. Hough. Machine Analysis Of Bubble Chamber Pictures. In *Proceedings, 2nd International Conference on High-Energy Accelerators and Instrumentation, HEACC 1959: CERN, Geneva, Switzerland, September 14-19, 1959*, volume C590914, pages 554–558, 1959.
- [91] J. S. Marshall and M. A. Thomson. The Pandora Software Development Kit for Pattern Recognition. *Eur. Phys. J.*, C75(9):439, 2015.
- [92] M. Wallbank. EMShower Reconstruction. Technical Report DUNE-doc-1369, June 2016.
- [93] J. B. Birks. The efficiency of organic scintillatois. *ORGANIC*, page 12, 1960.
- [94] R. Acciarri et al. A study of electron recombination using highly ionizing particles in the ArgoNeuT Liquid Argon TPC. *JINST*, 8:P08005, 2013.
- [95] J. Thomas and D. A. Imel. Recombination of electron-ion pairs in liquid argon and liquid xenon. *Phys. Rev. A*, 36:614–616, Jul 1987.
- [96] A. Blatter et al. Experimental study of electric breakdowns in liquid argon at centimeter scale. *Journal of Instrumentation*, 9(04):P04006, 2014.
- [97] S. C. Delaquis, R. Gornea, S. Janos, M. Lüthi, C. Rudolf von Rohr, M. Schenk, and J. L. Vuilleumier. Development of a camera casing suited for cryogenic and vacuum applications. *JINST*, 8:T12001, 2013.

- [98] K. Mavrokordis, F. Ball, J. Carroll, M. Lazos, K. J. McCormick, N. A. Smith, C. Touramanis, and J. Walker. Optical Readout of a Two Phase Liquid Argon TPC using CCD Camera and THGEMs. *JINST*, 9:P02006, 2014.
- [99] E. Erdal, L. Arazi, V. Chepe, M. L. Rappaport, D. Vartsky, and A. Breskin. Direct observation of bubble-assisted electroluminescence in liquid xeno. *JINST*, 10(11):P11002, 2015.
- [100] N. McConkey, N. Spooner, M. Thiesse, M. Wallbank, and T. K. Warburton. Cryogenic CMOS Cameras for High Voltage Monitoring in Liquid Argon. 2016.
- [101] G. Ghibaudo and F. Balestra. Low temperature characterization of silicon cmos devices. *Microelectronics Reliability*, 37(9):1353 – 1366, 1997.
- [102] H. Zhao and X. Liu. A low-power cryogenic analog to digital converter in standard CMOS technology. *Cryogenics*, 55:79–83, May 2013.
- [103] M. Antonello et al. A Proposal for a Three Detector Short-Baseline Neutrino Oscillation Program in the Fermilab Booster Neutrino Beam. 2015.
- [104] H. Bethe. Zur theorie des durchgangs schneller korpuskularstrahlen durch materie. *Annalen der Physik*, 397(3):325–400, 1930.
- [105] F. Bloch. Zur bremsung rasch bewegter teilchen beim durchgang durch materie. *Annalen der Physik*, 408(3):285–320, 1933.
- [106] X. Qian. A Four-Plane proposal for Single-Phase LArTPC. Far Detector Sim/Reco working group meeting, Sept 2016. [online] <https://indico.fnal.gov/getFile.py/access?contribId=78&sessionId=20&resId=0&materialId=slides&confId=10613>.
- [107] J. Insler. Module to unstick ADC codes. 35 ton working group meeting, March 2016. [online] <https://indico.fnal.gov/getFile.py/access?contribId=2&resId=0&materialId=slides&confId=11627>.
- [108] MicroBooNE Collaboration. Noise Characterization and Filtering in the MicroBooNE TPC. Technical Report MICROBOONE-NOTE-1016-PUB, July 2016.
- [109] J. Cooley and J. Turkey. An algorithm for the machine calculation of complex fourier series. *Math. Comp.*, 19:297–301, 1965.
- [110] N. Wiener. *Extrapolation, Interpolation, and Smoothing of Stationary Time Series*. [Cambridge]: Technology Press of the Massachusetts Institute of Technology., 1942.
- [111] M. Johnson et al. 35T Observations and Measurements. Technical Report DUNE-doc-1704, Aug 2016.
- [112] L. Bagby et al. 35T Noise Studies Summary - APA wire readout noise. Technical Report DUNE-doc-1834, Oct 2016.
- [113] T. Yang. Update on reconstruction of 35t data. 35 ton working group meeting, June 2016. [online] <https://indico.fnal.gov/getFile.py/access?contribId=1&resId=0&materialId=slides&confId=12349>.

- [114] P.H.S Torr and A. Zisserman. Mlesac: A new robust estimator with application to estimating image geometry. *Computer Vision and Image Understanding*, 78(1):138–156, 2000.
- [115] M. Thiesse. Hit reconstruction and purity. 35 ton working group meeting, Aug 2016. [online] <https://indico.fnal.gov/getFile.py/access?contribId=1&resId=0&materialId=slides&confId=12859>.
- [116] C. Anderson et al. The ArgoNeuT Detector in the NuMI Low-Energy beam line at Fermilab. *JINST*, 7:P10019, 2012.
- [117] T. Yang. Update on 35 ton analysis. 35 ton working group meeting, June 2016. [online] <https://indico.fnal.gov/getFile.py/access?contribId=1&resId=0&materialId=slides&confId=12396>.
- [118] S.E. Derenzo et al. Test of a liquid argon chamber with 20 μm RMS resolution. *Nuclear Instruments and Methods*, 122:319–327, December 1974.
- [119] S. E. Derenzo. LBL Physics Note No. 786: Electron diffusion and positive ion charge retention in liquid-filled high-resolution multi- strip ionization-mode chambers. unpublished, 1974.
- [120] E. Shibamura, T. Takahashi, S. Kubota, and T. Doke. Ratio of diffusion coefficient to mobility for electrons in liquid argon. *Phys. Rev. A*, 20:2547–2554, Dec 1979.
- [121] V. M. Atrazhev and I. V. Timoshkin. Trasport of electrons in atomic liquids in high electric fields. *IEEE Trans. Dielectrics and Electrical Insulation*, 5:450–457, 1998.
- [122] Y. Li et al. Measurement of Longitudinal Electron Diffusion in Liquid Argon. *Nucl. Instrum. Meth.*, A816:160–170, 2016.
- [123] D. Braillsford. Looking at electron diffusion in 35t data and MC. 35 ton working group meeting, Sept 2016. [online] <https://indico.fnal.gov/getFile.py/access?contribId=43&sessionId=19&resId=0&materialId=slides&confId=10613>.
- [124] C Bromberg et al. Design and operation of longbo: a 2 m long drift liquid argon tpc. *Journal of Instrumentation*, 10(07):P07015, 2015.
- [125] M. Richardson. *Cosmic ray background estimations in large liquid argon detectors for proton decay via $p \rightarrow K^+ \bar{\nu}$ and ν_e appearance from ν_μ beam*. PhD thesis, The University of Sheffield, 2016.
- [126] N. S. Bowden. Review Report: Mini-Review of Operation of the LBNE Far Detector at the Surface. Technical Report LBNE-doc-6493, Oct 2012.
- [127] D. Wright. Shielding Physics List Description, June 2012. [online] http://www.slac.stanford.edu/comp/physics/geant4/slac_physics_lists/shielding/physlistdoc.html.
- [128] B. Baller. LAr-FD Parameters Spreadsheet. Technical Report LBNE-doc-3383, Aug 2015.
- [129] D. Cherdack. The LBNE Fast MC. Technical Report LBNE-doc-7806, Sept 2013.

- [130] D. Barker et al. Muon-induced background for beam neutrinos at the surface. LBNE Reconfiguration Report, Aug 2012. [online] =http://www.fnal.gov/directorate/lbne_reconfiguration/files/LBNE-Reconfiguration-Surface-Detector-August2012.pdf.
- [131] D. Mei, C. Zhang, and D. Barker. USD Cosmogenics Backgrounds Simulation Overview. Technical Report LBNE-doc-6621, Nov 2012.
- [132] D. Coelho, M. Szydagis, and R. Svoboda. Improving Electron / Gamma Separation. Technical Report LBNE-doc-8458, Nov 2012.
- [133] A. Hitachi et al. Effect of ionization density on the time dependence of luminescence from liquid argon and xenon. *Phys. Rev. B*, 27:5279–5285, May 1983.
- [134] T. K. Gaisser. *Cosmic rays and particle physics*. Cambridge, UK: Univ. Pr. (1990) 279 p, 1990.
- [135] M. Aglietta et al. Muon “depth-intensity” relation measured by the lvd underground experiment and cosmic-ray muon spectrum at sea level. *Phys. Rev. D*, 58:092005, Oct 1998.
- [136] A. Dar. Atmospheric neutrinos, astrophysical neutrons, and proton-decay experiments. *Phys. Rev. Lett.*, 51:227–230, Jul 1983.
- [137] T. Blackwell, V. A. Kudryavtsev, and M. Richardson. Cosmic-ray Spectra from CRY. Technical Report LBNE-doc-7517, July 2013.
- [138] G. J. Feldman and R. D. Cousins. Unified approach to the classical statistical analysis of small signals. *Phys. Rev. D*, 57:3873–3889, Apr 1998.
- [139] D. M. Mei, C. Zhang, K. Thomas, and F. Gray. Early Results on Radioactive Background Characterization for Sanford Laboratory and DUSEL Experiments. *Astropart. Phys.*, 34:33–39, 2010.
- [140] M. L. Cherry, M. Deakyne, K. Lande, C. K. Lee, R. I. Steinberg, B. Cleveland, and E. J. Fenyves. Multiple muons in the homestake underground detector. *Phys. Rev. D*, 27:1444–1447, Apr 1983.
- [141] E. Church. September 2016 Progress Report from the Atmospheric Neutrinos, Nucleon Decay, and Cosmogenics Working Groups. Technical Report DUNE-doc-1644, Sept 2016.
- [142] V. A. Kudryavtsev et al. Muon simulations for LBNE using MUSIC and MUSUN. Technical Report LBNE-doc-9673, Sept 2014.
- [143] M. Robinson. Cosmogenic background to nucelon decay. Cosmogenics working group meeting, Jan 2017. [online] <https://indico.fnal.gov/getFile.py/access?contribId=104&sessionId=14&resId=0&materialId=slides&confId=10641>.

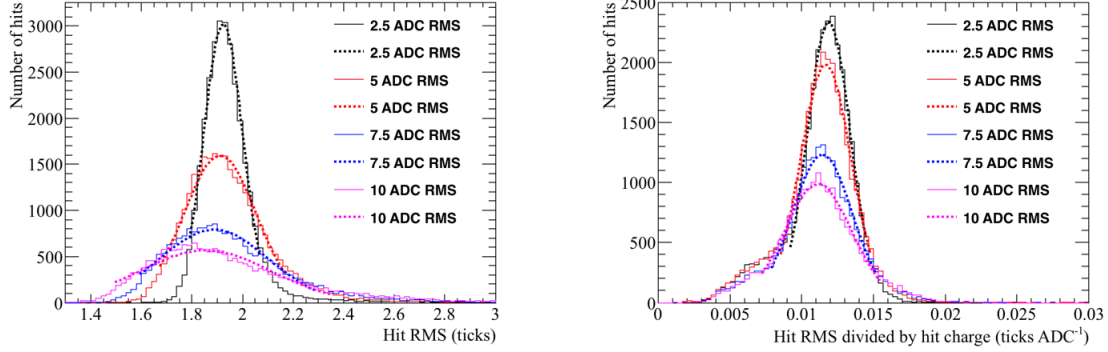
Appendix A

Supporting figures to Monte Carlo studies concerning determining interaction times using the effects of diffusion

Figure A.1, shows how the most probable values of the hit RMS and hit $RMS/Charge$ change as the electronics noise increases, for hits between 20 and 30 cm from the APAs. Figure A.2, shows how the most probable values of hit RMS changes as drift distance increases for track associated with counter differences of 4, for different values of the electronics noise. Figure A.3, shows how the most probable value of hit RMS next to the APAs changes for increasing counter difference. Figure A.4, shows the normalised hit charge distributions for increasing noise levels, and the cut which is applied to remove the tails of the distribution.

Figure A.5, shows how the most probable values of the hit RMS and hit $RMS/Charge$ change as the electron lifetime increases, for hits between 20 and 30 cm from the APAs. Figure A.6, shows how the most probable values of hit RMS changes as drift distance increases for track associated with counter differences of 4, for different values of the electron lifetime. Figure A.7, shows how the most probable value of hit RMS next to the APAs changes for increasing counter difference.

Figure A.9, shows how the most probable values of the hit RMS and hit $RMS/Charge$ change as the electric field increases, for hits between 20 and 30 cm from the APAs. Figure A.10, shows how the most probable values of hit RMS changes as drift distance increases



(a) The most probable hit *RMS* values for hits between $x = 20$ cm and $x = 30$ cm.
 (b) The most probably hit *RMS/Charge* values for hits between $x = 20$ cm and $x = 30$ cm.

Fig. A.1 The most probable values of the hit *RMS* and hit *RMS/Charge* distributions for hits between $x = 20$ cm and $x = 30$ cm, for tracks with a counter difference of 4, as the electronics noise changes.

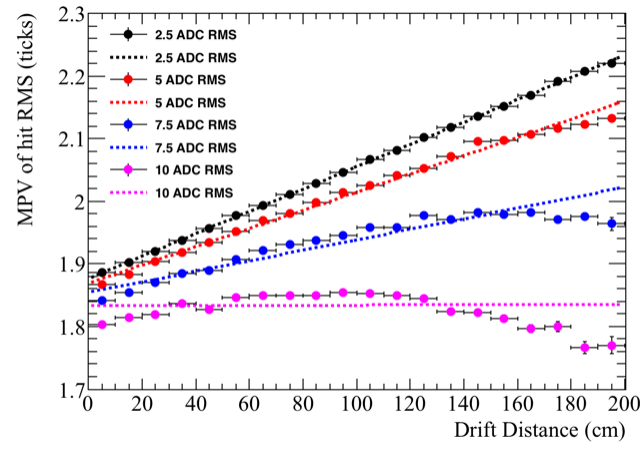


Fig. A.2 The most probable values of hit *RMS* as a function of drift distance, for tracks associated with a coincidence that had a counter difference of 4, as the electronics noise changes.

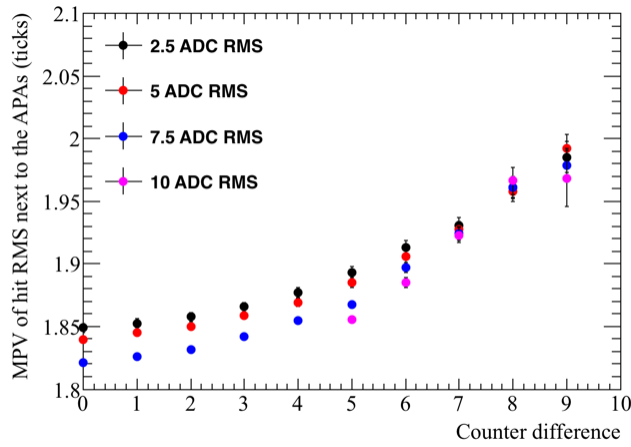


Fig. A.3 The most probable values of hit *RMS* within 10 cm of the APAs, as a function of the counter difference of the coincidence, that the track was associated with, as the electronics noise changes.

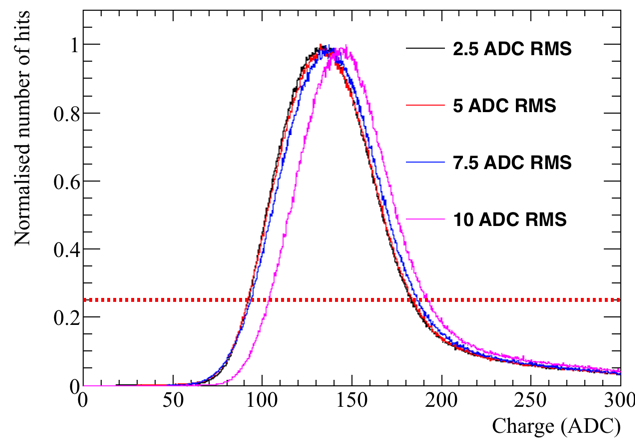
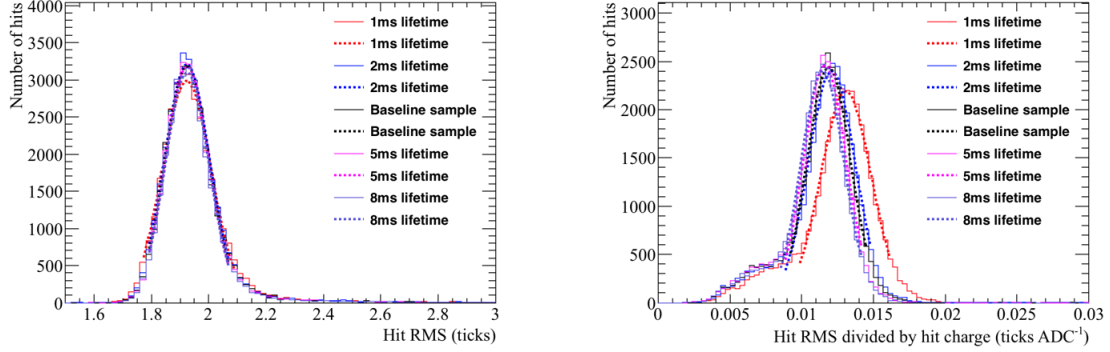


Fig. A.4 The normalised hit charge distribution as the electronics noise changes. The hit charge is shown in units of ADC, and is normalised so that the most common hit charge has a value of 1. A cut on the normalised number of hits being greater than 0.25 is shown, the aim of this cut is to remove the tails of the hit charge distribution.



(a) The most probable hit *RMS* values for hits between $x = 20$ cm and $x = 30$ cm.

(b) The most probably hit *RMS/Charge* values for hits between $x = 20$ cm and $x = 30$ cm.

Fig. A.5 The most probable values of the hit *RMS* and hit *RMS/Charge* distributions for hits between $x = 20$ cm and $x = 30$ cm, for tracks with a counter difference of 4, as the electron lifetime changes.

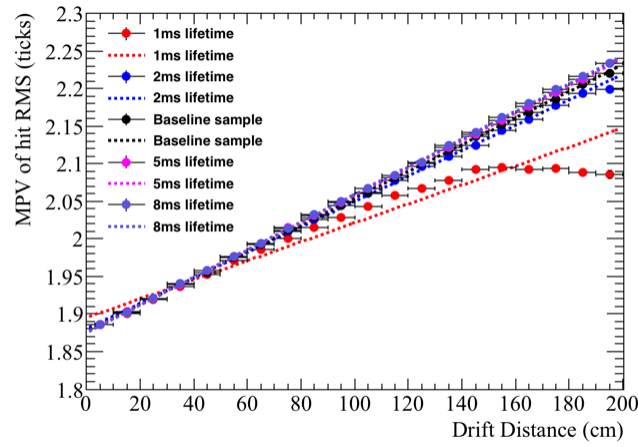


Fig. A.6 The most probable values of hit *RMS* as a function of drift distance, for tracks associated with a coincidence that had a counter difference of 4, as the electron lifetime changes.

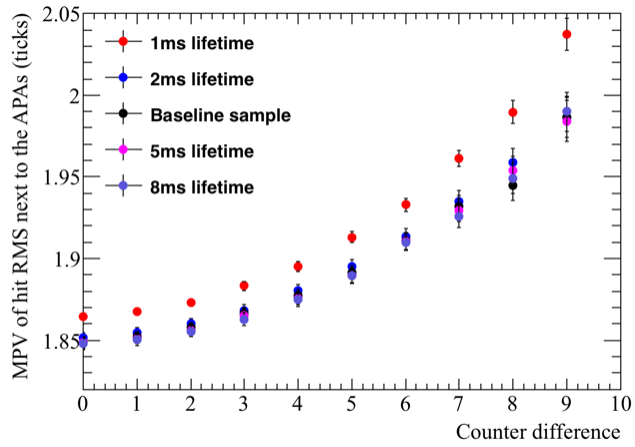


Fig. A.7 The most probable values of hit *RMS* within 10 cm of the APAs, as a function of the counter difference of the coincidence, that the track was associated with, as the electron lifetime changes.

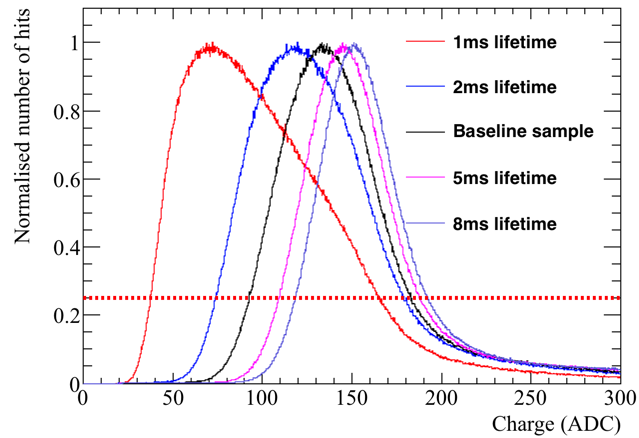
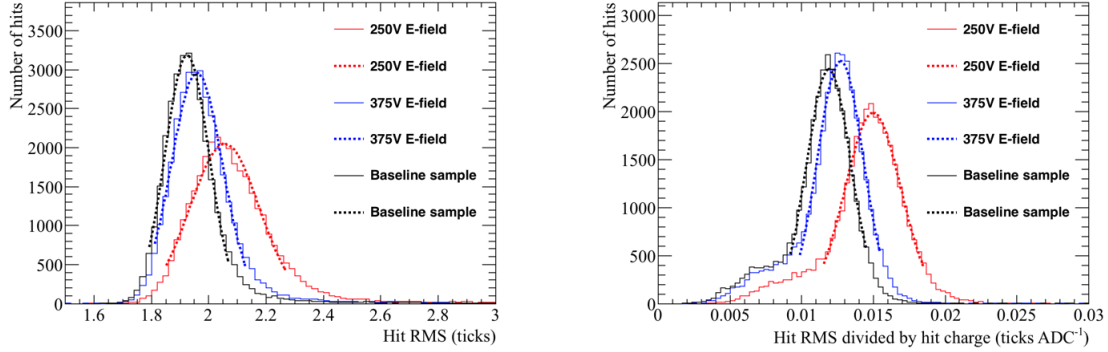


Fig. A.8 The normalised hit charge distribution as the electron lifetime changes. The hit charge is shown in units of ADC, and is normalised so that the most common hit charge has a value of 1. A cut on the normalised number of hits being greater than 0.25 is shown, the aim of this cut is to remove the tails of the hit charge distribution.



(a) The most probable hit *RMS* values for hits between $x = 20$ cm and $x = 30$ cm.
(b) The most probably hit *RMS/Charge* values for hits between $x = 20$ cm and $x = 30$ cm.

Fig. A.9 The most probable values of the hit *RMS* and hit *RMS/Charge* distributions for hits between $x = 20$ cm and $x = 30$ cm, for tracks with a counter difference of 4, as the electric field changes.

for track associated with counter differences of 4, for different values of the electric field. Figure A.11, shows how the most probable value of hit *RMS* next to the APAs changes for increasing counter difference.

Figure A.13, shows how the most probable values of the hit *RMS* and hit *RMS/Charge* change as the constant of longitudinal diffusion increases, for hits between 20 and 30 cm from the APAs. Figure A.14, shows how the most probable values of hit *RMS* changes as drift distance increases for track associated with counter differences of 4, for different values of the constant of longitudinal diffusion. Figure A.15, shows how the most probable value of hit *RMS* next to the APAs changes for increasing counter difference.

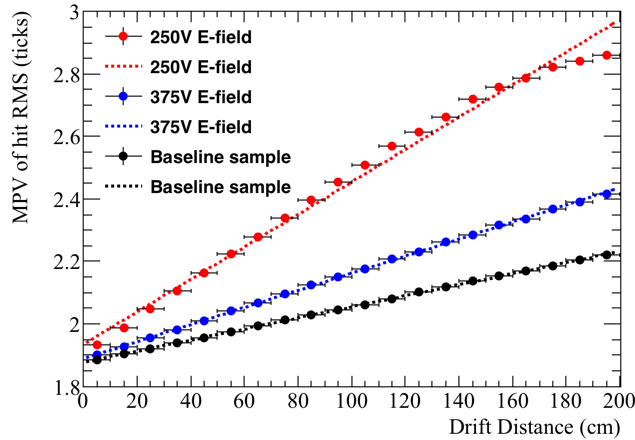


Fig. A.10 The most probable values of hit *RMS* as a function of drift distance, for tracks associated with a coincidence that had a counter difference of 4, as the electric field changes.

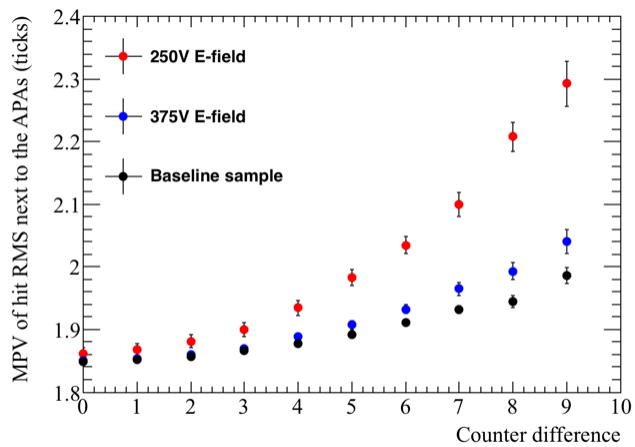


Fig. A.11 The most probable values of hit *RMS* within 10 cm of the APAs, as a function of the counter difference of the coincidence, that the track was associated with, as the electric field changes.

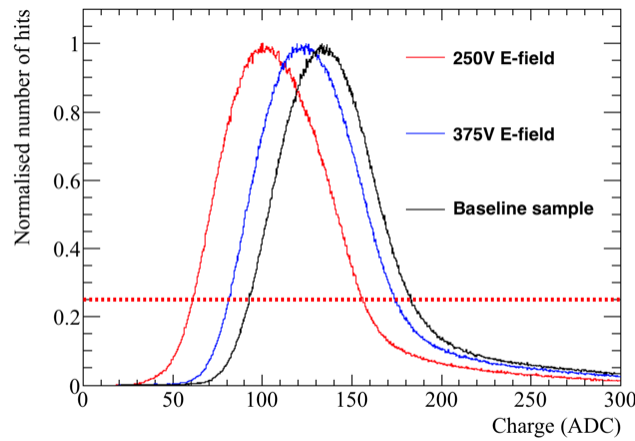
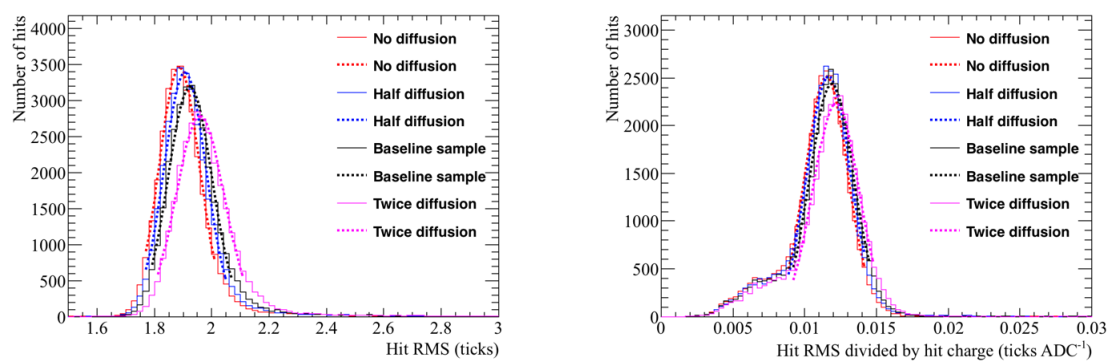


Fig. A.12 The normalised hit charge distribution as the electric field changes. The hit charge is shown in units of ADC, and is normalised so that the most common hit charge has a value of 1. A cut on the normalised number of hits being greater than 0.25 is shown, the aim of this cut is to remove the tails of the hit charge distribution.



(a) The most probable hit *RMS* values for hits between $x = 20$ cm and $x = 30$ cm.

(b) The most probable hit *RMS/Charge* values for hits between $x = 20$ cm and $x = 30$ cm.

Fig. A.13 The most probable values of the hit *RMS* and hit *RMS/Charge* distributions for hits between $x = 20$ cm and $x = 30$ cm, for tracks with a counter difference of 4, as the constant of longitudinal diffusion changes.

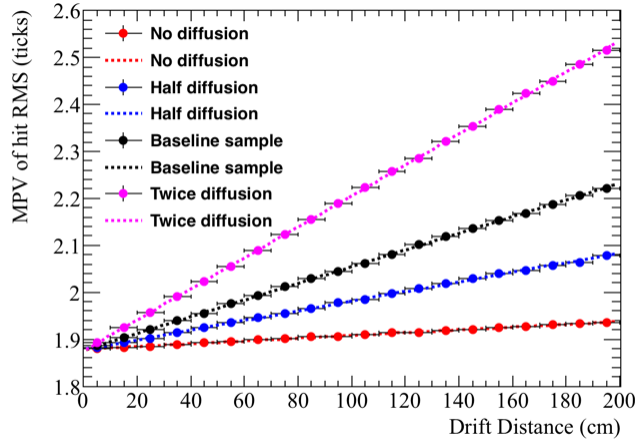


Fig. A.14 The most probable values of hit *RMS* as a function of drift distance, for tracks associated with a coincidence that had a counter difference of 4, as the constant of longitudinal diffusion changes.

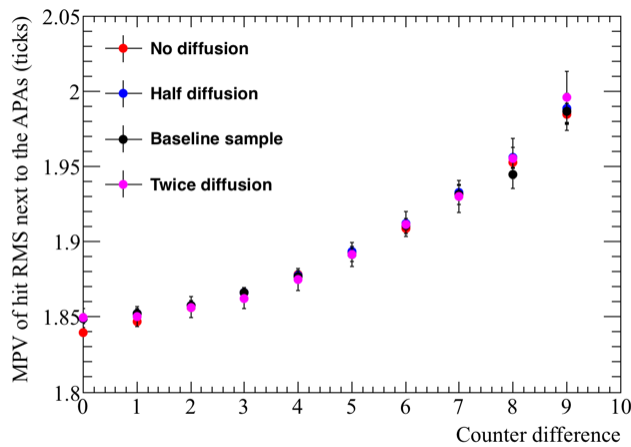


Fig. A.15 The most probable values of hit *RMS* within 10 cm of the APAs, as a function of the counter difference of the coincidence, that the track was associated with, as the constant of longitudinal diffusion changes.

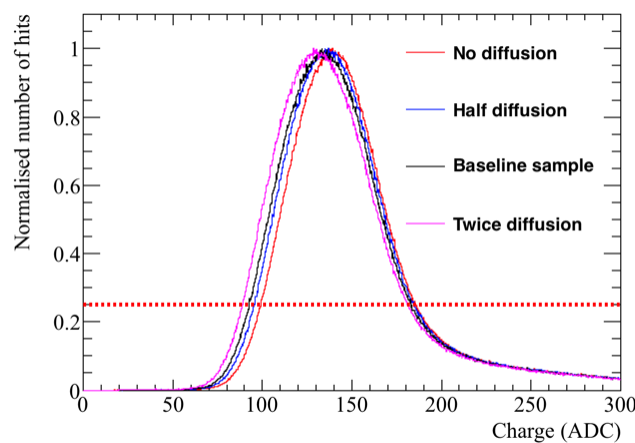


Fig. A.16 The normalised hit charge distribution as the constant of longitudinal diffusion changes. The hit charge is shown in units of ADC, and is normalised so that the most common hit charge has a value of 1. A cut on the normalised number of hits being greater than 0.25 is shown, the aim of this cut is to remove the tails of the hit charge distribution.

Appendix B

Something else mildly interesting